Middle Eocene Paleoceanography and Astrochronology in the Western North Atlantic

Dissertation

zur Erlangung des
Doktorgrades der Naturwissenschaften
-Dr. rer. nat.-
am Fachbereich Geowissenschaften
der Universität Bremen

Vorgelegt von
Maximilian Vahlenkamp
Bremen, Juli 2017

Gutachter/Reviewer

Prof. Dr. Heiko Pälike
University of Bremen
MARUM - Centre for Marine Environmental Sciences
Klagenfurter Str.
28359 Bremen, Germany
hpaelike@marum.de

Prof. Dr. Lucas Lourens
Utrecht University
Earth Sciences
Heidelberglaan 2
3584 CS Utrecht, The Netherlands
l.j.lourens@uu.nl

Versicherung an Eides Statt

gem. § 5 Abs. 5 der Promotionsordnung vom 15.07.2015

Ich, Maximilian Vahlenkamp, Parkstraße 79, 28209 Bremen, Matr.-Nr.:2283449
(Vorname, Name, Anschrift, ggf. Matr.-Nr.)

versichere an Eides Statt durch meine Unterschrift, dass ich die vorstehende Arbeit selbständig und ohne fremde Hilfe angefertigt und alle Stellen, die ich wörtlich dem Sinne nach aus Veröffentlichungen entnommen habe, als solche kenntlich gemacht habe, mich auch keiner anderen als der angegebenen Literatur oder sonstiger Hilfsmittel bedient habe, und die zu Prüfungszwecken beigelegte elektronische Version der Dissertation mit der abgegebenen gedruckten Version identisch ist.

Ich versichere an Eides Statt, dass ich die vorgenannten Angaben nach bestem Wissen und Gewissen gemacht habe und dass die Angaben der Wahrheit entsprechen und ich nichts verschwiegen habe.

Die Strafbarkeit einer falschen eidesstattlichen Versicherung ist mir bekannt, namentlich die Strafandrohung gemäß § 156 StGB bis zu drei Jahren Freiheitsstrafe oder Geldstrafe bei vorsätzlicher Begehung der Tat bzw. gemäß § 161 Abs. 1 StGB bis zu einem Jahr Freiheitsstrafe oder Geldstrafe bei fahrlässiger Begehung.

Bremen, 10.07.2017
Ort, Datum

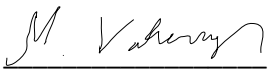
Unterschrift

Preface

The research for this dissertation was conducted at MARUM - Center for Marine Environmental Sciences at the University of Bremen, Germany from 16 July 2014 - 12 July 2017. The work was generously funded by the European Research Council Consolidator Grant EarthSequencing (617462) awarded to Prof. Dr. Heiko Pälike.

The research presented in this dissertation is based on data collected during Integrated Ocean Drilling Program (IODP) Expedition 342 - Paleogene Newfoundland Sediment Drifts. IODP Leg 342 sailed off Newfoundland between 1 June - 30 July 2012.

The work for this dissertation started in July 2014 in coordination with the science party of Leg 342. More than 1400 samples were taken in the IODP - Bremen Core Repository, washed, picked and analysed for benthic stable isotopes at MARUM. Some of the work for this dissertation was conducted during a research stay from 1 January 2016 - 13 March 2016 at the Department of Earth and Planetary Sciences of the University of California, Santa Cruz, USA in the laboratory of Prof. Dr. Jim Zachos.

Abstract

The middle Eocene (47.8-38 Ma) marks the transition from the early Cenozoic greenhouse into the late Cenozoic icehouse climate. The early Cenozoic was characterized by warm temperatures, high atmospheric CO_2 concentration (~1000 ppm) and a non-existent or minor cryosphere. The climatic cooling towards the major glaciation of Antarctica is only partially covered by sedimentary records from scientific deep-sea drilling, which allow for high-resolution paleoceanographic studies. In the context of anthropogenic CO_2 emissions and consequent global warming, the study of the nature and causes of climatic variability and the role of the ocean in the climate system during greenhouse climate is one of the fundamental challenges of paleoclimatology. Studying past times of extreme warmth and elevated CO_2 enables us to anticipate the magnitude and potential consequences of future climate change.

To understand the sequence of climatic, biotic and tectonic events before, during and after the middle Eocene cooling and to unravel cause-and-effect relationships, the determination of geological ages and rates of change are crucial. However, no robust astronomical timescale exists for large parts of the Eocene, the so-called “middle Eocene tuning gap”. Middle Eocene cyclic carbonate-rich sequences, drilled during IODP Expedition 342 demonstrate well-developed lithological alternations, offering a unique opportunity to build a high-resolution astrochronology across the “middle Eocene tuning gap”. The ratio between the elemental intensities of calcium and iron (Ca/Fe) of sediments from Sites U1408 and U1410 trace the lithological alternations particularly well, and form the basis of an astronomically-tuned chronology spanning the astrochronological gap. It is noteworthy that this study utilizes, for the first time, the stable 173-kyr amplitude modulation of obliquity as an astronomical tuning target. Combining the elemental intensities of calcium and iron of sediments from Site U1410 with a newly generated high-resolution record of benthic stable oxygen and carbon isotope provides a unique archive of paleoceanographic change. This new archive allows for the characterization of orbital-scale ocean circulation changes in the North Atlantic, in a climate system that transitioned from the extreme warmth of the early Eocene towards major glaciation at the Eocene-Oligocene boundary.

Based on the dominant 41-kyr period in proxy records from the western North Atlantic, obliquity is interpreted to be the main driver of middle Eocene North Atlantic overturning circulation variability. Cool periods are interpreted as obliquity minima and characterized by nutrient-depleted deep waters in the western North Atlantic. At the same time, the Deep Western Boundary Current strengthened. Northern Component Water formation is thus associated with obliquity minima. During obliquity maxima, the Deep Western Boundary Currents are weaker and warmer, while nutrients are more abundant. These aspects reflect a more sluggish Northern Component Water formation. This obliquity-driven paleoceanographic regime is in excellent agreement with results from a fully-coupled Earth System Model for the middle

Eocene. It shows that decreased vertical density gradients resulting from cool temperatures in the North Atlantic were the primary causes of intensification of Atlantic Meridional Overturning Circulation during obliquity minima and vice versa.

The Earth System Model *COSMOS* was used to constrain the physical properties involved in early Cenozoic deep-water formation and to evaluate the sensitivity of the middle Eocene ocean circulation to changes in atmospheric CO_2 and seaway configurations. It showed that substantial deepening of Northern Component Water and an invigoration of the thermohaline circulation results from the drawdown of atmospheric CO_2. Increased surface water density at the primary deep-water formation site, the southern Greenland-Norwegian Sea, is the facilitator of convection. The critical role of the Greenland-Scotland Ridge for the formation of Northern Component Water is reflected in our simulations with different sill depths. A sill depth of 50-200 m is the necessary threshold to allow for sufficient inflow of warm, salty Atlantic surface waters into the Greenland-Norwegian Sea, which initiate convection during winter cooling. Further deepening of the sill leads to an increase of the overflow capacity of the sill and results in invigoration and deepening of the thermohaline circulation. A seaway between the Greenland-Norwegian Sea and the Arctic hinders the formation of Northern Component Waters via the inflow of brackish waters from the Arctic into the Greenland-Norwegian Sea. The influence of Tethyan waters to the subtropical North Atlantic does not substantially influence the strength or geometry of Northern Component Water formation in the simulations.

This dissertation provides new stratigraphic and paleoceanographic insights into the transition from the early Cenozoic greenhouse towards the modern icehouse world. Using the 173-kyr obliquity amplitude modulation provides a key methodological advance that can be utilized by future studies. The presented oxygen isotope record is the highest resolution benthic isotope record of the middle Eocene currently available. It contributes significantly to the effort for a single locality benthic stable isotope composite of orbital resolution covering the entire Eocene. When complete, this composite record will provide the middle Eocene backbone of the global benthic isotope compilations and can be used as a record of the North Atlantic deep ocean endmember. Insights about the early Northern Component Water formation help to elaborate our knowledge about the governing processes of ocean circulation under greenhouse conditions.

Zusammenfassung

Das mittlere Eozän (47.8-38 Ma) wird gekennzeichnet durch den Übergang vom warmen Treibhausklima des frühen Känozoikums bis hin zum deutlich kälteren Klima des späten Känozoikums. Im frühen Känozoikum verhinderten hohe Temperaturen und ein deutlich erhöhter atmosphärischer Kohlendioxidgehalt (~1000 ppm) die Bildung von großen Eisschilden und Meereis. Die Abkühlung von der wärmsten Phase des Känozoikums, dem frühen Eozän, bis zur Bildung großer Eisschilde in der Antarktis an der Eozän-Oligozän Grenze ist bisher anhand von wissenschaftlichen Bohrkernen nur lückenhaft dokumentiert. Im Zusammenhang mit dem anthropogenen CO_2-Ausstoß und der daraus folgenden globalen Erwärmung ist es jedoch von essentieller Bedeutung, die Gründe für Klimaveränderungen und die Rolle der Ozeane in besonders warmen Zeiten der Erdgeschichte zu verstehen. Diese können uns helfen, die Größenordnung und potentiellen Folgen des zukünftigen Klimawandels einzuordnen.

Um die klimatischen, biotischen und tektonischen Veränderungen vor, während und nach der mitteleozänen Abkühlung zu verstehen, ist es wichtig, geologische Alter genau zu bestimmen, damit Ursache und Wirkung von Veränderungen aufgeschlüsselt werden können. Bisher existiert jedoch kein unumstrittenes astronomisches Altersmodell für die so genannte „mitteleozäne Lücke“ (engl.: „middle Eocene tuning gap“). Mitteleozäne Bohrkerne des Integrated Ocean Drilling Program (IODP Expedition 342) aus dem westlichen Nordatlantik sind von ausgeprägten lithologischen Wechselfolgen zwischen terrigenem und biogenem Schlamm gekennzeichnet. Das Elementverhältnis von Calcium zu Eisen in den Sedimenten der Kernlokationen U1408 und U1410 wurde benutzt, um ein astronomisch getuntes Altersmodell für das mittlere Eozän zu erstellen. Hierbei wurde die stabile Amplitudenmodulation (173.000 Jahre) der Obliquität zum ersten Mal als astronomische Zielkurve genutzt.

Kombiniert mit einem neuen, hochauflösenden Datensatz von stabilen Isotopen an benthischen Foraminiferen, welcher im Rahmen dieser Arbeit erstellt wurde, bieten diese Elementverhältnisse ein Archiv des eozänen paläozeanographischen Wandels. Dieses Archiv ermöglicht eine Untersuchung der Ozeanzirkulation des Nordatlantiks auf orbitalen Zeitskalen während des Übergangs von den Zeiten extremer Wärme des Paleozäns in die Abkühlungsphase des mittleren Eozäns.

Der dominante Einundvierzigtausendjahreszyklus in den Proxys aus dem westlichen Nordatlantik lässt auf Obliquitätsschwankungen als Hauptursache für Veränderungen in der Tiefenwasserzirkulation des Nordatlantiks schließen. Kalte Phasen werden als Obliquitätsminima interpretiert, in denen der Nordatlantik von nährstoffarmen Tiefenwassern geprägt wird, die im europäischen Nordmeer gebildet wurden. Dagegen sind warme Obliquitätsmaxima mit schwächerer Tiefenwasserzirkulation und nährstoffreicheren

Tiefenwassern im westlichen Nordatlantik verbunden, die eine geminderte Tiefenwasserkonvektion im europäischen Nordmeer widerspiegeln. Das beschriebene obliquitätsgesteuerte paläozeanographische Regime stimmt exzellent mit den Ergebnissen des gekoppelten Klimamodells *COSMOS* für das mittlere Eozän überein, welches zeigt, dass verminderte (erhöhte) vertikale Dichtegradienten durch kühle (warme) Temperaturen im Europäischen Nordmeer die Hauptursachen für die Intensivierung (Abschwächung) des Nordatlantischen Tiefenwassers sind.

Weitere Experimente mit dem Klimamodell *COSMOS* wurden genutzt, um die Resonanz des Klimasystems und der Ozeanzirkulation auf Veränderungen im atmosphärischen CO_2-Gehalt und die tektonische Öffnung und Schließung von ozeanischen Verbindungen zu überprüfen. Eine wesentliche Verstärkung und Vertiefung des nordatlantischen Tiefenwassers resultiert aus dem Absinken des atmosphärischen CO_2, ausgelöst durch die erhöhte Dichte des Oberflächenwassers in den primären nordatlantischen Tiefenwasserbildungsgebieten des Europäischen Nordmeers. Die maßgebliche Rolle des Grönland-Schottland-Rückens wird in Simulationen mit unterschiedlicher Schwellentiefe deutlich. Ein Grenzwert zwischen 50-200 m Schwellentiefe ist notwendig um eine Überlaufkapazität zu gewährleisten, die Tiefenwasserbildung zulässt. Im Gegensatz dazu wird die Tiefenwasserzirkulation im mittleren Eozän von der Isolation der Arktis begünstigt. Tiefenwasserbildung wird unter eozänen Bedingungen selbst von einer Flachwasserverbindung zwischen dem Europäischen Nordmeer und der Arktis aufgrund des geringen Salzgehalts im Oberflächenwasser verhindert. Der Einfluss der Öffnung zwischen Tethys und Atlantik im Bereich der heutigen Straße von Gibraltar hat einen vernachlässigbaren Effekt auf Ozeanzirkulation und Klima. Diese Dissertation gibt neue stratigraphische und paläozeanographische Einsichten in den Übergang vom Treibhausklima des frühen Känozoikums in das moderne, von glazialen und interglazialen geprägte Klima. Die erstmalige Benutzung der stabilen Obliquitätsamplitudenmodulation repräsentiert dabei einen methodischen Fortschritt, der von zukünftigen Studien genutzt werden kann.

Der hier vorgestellte Isotopendatensatz kann dank einer bisher unerreicht hohen Auflösung im Verbund mit anderen Isotopendaten der IODP-Expedition 342 die Referenz für das gesamte mittlere Eozän bilden. Die neuen Einblicke in die Tiefenwasserbildungsprozesse im Nordatlantik des mittleren Eozäns können helfen, unser Wissen über die vorherrschenden Prozesse der Ozeanzirkulation während warmer Klimaphasen zu erweitern.

Table of Contents

Motivation

With modern atmospheric CO_2 levels predicted to rise up to 500-1000 ppm by the year 2100 (Houghton et al., 2001) the study of climatic behaviour during greenhouse periods such as the Eocene is crucial to understand the implications of climatic perturbations of the Anthropocene. While the Eocene is not a perfect analogue to the near future due to differences in the tectonic configuration and the initial state of the cryosphere, improving our understanding of Eocene climate dynamics can help to constrain what to expect from a much warmer planet. The overarching objective of this dissertation is therefore to improve our understanding of the exact timing, environmental conditions and evolution of climate during the transition from the early Eocene greenhouse towards the glaciation of Antarctica near the Eocene/Oligocene boundary. Very few paleoceanographic deep-sea proxy records cover the middle Eocene at high (sub-orbital) resolution. As high-resolution records are sparse, no robust astronomical timescale yet exists for the so-called "middle Eocene tuning gap" that is firmly anchored to other records. The existence of this long-standing gap has so far prevented the establishment of a fully anchored comprehensive astrochronologic framework for the Cenozoic.

In paleoceanography, benthic carbon and oxygen isotope records are key to reconstructing global mean climate as they are thought to represent conditions averaged over large-scale ocean basins. Before this study, ~1100 benthic foraminiferal isotope measurements from deep sea drilling sites distributed over all ocean basins cover the 10 Ma of the middle Eocene (38-47.8 Ma) (Cramer et al., 2009). For comparison, the 11 Ma of the Oligocene are covered by almost 7000 measurements. The highest resolution record of the middle Eocene at a single location (Sites 1258 and 1260) is ~10 kyr/sample at best, which is much lower than during most other epochs of the Cenozoic. This prevents a detailed analysis of orbital scale variations. The low data coverage results from large-scale erosion, carbonate starvation in large areas of the ocean due to a highly variable carbonate compensation depth, and recovery problems due to large-scale paleoceanographic changes. Sedimentary sections drilled at the Newfoundland Ridge during IODP Expedition 342 are characterized by sedimentation rates high enough to allow us to improve the resolution of existing single location benthic foraminiferal carbon and oxygen isotope records by 5-10 times. In this work, these sedimentary sections are used to address the following research objectives and hypotheses:

Hypothesis 1: *The carbonate-rich middle Eocene successions at IODP Sites U1408 and U1410 allow for the construction of an astrochronologic framework that spans the long standing "middle Eocene astronomical time scale gap".*

Expedition 342 sites are expected to contain a complete stratigraphic record of the middle Eocene tuning gap between magnetic reversal (chron) boundaries C18-C21. This dissertation aims to confirm the completeness of these records and to evaluate the astronomical imprint causing the lithologic alternations. The aim is to use these lithological alternations to develop

the first complete cyclostratigraphic age model for the middle Eocene based on a single locale from IODP Expedition 342. If the dominant cycle is not related to eccentricity, a stable tuning target has to be found and its stability needs to be evaluated for the middle Eocene. The 173-kyr obliquity amplitude modulation could provide a tuning target that may be stable over the last 48 Ma. In particular, integrating age estimates for chron boundaries and durations with previous estimates on both sides of the geological record to obtain a fully-anchored and comprehensive astronomical time scale for the Cenozoic is a major goal of this dissertation.

Hypothesis 2a: *The onset of the Newfoundland Drifts, characterized by a sharp lithologic boundary between calcareous ooze and muddy drift sediments reflects the onset of deep water formation in the North Atlantic.*
Hypothesis 2b: *The lithological alternations characterizing the middle Eocene drift sediments at Site U1410 reflect variations in the intensity of the Deep Western Boundary Currents on orbital timescales.*
The onset of the Newfoundland Drifts at the early-middle Eocene boundary has been linked to the first major influence of a deep-water source in the North Atlantic. However, it is to-date unclear, what astronomical or other mechanisms govern sedimentation patterns and deep-water circulation at the Newfoundland Drifts. Are the alternations in the sedimentary record reflecting local insolation or a high latitude climate signal introduced by teleconnections in the climate system such as deep-water formation in the high Northern latitudes? By what mechanism is the ocean circulation responding to astronomical pacing (via temperature, the hydrological cycle, the carbon cycle or something else)?

Hypothesis 3: *The onset of deep-water formation in the North Atlantic is primarily driven by either the tectonic developments during the late early Eocene or the drawdown of atmospheric CO_2 at the early-middle Eocene boundary.*
The early-middle Eocene was characterized by rapidly declining atmospheric CO_2 concentration and tectonic changes in the North Atlantic. However, the exact role of changing ocean gateway configurations such as the Greenland-Scotland Ridge, the Arctic isolation and the closure of the Tethyan seaway on the initiation of Northern Component Water remains enigmatic. In particular, the importance of declining atmospheric CO_2 with respect to the onset of deep-water formation in the North Atlantic is yet unconstrained. Thus, the sensitivity of the middle Eocene climate and ocean circulation to changes in the atmospheric greenhouse gas concentration and seaway opening/closing needs to be evaluated. This will enable us to shed light on the exact sequence of events and the proportional effect of these changes on ocean circulation.

Outline

This dissertation is subdivided into five main chapters. **Chapter 1** gives an introduction into the motivation, scientific background and wider context of this work. Particular topics addressed in the introduction are the climatic and tectonic evolution of the Cenozoic particularly the Eocene; the forcing of climatic change through astronomical parameters, and how climatic variations in response to astronomical forcing can be used in a stratigraphic framework. Furthermore, I discuss the driving processes and development of the modern thermohaline circulation. The final part of the introduction is dedicated to the deposition of contourite drift sediments, such as those recovered during IODP Expedition 342 – Paleogene Newfoundland Sediment Drifts, which are the foundation of this dissertation.

The **Chapters 2, 3** and **4** have been written for individual publication in international peer-reviewed scientific journals. Due to the stand-alone character of these manuscripts, repetition of some key concepts has been unavoidable.

Chapter 2: Towards a Robust and Consistent Middle Eocene Astronomical Timescale

Slah Boulila, Maximilian Vahlenkamp, David De Vleeschouwer, Jacques Laskar, Yuhji Yamamoto, Heiko Pälike, Sandra Kirtland Turner, Philip Sexton, Thomas Westerhold, Ursula Röhl

Manuscript submitted to *Earth and Planetary Science Letters*

This chapter addresses the closure of the middle Eocene “astronomical timescale gap” based on XRF-derived proxy data from IODP Expedition 342. Due to the dominant imprint of obliquity at the middle Eocene sections of the Newfoundland Drifts, the relatively stable 173-kyr obliquity amplitude modulation is used as a tuning target in a novel approach. The closure of this long-standing gap in the astronomical timescale for the Cenozoic represents the missing link between the Pleistocene-Oligocene astronomical timescale and the early Eocene-Paleocene astronomical timescale. It is therefore essential for the generation of a fully anchored astronomical timescale for the Cenozoic.

This study was designed independently in two different labs, one in Bremen (led by Maximilian Vahlenkamp) and one in Paris (led by Slah Boulila). In Bremen, Maximilian Vahlenkamp and David De Vleeschouwer revised shipboard splices, provided core-core correlation to the scientific party of IODP Expedition 342 analysed the data and a created a cyclostratigraphic and astrochronologic framework for IODP Expedition 342 sediments. Maximilian Vahlenkamp wrote the draft with support of David De Vleeschouwer and Heiko Pälike. At this point in time, the Bremen and Paris group became aware of their respective work and the astrochronologies and manuscripts were exchanged and combined into a single manuscript, first-authored by

Slah Boulila to acknowledge his role as a shipboard scientist on Expedition 342 and in order to fulfil IODP Publication requirements.

Chapter 3: Astronomically Paced Changes in Overturning Circulation in the Western North Atlantic during the Middle Eocene

Maximilian Vahlenkamp, Igor Niezgodzki, David De Vleeschouwer, Torsten Bickert, Dustin Harper, Sandra Kirtland Turner, Gerrit Lohmann, Philip Sexton, James Zachos, Heiko Pälike

Manuscript submitted to Nature Communications, now under revision.

This chapter utilises a new benthic oxygen and carbon isotope record of unprecedented resolution for the middle Eocene (~2 kyr/sample) together with XRF-derived ratio of Ca/Fe to study the astronomical pacing of Atlantic deep ocean circulation during the middle Eocene and to constrain its response to orbital cycles. It discusses invigoration of Deep Western Boundary Currents that have led to the deposition of the Newfoundland Drifts. It thereby contributes to solving the long-held debate about whether the onset of Northern Component Water occurred at the early-middle Eocene boundary or at the Eocene/Oligocene boundary. The coupled Earth System Model *COSMOS* is used to investigate the physical background of these changes in ocean circulation

Maximilian Vahlenkamp designed the study, conducted isotope analysis and drafted the manuscript. Maximilian Vahlenkamp and Igor Niezgodzki designed, performed and analysed simulations in the Earth System Model *COSMOS*. Maximilian Vahlenkamp performed time series analysis with contributions from David De Vleeschouwer. Sandra Kirtland-Turner collected XRF data of Site U1410. All other authors contributed to the interpretation and discussion of the results and the preparation of the final manuscript.

Chapter 4: Sensitivity of the Climate System and Ocean Circulation to *Atmospheric CO_2 and Ocean Gateway Configurations during the Middle Eocene*

Maximilian Vahlenkamp, Igor Niezgodzki, David De Vleeschouwer, Gerrit Lohmann, Heiko Pälike

Manuscript in preparation for *Climate of the Past*

In this chapter, the Earth System Model *COSMOS* is used to evaluate the sensitivity of the early deep-water formation in the North Atlantic during the middle Eocene to changes in atmospheric CO_2 and seaway configurations. Setups that simulate a drawdown of CO_2 due to the burial of organic matter (i.e. during the Azolla event at ~49 Ma), the onset of North Atlantic

Deep Water in response to the subsidence of the Greenland-Scotland Ridge, the overspill of Arctic waters into the Greenland-Norwegian Sea via a shallow seaway and the role of the Tethyan Indian Saline Water for the Meridional Overturning circulation are assessed.
Maximilian Vahlenkamp designed the study and drafted the manuscript. Maximilian Vahlenkamp and Igor Niezgodzki designed, performed and analysed simulations in the Earth System Model *COSMOS*. All authors contributed to the discussion of the results.

Chapter 5 summarises the main conclusions of this dissertation in its entirety and discusses the remaining limitations of this work as well as providing suggestions for future research.

Chapter 1: *Introduction*

1.1 Cenozoic Climate Evolution

Geological archives reveal that the global climate has undergone drastic changes throughout Earth's history. These changes have occurred gradually in some cases and more rapidly in others. The Cenozoic (past 66 Myr) is the latest era of geological history and comprises the Paleogene, Neogene and Quarternary periods respectively. The Paleogene is subdivided into the Paleocene, the Eocene and the Oligocene epochs itself.

At the beginning of the Paleogene, during the Paleocene and early Eocene epochs, greenhouse gas concentrations and temperatures were distinctively higher with respect to modern. Deep-water temperatures were approximately 10 °C higher than present day (Zachos et al., 2001) and peaked during the Early Eocene Climatic Optimum at 52-50 Ma (Figure 1.1), likely caused by CO_2 emissions from increased oceanic rifting and volcanism. These emissions increased early Eocene atmospheric CO_2 concentrations to up to 1500 ppm (Liu et al., 2016), which drove global bottom water temperatures up to 12 °C higher than today (Zachos et al., 2001).

Elevated Arctic temperatures amplified by feedback mechanisms in high latitudes kept water temperatures above the freezing point of water (>0 °C) year-round. The overproportional warming of the Arctic led to greatly reduced meridional temperature gradients (Tripati et al., 2003). Proxy derived Arctic mean annual temperatures of 8-17 °C have been reconstructed for the early Eocene (Eberle et al., 2010; Greenwood and Wing, 1995; Sluijs et al., 2006; Weijers et al., 2007). However, climate models fall short in reproducing the warm continental temperatures derived from proxies. This proxy-model mismatch has become known as the Early Eocene equable climate problem (Sloan, 1994; Sloan and Barron, 1990, 1992). The difference between proxy-derived temperature and model temperature is consistently higher than 10-20 °C for mean annual temperature near the poles (Huber and Caballero, 2003; Roberts et al., 2009; Shellito et al., 2009; Shellito et al., 2003; Winguth et al., 2010)

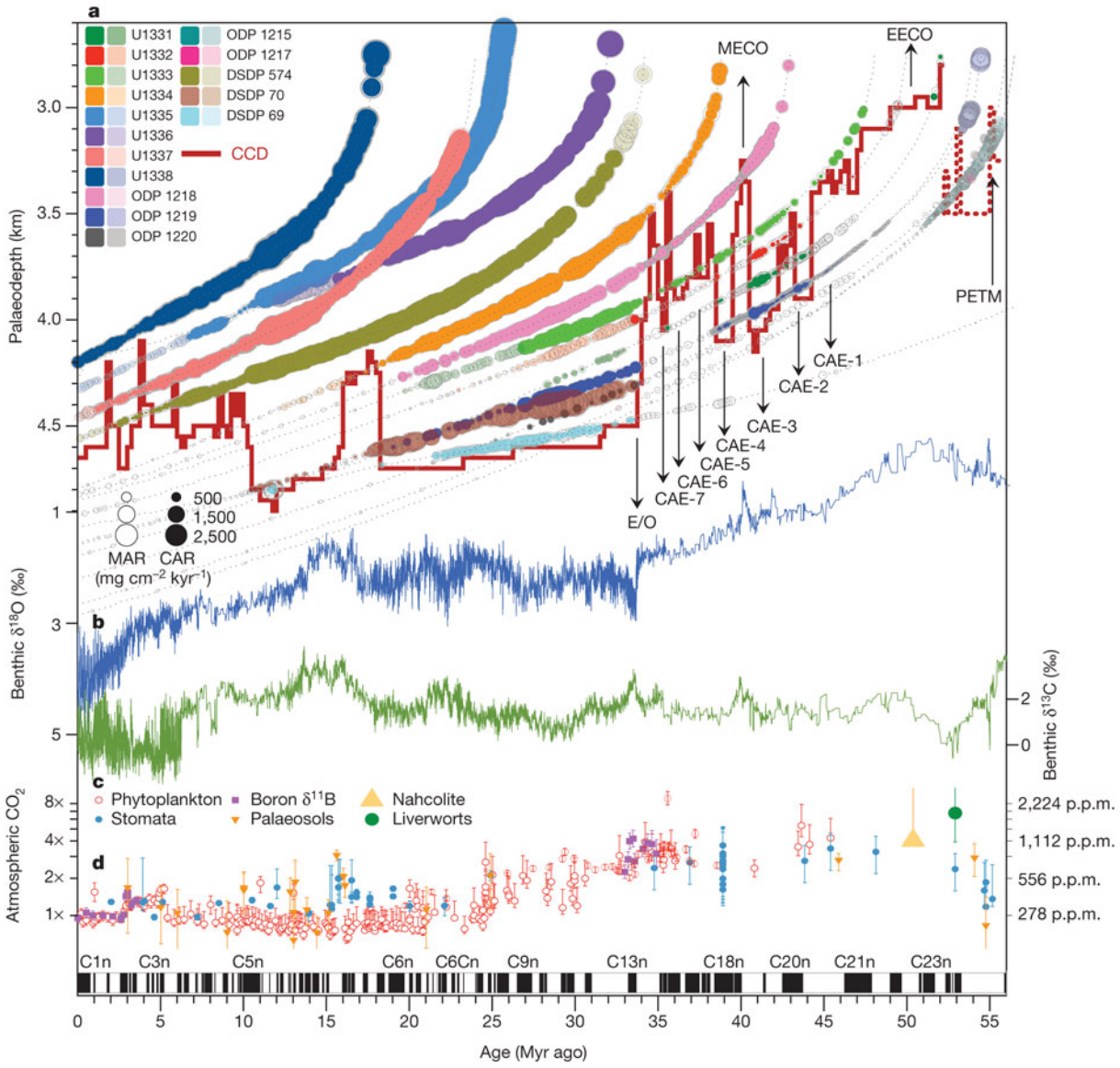

Figure 1.1: Climatic evolution since the early Eocene (from Pälike et al., 2012). A) Reconstruction of the equatorial pacific carbonate compensation depth from carbonate content in PEAT (IODP Expedition 320/321) sites. b) Global stack of benthic oxygen as a proxy for global ice volume and bottom water temperatures and c) carbon isotopes (Zachos et al., 2008) d) reconstruction of atmospheric CO_2 during the Cenozoic (Beerling and Royer, 2011; Pagani et al., 2011). The estimate from Nahcolite for the Early Eocene Climatic Optimum has been recently updated to lower values of 680-1260 ppm by Jagniecki et al. (2015).

The middle Eocene (47.8-38 Ma) marks the initiation of the transition from the early Eocene (56-47.8 Ma) warmhouse towards the cooler modern climate. From approximately 49 Ma onwards, until just after the Eocene-Oligocene boundary (33.9 Ma), which marks the beginning of the Cenozoic icehouse world and the expansion of the Antarctic ice cap, the Cenozoic climate was characterized by decreasing temperatures. At ~49 Ma global temperatures started to decline and polar regions, which were previously ice-free now hosted northern and southern hemisphere glaciation. The first evidence for ice in the Arctic (St John, 2008), the Nordic Seas (Tripati et al., 2008), and the Southern Ocean (Ehrmann and

Mackensen, 1992) occurs during the middle Eocene. The onset of the Cenozoic cooling trend has been related to reduced CO_2 volcanic emissions, which, as mentioned, were particularly high during the early Cenozoic and declined thereafter (Zachos et al., 2008). Between the early Eocene and the glaciation of Antarctica at the Eocene/Oligocene boundary atmospheric CO_2 likely declined by as much as 500 to 1000 ppm (Beerling and Royer, 2011; Liu et al., 2016). Increased organic burial (e.g. during the *Azolla* event) in low ventilated oceanic environments could have removed CO_2 on relatively short timescales (≤1 Myr) (Pearson and Palmer, 2000; Speelman et al., 2009), while chemical weathering of silicate rocks was important on longer timescales (i.e. multi million years). In this climate-stabilizing feedback process, rain and CO_2 from the atmosphere form carbonic acid and react with silicate minerals. The removal of atmospheric CO_2 keeps Earth climate within certain boundary conditions, as higher atmospheric CO_2 concentration elevates temperatures and invigorates the hydrological cycle. More precipitation in turn enhances chemical weathering of silicate rock and warmer surface conditions lead to higher chemical reaction rates, processes that removes CO_2 from the atmosphere (Walker et al., 1981). The drawdown of atmospheric CO_2 between 49-44 Ma, led to bottom water cooling of 3-4 °C (Zachos et al., 2001). In addition, tectonic events such as the collision between Asia and India (Meng et al., 2012) and the opening of the Tasmanian Gateway (Bijl et al., 2013) ~50-49 Ma may have favoured the long-term climate cooling during the middle Eocene by enhancing interbasinal exchange and reshaping global ocean circulation. Even though the Eocene comprises exactly one third of Cenozoic time (Gradstein et al., 2012), it is difficult to gain information about Eocene climate due to a lack of carbonate bearing deep ocean sediments. Very little is known about the exact sequence of events that led to the onset of the Eocene cooling, one of the most distinct climate transitions of the Cenozoic.

Sediment cores from scientific drilling are in general the primary method to investigate Cenozoic climate. Unfortunately, the middle Eocene stands out for a lack of highly resolved carbonate bearing deep ocean sediment sequences. The reason for the shortage of adequate sections is due to various problems including the shallow and variable carbonate compensation depth of the interval (Pälike et al., 2012), condensation of sections, hiatuses spanning multiple biozones and recovery problems during coring, in particular for the middle Eocene. For this reason, no high-resolution benthic isotope record or unambiguous astronomically tuned age model existed for the so-called “middle Eocene tuning gap” so far. After approximately 15 Myr of gradual middle Eocene cooling, the Oi-1 at the beginning of the Oligocene is associated with large-scale Antarctic glaciation, followed by ten million years of relatively stable and cool conditions after the abrupt climate cooling. The final significant warming of the Cenozoic at ~25 Ma was followed by stable climate conditions for roughly 10 Myrs during the early Miocene. Even though atmospheric CO_2 levels reached relatively low

near-modern levels by 25 Ma (Figure 1.1), warm conditions relative to the Pleistocene persisted during the Miocene and Pliocene. Thereafter the cooling largely continued, leading to modern day climate.

While the glaciation history of Antarctica is relatively well-studied and the onset of large-scale Antarctic glaciation is pinpointed at the Eocene/Oligocene boundary (Barker et al., 2007), Northern Hemisphere Glaciation remains relatively unknown (Thiede et al., 1998). Before the Arctic Coring Expedition (ACEX - IODP Expedition 302), the understanding of the palaeoenvironmental conditions in the Arctic Ocean and the onset of Northern Hemisphere Glaciation was restricted to sediment cores from the Subarctic region. The results from these studies were not conclusive as to the onset of Arctic Ocean ice cover and could not constrain when the first major continental ice sheets were built (Thiede et al., 1998). On the basis of the sediment core data available prior to ACEX the estimated onset of major Northern Hemisphere Glaciation was ~14 Ma. This age has changed drastically with the new results of the ACEX studies. The first occurrence of a dropstone at ACEX sites in the Central Arctic as early as 46 Ma (Moran et al., 2006) was interpreted as possible evidence for an earlier onset of Northern Hemisphere Glaciation, or at least some continental glaciation. The new estimate predates the previous one by more than 30 Myr. At the same time, polar sea surface temperature dropped by ~7.5 °C, decreasing the average absolute regional SST to ~10–17 °C from 46.3 Ma to 44.8 Ma (Weller and Stein, 2008). An early onset or intensification of Northern Hemisphere Glaciation during the Eocene has also been proposed from observations of changes in oxygen-isotope composition across the Eocene/Oligocene boundary, and in the late Eocene records from the tropical Pacific and South Atlantic (Coxall et al., 2005). The increase in ice-rafted debris at ACEX coincides with the decline of atmospheric concentrations of CO_2. Decreased atmospheric CO_2 may have driven both poles across the temperature threshold that enabled the initiation of glaciers on land and partial freezing of the surface Arctic Ocean, especially during times of low insolation (St. John, 2008). These data suggest a relatively short time gap between initial glaciation in the Northern and Southern Hemisphere during the middle Eocene, which points to a greater greenhouse gas control of global cooling, in contrast to tectonic forcing (Moran et al., 2006). However, independent of their comparative influence and the exact timing of the bipolar glaciation, Cenozoic climate is above all driven by three major factors: (1) atmospheric CO_2 and (2) tectonics on long timescales and (3) astronomical cycles on shorter timescales.

1.2 Cenozoic Tectonic Evolution

In addition to a dynamic global climate, paleogeography also underwent large-scale changes during the Cenozoic (Figure 1.2). Firstly, there was a seaway connecting all ocean basins at the Northern mid-latitudes via the Tethys Sea and the Central American Seaway. The closure of the so-called “Tethyan Seaway” initiated with the collision of India and Asia in the late Paleocene and Early Eocene, and continues today as Africa and Europe converge. This closure as well as the closure of the Central American Seaway caused changes in the circulation regime of the Atlantic during the Cenozoic. The emergence of the Isthmus of Panama separated Pacific and Atlantic waters and has been interpreted as an important trigger for the onset of Northern Hemisphere Glaciation in many studies (Burton et al., 1997; Haug et al., 2001; Lear et al., 2003). The timing of the emergence of the Panama Isthmus and the resulting closure of the Central American Seaway has been constrained to late Miocene to Pliocene (Coates et al., 2004; Coates et al., 1992; Collins et al., 1996; Kameo and Sato, 2000; Keigwin, 1982; Keigwin, 1978; Newkirk and Martin, 2009). Recently, Molnar (2008) challenged the importance of the Central American Seaway as a moderator of large-scale climate change, and Montes et al., (2012) suggest that narrowing began long before the Miocene, during the middle Eocene. The last significant low-latitude connection, an important connection in the thermohaline circulation between major ocean basins, is the Indonesian throughflow region. This region has also been narrowing since the Miocene with far reaching climatic consequences for the North and South Pacific, and Africa (Cane and Molnar, 2001).

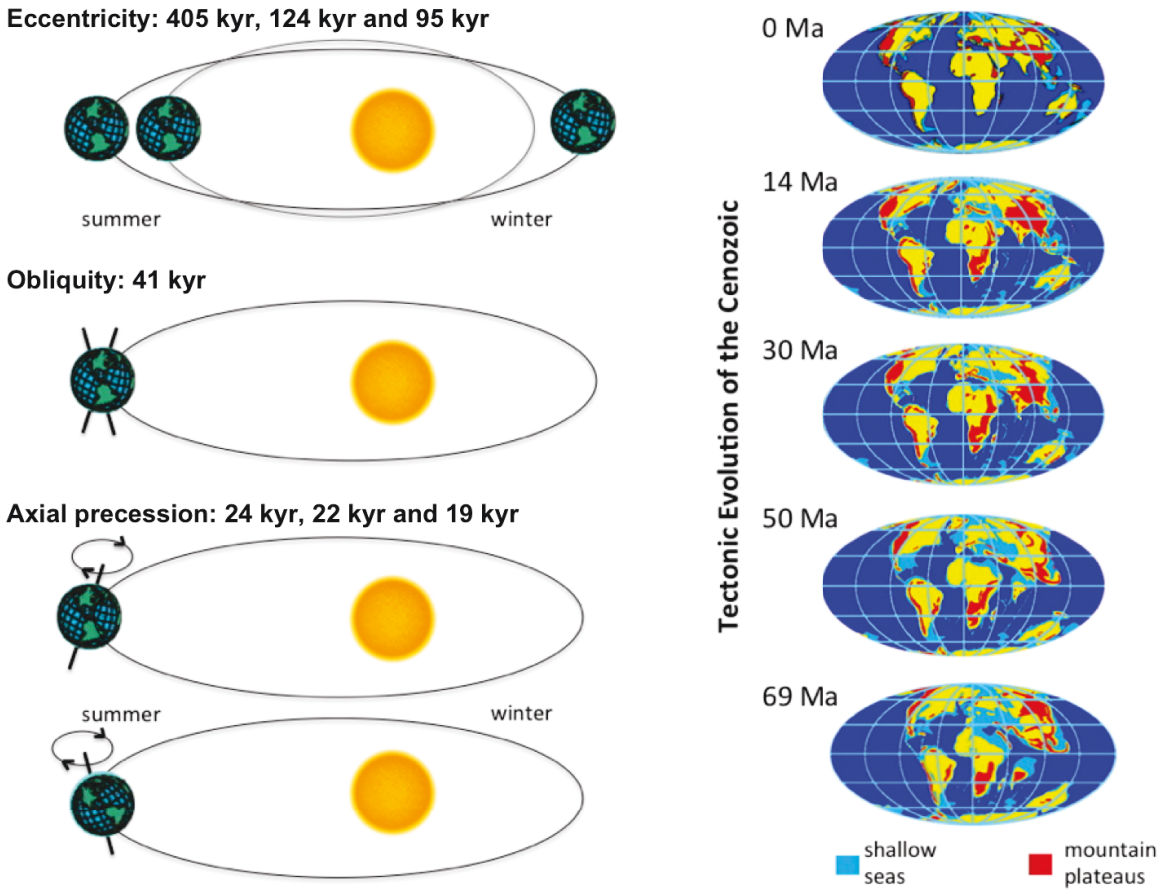

Figure 1.2: Astronomical parameters and tectonic evolution of the Cenozoic (after Zachos et al., 2001). Mechanisms and time scales of eccentricity, obliquity and axial precession and the tectonic evolution of the Cenozoic.

During the early Cenozoic, the Southern Ocean was divided into two separate domains: the Atlantic-Indian and the Pacific domain. The Scotia Arc joining Antarctica with South America and the connection between Australia and Antarctica separated these domains. With the opening of the Drake Passage (between Antarctica and South America) and the Tasmanian Passage (between Antarctica and Australia) the reorganization of ocean circulation and the formation of the cold Antarctic Circumpolar Current led to the thermal isolation of Antarctica. This thermal isolation has been used to explain the growth of the East Antarctic Ice Sheet across the Eocene/Oligocene boundary (Exon et al., 2002; Kennett, 1977). However, more recently the view that progressive atmospheric CO_2 decline between the Eocene and Oligocene was the primary driver of the large-scale glaciation of Antarctica has become widely accepted (DeConto and Pollard, 2003a, b; Huber and Nof, 2006).

The Arctic Ocean was connected to the global ocean only through shallow water seaways at the beginning of the Cenozoic (Jakobsson et al., 2007; Mutterlose et al., 2003). As a result, the early Cenozoic Arctic Ocean was characterized by low salinity and euxinic conditions during this time. The *Azolla* event marks the culmination of euxinic conditions in the Arctic

Ocean at 49 Ma. The geographic isolation of the Arctic at this time created Black-sea-like conditions (Stein et al., 2006), led to brackish surface waters and to the deposition of organic-rich sediments in the anoxic, well stratified water column. The *Azolla* event may have been one of the major contributors to the drawdown in CO_2 after the Early Eocene Climatic Optimum (Speelman et al., 2009). As stated before, the ACEX cores are key in documenting Cenozoic paleoceanographic change in the Arctic Region. Unfortunately, core recovery between the middle Eocene and the early Miocene is very limited, possibly due to uplift of the Lomonosov Ridge in the central Arctic (O'Regan et al., 2008). Based on the Miocene sections of ACEX Jakobsson et al. (2007) suggested a transition from the lake stage to a fully ventilated phase during the Miocene as a response to the opening and deepening of the Fram Strait. Later, deep-water inflow into the Arctic Ocean became possible. At this time, deep ocean communication between the Arctic and the North Atlantic was fully enabled (Figure 1.3).

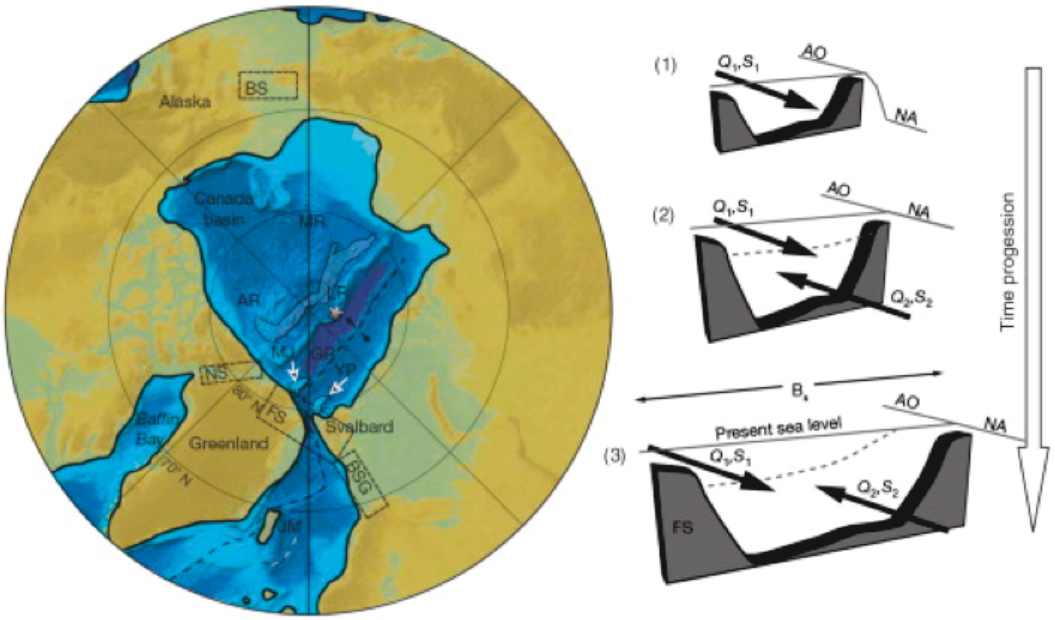

Figure 1.3: The opening of the Fram Strait (from Jakobsson et al., 2007). A) Paleomap for the late early Eocene paleogeography and B) schematic illustration of the mechanism by which the opening of the Fram Strait is likely to have affected ocean circulation.

1.3 Astronomical Forcing of Climate

The idea of astronomical mechanisms controlling Earth's climate originated long before Milutin Milankovitch was the first to quantify variations in incoming solar radiation and relate them to climatic problems (Milankovitch, 1941). Almost half a century after John Herschel (1832) related the mean annual average solar radiation to the eccentricity of Earth's orbit, the theory of James Croll (1875) explained glacial cycles by a combined effect of the three major astronomical factors (eccentricity, obliquity and precession) on seasonal insolation during

perihelion and aphelion. At this time, the astronomical forcing of the ice ages was far from being agreed as scientific consensus and Sir Charles Lyell (1872) turned to tectonic rearrangement of land and sea to explain variations in climate. It was also around this time that the greenhouse theory became more popular and elaborated (Chamberlin, 1899; Tyndall, 1861). Today, it is widely accepted that all three mechanisms are important drivers of global climatic change on different timescales. Long before Milankovitch published the first full astronomical theory of Pleistocene ice ages (Milankovitch, 1941) and computed the subsequent changes in the insolation and climate, cycles of lacustrine expansion and contraction in the Eocene Green River Formation (Wyoming, USA) had been attributed to climatic precession. Milankovitch's theory was initially rejected by the majority of the scientific community for a number of reasons: The absolute timescales were inaccurate, sedimentary records were fragmented, and the global climate system was widely considered too stable to react to relatively small insolation changes (Simpson, 1940). 35 years after Milankovitch had published his astronomical theory, Hays et al. (1976) used spectral analysis of benthic foraminiferal oxygen-isotopes as an indication of global ice volume and temperature and established a clear link between glacial-interglacial climate change and the independently calculated orbital periods (Berger, 1976; Berger, 1978). This key finding decisively revitalized Milutin Milankovitch's astronomical climate theory. Indeed, since then, paleoclimatologists widely accept that Earth´s climate system responds sensitively to variations in the Earth's astronomical configuration. Changes in this configuration are caused by the interactions between the gravitational bodies in our solar system. At present, astronomers are able to accurately calculate the incoming solar radiation at the top of the atmosphere for at least the last 26 Ma (Laskar et al., 2004). Solar energy is the primary energy source driving all climatic processes on Earth. For a detailed reconstruction of climate, however, it is crucial to understand the response of the climate system with its various feedback mechanisms to the amount of incoming solar energy. Among the most important feedback mechanisms are the absorption and reflection of incoming shortwave and outgoing longwave radiation via the albedo effect and the greenhouse gas effect. Variations in Earth's astronomical parameters influence the amount of radiation that is received at different latitudes. To quantify the changing response to astronomical forcing after shifts in key boundary conditions like continental distribution, atmospheric CO_2 and the extend and distribution of the cryosphere, De Vleeschouwer et al. (2017), created a "Megasplice" covering the past 35 Myr by linking together existing single location benthic isotope records of high resolution from the International Ocean Discovery Program and its predecessors. In contrast to existing global isotope compilations or stacks, De Vleeschouwer et al. (2017) compiled a record consisting of data from a single site at any point in time allowing for long-term analyses of orbital resolution. Analysing this dataset using a Gaussian process, they found alternations between

the Northern and the Southern Hemisphere as the primary driver of global climate based primarily on the size of continental ice sheets and the extent of sea ice in the respective hemispheres during the past 35 Myr.

1.4 Eccentricity

Earth's orbital eccentricity *(e)* determines the amount by which the Earth's orbital path around the sun deviates from a perfect circle (Figure 1.2). Eccentricity is the only orbital parameter that directly influences the total annual insolation received by Earth. However, changes in Earth's orbital eccentricity are very small and the influence of these changes in eccentricity on total annual insolation is negligible (0.2 % change in solar insolation). The influence eccentricity has on the Earth-Sun distance throughout the year is much more significant. Differences in the intensity and length of the seasons on Earth, during the precession cycle are caused by changes in the Earth-Sun distance and the changing orbital speed of the Earth. Eccentricity modulates the amplitude of the precession cycle as increased ellipticity of Earth's orbit around the sun increases the effect of precession. Eccentricity varies at periods of about 95 kyr, 124 kyr and 405 kyr (Figure 1.4).

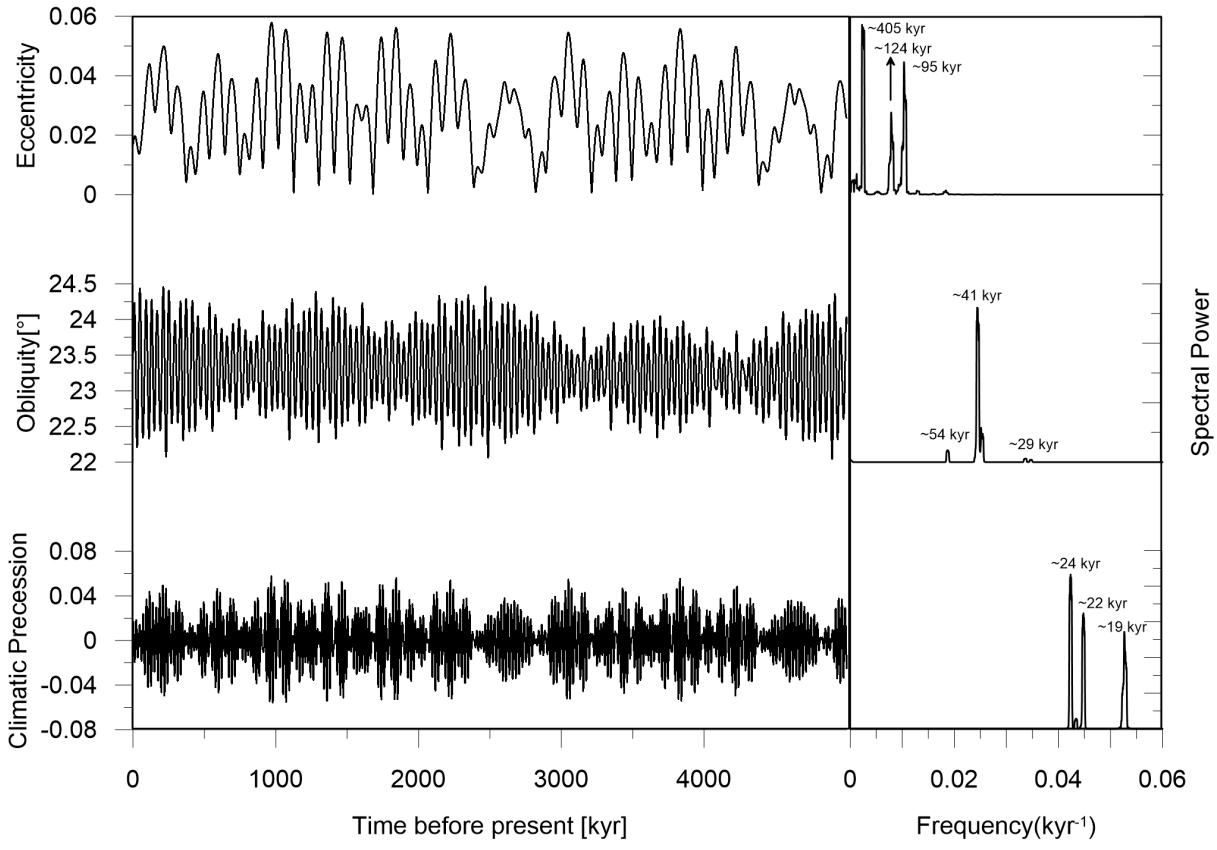

Figure 1.4: Earths orbital parameters over the last 5 Ma and their respective power spectra. The time series (displayed on the left) are calculated from La04 using R Astrochron (Meyers, 2014). The right panels show multi-tapered power spectra (Thomson, 1982) on a linear scale. Labelled peaks identify main astronomical periods.

1.5 Precession

The precession ($\tilde{\omega}$) describes the direction of the Earth's rotational axis and thereby, determines at what time of the year Earth reaches aphelion (furthest point from the sun) and perihelion (nearest point to the sun) (Figure 1.2). Due to the precessional movement of Earth's axis the Northern Hemisphere summer solstice occurs at perihelion once every precessional cycle (once every ~21 kyr) (Figure 1.4). Obviously, the same is true for the Southern Hemisphere summer solstice. When eccentricity is zero, the Earth's orbit is perfectly circular, and the effect of precession is nullified. In other words, the effect of precession increases with a more elliptic orbit of the Earth around the sun. Since eccentricity has a very small influence on the annual incoming solar radiation, it is especially important as the amplitude modulator of precession. To measure the combined effect of precession and eccentricity ($P=e^* \sin\tilde{\omega}$) is referred to as climatic precession and known as a driver of Earth climate via the interhemispheric distribution of insolation. Annual total insolation is not affected by climatic precession, but of the astronomical parameters it has the largest effect on seasonal insolation at low latitudes and is approximately equally strong as obliquity near the poles (Imbrie et al., 1993). As a result of precessional changes, the length of the season between the hemispheres varies with a phase relation of 180°.

1.6 Obliquity

The tilt of the Earth's axis, or obliquity *(ε)*, is the angle between the rotational and orbital axis of the Earth (Figure 1.2). Obliquity varies between ~22-24.5° with a dominant periodicity of 41 kyr (Figure 1.4), and with major amplitude modulations at 173 kyr and 1.2 Myr (Laskar et al., 2004). The intensity of the seasonal cycle in insolation is driven by obliquity. The more the Earth's axis is tilted, the stronger the seasonality. Annual changes in insolation related to obliquity are greatest at high latitudes, where seasonal changes in insolation due to obliquity and precession are comparable (Imbrie et al., 1993). Like precession, obliquity does not affect the total annual energy received by the Earth, but it does control the annual course of the declination, the angle of incoming solar energy and the length of the day. With increasing obliquity, the latitudinal variability in annual incoming solar energy is decreased but seasonality is increased.

1.7 Geochronology and Astronomical Cycles

A fundamental challenge in Earth Sciences is to determine the geological age and the rate at which changes in climate occurred. Better constrains on these timescales will allow rates of change to be calculate and to unravel the cause-and-effect relationship between different components of the climate system. Three main approaches have traditionally been used to

generate geological time scales: (1) radioisotopic numerical dating of key stratigraphic horizons, (2) correlation between different locations based on standard stratigraphic methods (bio-, chemo-, magneto- and cyclostratigraphy) and (3) comparison of geological palaeoclimate time series to astronomically calculated variations of Earth's orbit ("Milankovitch cycles"). The term "astronomical tuning" refers to the alignment of a sedimentary record to matching patterns of variations in a target orbital curve. These target curves are usually orbital solutions based on numerical integration of an idealized version of our solar system. Thus, astronomical tuning can provide age constraints and drastically reduce the uncertainties of other dating techniques such as radioisotopic dating in deep time. The uncertainties of radioisotopic dating techniques, such as U/Pb and Ar^{40}/Ar^{39} (most common methods used for the Cenozoic era) are in the order 2.5 % (Min et al., 2000). For the middle Eocene, this is equivalent to an uncertainty of > 1 Myr. Recently, lithostratigraphy, magnetostratigraphy, biostratigraphy, cyclostratigraphy, and radioisotopic dating have been combined to establish a high-resolution age scale of climate proxy records to reduce this uncertainty to less than 40 kyr for most of the Cenozoic. Two major improvements helped to substantiate astronomical tuning methods as a standard technique for the Neogene timescale (last ~23 Myr) with minor uncertainties of ~20-40 kyr: (1) the expansion and improvement of deep-sea drilling by DSDP and subsequent drilling programs, together with non-destructive core measurement and splicing techniques, and (2) significant progress in the understanding of celestial mechanics. These improvements create possibilities of a, so far unrealisable, fully integrated Cenozoic astrochronologic timescale

Earth's precession rate *k* (Berger, 1978; Berger et al., 1993) or *p* (Laskar et al., 2011; Laskar and Robutel, 1993; Laskar et al., 2004) plays a central role in the calculations of the obliquity and precession periods. Unfortunately, it is dependent on Earth's rotational speed, dynamical ellipticity and the Earth-Moon distance which have varied through geologic time (Berger et al., 1992). The continuous decrease of *p* throughout geologic time has led to a lengthening of the obliquity and precession index (Figure 1.5). In addition to the long-term evolution of the precession rate, short-term variations in *p* can be induced by changes in the growth of large ice sheets, triggering an ellipticity response of the Earth's orbit (Thomson, 1990). For this reason, the accuracy of the solution for precession and obliquity is limited beyond ~20 Myr (Laskar et al., 2004). On the other hand, the solution for eccentricity is independent of *p* and presently valid over more than 50 Myr (Laskar et al., 2011).

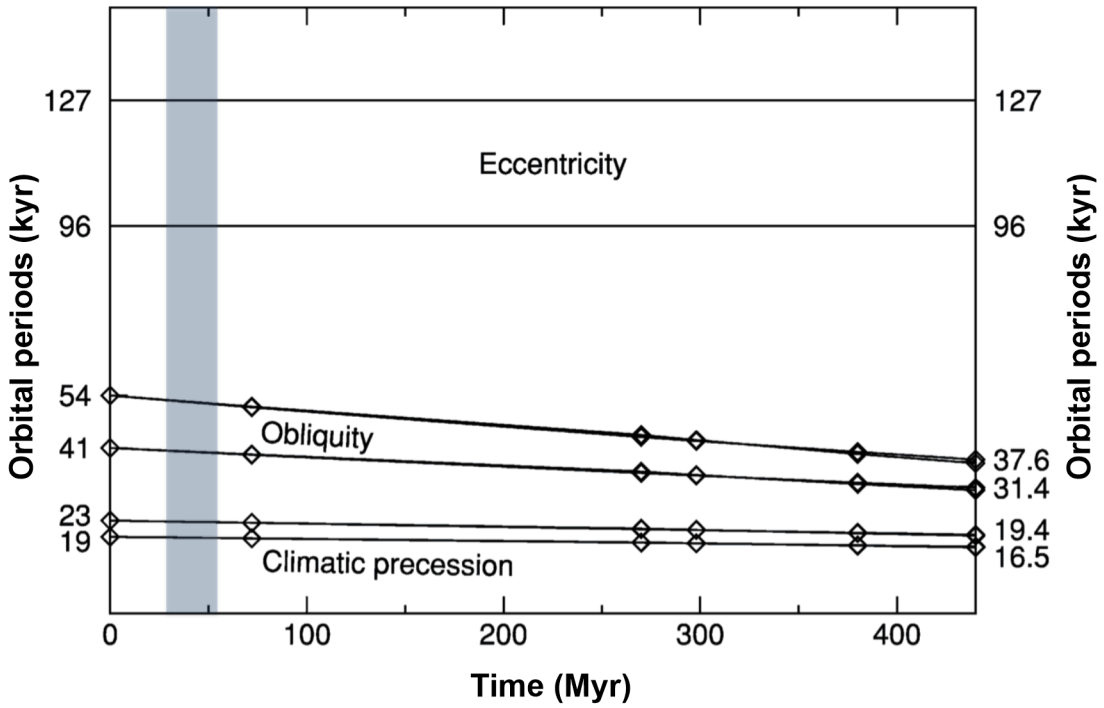

Figure 1.5: Estimated changes in the orbital periods over the past 440 Myrs. Lengthening of precession and obliquity related periods is attributed to changes in the precession constant *p* as calculated by Berger and Loutre (1994) while eccentricity remains unaffected by these changes. Only for illustrative purposes as exact variations of orbital frequencies remain unknown. The Eocene is highlighted in grey.

The very stable 405-kyr periodicity of eccentricity can be used as a tuning target as far back in time as the early Mesozoic. At that point in time, the maximum error of the La2010 eccentricity solution exceeds the duration of one long eccentricity cycle (405 kyr) (Laskar et al., 2011). Over the last decade, the astronomically-tuned geologic timescale has been extended into the Paleogene by using the 405-kyr eccentricity component as a prime target for tuning. To further extend the Neogene timescale, Pälike et al. (2006) tuned the entire Oligocene using climatic proxy records of ODP Site 1218 in the Pacific suitable for this study due to its excellent magneto-bio-cyclostratigraphy. In a similar approach, Westerhold et al. (2008) attempted to tune the entire Paleocene, recognizing 24 eccentricity-related 405-kyr cycles in their paleoceanographic proxy data. However, because no unambiguous astrochronological age scale existed for the Eocene, they had to present three different options, offset by 405 kyrs each. In 2010, Hilgen et al. (2010) revised the duration of the Paleocene from 24 to 25 405-kyr eccentricity cycles starting from an age of 65.95 Ma for the K/Pg boundary, after stratigraphic records from ODP Sites 1258 (Leg 207, Demerara Rise) and 1262 (Leg 208, Walvis Ridge) (Lourens et al., 2005; Westerhold and Röhl, 2009; Westerhold et al., 2007; Westerhold et al., 2008) had been used to extend the Paleocene astronomical time scale into the early Eocene. An astronomically-tuned timescale has been generated across the Eocene-Oligocene Transition and into the middle Eocene (Westerhold

et al., 2014). However, no reliable astronomical tuning exists for most of the Eocene and results in the so-called “Eocene tuning gap”, the last standing breach in the astronomical time scale for the Cenozoic and one of the major objectives of this dissertation.

Sediments deposited during the “Eocene tuning gap” reflect the very shallow carbonate compensation depth (CCD) during this time (Pälike et al., 2012), which prevented the deposition of cyclic carbonate-rich sediments. Therefore, very few suitable sections for astrochronologic studies have been collected for this time interval. Previous tuning attempts across the “Eocene tuning gap” are presented in Jovane et al. (2010) and Westerhold et al. (2015). However, the first study has been questioned in Vandenberghe et al. (2012) as their magnetostratigraphic reversals remain very close to the geomagnetic polarity time scale (GPTS) used for their initial time calibration. The second study by Westerhold et al. (2015) uses a relatively low-resolution dataset for tuning. Therefore, these authors only recognize eccentricity components, and not higher-frequency precession or obliquity components.

The orbital theory has not been discussed without controversy. Firstly, the method is prone to circular reasoning and there is potential to introduce Milankovitch frequencies that are not present in the original data through the tuning process (e.g. Hinnov and Park, 1998; Proistosescu et al., 2012; Rial, 1999; Shackleton et al., 1995). For example, if random noise is tuned to an arbitrary target curve, power will be shifted to the dominant periods of the target curve. However, amplitude variations in proxy records, reflecting amplitude modulations in astronomical cycles (e.g. the eccentricity modulation of the precession amplitude or the 173 kyr amplitude modulation of obliquity), are not altered by the tuning process but inherent to the climate proxy data itself. They can therefore be used as an independent assessment of the consistency of a data series with the target curve (Pälike et al., 2004; Pälike and Shackleton, 2000; Shackleton et al., 1999; Shackleton and Crowhurst, 1997; Westerhold et al., 2007; Zeeden et al., 2013). Furthermore, the observed strength of orbital variations varies in time and does not always correspond to the expected strength of the calculations for insolation. Instead, the incoming insolation is filtered by the climate system and altered by factors like paleogeography, global ice volume, and others, revealing nonlinear responses of the climate system. A prominent example is the so-called 100-kyr problem of the past 800 kyr, during which a dominant 100-kyr cycle of ice sheet buildup and decay in benthic isotope datasets (likely the imprint of eccentricity) has been overamplified compared to its effect on incoming solar radiation.

The sensitivity of the climate and carbon cycle to orbital configuration has changed, as evidenced by deep-sea proxy records, between warm greenhouse and cold icehouse periods (Lourens et al., 2005; Pälike et al., 2004; Pälike et al., 2006; Westerhold et al., 2011). A strong sensitivity to eccentricity and precession has been observed in climate records from the early Cenozoic, while the presence of continental ice sheets during cold periods appears

to pronounce the climate response to obliquity, which has been weak or absent in most Paleogene records (Lisiecki and Raymo, 2007; Lourens et al., 2005; Westerhold et al., 2011). The ice albedo effect, (i.e. waxing and waning periods of continental ice sheets based on their size and sea level effects) could be a potential amplifier of high-latitude insolation changes as a response to variations in obliquity during the more recent icehouse climate (33-0 Ma). Variations in the carbonate compensation depth close to the periodicity of the eccentricity amplitude modulation (2.4 Myrs) in the middle Eocene, and more frequent obliquity amplitude modulation (1.2 Myrs) in the late Eocene (Pälike et al., 2012) potentially link astronomical forcing with the carbon cycle of the deep ocean. If this link is further substantiated, it provides evidence for a regime shift from eccentricity to obliquity as the moderator of oceanic circulation and climatic change during the Eocene.

1.8 Meridional Overturning Circulation

The Meridional Overturning Circulation (MOC) is the global system of surface, intermediate and deep ocean currents that interchanges considerable amounts of water, heat, salt, carbon, nutrients and other tracers between the different ocean basins and connects the atmosphere and the surface ocean with the massive reservoir of the deep sea (Figure 1.6).

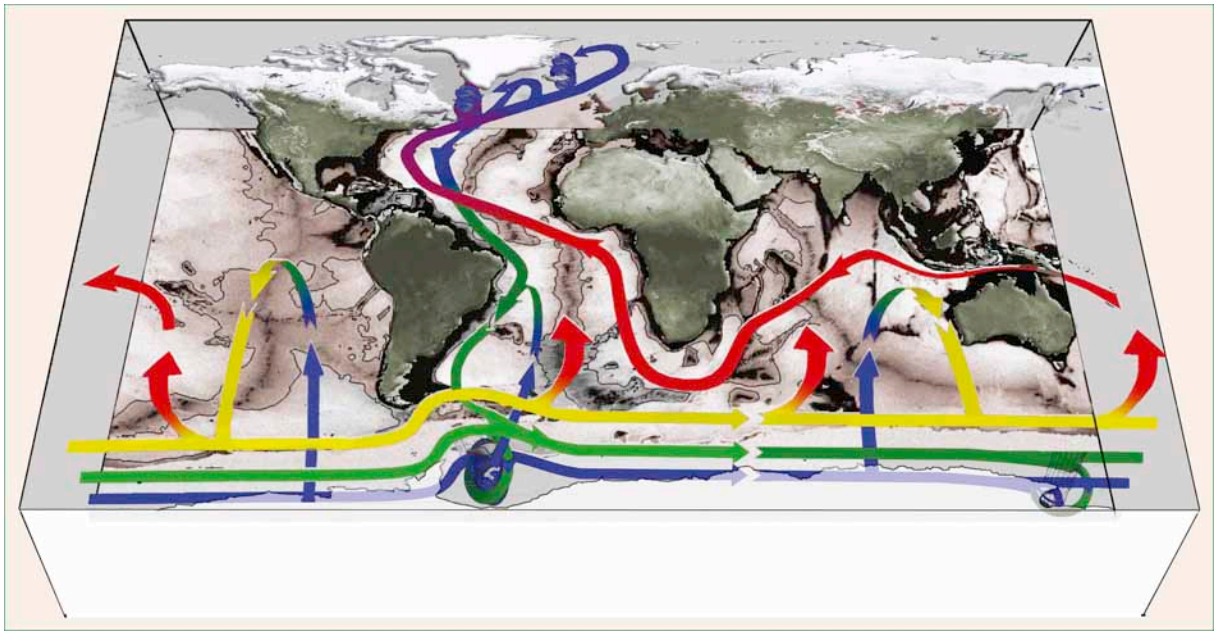

Figure 1.6: Modern Global Meridional Overturning Circulation (Marshall and Speer, 2012). Global ocean conveyer belt inspired by (Broecker, 1992). Warm surface currents=red, intermediate currents= yellow and green, cold deep currents= blue.

The most prominent branch of the Global Meridional Overturning Circulation is the Atlantic Meridional Overturning Circulation (AMOC), which consists of a surface flow with net northward transport between the surface and ~1200 m depth. The northward flow comprises

the Benguela Current and the Gulf Stream, and flows over the Greenland-Scotland Ridge into the Greenland-Norwegian Sea and, in part, into the Arctic.

However, about half of the ocean's deep water forms in the Greenland-Norwegian Sea and the Labrador Sea where the warm, salty surface-water cools and sinks, and returns southward between 1200 m and 5000 m as North Atlantic Deep Water (NADW) (Figure 1.7). The term MOC is often used synonymously with the term thermohaline circulation (THC), but each term refers to a different concept. AMOC refers to the basin-wide circulation in the latitude-depth plane as typically quantified by a meridional transport streamfunction (e.g. in the Atlantic the northward surface transport and the southward deep ocean currents). In contrast, THC refers to a certain mechanism driving ocean currents. It has been defined as "currents driven by fluxes of heat and fresh water across the sea surface and subsequent interior mixing of heat and salt" by Rahmstorf (2002) and relates to movements of water driven by density differences through temperature and salinity gradients between water masses (Figure 1.8).

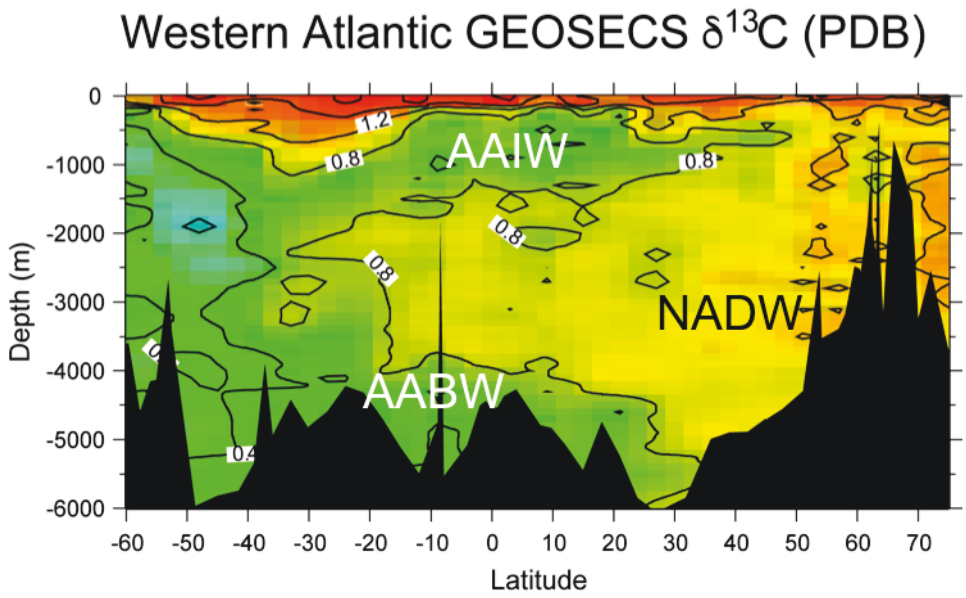

Figure 1.7: Modern Atlantic water mass and δ13C distribution (modified from Curry and Oppo, 2005). Water masses as distinguished by their carbon isotopic ratios. North Atlantic Deep Water= NADW; Antarctic Bottom Water=AABW; Antarctic Intermediate Water=AAIW).

The AMOC however consists of contributions from both the thermohaline driven component and the wind driven component. It is not trivial to distinguish between the two when measuring meridional flow, therefore it is common practice to focus on the measurable AMOC in paleoceanography, while acknowledging that the thermohaline forcing of the AMOC is most susceptible to changes in climate due to the sensitive buoyancy balance at the deep-water formation areas.

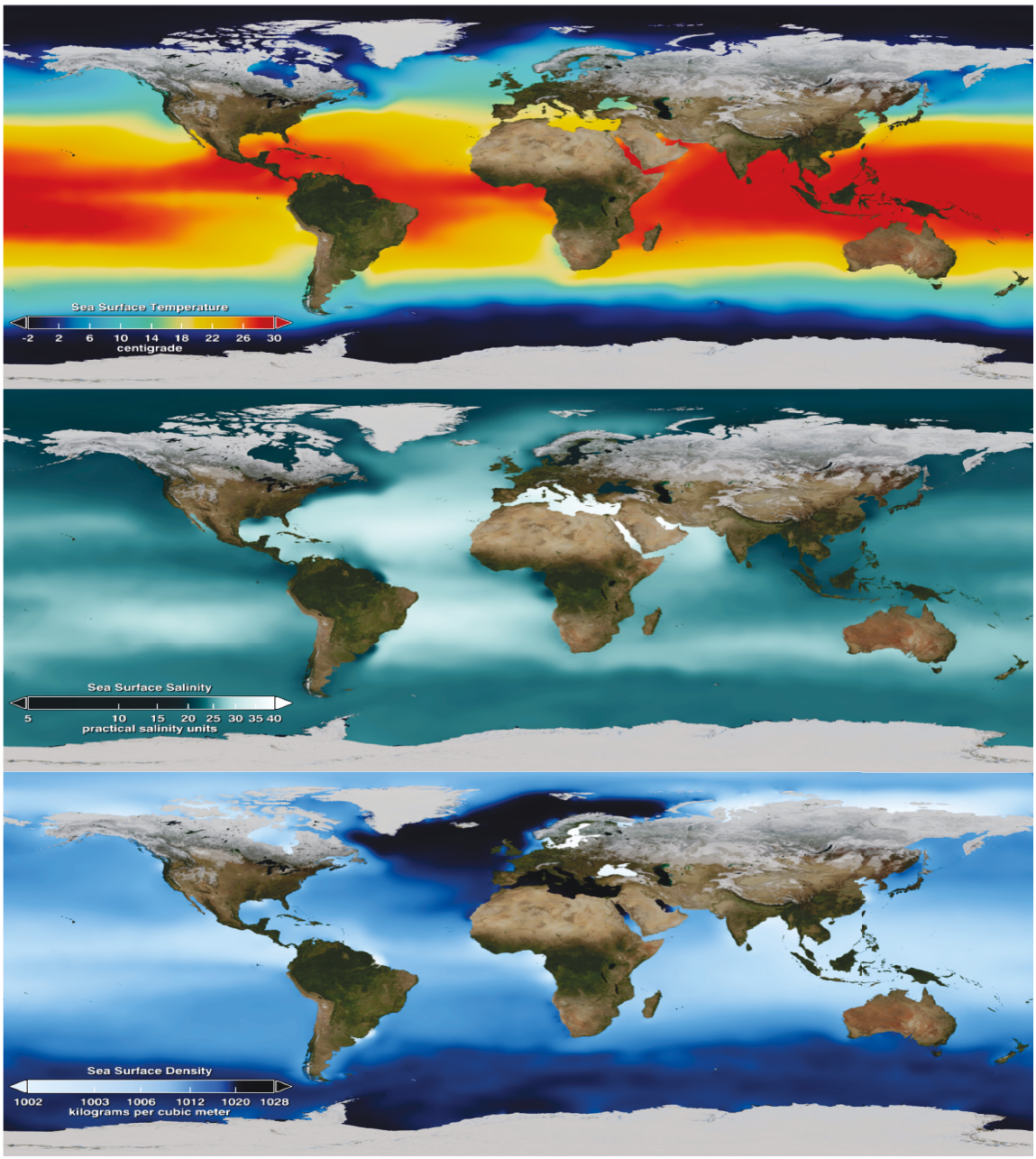

Figure 1.8: Modern sea surface properties in the global ocean. Sea surface temperature, salinity and resulting density. Deep-water formation is initiated in the densest oceanic regions of the global ocean in the North Atlantic and the Atlantic sector of the Southern Ocean (modified from NASA Scientific Visualization Studio).

The meridional overturning circulation has always been highly sensitive to changes in climate and geography and thus a very dynamic system. Paleoclimatic evidence from proxy records and Earth System Models suggest that large and abrupt shifts in the state of Atlantic Ocean circulation have occurred on different timescales, but are particularly dynamic for both, millennial-scale climate variability across the last glacial transition and future climate change. With global temperatures projected to increase by up to 6.4 °C within the coming 100 years (Solomon, 2007), several feedback processes are hypothesized to destabilize NADW formation. Higher surface water temperatures have been hypothesized to decrease the

density of waters in the Greenland-Norwegian Sea and thus slow deep-water formation. Warmer climates are also associated with an enhanced hydrological cycle (Barron et al., 1989; Pagani et al., 2006), transporting freshwater poleward, which further reduces density in the NADW formation areas. Even more important is the meltwater flux from a shrinking Greenland Ice Sheet, releasing freshwater into the Greenland-Norwegian Sea and Labrador Sea and consequently hampering NADW formation. However, the study of Cenozoic thermohaline circulation is relatively new and a vigorous debate is still ongoing about the timing of the onset and the dynamics of the early AMOC in a world with no or much smaller continental ice sheets.

1.9 Evolution of the Thermohaline Circulation

The evolution of ocean circulation is dependent on the geography of ocean basins and on climate. Locations and modes of deep-water formation are thought to have varied through Earth history and during the course of the Cenozoic, reflecting changes in paleogeography and a dynamic climate. Today, deep waters originate only in the high latitudes of the North Atlantic and the Atlantic sector of the Southern Ocean. This is due to the elevated salinity of the Atlantic with respect to the Pacific, and that the Atlantic extends further northward to higher latitudes where surface water cools and gains density. The Greenland-Norwegian Sea was just opening during the early Cenozoic as part of a subsiding continental rift system, therefore deep-water formation cannot have occurred at the same location during the early Cenozoic and modern times. At this time, deep-water formation occurred principally in the Southern Ocean (Mountain and Miller, 1992; Pak and Miller, 1992; Thomas et al., 2003; Via and Thomas, 2006).

The extremely small latitudinal sea surface temperature gradients and the high latitude warmth of the Early Eocene (Zachos et al., 1994) have been interpreted to require sluggish deep ocean circulation or a “haline” Warm Saline Deep Water (Brass et al., 1982). In the recent decades this view has been challenged (Lyle, 1997; Munk and Wunsch, 1998; Nilsson et al., 2003). Furthermore, numerical models have struggled to reproduce low-latitude formation of deep-water, even though it could not be ruled out (Bice and Marotzke, 2001; Huber and Sloan, 2001; O'Connell et al., 1996). High-latitude sources of deep-water formation are clearly favoured in the models.

The commonly held assumption that ocean circulation was more sluggish during the warm early Cenozoic has not yet been unambiguously confirmed. Contrarily, at warmer temperatures, surface cooling is even more effective than salinization at densifying fresh polar waters and initiating convection (De Boer et al., 2007).

While models can be used to estimate when and where deep waters might form, the dependence on local conditions (Bice, 1997; von der Heydt and Dijkstra, 2006) requires the

comparison of model simulations and paleoceanographic tracers in order to adequately constrain the timing of local deep-water formation in the past. Several estimates have been made for the onset of NADW formation (or its ancient counterpart Northern Component Water - NCW) and range from the early-middle Eocene boundary (Berggren and Hollister, 1977; Boyle et al., 2017; Hohbein et al., 2012) to the Eocene-Oligocene boundary (Davies et al., 2001; Via and Thomas, 2006), with some estimates as late as the early Miocene (Stoker et al., 2005) (Figure 1.9). These studies are based on low resolution Nd and carbon isotope tracer studies or the interpretation of contourite drifts formed by Deep Western Boundary Currents.

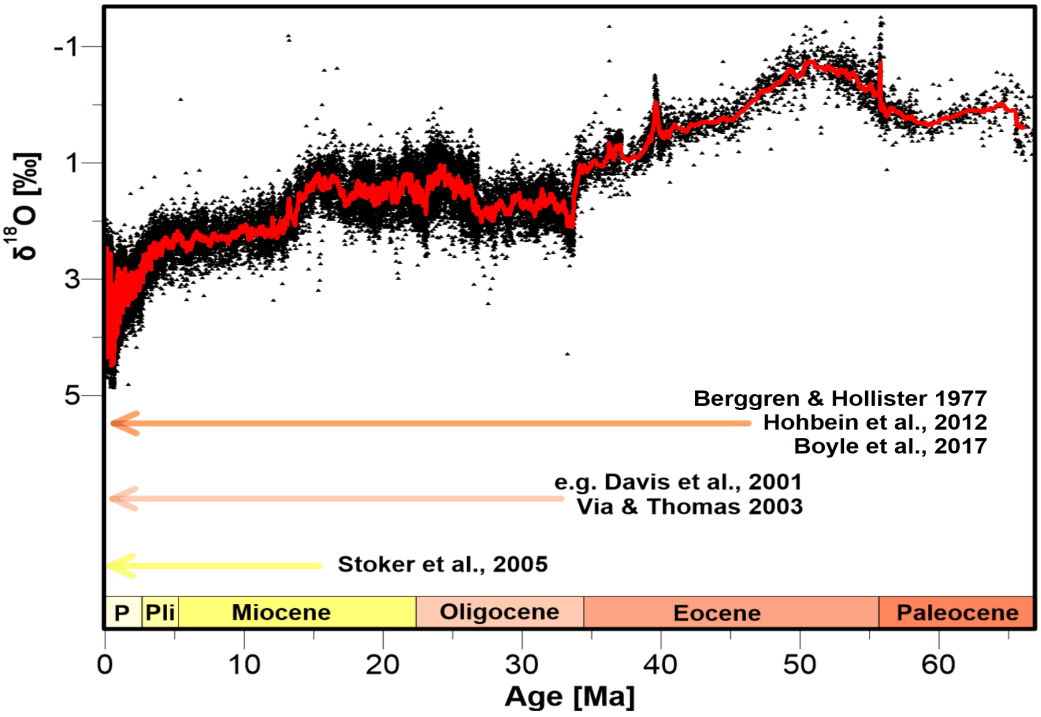

Figure 1.9: Estimated onsets for a bimodal AMOC with overturning cells in the North Atlantic and the Southern Ocean. Estimates are based on the interpretation of contourites or low-resolution carbon isotope and Nd isotope studies. Global benthic oxygen isotope stack by Cramer et al. (2011).

1.10 Drift Sediments and Contourites

Deep Western Boundary Currents form the deep, southward flowing limb of the AMOC. Bottom waters generally flow relatively slowly with velocities around 1-2 cm/s. Close to western margins of their respective basins they can intensify due to geographic restriction and obtain velocities of 10-20 cm/s. These bottom currents act as a semi-permanent part of the thermohaline circulation and can locally erode the clay, silt and fine-grained sand, transporting suspended sediment over relatively long distances. The relocation of sediments by Deep Western Boundary Currents leads to the formation of contourites. Contourites are sediment bodies that “are deposited or significantly affected by bottom currents” (Stow and Faugères, 2008; Stow et al., 2002). For this reason they have been used to study deep-water

circulation throughout the Cenozoic (Berggren and Hollister, 1974; Boyle et al., 2017; Davies et al., 2001; Hohbein et al., 2012; Mountain and Tucholke, 1985; Tucholke and Ewing, 1974; Tucholke and Mountain, 1979). In the North Atlantic Ocean these bottom currents have led to the deposition of contourite drifts that exceed 2 km in thickness and extend for 100's of km and include the Newfoundland Drifts sediments, which were drilled during Expedition 342 (Boyle et al., 2017; Mountain and Tucholke, 1985; Norris et al., 2012; Norris, 2014; Stow et al., 2002; Tucholke and Mountain, 1979).

1.11 IODP Expedition 342 – Newfoundland Drifts

Scientific drilling techniques and strategies have been steadily improved since the existence of the International Ocean Discovery Program (IODP) and its predecessors. These advances, including multiple hole composite sections and advanced coring technology such as advanced hydraulic piston coring and extended core barrel drilling (APC/XCB), and the identification of highly resolved contourite drifts of Paleogene age enabled IODP Expedition 342 to drill cyclic, carbonate-rich sequences of unprecedented resolution.

Sediments at Site U1410, drilled during IODP Expedition 342 at the Newfoundland Ridge (Figure 1.10), contain an extended carbonate record of the middle Eocene, a time during which large parts of the ocean were starved of carbonate as a result of a relatively shallow and variable CCD, leaving behind little to no material to generate paleoceanographic records (Pälike et al., 2012). The drift sediments reveal that from the Late Cretaceous through the early Eocene biogenic pelagic sedimentation dominated, but at ~47 Ma, near the early-middle Eocene boundary, well-developed contourite drifts began to deposit in depths between 2500-4500 m.

These contourite drifts are precious middle Eocene climate archives for several reasons:

1) Contourite drifts typically exhibit high sedimentation rates. Therefore Expedition 342 sites can be used for higher resolution paleoceanographic studies compared to typical previous Paleogene drilling targets (e.g. Norris et al., 2001)

2) Sediments at the Newfoundland Ridges have been largely deposited above the paleodepth of the carbonate compensation depth, which allows for the construction of benthic foraminiferal stable oxygen and carbon isotope records. These records form the backbone of Cenozoic paleoceanographic and paleoclimatic studies and can be used to constrain paleotemperature and to trace water masses in the western North Atlantic.

3) Records from Expedition 342 are characterized by outstanding middle Eocene preservation of foraminifera and exhibit good bio- and magnetostratigraphic control.

4) The location of the Newfoundland Ridge is sensitive to changes in ocean circulation and its location is ideal for constraining variations in NADW formation and Deep Western Boundary Current velocity as the current initiates and contourite deposition begins.

5) The ridge is geographically isolated from downslope transport, which prevents deposition of large scale turbidites and provides continuous sections, as the sedimentary record has been formed from pelagic and bottom current-controlled sedimentation (Boyle et al., 2017).

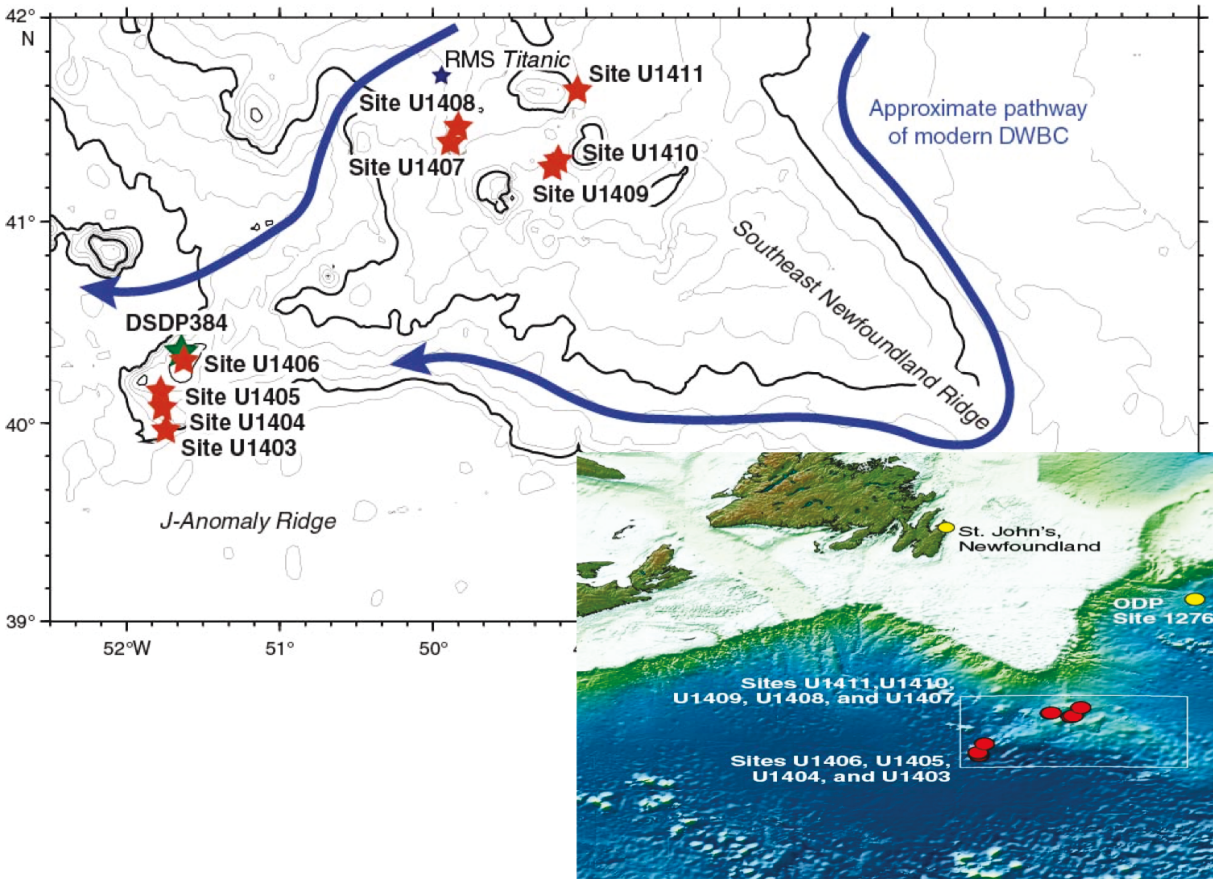

Figure 1.10: Paleogeographic map of the IODP Expedition 342 study area at the Newfoundland and J-Anomaly Ridge including drill Sites U1403-U1411 and the pathway of the modern Deep Western Boundary Current (modified after Norris et al., 2014).

References

Barker, P. F., Diekmann, B., and Escutia, C., 2007, Onset of Cenozoic Antarctic glaciation: Deep Sea Research Part II: Topical Studies in Oceanography, v. 54, no. 21, p. 2293-2307.

Barron, E. J., Hay, W. W., and Thompson, S., 1989, The hydrologic cycle: A major variable during Earth history: Palaeogeography, Palaeoclimatology, Palaeoecology, v. 75, no. 3, p. 157-174.

Beerling, D. J., and Royer, D. L., 2011, Convergent Cenozoic CO2 history: Nature Geosci, v. 4, no. 7, p. 418-420.

Berger, A., LONG-TERM VARIATION OF DAILY AND MONTHLY INSOLATION DURING LAST ICE AGE, *in* Proceedings TRANSACTIONS-AMERICAN GEOPHYSICAL UNION1976, Volume 57, AMER GEOPHYSICAL UNION 2000 FLORIDA AVE NW, WASHINGTON, DC 20009, p. 254-254.

Berger, A., 1978, Long-term variations of daily insolation and Quaternary climatic changes: Journal of the Atmospheric Sciences, v. 35, no. 12, p. 2362-2367.

Berger, A., and Loutre, M., 1994, Astronomical forcing through geological time: Orbital forcing and cyclic sequences (IAS Special Publication), PL de Boer and DG Smith, eds, v. 19, p. 15-24.

Berger, A., Loutre, M., and Laskar, J., 1992, Stability of the astronomical frequencies over the Earth's history for paleoclimate studies: Science, v. 255, no. 5044, p. 560.

Berger, A., Loutre, M. F., and Tricot, C., 1993, Insolation and Earth's orbital periods: Journal of Geophysical Research: Atmospheres, v. 98, no. D6, p. 10341-10362.

Berggren, W. A., and Hollister, C., 1977, Plate tectonics and paleocirculation—commotion in the ocean: Tectonophysics, v. 38, no. 1, p. 11-48.
Berggren, W. A., and Hollister, C. D., 1974, Paleogeography, paleobiogeography and the history of circulation in the Atlantic Ocean.
Bice, K. L., 1997, An investigation of early Eocene deep water warmth using uncoupled atmosphere and ocean general circulation models: Model sensitivity to geography, initial temperatures, atmospheric forcing and continental runoff.
Bice, K. L., and Marotzke, J., 2001, Numerical evidence against reversed thermohaline circulation in the warm Paleocene/Eocene ocean: Journal of Geophysical Research: Oceans, v. 106, no. C6, p. 11529-11542.
Bijl, P. K., Bendle, J. A. P., Bohaty, S. M., Pross, J., Schouten, S., Tauxe, L., Stickley, C. E., McKay, R. M., Röhl, U., Olney, M., Sluijs, A., Escutia, C., Brinkhuis, H., and Scientists, E., 2013, Eocene cooling linked to early flow across the Tasmanian Gateway: Proceedings of the National Academy of Sciences, v. 110, no. 24, p. 9645-9650.
Boyle, P. R., Romans, B. W., Tucholke, B. E., Norris, R. D., Swift, S. A., and Sexton, P. F., 2017, Cenozoic North Atlantic deep circulation history recorded in contourite drifts, offshore Newfoundland, Canada: Marine Geology, v. 385, p. 185-203.
Brass, G., Southam, J., and Peterson, W., 1982, Warm saline bottom water in the ancient ocean: Nature, v. 296, no. 5858, p. 620-623.
Broecker, W. S., The great ocean conveyor, *in* Proceedings AIP Conference Proceedings1992, Volume 247, AIP, p. 129-161.
Burton, K. W., Hong-Fei, L., and O'nions, R. K., 1997, Closure of the Central American Isthmus and its effect on deep-water formation in the North Atlantic: Nature, v. 386, no. 6623, p. 382.
Cane, M. A., and Molnar, P., 2001, Closing of the Indonesian seaway as a precursor to east African aridification around 3–4 million years ago: Nature, v. 411, no. 6834, p. 157-162.
Chamberlin, T. C., 1899, An attempt to frame a working hypothesis of the cause of glacial periods on an atmospheric basis: The Journal of Geology, v. 7, no. 6, p. 545-584.
Coates, A. G., Collins, L. S., Aubry, M.-P., and Berggren, W. A., 2004, The geology of the Darien, Panama, and the late Miocene-Pliocene collision of the Panama arc with northwestern South America: Geological Society of America Bulletin, v. 116, no. 11-12, p. 1327-1344.
Coates, A. G., Jackson, J. B., Collins, L. S., Cronin, T. M., Dowsett, H. J., Bybell, L. M., Jung, P., and Obando, J. A., 1992, Closure of the Isthmus of Panama: the near-shore marine record of Costa Rica and western Panama: Geological Society of America Bulletin, v. 104, no. 7, p. 814-828.
Collins, L. S., Coates, A. G., Berggren, W. A., Aubry, M.-P., and Zhang, J., 1996, The late Miocene Panama isthmian strait: Geology, v. 24, no. 8, p. 687-690.
Coxall, H. K., Wilson, P. A., Pälike, H., Lear, C. H., and Backman, J., 2005, Rapid stepwise onset of Antarctic glaciation and deeper calcite compensation in the Pacific Ocean: Nature, v. 433, no. 7021, p. 53-57.
Cramer, B., Miller, K., Barrett, P., and Wright, J., 2011, Late Cretaceous–Neogene trends in deep ocean temperature and continental ice volume: Reconciling records of benthic foraminiferal geochemistry (δ18O and Mg/Ca) with sea level history: Journal of Geophysical Research: Oceans, v. 116, no. C12.
Cramer, B., Toggweiler, J., Wright, J., Katz, M., and Miller, K., 2009, Ocean overturning since the Late Cretaceous: Inferences from a new benthic foraminiferal isotope compilation: Paleoceanography, v. 24, no. 4.
Croll, J., 1875, ``Climate and Time'': Nature, v. 12, p. 329.
Curry, W. B., and Oppo, D. W., 2005, Glacial water mass geometry and the distribution of δ13C of ΣCO2 in the western Atlantic Ocean: Paleoceanography, v. 20, no. 1.
Davies, R., Cartwright, J., Pike, J., and Line, C., 2001, Early Oligocene initiation of North Atlantic deep water formation: Nature, v. 410, no. 6831, p. 917-920.
De Boer, A., Sigman, D., Toggweiler, J., and Russell, J., 2007, Effect of global ocean temperature change on deep ocean ventilation: Paleoceanography, v. 22, no. 2.
De Vleeschouwer, D., Vahlenkamp, M., Crucifix, M., and Pälike, H., 2017, Alternating Southern and Northern Hemisphere climate response to astronomical forcing during the past 35 m.y: Geology.
DeConto, R. M., and Pollard, D., 2003a, A coupled climate–ice sheet modeling approach to the early Cenozoic history of the Antarctic ice sheet: Palaeogeography, Palaeoclimatology, Palaeoecology, v. 198, no. 1, p. 39-52.
-, 2003b, Rapid Cenozoic glaciation of Antarctica induced by declining atmospheric CO2: Nature, v. 421, no. 6920, p. 245-249.

Eberle, J. J., Fricke, H. C., Humphrey, J. D., Hackett, L., Newbrey, M. G., and Hutchison, J. H., 2010, Seasonal variability in Arctic temperatures during early Eocene time: Earth and Planetary Science Letters, v. 296, no. 3–4, p. 481-486.

Ehrmann, W. U., and Mackensen, A., 1992, Sedimentological evidence for the formation of an East Antarctic ice sheet in Eocene/Oligocene time: Palaeogeography, Palaeoclimatology, Palaeoecology, v. 93, no. 1–2, p. 85-112.

Exon, N., Kennett, J., Malone, M., Brinkhuis, H., Chaproniere, G., Ennyu, A., Fothergill, P., Fuller, M., Grauert, M., and Hill, P., 2002, Drilling reveals climatic consequences of Tasmanian Gateway opening: Eos, Transactions American Geophysical Union, v. 83, no. 23, p. 253-259.

Gradstein, F. M., Ogg, J. G., Schmitz, M., and Ogg, G., 2012, The geologic time scale 2012, elsevier.

Greenwood, D. R., and Wing, S. L., 1995, Eocene continental climates and latitudinal temperature gradients: Geology, v. 23, no. 11, p. 1044-1048.

Haug, G. H., Tiedemann, R., Zahn, R., and Ravelo, A. C., 2001, Role of Panama uplift on oceanic freshwater balance: Geology, v. 29, no. 3, p. 207-210.

Hays, J. D., Imbrie, J., and Shackleton, N. J., Variations in the Earth's orbit: pacemaker of the ice ages1976, American Association for the Advancement of Science.

Herschel, J. F. W., 1832, XVII.—On the Astronomical Causes which may influence Geological Phænomena: Transactions of the Geological Society of London, no. 2, p. 293-300.

Hilgen, F. J., Kuiper, K. F., and Lourens, L. J., 2010, Evaluation of the astronomical time scale for the Paleocene and earliest Eocene: Earth and Planetary Science Letters, v. 300, no. 1–2, p. 139-151.

Hinnov, L. A., and Park, J., 1998, Detection of astronomical cycles in the stratigraphic record by frequency modulation (FM) analysis: Journal of Sedimentary Research, v. 68, no. 4.

Hohbein, M. W., Sexton, P. F., and Cartwright, J. A., 2012, Onset of North Atlantic Deep Water production coincident with inception of the Cenozoic global cooling trend: Geology, v. 40, no. 3, p. 255-258.

Houghton, J. T., Ding, Y., Griggs, D. J., Noguer, M., van der Linden, P. J., Dai, X., Maskell, K., and Johnson, C., 2001, Climate change 2001: the scientific basis, The Press Syndicate of the University of Cambridge.

Huber, M., and Caballero, R., 2003, Eocene El Nino: Evidence for robust tropical dynamics in the" hothouse": Science, v. 299, no. 5608, p. 877-881.

Huber, M., and Nof, D., 2006, The ocean circulation in the southern hemisphere and its climatic impacts in the Eocene: Palaeogeography, Palaeoclimatology, Palaeoecology, v. 231, no. 1, p. 9-28.

Huber, M., and Sloan, L. C., 2001, Heat transport, deep waters, and thermal gradients: Coupled simulation of an Eocene greenhouse climate: Geophysical Research Letters, v. 28, no. 18, p. 3481-3484.

Imbrie, J., Berger, A., Boyle, E., Clemens, S., Duffy, A., Howard, W., Kukla, G., Kutzbach, J., Martinson, D., and McIntyre, A., 1993, On the structure and origin of major glaciation cycles 2. The 100,000-year cycle: Paleoceanography, v. 8, no. 6, p. 699-735.

Jagniecki, E. A., Lowenstein, T. K., Jenkins, D. M., and Demicco, R. V., 2015, Eocene atmospheric CO2 from the nahcolite proxy: Geology, v. 43, no. 12, p. 1075-1078.

Jakobsson, M., Backman, J., Rudels, B., Nycander, J., Frank, M., Mayer, L., Jokat, W., Sangiorgi, F., O'Regan, M., and Brinkhuis, H., 2007, The early Miocene onset of a ventilated circulation regime in the Arctic Ocean: Nature, v. 447, no. 7147, p. 986-990.

Jovane, L., Sprovieri, M., Coccioni, R., Florindo, F., Marsili, A., and Laskar, J., 2010, Astronomical calibration of the middle Eocene contessa Highway section (Gubbio, Italy): Earth and Planetary Science Letters, v. 298, no. 1, p. 77-88.

Kameo, K., and Sato, T., 2000, Biogeography of Neogene calcareous nannofossils in the Caribbean and the eastern equatorial Pacific—floral response to the emergence of the Isthmus of Panama: Marine Micropaleontology, v. 39, no. 1, p. 201-218.

Keigwin, L., 1982, Isotopic paleoceanography of the Caribbean and East Pacific: role of Panama uplift in late Neogene time: Science, v. 217, no. 4557, p. 350-353.

Keigwin, L. D., 1978, Pliocene closing of the Isthmus of Panama, based on biostratigraphic evidence from nearby Pacific Ocean and Caribbean Sea cores: Geology, v. 6, no. 10, p. 630-634.

Kennett, J. P., 1977, Cenozoic evolution of Antarctic glaciation, the circum-Antarctic Ocean, and their impact on global paleoceanography: Journal of geophysical research, v. 82, no. 27, p. 3843-3860.

Laskar, J., Fienga, A., Gastineau, M., and Manche, H., 2011, La2010: a new orbital solution for the long-term motion of the Earth: Astronomy & Astrophysics, v. 532, p. A89.

Laskar, J., and Robutel, P., 1993, The chaotic obliquity of the planets: Nature, v. 361, no. 6413, p. 608-612.

Laskar, J., Robutel, P., Joutel, F., Gastineau, M., Correia, A., and Levrard, B., 2004, A long-term numerical solution for the insolation quantities of the Earth: Astronomy & Astrophysics, v. 428, no. 1, p. 261-285.
Lear, C. H., Rosenthal, Y., and Wright, J. D., 2003, The closing of a seaway: ocean water masses and global climate change: Earth and Planetary Science Letters, v. 210, no. 3, p. 425-436.
Lisiecki, L. E., and Raymo, M. E., 2007, Plio–Pleistocene climate evolution: trends and transitions in glacial cycle dynamics: Quaternary Science Reviews, v. 26, no. 1, p. 56-69.
Liu, X., Gao, Q., Han, M., and Jin, J., 2016, Estimates of late middle Eocene pCO 2 based on stomatal density of modern and fossil Nageia leaves: Climate of the Past, v. 12, no. 2, p. 241-253.
Lourens, L. J., Sluijs, A., Kroon, D., Zachos, J. C., Thomas, E., Röhl, U., Bowles, J., and Raffi, I., 2005, Astronomical pacing of late Palaeocene to early Eocene global warming events: Nature, v. 435, no. 7045, p. 1083-1087.
Lyell, S. C., 1872, Principles of Geology (1872): Vol. I, p. 426.
Lyle, M., 1997, Could early Cenozoic thermohaline circulation have warmed the poles?: Paleoceanography, v. 12, no. 2, p. 161-167.
Marshall, J., and Speer, K., 2012, Closure of the meridional overturning circulation through Southern Ocean upwelling: Nature Geoscience, v. 5, no. 3, p. 171-180.
Meng, J., Wang, C., Zhao, X., Coe, R., Li, Y., and Finn, D., 2012, India-Asia collision was at 24 N and 50 Ma: palaeomagnetic proof from southernmost Asia: Scientific reports, v. 2, p. 925.
Meyers, S. R., 2014, astrochron: AN R Package for Astrochronology. http://cran.r-project.org/package=astrochron.
Milankovitch, M., 1941, Kanon der Erdebestrahlung und seine Anwendung auf das Eiszeitenproblem, Königlich Serbische Akademie.
Min, K., Mundil, R., Renne, P. R., and Ludwig, K. R., 2000, A test for systematic errors in 40 Ar/39 Ar geochronology through comparison with U/Pb analysis of a 1.1-Ga rhyolite: Geochimica et Cosmochimica Acta, v. 64, no. 1, p. 73-98.
Moran, K., Backman, J., Brinkhuis, H., Clemens, S. C., Cronin, T., Dickens, G. R., Eynaud, F., Gattacceca, J., Jakobsson, M., and Jordan, R. W., 2006, The cenozoic palaeoenvironment of the arctic ocean: Nature, v. 441, no. 7093, p. 601-605.
Mountain, G. S., and Miller, K. G., 1992, Seismic and geologic evidence for early Paleogene deepwater circulation in the western North Atlantic: Paleoceanography, v. 7, no. 4, p. 423-439.
Mountain, G. S., and Tucholke, B. E., 1985, Mesozoic and Cenozoic geology of the US Atlantic continental slope and rise, Van Nostrand Reinhold Co.
Munk, W., and Wunsch, C., 1998, Abyssal recipes II: energetics of tidal and wind mixing: Deep Sea Research Part I: Oceanographic Research Papers, v. 45, no. 12, p. 1977-2010.
Mutterlose, J., Brumsack, H., Flögel, S., Hay, W., Klein, C., Langrock, U., Lipinski, M., Ricken, W., Söding, E., and Stein, R., 2003, The Greenland-Norwegian Seaway: A key area for understanding Late Jurassic to Early Cretaceous paleoenvironments: Paleoceanography, v. 18, no. 1.
Newkirk, D. R., and Martin, E. E., 2009, Circulation through the Central American Seaway during the Miocene carbonate crash: Geology, v. 37, no. 1, p. 87-90.
Nilsson, J., Broström, G., and Walin, G., 2003, The thermohaline circulation and vertical mixing: Does weaker density stratification give stronger overturning?: Journal of Physical Oceanography, v. 33, no. 12, p. 2781-2795.
Norris, R., Wilson, P., Blum, P., Fehr, A., Agnini, C., Bornemann, A., Boulila, S., Bown, P., Cournede, C., and Friedrich, O., 2014, Expedition 342 Summary: Norris, RD, Wilson, PA, Blum, P., the Expedition, v. 342.
Norris, R. D., Kroon, D., Huber, B. T., and Erbacher, J., 2001, Cretaceous-Palaeogene ocean and climate change in the subtropical North Atlantic: Geological Society, London, Special Publications, v. 183, no. 1, p. 1-22.
Norris, R. D., Wilson, P. A., Blum, P., Fehr, A., Agnini, C., Bornemann, A., Boulila, S., Brown, P. R., Cournede, C., and Friedrich, O., 2012, Paleogene Newfoundland sediment drifts, Integrated Ocean Drilling Program Management International, Inc.
Norris, R. D., Wilson, P.A., Blum, P., Fehr, A., Agnini, C., Bornemann, A., Boulila, S., Bown, P.R., Cournede, C., Friedrich, O., Ghosh, A.K., Hollis, C.J., Hull, P.M., Jo, K., Junium, C.K., Kaneko, M., Liebrand, D., Lippert, P.C., Liu, Z., Matsui, H., Moriya, K., Nishi, H., Opdyke, B.N., Penman, D., Romans, B., Scher, H.D., Sexton, P., Takagi, H., Turner, S.K., Whiteside, J.H., Yamaguchi, T., and Yamamoto, Y., 2014. Site U1410. In Norris, R.D., Wilson, P.A., Blum, P., and the Expedition 342 Scientists, 2014, Proc. IODP, 342: College Station, TX (Integrated Ocean Drilling Program).

O'Connell, S., Chandler, M. A., and Ruedy, R., 1996, Implications for the creation of warm saline deep water: Late Paleocene reconstructions and global climate model simulations: Geological Society of America Bulletin, v. 108, no. 3, p. 270-284.

O'Regan, M., Moran, K., Backman, J., Jakobsson, M., Sangiorgi, F., Brinkhuis, H., Pockalny, R., Skelton, A., Stickley, C., and Koç, N., 2008, Mid-Cenozoic tectonic and paleoenvironmental setting of the central Arctic Ocean: Paleoceanography, v. 23, no. 1.

Pagani, M., Huber, M., Liu, Z., Bohaty, S. M., Henderiks, J., Sijp, W., Krishnan, S., and DeConto, R. M., 2011, The role of carbon dioxide during the onset of Antarctic glaciation: Science, v. 334, no. 6060, p. 1261-1264.

Pagani, M., Pedentchouk, N., Huber, M., Sluijs, A., Schouten, S., Brinkhuis, H., Damsté, J. S. S., Dickens, G. R., Backman, J., and Clemens, S., 2006, Arctic hydrology during global warming at the Palaeocene/Eocene thermal maximum: Nature, v. 442, no. 7103, p. 671-675.

Pak, D. K., and Miller, K. G., 1992, Paleocene to Eocene benthic foraminiferal isotopes and assemblages: Implications for deepwater circulation: Paleoceanography, v. 7, no. 4, p. 405-422.

Pälike, H., Laskar, J., and Shackleton, N. J., 2004, Geologic constraints on the chaotic diffusion of the solar system: Geology, v. 32, no. 11, p. 929-932.

Pälike, H., Lyle, M. W., Nishi, H., Raffi, I., Ridgwell, A., Gamage, K., Klaus, A., Acton, G., Anderson, L., Backman, J., Baldauf, J., Beltran, C., Bohaty, S. M., BownPaul, Busch, W., Channell, J. E. T., Chun, C. O. J., Delaney, M., Dewangan, P., Dunkley Jones, T., Edgar, K. M., Evans, H., Fitch, P., Foster, G. L., Gussone, N., Hasegawa, H., Hathorne, E. C., Hayashi, H., Herrle, J. O., Holbourn, A., Hovan, S., Hyeong, K., Iijima, K., Ito, T., Kamikuri, S.-i., Kimoto, K., Kuroda, J., Leon-Rodriguez, L., Malinverno, A., Moore Jr, T. C., Murphy, B. H., Murphy, D. P., Nakamura, H., Ogane, K., Ohneiser, C., Richter, C., Robinson, R., Rohling, E. J., Romero, O., Sawada, K., Scher, H., Schneider, L., Sluijs, A., Takata, H., Tian, J., Tsujimoto, A., Wade, B. S., Westerhold, T., Wilkens, R., Williams, T., Wilson, P. A., Yamamoto, Y., Yamamoto, S., Yamazaki, T., and Zeebe, R. E., 2012, A Cenozoic record of the equatorial Pacific carbonate compensation depth: Nature, v. 488, no. 7413, p. 609-614.

Pälike, H., Norris, R. D., Herrle, J. O., Wilson, P. A., Coxall, H. K., Lear, C. H., Shackleton, N. J., Tripati, A. K., and Wade, B. S., 2006, The heartbeat of the Oligocene climate system: science, v. 314, no. 5807, p. 1894-1898.

Pälike, H., and Shackleton, N. J., 2000, Constraints on astronomical parameters from the geological record for the last 25 Myr: Earth and Planetary Science Letters, v. 182, no. 1, p. 1-14.

Pearson, P. N., and Palmer, M. R., 2000, Atmospheric carbon dioxide concentrations over the past 60 million years: Nature, v. 406, no. 6797, p. 695-699.

Proistosescu, C., Huybers, P., and Maloof, A. C., 2012, To tune or not to tune: Detecting orbital variability in Oligo-Miocene climate records: Earth and Planetary Science Letters, v. 325, p. 100-107.

Rahmstorf, S., 2002, Ocean circulation and climate during the past 120,000 years: Nature, v. 419, no. 6903, p. 207-214.

Rial, J. A., 1999, Pacemaking the ice ages by frequency modulation of Earth's orbital eccentricity: Science, v. 285, no. 5427, p. 564-568.

Roberts, C. D., LeGrande, A. N., and Tripati, A. K., 2009, Climate sensitivity to Arctic seaway restriction during the early Paleogene: Earth and Planetary Science Letters, v. 286, no. 3, p. 576-585.

Shackleton, N., Crowhurst, S., Hagelberg, T., Pisias, N., and Schneider, D., A new late Neogene time scale: application to Leg 138 sites, *in* Proceedings Proc. ODP, Sci. Results1995, Volume 138, p. 73-101.

Shackleton, N., Crowhurst, S., Weedon, G., and Laskar, J., 1999, Astronomical calibration of Oligocene--Miocene time: Philosophical Transactions of the Royal Society of London. Series A: Mathematical, Physical and Engineering Sciences, v. 357, no. 1757, p. 1907-1929.

Shackleton, N. J., and Crowhurst, S., Sediment fluxes based on an orbitally tuned time scale 5 Ma to 14 Ma, Site 926, *in* Proceedings Proc. ODP, Sci. Results1997, Volume 154, p. 69-82.

Shellito, C. J., Lamarque, J. F., and Sloan, L. C., 2009, Early Eocene Arctic climate sensitivity to pCO2 and basin geography: Geophysical Research Letters, v. 36, no. 9.

Shellito, C. J., Sloan, L. C., and Huber, M., 2003, Climate model sensitivity to atmospheric CO 2 levels in the Early–Middle Paleogene: Palaeogeography, Palaeoclimatology, Palaeoecology, v. 193, no. 1, p. 113-123.

Simpson, G. C., POSSIBLE CAUSES OF CHANGE IN CLIMATE AND THEIR LIMITATIONS, *in* Proceedings Proceedings of the Linnean Society of London1940, Volume 152, Wiley Online Library, p. 190-219.

Sloan, L. C., 1994, Equable climates during the early Eocene: Significance of regional paleogeography for North American climate: Geology, v. 22, no. 10, p. 881-884.
Sloan, L. C., and Barron, E. J., 1990, " Equable" climates during Earth history?: Geology, v. 18, no. 6, p. 489-492.
-, 1992, A comparison of Eocene climate model results to quantified paleoclimatic interpretations: Palaeogeography, Palaeoclimatology, Palaeoecology, v. 93, no. 3-4, p. 183-202.
Sluijs, A., Schouten, S., Pagani, M., Woltering, M., Brinkhuis, H., Damsté, J. S. S., Dickens, G. R., Huber, M., Reichart, G.-J., Stein, R., Matthiessen, J., Lourens, L. J., Pedentchouk, N., Backman, J., Moran, K., and the Expedition, S., 2006, Subtropical Arctic Ocean temperatures during the Palaeocene/Eocene thermal maximum: Nature, v. 441, no. 7093, p. 610-613.
Solomon, S., 2007, Climate change 2007-the physical science basis: Working group I contribution to the fourth assessment report of the IPCC, Cambridge University Press.
Speelman, E. N., van Kempen, M. M., Barke, J., Brinkhuis, H., Reichart, G.-J., Smolders, A. J., Roelofs, J. G., Sangiorgi, F., de Leeuw, J. W., and Lotter, A. F., 2009, The Eocene Arctic Azolla bloom: environmental conditions, productivity and carbon drawdown: Geobiology, v. 7, no. 2, p. 155-170.
St John, K., 2008, Cenozoic ice-rafting history of the central Arctic Ocean: Terrigenous sands on the Lomonosov Ridge: Paleoceanography, v. 23, no. 1.
St. John, K., 2008, Cenozoic ice-rafting history of the central Arctic Ocean: Terrigenous sands on the Lomonosov Ridge: Paleoceanography, v. 23, no. 1, p. PA1S05.
Stein, R., Boucsein, B., and Meyer, H., 2006, Anoxia and high primary production in the Paleogene central Arctic Ocean: First detailed records from Lomonosov Ridge: Geophysical Research Letters, v. 33, no. 18.
Stoker, M. S., Praeg, D., Hjelstuen, B. O., Laberg, J. S., Nielsen, T., and Shannon, P. M., 2005, Neogene stratigraphy and the sedimentary and oceanographic development of the NW European Atlantic margin: Marine and Petroleum Geology, v. 22, no. 9, p. 977-1005.
Stow, D., and Faugères, J.-C., 2008, Contourite facies and the facies model: Developments in Sedimentology, v. 60, p. 223-256.
Stow, D. A., Faugères, J.-C., Howe, J. A., Pudsey, C. J., and Viana, A. R., 2002, Bottom currents, contourites and deep-sea sediment drifts: current state-of-the-art: Geological Society, London, Memoirs, v. 22, no. 1, p. 7-20.
Thiede, J., Winkler, A., Wolf-Welling, T., Eldholm, O., Myhre, A. M., Baumann, K.-H., Henrich, R., and Stein, R., 1998, Late Cenozoic history of the polar North Atlantic: results from ocean drilling: Quaternary Science Reviews, v. 17, no. 1-3, p. 185-208.
Thomas, D. J., Bralower, T. J., and Jones, C. E., 2003, Neodymium isotopic reconstruction of late Paleocene–early Eocene thermohaline circulation: Earth and Planetary Science Letters, v. 209, no. 3, p. 309-322.
Thomson, D. J., 1982, Spectrum estimation and harmonic analysis: Proceedings of the IEEE, v. 70, no. 9, p. 1055-1096.
Thomson, D. J., 1990, Quadratic-inverse spectrum estimates: applications to palaeoclimatology: Philosophical Transactions of the Royal Society of London A: Mathematical, Physical and Engineering Sciences, v. 332, no. 1627, p. 539-597.
Tripati, A. K., Delaney, M. L., Zachos, J. C., Anderson, L. D., Kelly, D. C., and Elderfield, H., 2003, Tropical sea-surface temperature reconstruction for the early Paleogene using Mg/Ca ratios of planktonic foraminifera: Paleoceanography, v. 18, no. 4.
Tripati, A. K., Eagle, R. A., Morton, A., Dowdeswell, J. A., Atkinson, K. L., Bahé, Y., Dawber, C. F., Khadun, E., Shaw, R. M., and Shorttle, O., 2008, Evidence for glaciation in the Northern Hemisphere back to 44 Ma from ice-rafted debris in the Greenland Sea: Earth and Planetary Science Letters, v. 265, no. 1, p. 112-122.
Tucholke, B. E., and Ewing, J. I., 1974, Bathymetry and sediment geometry of the Greater Antilles Outer Ridge and vicinity: Geological Society of America Bulletin, v. 85, no. 11, p. 1789-1802.
Tucholke, B. E., and Mountain, G. S., 1979, Seismic stratigraphy, lithostratigraphy and paleosedimentation patterns in the North American Basin, Wiley Online Library.
Tyndall, J., 1861, XXIII. On the absorption and radiation of heat by gases and vapours, and on the physical connexion of radiation, absorption, and conduction.—The bakerian lecture: The London, Edinburgh, and Dublin Philosophical Magazine and Journal of Science, v. 22, no. 146, p. 169-194.
Vandenberghe, N., Hilgen, F., and Speijer, R., 2012, The paleogene period.
Via, R. K., and Thomas, D. J., 2006, Evolution of Atlantic thermohaline circulation: Early Oligocene onset of deep-water production in the North Atlantic: Geology, v. 34, no. 6, p. 441-444.
von der Heydt, A., and Dijkstra, H. A., 2006, Effect of ocean gateways on the global ocean circulation in the late Oligocene and early Miocene: Paleoceanography, v. 21, no. 1.

Walker, J. C., Hays, P., and Kasting, J. F., 1981, A negative feedback mechanism for the long-term stabilization of Earth's surface temperature: Journal of Geophysical Research: Oceans, v. 86, no. C10, p. 9776-9782.

Weijers, J. W. H., Schouten, S., Sluijs, A., Brinkhuis, H., and Sinninghe Damsté, J. S., 2007, Warm arctic continents during the Palaeocene–Eocene thermal maximum: Earth and Planetary Science Letters, v. 261, no. 1–2, p. 230-238.

Weller, P., and Stein, R., 2008, Paleogene biomarker records from the central Arctic Ocean (Integrated Ocean Drilling Program Expedition 302): Organic carbon sources, anoxia, and sea surface temperature: Paleoceanography, v. 23, no. 1.

Westerhold, T., and Röhl, U., 2009, High resolution cyclostratigraphy of the early Eocene–new insights into the origin of the Cenozoic cooling trend: Climate of the Past, v. 5, no. 3, p. 309-327.

Westerhold, T., Röhl, U., Donner, B., McCarren, H. K., and Zachos, J. C., 2011, A complete high-resolution Paleocene benthic stable isotope record for the central Pacific (ODP Site 1209): Paleoceanography, v. 26, no. 2.

Westerhold, T., Röhl, U., Frederichs, T., Bohaty, S., and Zachos, J., 2015, Astronomical calibration of the geological timescale: closing the middle Eocene gap: Climate of the Past, v. 11, no. 9, p. 1181.

Westerhold, T., Röhl, U., Laskar, J., Raffi, I., Bowles, J., Lourens, L. J., and Zachos, J. C., 2007, On the duration of magnetochrons C24r and C25n and the timing of early Eocene global warming events: Implications from the Ocean Drilling Program Leg 208 Walvis Ridge depth transect: Paleoceanography, v. 22, no. 2.

Westerhold, T., Röhl, U., Pälike, H., Wilkens, R., Wilson, P., and Acton, G., 2014, Orbitally tuned timescale and astronomical forcing in the middle Eocene to early Oligocene: Climate of the Past, v. 10, no. 3, p. 955-973.

Westerhold, T., Röhl, U., Raffi, I., Fornaciari, E., Monechi, S., Reale, V., Bowles, J., and Evans, H. F., 2008, Astronomical calibration of the Paleocene time: Palaeogeography, Palaeoclimatology, Palaeoecology, v. 257, no. 4, p. 377-403.

Winguth, A., Shellito, C., Shields, C., and Winguth, C., 2010, Climate response at the Paleocene–Eocene thermal maximum to greenhouse gas forcing—a model study with CCSM3: Journal of Climate, v. 23, no. 10, p. 2562-2584.

Zachos, J., Pagani, M., Sloan, L., Thomas, E., and Billups, K., 2001, Trends, rhythms, and aberrations in global climate 65 Ma to present: Science, v. 292, no. 5517, p. 686-693.

Zachos, J. C., Dickens, G. R., and Zeebe, R. E., 2008, An early Cenozoic perspective on greenhouse warming and carbon-cycle dynamics: Nature, v. 451, no. 7176, p. 279-283.

Zachos, J. C., Stott, L. D., and Lohmann, K. C., 1994, Evolution of early Cenozoic marine temperatures: Paleoceanography, v. 9, no. 2, p. 353-387.

Zeeden, C., Hilgen, F., Westerhold, T., Lourens, L., Röhl, U., and Bickert, T., 2013, Revised Miocene splice, astronomical tuning and calcareous plankton biochronology of ODP Site 926 between 5 and 14.4 Ma: Palaeogeography, Palaeoclimatology, Palaeoecology, v. 369, p. 430-451.

Chapter 2: *Towards a Robust and Consistent Middle Eocene Astronomical Timescale*

Slah Boulila[1,2], Maximilian Vahlenkamp[3], David De Vleeschouwer[3], Jacques Laskar[2], Yuhji Yamamoto[4], Heiko Pälike[3], Sandra Kirtland Turner[5], Philip F. Sexton[6], Thomas Westerhold[3], and Ursula Röhl[3]

[1] Université Paris VI, CNRS - UMR 7193 ISTeP 'Institut des Sciences de la Terre-Paris', case 117, 4, place Jussieu, 75252 Paris cedex 05, France.

[2] ASD, IMCCE-CNRS UMR 8028, Observatoire de Paris, UPMC, 77 avenue Denfert-Rochereau, 75014 Paris, France.

[3] MARUM - Center for Marine Environmental Sciences, University of Bremen, Leobener Strasse 8, 28359 Bremen, Germany.

[4] Center for Advanced Marine Core Research, Kochi University, B200 Monobe, Nankoku, Kochi 783-8502, Japan.

[5] Department of Earth Sciences, University of California, Riverside, CA 92521, USA.

[6] School of Environment, Earth and Ecosystem Sciences, The Open University, Walton Hall, Milton Keynes, Buckinghamshire, MK7 6AA, UK.

Abstract

Until now, the middle Eocene geologic timescale has remained a poorly constrained interval of the Cenozoic, the so-called “Eocene astronomical timescale gap". The establishment of a high-resolution orbital calibration for this interval has been difficult due to a lack of carbonate-rich cyclic deep-marine sections from that time. In this paper, we present a middle Eocene record from the North Atlantic Southeast Newfoundland Ridge (IODP 342, Sites U1408 and U1410), allowing for an orbital calibration of geologic time between ~38 and ~48 Ma. These carbonate-rich, cyclic sequences at Sites U1408 and U1410 were deposited as contourite drifts and exhibit prominent lithological alternations (couplets) between greenish nannofossil clay and white nannofossil ooze. The principal lithological couplet is driven by the obliquity of Earth’s axial tilt, and the intensity of their expression is modulated by a cycle of about 173 kyr. This cycle corresponds to the interference of the secular frequencies s3 and s6 (related to the precession of nodes of the Earth and Saturn, respectively). The 173-kyr obliquity amplitude modulation cycle is exceptionally well recorded in the XRF-derived (X-ray fluorescence) Ca/Fe ratio of the middle Eocene sediments at Sites U1408 and U1410. In this work, we first demonstrate the stability of the (s3–s6) cycles using the latest astronomical solutions. Results show that this orbital component is stable back to at least 50 Ma, and can thus serve as a powerful geochronometer of the Cenozoic timescale until the Eocene. We then exploit this potential by calibrating the geochronology of the recovered middle Eocene timescale between chrons C18n.1n and C21n. Comparison with previous timescales shows similarities, as well as notable differences in the durations of certain chrons. We present a revision of previous astronomical timescales from the Equatorial and South Atlantic, to overcome the differences between the existing middle Eocene astrochronologies. Using our new records from the North Atlantic (U1408 and U1410), combined with existing records from the South Atlantic (ODP Site 1263 and Hole 702B) and Equatorial Atlantic (ODP Site 1260), we revise the durations of chrons C18n.1n to C21n, thereby achieving a robust and self-consistent middle Eocene astronomical timescale.

2.1 Introduction

Astronomical (Milankovitch) pacing of climate change is documented in the sedimentary record through changes in the chemical, physical, paleontological and sedimentological characteristics of the sediment. The detection of the link between climatic cycles in the sedimentary record (e.g., Lourens et al., 2004) and calculated Milankovitch cycles (e.g., Laskar et al., 2004) has resulted in the astronomical time calibration (or tuning) of the Geological Time Scale, GTS (e.g., GTS2012, Gradstein et al., 2012). Thus, astronomical tuning has now become a standard technique for most geological epochs because of its high temporal precision. In particular, multiple efforts have been made in order to achieve an Astronomical Time Scale (ATS) for the entire Cenozoic era (past 66 Ma).

The Neogene ATS in the latest GTS2012 (Hilgen et al., 2012) is very similar to its predecessor in GTS2004 (Lourens et al., 2004). It is based on direct astronomical tuning to the full astronomical solution, and is essentially stable (Hilgen et al., 2012). This ATS was extended towards older time intervals. The entire Oligocene was calibrated from ODP Site 1218 in the equatorial Pacific (Pälike et al., 2006). However, the Eocene proved difficult to tune because of a shallow paleo-CCD (Carbonate Compensation Depth) in large areas of the global ocean (Pälike et al., 2012) that prevented deposition of the carbonate-rich sequences that are most suitable for cyclostratigraphy. Initial attempts were made to tune the late Eocene at ODP Site 1052 (Pälike et al.,2001). Later, important efforts focused on older parts of the Eocene from ODP sites 1258 and 1262 (Lourens et al., 2005, Westerhold et al., 2007, Westerhold and Röhl, 2009), in conjunction with tuning the entire Paleocene down to the Cretaceous-Paleogene (K/Pg) boundary (Westerhold et al., 2008). This resulted in multiple options, based on a difference of one 405-kyr eccentricity related cycle within the Paleocene: 24 cycles as suggested by Westerhold et al. (2008, 2012) versus 25 cycles according to Hilgen et al. (2010). This difference affects the age of the K/Pg boundary: ~65.5 Ma versus ~66 Ma, respectively. More recent studies support the 66 Ma age of the K/Pg boundary, and the existence of 25 405-kyr-eccentricity related cycles within the Paleocene (Dinarès-Turell et al., 2014; Hilgen et al., 2015; Clyde et al., 2016).

In contrast to the Paleocene and Oligocene, which now have a relatively stable ATS, the Eocene ATS is still under revision, resulting in the so-called middle-late Eocene ATS gap (from 34 to 48 Ma) in the Cenozoic timescale (Hilgen et al., 2012 and Figure 2.1). The existence of this gap derives primarily from the scarcity of highly resolved sedimentary records from the middle Eocene hampering the establishment of a stable ATS for the entire Cenozoic era.

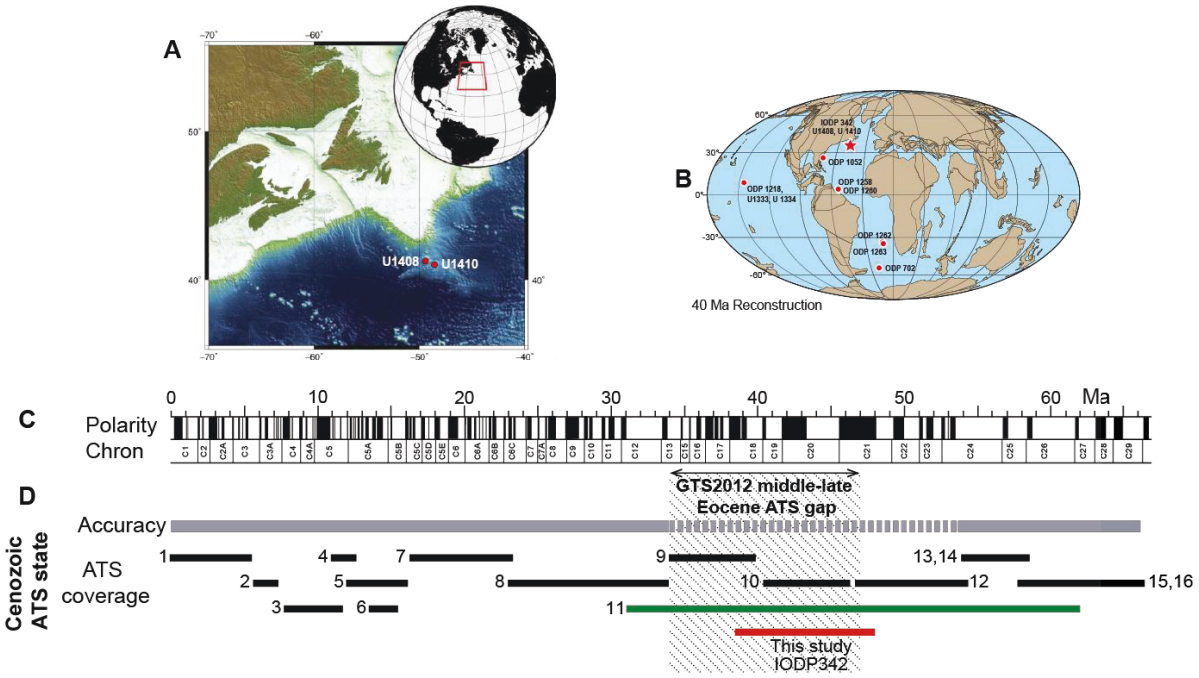

Figure 2.1: Main ocean drilling sites used to close the Eocene Astronomical Time Scale (ATS) gap, and state-of-the-art of the Cenozoic ATS. (A) IODP Expedition 342 sites on Newfoundland Ridge: U1408 (3022 m present-day waterdepth) and U1410 (3400 m). (B) Paleolocation of the main ocean drilling sites used for the Eocene ATS. IODP Expedition 342 sites (U1408 and U1410) are indicated by a red star. (C) Geomagnetic Polarity timescale defined by Cande and Kent (1992) using the revised ages from the Geological Time Scale 2012, GTS2012 (Gradstein et al., 2012). (D) Cenozoic ATS state-of-the-art. The upper horizontal grey bar (accuracy), solid for stable ATS, and dashed for unstable ATS (needs revisions). The lower horizontal bars indicate ATS stratigraphic coverage. 1. Lourens et al. (2004), 2. Hilgen et al. (2007), 3. Hüsing et al. (2009); 4. Hilgen et al. (2003), 5. Holbourn et al. (2007), 6. Hüsing et al. (2010), 7. Billups et al. (2004), 8. Pälike et al. (2006), 9. Pälike et al. (2001), 10. Jovane et al. (2010), 11. Westerhold et al. (2012, 2014, 2015) and Westerhold and Röhl (2013), 12. Westerhold and Röhl (2009), 13. Lourens et al. (2005), 14. Westerhold et al. (2007), 15. Westerhold et al. (2008), 16. Kuiper et al. (2008). The crosshatched area shows the middle-late Eocene ATS gap, as described in the GTS2012. Green horizontal bar indicates post-GTS2012 first attempts to bridge the middle-late Eocene gap. Red horizontal bar indicates stratigraphic coverage in the present study from IODP342 Sites U1408-U1410, providing new constraints on the middle-late Eocene ATS gap.

Recently, attempts have been made in order to close this gap (Westerhold and Röhl, 2013; Westerhold et al., 2014, 2015). In detail, the latest efforts to bridge the middle-late Eocene gap, including the Eocene-Oligocene transition, used principally the 405 kyr eccentricity tuning of the intervals spanning C18r through C20r from the tropical western Atlantic (Leg 207, ODP Site 1260, Westerhold and Röhl, 2013), C12n through C20n mainly from the Pacific Equatorial Age Transect (PEAT) sites (Westerhold et al., 2014), and C19r through C21r from the South Atlantic Ocean (Leg 114 ODP Site 702, Leg 208 ODP Site 1263, Westerhold et al., 2015). Among these previously studied deep-ocean sites only ODP Site 1260 has a sufficient resolution to capture paleoceanographic variability in the precession band. Such resolution is desirable to accurately detect amplitude modulation cycles, reflecting the eccentricity of Earth's orbit (Westerhold and Röhl, 2013).

Despite these significant efforts made to link the Paleocene and early Eocene ATS (Westerhold et al., 2008, 2015; Hilgen et al., 2010) to the late Eocene, Oligocene (Pälike et al., 2006) and Neogene ATS (Lourens et al., 2004), the fragmentary character of good quality, middle Eocene carbonate-rich sequences in deep-sea environments (e.g., Sexton et al., 2006; Hilgen and Kuiper, 2009) hampers the construction of an astronomically calibrated Cenozoic timescale (Vandenberghe et al., 2012).

In this study, we present two unique continuous carbonate-rich middle Eocene (chrons C18n.1n through C21n, ~38.5 to ~48 Ma) sedimentary records from IODP Sites U1408 and U1410 (Boyle et al., 2017; Norris et al., 2014, (Fig. 2.1)), alleviating the scarcity of high-resolution paleoceanographic records from the middle Eocene. Moreover, both sites exhibit prominent lithological cycles that are interpreted as obliquity cycles. We apply a new tuning strategy that utilizes the well-expressed amplitude modulation of obliquity (s3–s6, ~173 kyr, Figure 2.2 and Supplementary Figure 2.1) in high-resolution (2 cm) XRF Ca/Fe data. We choose this specific elemental ratio because it neatly captures the lithological variance expressed in these sedimentary cycles (Figure 2.3 and Supplementary Figure 2.2).

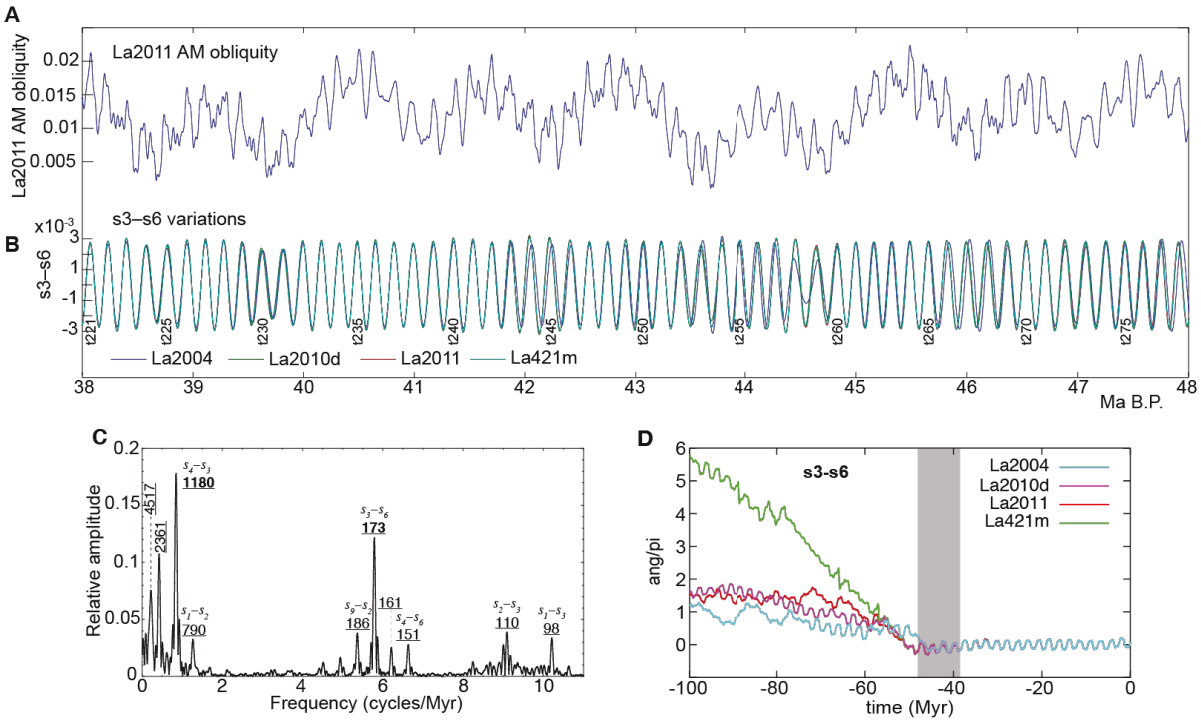

Figure 2.2: Obliquity amplitude modulation components and tests for the stability of the s3-s6 component used for orbital tuning. (A) La2011 obliquity amplitude modulation variations over the interval from 38 to 48 Ma. (B) Astronomical variations in obliquity modulation cycle s3-s6, using the four orbital solutions La2004, La2010d, La2011 and La421m. s3-s6 related "t" (tilt) cycles are numbered from 1 for present back in time. (C) 2π-MTM amplitude spectrum of the signal in 'A'. Origin of the main periods are shown, with the two leading terms s4-s3 and s3-s6 in bold. (D) Variations of the arguments related to s3-s6 using the four orbital solutions La2004, La2010d, La2011 and La421m. The vertical pink-shaded bar indicates the studied interval (38.5 to 48 Ma). Note that except La2004, the three other solutions start to diverge only at ~56 Ma, long before the time interval considered in this study. The s3-s6 variations can be used as a target tuning period with high-precision over the time interval 0 to 50 Ma and eventually up to ~56 Ma.

2.2 Material and Methods

2.2.1 Data

The recovered middle Eocene (chrons C18n.1n through C21n) sedimentary sequences at Sites U1408 and U1410, drilled during IODP Expedition 342 “North Atlantic Southeast Newfoundland Ridge”, contain drift deposits, with sedimentation at paleodepths above the carbonate compensation depth (CCD) (Norris et al., 2014). These drift sediments are composed of rhythmic alternations between greenish nannofossil clay and whitish nannofossil ooze (Figure 2.3 and Norris et al., 2014).

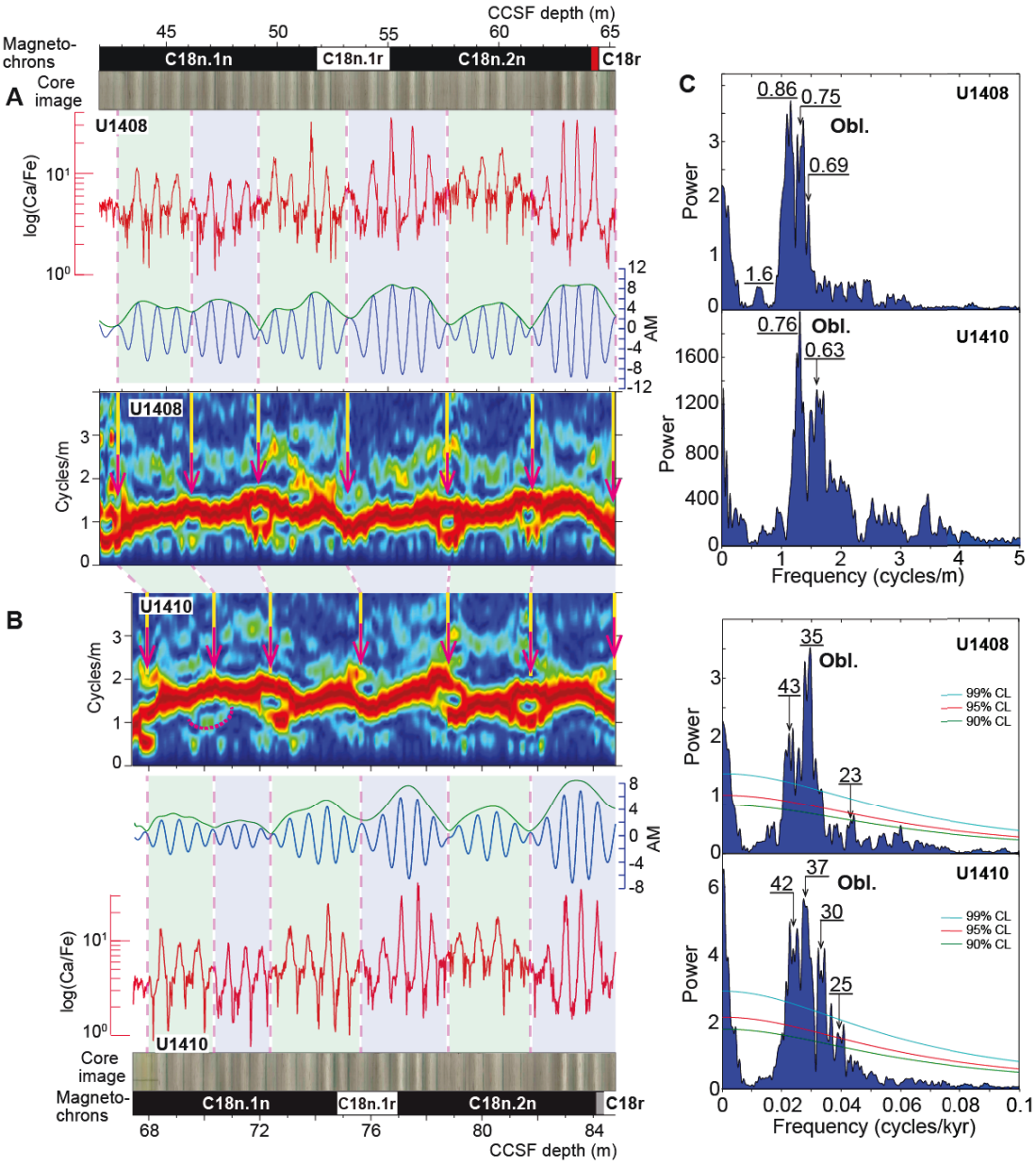

Figure 2.3: Time-series analysis and correlation between Sites U1408 and U1410 in the upper part of the studied interval. (A) and (B) Obliquity amplitude modulation analysis of Sites U1408 (A) and U1410 (B) using both Hilbert transform and evolutive FFT in depth domain, and correlation between the two sites. Note the exceptional expression of amplitude modulation envelope cycles through the spectrogram, as bifurcations (pink arrows) in the spectral line depicting the obliquity cycles. (C) 2π-MTM power spectra of the correlated interval in depth and time domains, at the two sites. Spectral analysis in the time domain is applied to 173 kyr (s3-s6) tuned signals.

Shipboard age models based on linear interpolation between chron boundary ages from GTS 2012 indicate that durations of the main lithologic alternations primarily fall within the obliquity frequency band. The amplitude of the principal lithologic cycle is strongly modulated by longer-term cycles (Figures. 2.3, 2.4 and 2.5).

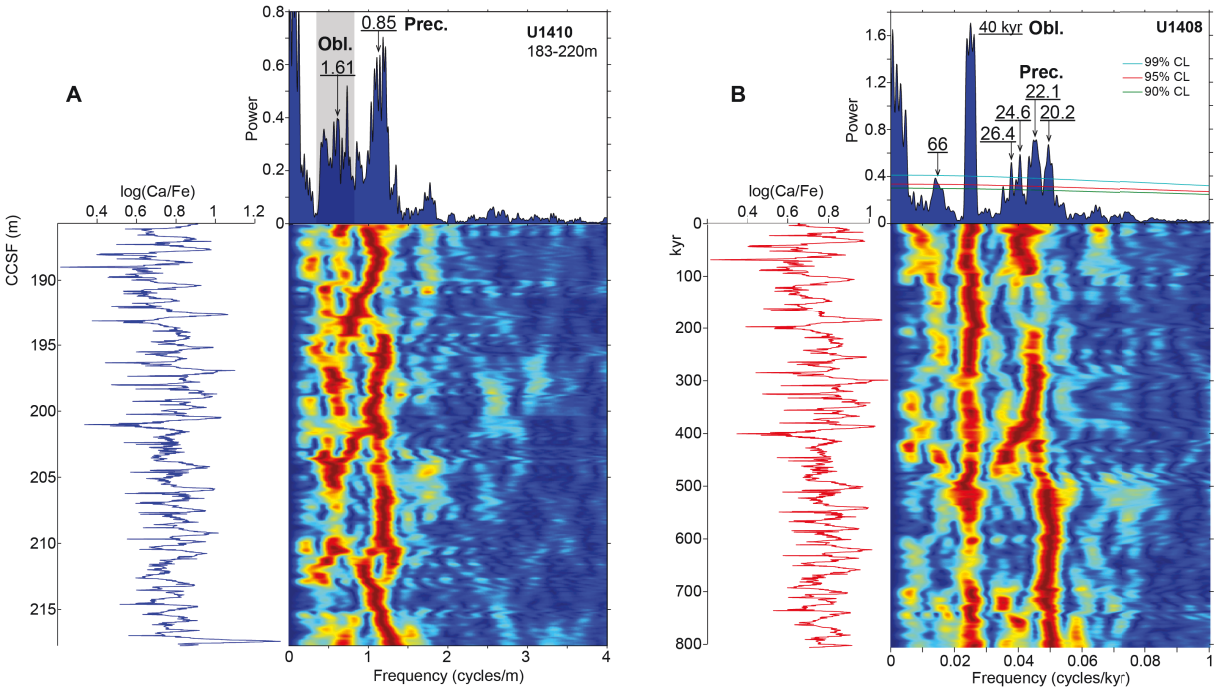

Figure 2.4: Time-series analysis of the lower part of Site U1410 (interval from 183 m to 220 m) to show the record of dominant precession and obliquity cycles. (A) Time-series analysis in depth domain. (B) Time-series analysis in time domain after tuning the spectral peak at around 1.61 m (frequency band: 0.6±0.22 cycles/m) to a 40 kyr period. This calibrates the precession wavelength, around 0.85 m, to 20.2 kyr, 22.1 kyr, and possibly 24.6 kyr and 26.4 kyr. Simultaneous record of precession and obliquity cycles along the studied section is highlighted via amplitude spectrogram, through the spectral lines.

In order to better understand the geochemical character of these lithologic variations, an IODP Expedition 342 consortium acquired XRF (X-ray fluorescence) elemental data. The ratio between calcium (Ca) and iron (Fe) (Ca/Fe) traces climatically driven variations in carbonate production and/or preservation and detrital input. All XRF data were measured at 2 cm resolution at the sediment surface of the archive halves, at Scripps Institution of Oceanography and MARUM, University of Bremen. XRF data were used to revise and improve the shipboard composite depth scale and spliced composite. Our tuning is based on the log(Ca/Fe) proxy because it shows a high signal-to-noise ratio, has a strong relationship with lower resolution shipboard wt% CaCO3 measurements, and consistently reflects modulation cycles.

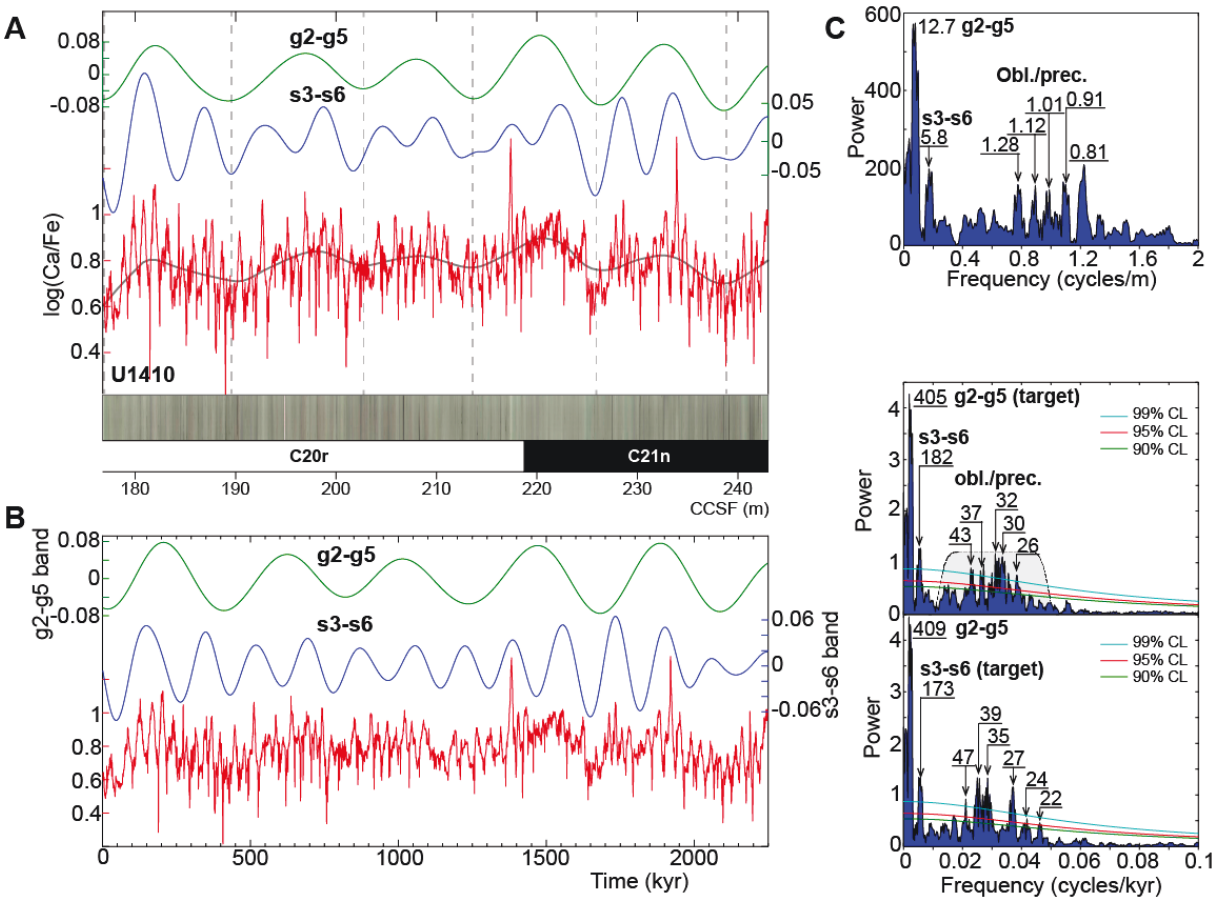

Figure 2.5: Example of expression of both precession and obliquity cycles in the lower part of Site U1410, rendering obliquity amplitude modulation envelope (s3-s6) cycles less expressed than in the upper part (see Section 3.2). Obliquity envelopes can, however, be retrieved by bandpass filtering. (A) Bandpass filtering in depth domain to extract g2-g5 and s3-s6 related wavelengths (see the expression of these cycles in the power spectrum in 'C'). (B) Bandpass filtering in time domain; tuning is performed at s3-s6 cycles (173 kyr tuning). (C) 2π-MTM power spectra in depth (upper spectrum) and time (lower spectra) domains. Note that tuning at s3-s6 better aligns the obliquity cycle band than tuning at g2-g5.

The recovered drift sediments include well-preserved calcareous microfossils, providing excellent biostratigraphic control. The studied stratigraphic interval at Site U1408 contains 18 biostratigraphic datums, while Site U1410 contains 19 datums (Expedition 342 Scientists, 2012).

Magnetostratigraphic data were initially acquired offshore (Fig. 2.6). These data are based on the remanence measurements of the archive halves with a resolution of 2.5 cm for the interval recovered by the Advanced Piston Corer (APC), and discrete samples with a resolution of 1-1.5 m for the interval recovered by the Extended Core Barrel (XCB), after alternating field (AF) demagnetization at 20 mT. They formed the basis of the shipboard age model by providing depth information for magnetic reversal boundaries (Expedition 342 Scientists, 2012). Post-cruise U-channel samples were taken from central parts of the archive halves of the APC-cored interval for more precise determination of the chron boundaries. They were progressively AF demagnetized from 20 to 80 mT, and remanence measurements were performed every 1

cm. Using this information, we have updated the depths of chron boundaries (after Norris et al., 2014), with uncertainty of only a few decimeters on their stratigraphic positions.
chrons were correlated to the standard geomagnetic polarity timescale (GPTS) using radiolarian, foraminifer and nannofossil biostratigraphic datums (Norris et al., 2014). At Site U1408, chrons C18n.1n through C20r (except C19n) were unambiguously recognized. At Site U1410, chrons C18n.1n through C21r were unambiguously identified. The studied sites therefore offer a unique cyclic carbonate-rich sequence of the middle Eocene interval, with excellent bio- and magnetostratigraphic control (Fig. 2.6) and comparatively high sedimentation rates.

2.2.2 Obliquity Amplitude Modulation Analysis and Orbital Tuning

Sedimentary cycles were evaluated using the multitaper method (MTM, Thomson, 1982) for spectral analysis, together with the robust red noise test (Mann and Lees, 1996). The amplitude envelopes of the dominant obliquity signal in the sedimentary records is extracted via the Hilbert transform. The 173-kyr (s3-s6) component in the amplitude envelopes is subsequently used for orbital tuning to the astronomical solution. Tuning to the s3-s6 component is an unconventional tuning strategy so we demonstrate its stability in the following sections.
Amplitude modulation analysis of stratigraphic paleoclimate records is a powerful tool to characterize astronomical forcing patterns in cyclostratigraphy. Indeed, the astronomical solution displays numerous amplitude and frequency modulations, which could be detected in stratigraphic records (see Hinnov, 2000 for a review).
Well known amplitude modulation patterns include the amplitude modulation of climatic precession by eccentricity. Short eccentricity cycles are in turn amplitude modulated by long eccentricity cycles. These features of the astronomical solution can be recorded in the stratigraphic signal. The amplitude modulation of precession by eccentricity has been frequently observed throughout the Phanerozoic (e.g., Fischer, 1991; Herbert, 1992; Olsen and Kent 1999).
Amplitude modulation of obliquity cycles has been occasionally observed in the Cenozoic (Shackleton et al., 1999, Zachos et al., 2001), but never in the pre-Cenozoic strata. Indeed, the origin of obliquity amplitude modulation is more complicated (Hinnov, 2000), and such amplitude modulation observation requires a long and continuous record registering the obliquity signal, which is not usually the case in greenhouse periods (Boulila et al., 2011).
Middle Eocene sedimentary records from IODP 342 (U1408 and U1410 Sites) document an exceptionally strong obliquity imprint over several million years, amplitude modulated by lower-frequency cycles (Figs. 2.3 and 2.6). We extract and interpret amplitude modulation patterns in the depth domain, aided by evolutive Fast Fourier Transform (FFT) for detection of

frequency-amplitude modulation cycles expressed as nodes in the carrier signal (obliquity) (Fig. 2.3). Evolutive FFT was performed on short intervals in order to isolate nodes related to the dominant amplitude modulation cycles (Figure. 2.3 and Supplementary Figure 2.2). Dominant amplitude modulation envelopes related to s3–s6 cycles are then assigned a 173-kyr duration, so to obtain an initial floating timescale. The mean 173 kyr cycle period in astronomical solutions is stable and remains almost constant until ~56 Ma.

The obtained floating timescale was then subject to "semi-absolute" s3–s6 orbital tuning after extraction of amplitude modulation envelopes of the obliquity cycles in the time domain. We tied the dominant amplitude modulation cycle related to s3–s6 to its equivalent in the La2011 astronomical model.

2.2.3 Testing the Stability of the s3-s6 Obliquity Amplitude Modulation in the Cenozoic

The orbital motion in the Solar System was demonstrated to be chaotic because of the presence of multiple secular resonances in the inner planet system, with an exponential divergence that leads to an increase of the uncertainties by an order of magnitude every 10 Myr (Laskar, 1989, 1990). As a result, the precision for the calculations of some of Earth's orbital eccentricity cycles are limited (Laskar et al., 2004).

However, the 405 kyr long eccentricity (i.e., g2–g5), which is the leading periodic eccentricity term with the highest amplitude, has a relatively stable phase (Laskar et al., 2004). Indeed, the 405-kyr cycle results from the gravitational interaction of Venus and Jupiter. Both of these planets have relatively stable orbits. The shorter period eccentricity terms (~100 kyr) result mostly from the orbital motion of the inner planets and are subject to instabilities. They thus cannot be confidently used for a direct astronomical tuning of records older than 50 Ma.

The new astronomical solutions La2010 and La2011 (Laskar et al., 2011a, 2011b) extended the accuracy of La2004 orbital eccentricity model (Laskar et al., 2004) back from 40 to about 50 Ma. The validity of this model, however, rapidly decreases back in time and it is unlikely to obtain an accurate model beyond 60 Ma due to the strong instabilities in the orbits of the main asteroids (Laskar et al., 2011b). Nevertheless, correlation of astronomical and geological data at long-period (g4-g3, 2.4 Myr) cycles indicates that the La2011 eccentricity is valid back to at least 48 Ma (Westerhold et al., 2012, 2015). Other previous cyclostratigraphic studies have tested the stability of orbital solutions by focusing on the eccentricity terms, and have used the stable g2-g5 (405 kyr) term as a geochronometer to calibrate the Paleogene timescale (e.g., Pälike et al., 2006; Westerhold et al., 2007, 2008, 2015; Hilgen et al., 2010).

The 405-kyr cycle is, however, not the only periodic term that is usable for long-term astronomical tuning. Earth's obliquity exhibits several modulation cycles, of which the s4–s3 (~1.2 Myr) and s3–s6 (~173 kyr) are the two leading terms (Fig. 2.2). Both terms depend solely

on the orbital motions of the planets, and are thus independent of the precession frequency p (see Laskar et al., 2004, Table 7). In particular, the shorter s3–s6 term results from the beat between high-frequency obliquity components p-s3 (~40.8 kyr present-day value) and p-s6 (~53.4 kyr present-day value), where p is the axial precession frequency, and s3, s4 and s6 are secular frequencies related to the precession of the ascending node of the Earth and Saturn respectively. In the expression of such interference in the obliquity signal, the precession frequency p cancels and the term (s3-s6) remains, which thus solely depends on the orbital motion.

$$p - s3 = 40.8\ kyr$$
$$\underline{p - s6 = 53.4\ kyr}$$
$$s3 - s6 = 173\ kyr$$

We tested the stability of s3–s6 using four astronomical solutions: La2004, La2010d, La2011 and La421m (described below, see Laskar et al., 2004, 2011a, b for details).

The La2004 model was demonstrated to be precise for the past 40 Ma (Laskar et al., 2004, Laskar et al., 2011a). The La2010d is thought to be the best-constrained version of the La2010 astronomical model that extends the precision to the past 50 Ma (see below).

The main difference between La2004 and La2010 models is that the La2004 initial conditions are adjusted to the JPL numerical ephemeris DE406 (Standish, 1998) over −5000 yr to +1000 yr from the present date, while La2010 includes the five major asteroids, Ceres, Vesta, Pallas, Iris and Bamberga and is fitted to the high-precision planetary ephemeris INPOP06 and INPOP08 (Fienga et al., 2008, 2009) over 1 Ma. Due to their close encounters, the orbits of Ceres and Vesta present a strong chaotic behavior, and consequently their motion is unpredictable over 400 kyr, which in turn influences the Earth's orbital eccentricity calculation (Laskar et al., 2011b).

La2010a, La2010b and La2010c are fitted to the INPOP08 (Fienga et al., 2008) but it was later realized that the INPOP06 version is more accurate (Fienga et al., 2011). Thus, the La2010d version is likely to be the best-constrained version in the La2010 model (Laskar et al., 2011) as indicated by comparisons with geological data (Boulila et al., 2012; Westerhold et al., 2012).

The La2011 model is considered to represent the most precise solution up today (Laskar et al., 2011b). It was obtained by fitting the numerically enhanced La2010 model to the most precise INPOP10a (Fienga et al., 2011) over the past 1 Ma, which in addition includes the five major asteroids.

Finally, the La421m model is based on La2011 numerical calculation adjusted to a special version of the INPOP ephemerides, fitted over the DE421 planetary ephemeris (Folkner et al., 2009). This model is used to substantially check the stability of solutions since it is based on an independent set of initial conditions for the planetary ephemeris.

The study of the argument related to s3–s6 (Fig. 2.2) indicates that except for La2004, which significantly starts diverging at around 47.8 Ma, the other solutions remain in phase till ~56.2 Ma (Figs. 2.2 and Supplementary Figure 2.1). Thus, this cyclicity (s3–s6) can be considered to be stable back to at least 50 Ma. The recovered geological interval in the present study spans chrons C18n.1n through C21n (~38.5 to ~48 Ma), meaning that the obliquity modulation cycle (s3–s6) could be used as a high-precision geochronometer for orbital tuning of this part of the Eocene timescale.

2.3 Results

2.3.1 Correlation of Sites U1408 and U1410

The Ca/Fe records of the middle Eocene sequences at sites U1408 and U1410 share similar patterns, especially in terms of amplitude modulation of the obliquity related cycles (Figure 2.3). We use amplitude modulation envelopes of the obliquity cycles in the depth domain to perform a high-resolution correlation between the two sites (Figures 2.3 and 2.6). In particular, the interval spanning chrons C18n.1n through the upper part of C20r exhibits a dominant obliquity signal, which can potentially be used to extract amplitude modulation envelopes and then to perform correlation (Figures 2.3, 2.6 and Supplementary Figure 2.2).

Correlation was conducted at the scale of s3-s6 obliquity modulation cycles. Minima of s3-s6 cycles are well expressed in the Ca/Fe data, and amplitude modulation analysis together with evolutive FFTs allow us to reliably detect such obliquity modulation patterns (e.g., Figure 2.3 and Supplementary Figure 2.2).

Correlation results indicate that both records are fairly complete, except for one hiatus that occurs in the middle interval of chron C19r at Site U1408. This hiatus is equivalent to almost four obliquity cycles (or one s3-s6 modulation cycle). In addition, the high-resolution cyclostratigraphic correlation allows us to constrain chron boundaries between the two sites. In particular, the boundary between chrons C18r and C18n.2n is well defined at U1408 but less clear at U1410. Hence, the position of this reversal at Site U1410 was revised according to the correlation to Site 1408. Chron C19n is not recognized at U1408, but its stratigraphic position was deduced from the correlation (Figures 2.3 and 2.6).

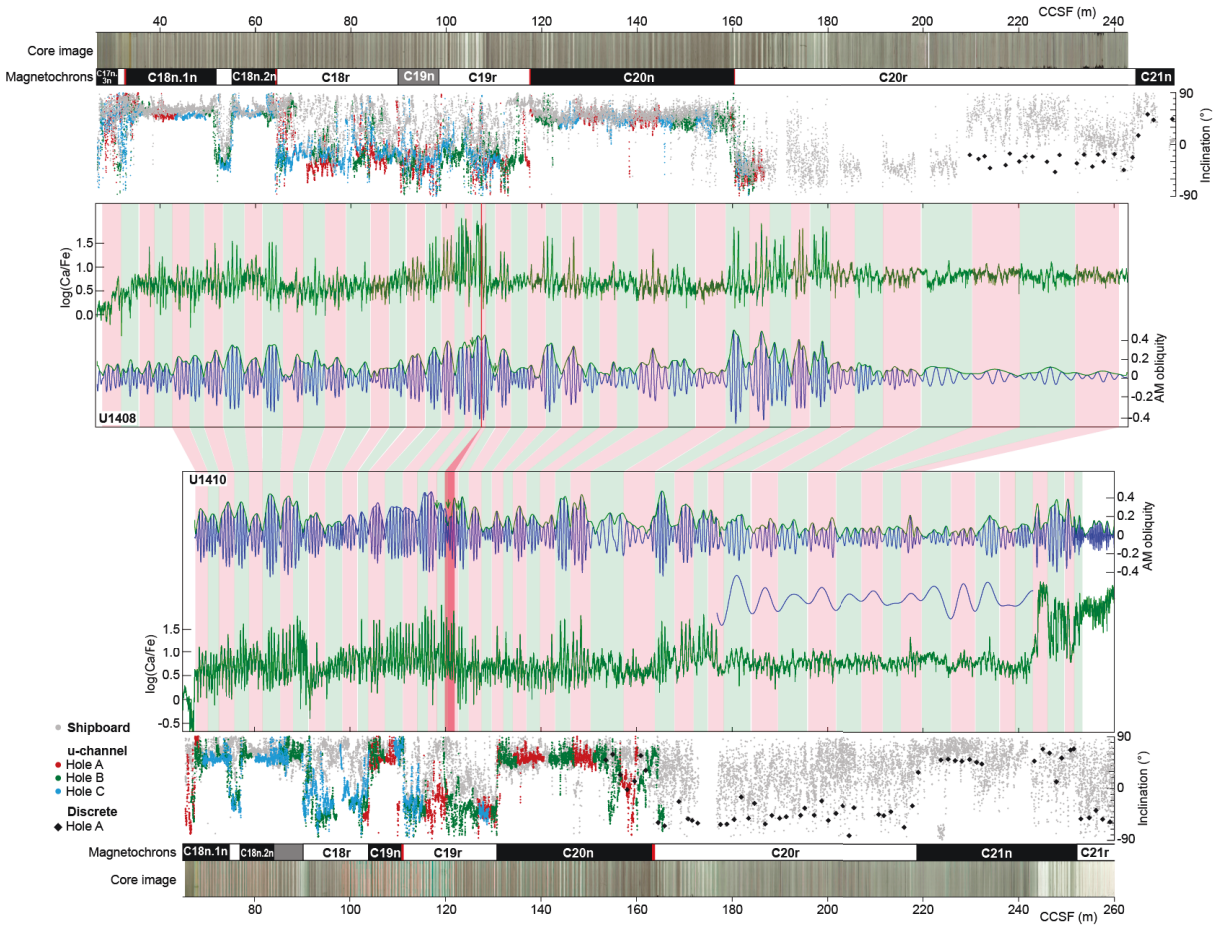

Figure 2.6: Integrated cyclo-magnetostratigraphy and XRF log(Ca/Fe) signals at Sites U1408 and U1410, and high-resolution correlation between the two sites. The vertical red line indicates a hiatus detected at Site U1408 (within chron C19r), and its equivalent sediment at U1410 is in vertical red bar. C19n is recognized at U1410, but not at U1408. It is represented in grey since it is deduced from the correlation. Also, the base of C18n.2n is well recognized at Site U1410, but not at Site U1408, thus its position at U1410 is revised according to the cyclostratigraphic correlation (see also Figure 2.3 for detailed correlation). Note that the lower part of U1410 from 179-240 m is dominated by both precession and obliquity, thus extraction of s3-s6 cycles was realized via bandpass filtering (see Figures. 2.4 and 2.5 for details).

Finally, the correlation between the two sites provides constraints on the number of the recorded s3-s6 cycles within each recovered chron, especially when cycles are better recorded (preserved) at one site compared to the other.

2.3.2 Time-Series Analysis

Spectral analysis of Ca/Fe data was performed in intervals together with evolutive FFTs in order to detect changes in the sedimentation rate between sites and within each site (Figure. 2.3, and Supplementary Figure 2.2). The upper interval (C18n.1n down to the upper part of C20r) exhibits strong obliquity amplitude modulation, and is thus primarily calibrated by the use of amplitude modulations (Figures. 2.3 and 2.6). The lower interval (C20r and C21n) shows a weaker amplitude modulation, but strong g2-g5 (405 kyr) and s3-s6 (173 kyr) imprints that

are dominating over the higher frequencies of precession and obliquity bands (Figures. 2.4 and 2.5). The extraction of the 173 kyr component (s3-s6) in this interval was therefore realized through bandpass filtering, rather than amplitude modulation analysis because the interference of precession and obliquity makes the reliable extraction of wavelengths related to obliquity difficult (Figure 2.4).

Spectral analysis of the uppermost part (Figure 2.3) shows two primary peaks at the two sites, with shorter wavelengths at Site U1410 (0.75 and 0.86 m at U1408 vs 0.63 and 0.76 m at U1410). This indicates lower sedimentation rates at Site U1410. The two peaks occur within the obliquity band, after the initial calibration based on assigning a 173-kyr duration to amplitude modulation cycles. The interpretations that led to the initial calibration are based on both the Hilbert transform of filtered obliquity cycles and the evolutive FFT in the depth domain. The s3-s6 cycles can be detected in the spectrogram through bifurcations in spectral lines, depicting obliquity wavelength cycles. These bifurcations mark Ca/Fe minima in s3-s6 related cycles, which correlate between the two sites (Figure 2.3A, B).

Time-series analysis over an extended interval highlights convincing amplitude modulation variations related to s3-s6, detected by either Hilbert transform or evolutive FFT (Supplementary Figure 2.2). Spectral analysis of the lower and upper parts of this interval shows two to three peaks, which are again calibrated to periods close to obliquity band based on the 173 kyr tuning (Supplementary Figure 2.2B).

Spectral analysis of the C20r-C21n interval (Figure 2.5) shows two strong peaks of 5.8 and 12.7 m, matching the s3-s6 and g2-g5 components respectively (Figure 2.5C). A multitude of peaks of wavelengths ranging from 0.81 to 1.28 m represents precession and obliquity cycles (Figure 2.4). s3-s6 and g2-g5 related cycles were extracted via bandpass filtering and then used to time calibrate precession and obliquity wavelengths (Figure 2.5B, C). Tuning to s3-s6 (173 kyr) better aligns precession and obliquity periods, compared to tuning solely to g2-g5 (405 kyr) (Figure 2.5C). Therefore, we use an s3-s6 tuning to then extract obliquity amplitude modulation envelopes in the time domain.

2.3.3 Astronomical Time Calibration of Chrons C18n.1n through C21n

We bandpass filtered s3-s6 related cycles from the amplitude modulation output to tune them to their equivalent s3-s6 cycles in the La2011 astronomical model, and thus obtain numerical ages. However, this step needs at least one anchoring age point. We anchored our floating timescale to the base of chron C18n.1r because it is well-defined at both sites and shows a brief transition (< 20 kyr) compared to the base of the youngest chron C18n.1n, which has a longer transition time of ~80 kyr (Expedition 342 Scientists, 2012).

We use the previously obtained astronomical ages of this boundary at 39.666 Ma (Westerhold et al., 2014) and at 39.602 Ma (Pälike et al., 2006), which are not very different to the 39.698

Ma age, reported in GTS2012 (Gradstein et al., 2012). Starting from this age point we slightly shift the floating timescales to the closest s3-s6 extremum (lower minimum of t229: 39.526 Ma, Fig. 2.7) in the La2011 astronomical model. This operation results in an age offset of 60 kyr compared to 39.666 Ma (Westerhold et al., 2014) and of only 4 kyr relative to 39.602 Ma (Pälike et al., 2006). Then, we match s3-s6 variations, cycle-to-cycle (minima) between the floating timescale and the La2011 astronomical model. In this way, we obtain a semi-absolute orbital (s3-s6) timescale of the middle Eocene chrons C18n.1n through C21n, which is illustrated in Figure 2.7.

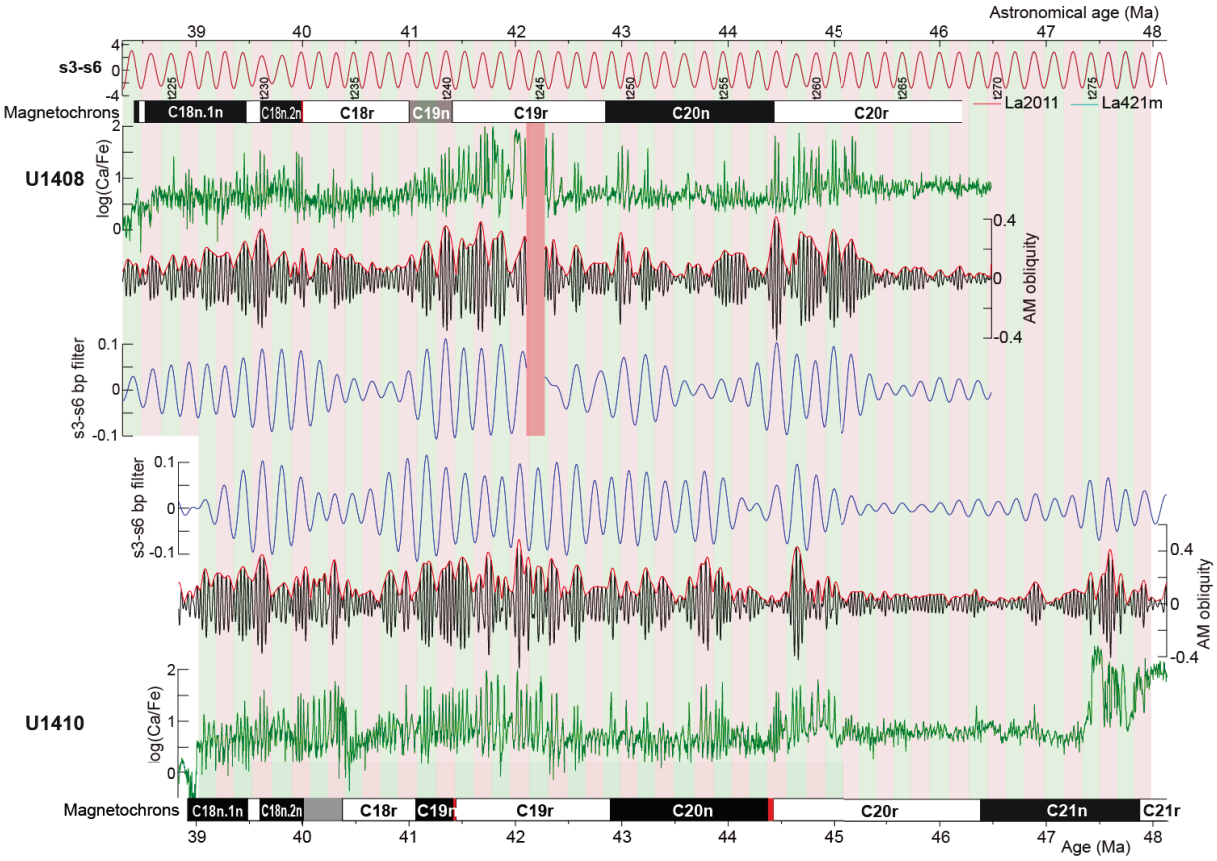

Figure 2.7: Astronomical timescale of Sites U1408 and U1410. Tuning was performed to the stable s3-s6 (173 kyr) obliquity cycles using the La2011 astronomical model. The vertical red bar indicates a hiatus within chron C19r at Site U1408, equivalent to almost one s3-s6 cycle. La421m astronomical model is plotted versus La2011, to show the high stability of s3-s6 cyclicity within the studied interval, see Fig. 2.2 for s3-s6 cycle numbering. Obliquity amplitude modulation curve: amplitude modulation at the obliquity cycle band, black curve is bandpass (0.0275±0.0125 cycles/kyr) filtered obliquity of the tuned log(Ca/Fe) signal, red curve represents amplitude modulation envelopes. s3-s6 bandpass filter: bandpass filtered s3-s6 (0.0055 ±0.00134 cycles/kyr) from amplitude modulation envelopes.

2.4 Discussion

2.4.1 Comparison of IODP342 Chron Durations with previous Timescales

The present astronomical timescale (ATS) provides durations of chrons C18n.1n through C21n (Figure 2.8, Tables 2.1 and 2.2). Because ages of chron boundaries depend on the age of the

base of C18n.1r, used as an anchoring point in our tuning, we focus on durations (Table 2.2) rather than on ages (Table 2.1).

Table 2.1: Ages (in Ma) of boundaries of chrons C18n.1n through C21n at Sites IODP342 U1408 and U1410 compared to previous studies.

Basal chron Boundary	CK95 (Cande and Kent, 1995)	ODP Site 1052 (Pälike et al., 2001)	GTS2004 (Ogg and Smith, 2004)	ODP Site 1218 (Pälike et al., 2006)	GTS2012(Vandenberghe et al. 2012; Ogg, 2012)	Contessa Highway (Jovane e al., 2010)	New Willwood model (Tsukui and Clyde,	ODP Site 1260 (Westerhold and Rhöl,	ODP PEAT Sites (Westerhold et al., 2014)	ODP Site 1263 (Westerhold et al., 2015)	ODP Site 702B (Westerhold et al., 2015)	IODP Site U1408 (This study)	IODP Site U1410 (This study)
C17n.3	38.426	38.186	38.032	38.449	38.615				38.398			38.507–38.53	
C18n.1	39.552	39.441	38.975	39.554	39.627				39.582			39.463	39.470
C18n.1	39.631	39.486	39.041	39.602	39.698				39.666			39.595	39.592
C18n.2	40.130	39.828	39.464	40.084	40.145				40.073			39.991–40.00	40.009
C18r	41.257		40.439	41.358	41.154	40.120	40.210	41.061	41.072	41.030		not recong.	41.090
C19n	41.521		40.671	41.510	41.390	41.250	40.530	41.261	41.306	41.180		not recong.	41.423–41.44
C19r	42.536		41.590		42.301	41.510	41.790	42.151	42.188	42.107	42.124	42.840–42.84	42.896
C20n	43.789		42.774		43.430	42.540	43.340	43.449		43.517	43.426	44.431–44.44	44.384–44.40
C20r	46.264		45.346		45.720	43.790	45.570			46.151	46.080		46.393
C21n	47.906		47.235		47.349		48.03			47.575			47.874

The main feature of our orbital timescale is that the duration of the total recovered interval is comparable with previous timescales. However, durations of some individual chrons are substantially different (Table 2.2). For instance, the whole duration of recovered chrons C18n.1n through C21n is about 9.37 Myr, which is only 110 kyr shorter than the 9.48 Myr duration reported in CK95 timescale (Cande and Kent, 1995).

Table 2.2: Durations (in Myr) of chrons C18n.1n through C21n at Sites IODP342 U1408 and U1410, compared to previous studies.

chron	CK95 (Cande and Kent, 1995)	ODP Site 1052 (Pälike et al., 2001)	GTS2004 (Ogg and Smith, 2004)	ODP Site 1218 (Pälike et al., 2006)	GTS2012(Vandenberghe et al., 2012; Ogg, 2012)	Contessa Highway (Jovane et al., 2010)	New Willwood model (Tsukui and Clyde, 2012)	ODP Site 1260 (Westerhold and Rhöl, 2013)	ODP PEAT Sites (Westerhold et al., 2014)	ODP Site 1263 (Westerhold et al., 2015)	ODP Site 702B (Westerhold et al., 2015)	IODP Site U1408 (This study)	IODP Site U1410 (This study)
C17n.3r	0.313	0,28	0.261	0,2	0.28				0,31			not recov.	not recov.
C18n.1n	1.126	1,25	0.943	1,10	1.01				1,18			0.931–0.956	not recov.
C18n.1r	0.079	0,04	0.066	0,04	0.07				0,08			0.132	0.122
C18n.2n	0.499	0,34	0.424	0,48	0.45				0,40			0.396–0.406	0.417
C18r	1.127		0.975	1,27	1.01				0,99			not recogn.	1.081
C19n	0.264		0.232	0,15	0.24	1,1	0,3	0,2	0,23	0,1		not recogn.	0.333–0.353
C19r	1.015		0.919		0.91	0,2	1,2	0,89	0,88	0,92		not recogn.	1.453–1.473
C20n	1.253		1.184		1.13	1,0	1,5	1,298		1,4	1,30	1.591–1.601	1.488–1.508
C20r	2.475		2.572		2.29	1,2	2,2			2,63	2,65	not recov.	1.989–2.009
C21n	1.642		1.889		1.629		2.46			1.424		not recov.	1.481

The age of the base of the recovered interval (base of C21n, 47.874 Ma) is very close to that in CK95 age model (47.906 Ma, Cande and Kent, 1995), but older than in GPTS2004 and GPTS2012 age models (47.235 Ma and 47.349 Ma, respectively; Ogg and Smith, 2004; Vandenberghe et al., 2012). In contrast, the age of the top of the recovered interval (base of C17n.3r, 38.519 Ma) is 95 kyr younger than in GPTS2012 (38.615 Ma), significantly older in GPTS2004 (38.032 Ma), but 93 kyr older than in CK95 timescale (38.426 Ma).

Despite age differences between the base and top of the recovered interval (Figure 2.8 and Table 2.1), we note that our orbital timescale is consistent with previous key stratigraphic ages. For instance, the Mission Valley Ash bed has been correlated to chron C20n (Prothero and Emry, 1996; Walsh et al., 1996; Robinson et al., 2004). Smith et al. (2010) recalibrated the age of this tuff to 43.35 ± 0.49 Ma using the 28.201 Ma age for Fish Canyon sanidine. The new

Willwood model (Tsukui and Clyde, 2012) places the tuff within chron C20n based on its 40Ar/39Ar age, which is in agreement with our tuning ages of the top and the base of C20n at 42.896 Ma and 44.394 Ma respectively (Fig. 2.8).

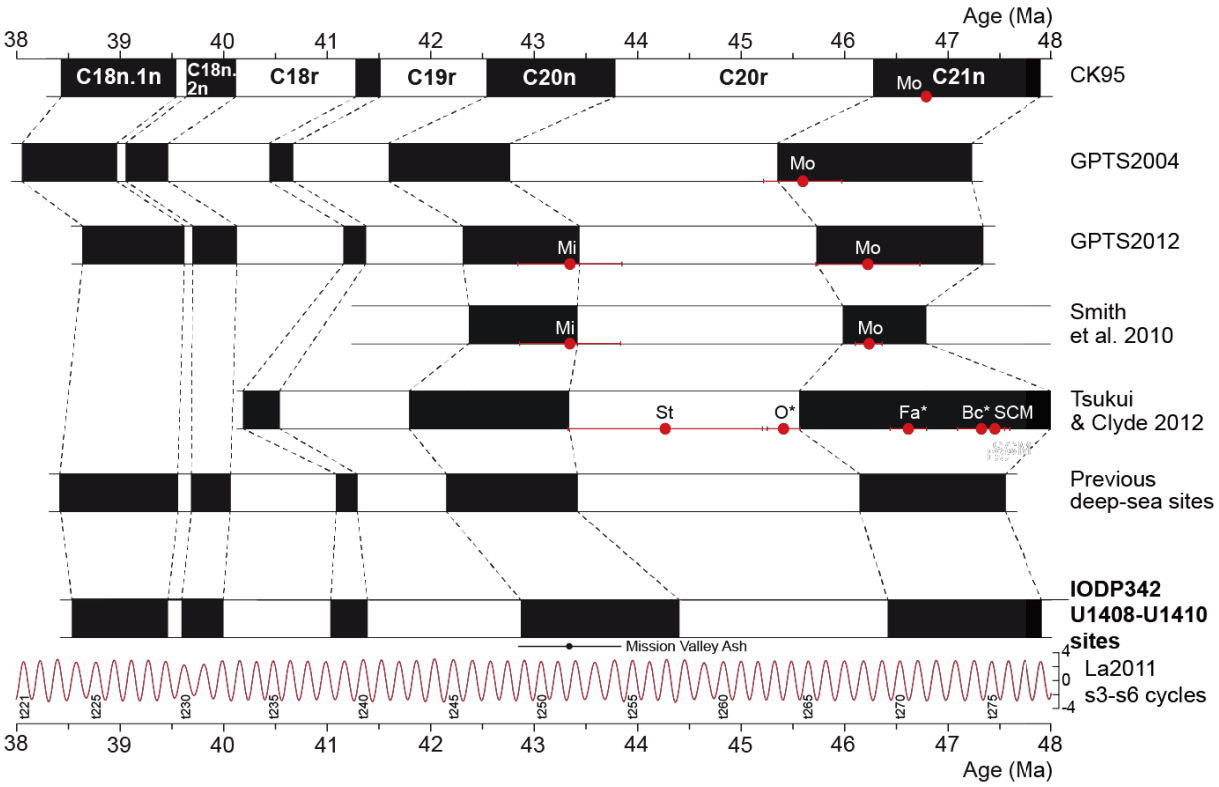

Figure 2.8: Chrons C18n.1n through C21n timescale at IODP 342 Sites U1408 and U1410, and comparison with previous timescales. Geomagnetic Polarity Time Scales: CK95 (Cande and Kent, 1995), GPTS2004 (Ogg and Smith, 2004) and GPTS2012 (Vandenberghe et al., 2012), and terrestrial GPTS of the Green River Formation according to Smith et al. (2010) and Tsukui and Clyde (2012). Previous deep-sea sites: combined PEAT and ODP 1260-1263 sites (Westerhold and Röhl, 2013, Westerhold et al., 2014, 2015). Also, plotted La2011 s3-s6 cycles, which are used to calibrate IODP342 sites (see Fig. 2.2 for cycle numbering). Mission Valley Ash (Mi) age (Smith et al., 2010) within C20n at IODP 342 cyclostratigraphic age calibration is also indicated. Small red circles with error bars mark the 40Ar/39Ar radioisotopic calibration age points: Mi=Mission Valley ash, Mo=Montanari ash, St=Strawberry Tuff, O*=Oily tuff, Fa*=Fat tuff, Bc*=Blind Canyon tuff, SCM=Sage Creek Mt. Pumice. All ages for terrestrial records from Smith et al. (2010) and Tsukui & Clyde (2012) are sanadine 40Ar/39Ar ages relative to 28.201 Ma for Fish Canyon sanadine (Kuiper et al. 2008); ashes marked by * are biotite ages.

The duration of the youngest recovered chron C18n.1n at Site U1410 (0.931 to 0.956 Myr) is close to those reported in GPTS2004 (0.943 Myr) and GPTS2012 (1.01 Myr), but significantly different from the CK95 timescale (1.126 Myr). Previous tuning attempts yielded durations that were closer to the CK95 timescale. For instance, data from IODP PEAT sites (Westerhold et al., 2014) provided a duration of 1.184 Myr, close to the 1.255 Ma duration inferred from ODP Site 1052 (Pälike et al., 2001), and data from ODP Site 1218 yielded a duration of 1.105 Myr (Pälike et al., 2006).

Chron C18n.1r is recovered at both sites U1408 and U1410 (Expedition 342 Scientists, 2012). Our astronomical interpretation suggests durations of 0.132 Myr and 0.122 Myr, respectively.

These durations are quite different from all previously published timescales, which assign a shorter duration ranging from 0.045 Myr to 0.084 Myr (Table 2.2). Chron C18n.2n has a duration of 0.417 Myr, which is consistent with previous timescales (0.342 Myr to 0.499 Myr), pointing to a stable C18n.2n timescale.

At Site U1410 the three following chrons C18r, C19n and C19r are completely recovered: Chron C18r is assessed at 1.081 Myr, which is close to the CK95 age model (1.127 Myr), 106 kyr longer than GPTS2004, but only 71 kyr longer than GPTS2012. Compared to previous cyclostratigraphies, our estimate is only 82 kyr longer than the 0.999 Myr duration inferred from IODP PEAT sites (Westerhold et al., 2014), but significantly shorter than the 1.274 Myr duration inferred from ODP Site 1218 (Pälike et al., 2006).

Chron C19n has a duration of 0.333 to 0.356 Myr and is thus almost 0.1 Myr longer than in most previous timescales, but close to the New Willwood model and the terrestrial calibration of the GPTS from the Green River Formation (0.32 Myr, Tsukui and Clyde, 2012, Table 2.2).

The duration of chron C19r is estimated at Site U1410 as 1.453 to 1.473 Myr, a duration considerably longer than in previous timescales. Except for the New Willwood model, which reports a duration of 1.26 Myr (Table 2.2), the other timescales assign a much shorter duration ranging from 0.882 Myr to 1.015 Myr. Also, the most recent cyclostratigraphic studies attribute shorter durations of 0.882 Myr, 0.89 Myr and 0.927 Myr to C19r (Westerhold and Röhl, 2013; Westerhold et al., 2014, 2015).

Chron C20n is represented at both sites U1408 and U1410, with durations of 1.591 to 1.601 Myr and 1.488 to 1.508 Myr respectively. The difference of about 100 kyr in duration of C20n between the two sites could be related to noisier obliquity amplitude modulation expression in the lower part of C20n (Figs. 2.6 and 2.7). Nevertheless, this duration is basically identical to the one provided in the New Willwood model (1.55 Myr), but shorter than those in previous GPTS. Previous cyclostratigraphic studies indicate a variable duration of 1.298 Myr from ODP Site 1260, 1.41 Myr from ODP Site 1263 and 1.302 Myr from ODP Site 702B (Westerhold and Röhl, 2013; Westerhold et al., 2014, 2015). Although Site 1263 does not possess high-resolution data (see Supplementary information), the inferred duration of chron C20n (1.41 Myr) is only ~0.1 Myr (~7 %) shorter than our estimates (~1.5 Myr at U1408). High-resolution cyclostratigraphic correlation between the two sites U1408 and U1410 (Fig. 2.6) indicates that C20n is complete. Therefore, we suggest that the duration of chron C20n in previous timescales, except in the New Willwood model, was underestimated.

Chron C20r is only recovered completely at Site U1410, and has a duration of 1.989 to 2.009 Myr, which is significantly shorter than most previous timescales. A cyclostratigraphic study of ODP Sites 1263 and 702B in the South Atlantic Ocean (Westerhold et al., 2015) assigned durations of 2.634 Myr and 2.654 Myr to C20r, significantly longer than our estimate.

The duration of chron C21n is 1.481 Myr at Site U1410, which is shorter than that in GPTS2004 (1.889 Myr), CK95 (1.642 Myr) and GPTS2012 (1.629 Myr). The New Willwood model infers an even longer duration of 2.46 Myr. Our 1.481 Myr duration is, however, close to that derived from cyclostratigraphy of ODP Site 1263 (1.424 Myr, Westerhold et al., 2015). Therefore, the independent cyclostratigraphic studies from ODP Site 1263 and IODP Site U1410 provide robust, consistent constraints on moving towards a stable duration of chron C21n.

The aforementioned similarities and differences in durations of chrons proposed here versus those inferred from previous studies allow us to proceed with a detailed comparison of attempts to close the middle Eocene astronomical timescale gap, with the goal of reaching a consistent and robust middle Eocene ATS.

2.4.2 Towards a Constrained Middle Eocene ATS: IODP 342 ATS versus previous ATS from Ocean Sites

Recent cyclostratigraphic studies (Westerhold et al., 2014, 2015) experienced difficulties in conducting an integrated cyclo-magnetostratigraphic approach at ODP sites, in order to precisely estimate chrons C18n.1n, C18n.1r and C18n.2n. For example, ODP 1172 (East Tasman Plateau) has a good cyclostratigraphic control, but inaccurate magnetostratigraphy, while ODP PEAT sites (Equatorial Pacific) possess good magnetostratigraphy, but no highly resolved cyclostratigraphy. The excellent magnetostratigraphic control at Sites U1408 and U1410 (Expedition 342 Scientists, 2012), and the high quality of cyclic sequences (Figures. 2.3 and 2.6), which have in this combination not been recovered elsewhere, make U1408 and U1410 the reference sites for establishing an astronomically calibrated high-resolution timescale for chrons C18n.1n, C18n.1r and C18n.2n.

We estimate durations of chron C18r as 1.081 Myr, which is only 82 kyr longer than the 0.999 Myr duration inferred from ODP PEAT sites (Westerhold et al., 2014), but significantly shorter than the 1.274 Myr duration inferred from ODP Site 1218 (Pälike et al., 2006). The difference of only around 100 kyr between our estimate and recent updated timescales, which consider both ODP PEAT and 1218 sites (Westerhold et al., 2014), indicate that we are moving towards a consistent duration of chron C18r.

The two preceding chrons C19n and C19r were previously orbitally calibrated at ODP Site 1260 (Westerhold and Röhl, 2013). Their durations at ODP 1260 are significantly different from those inferred from Site U1410 (Table 2.2). In particular, C19r is much longer (~570 kyr) at U1410 than at 1260.

The high quality of the cyclo-magnetostratigraphic record at Site U1410 indicates necessary revisions in the timescale for chrons C19n and C19r. In particular, the strong sedimentary expression of the s3-s6 obliquity modulation term (with high Ca/Fe amplitudes, see for e.g., Supplementary Figure 2.2) throughout this time interval points to the validity of our new orbital

tuning here, supporting a longer duration of C19r. Time-series analysis and cyclostratigraphic comparison of the two sites 1260 and U1410 point to a potential problem in stratigraphic completeness within C19n and C19r at Site 1260 (Supplementary Information, Supplementary Figures 2.3, 2.4 and 2.5).

Chrons C20n and C20r were calibrated at Site 1263 (Westerhold et al., 2015) and C20n was calibrated at Site 1260. A cyclostratigraphically revised C20n time interval at Site 1260 reassesses a duration close to that inferred from IODP 342 sites (Supplementary Information, Supplementary Figure 2.3).

When taken separately, durations of chrons C19r, C20n and C20r at Site 1263 show large differences with those assessed from IODP 342 sites (Table 2.2). Nevertheless, when all three chrons are considered together, they represent the same amount of time at both sites (4.95 to 4.97 Myr at U1410 versus 4.971 Myr at 1263, Table 2.2; Westerhold et al., 2015 their Table 2). We suggest that sedimentation is fairly continuous at Sites U1410 and 1263, while differences in duration within chrons may be related to a problem in magnetostratigraphy and/or cyclostratigraphic interpretation at Site 1263. We revise the cyclo-magnetostratigraphy of Site 1263 in the Supplementary Information and obtain durations of chrons that are close to those inferred from IODP 342 sites (Supplementary Information, Supplementary Figure 2.6 and 2.7). Additional evidence for a consistent, combined duration of the C20n-C20r interval comes from Hole 702B (Southwestern South Atlantic, Westerhold et al., 2015, see Supplementary Information, Supplementary Figures 2.8 and 2.9). Time-series analysis of Hole 702B data reveals a strong cyclostratigraphic signal, providing a duration of the C20n-C20r interval similar to that inferred from IODP 342 sites, and close to that deduced from the cyclostratigraphically revised 1263 data.

Cyclostratigraphic studies from Site 1263 (Westerhold et al., 2015) and Site U1410 provide good constraints on obtaining a constrained duration of chron C21n (Table 2.2).

In summary, comparison with previous timescales, in particular with previous ATS, indicates that IODP 342 sites are reference sections to construct a stable astronomically tuned timescale for chrons C18n.1n through C19r. Previous ATS showed comparable durations for C18n.2n and C18r, but used a lower resolution stratigraphy. The duration of chron C20n has been estimated with high confidence at Site U1410 in the North Atlantic, as well as at Site 1263 and in Hole 702B in the South Atlantic and at Site 1260 in the equatorial Atlantic Ocean, suggesting that a conclusive and stable ATS has been reached for C20n. Similarly, the chronology of chrons C20r and C21n have been validated independently in both the North (U1410) and South (1263 and 702B) Atlantic Ocean.

2.5 Conclusions

High-resolution middle Eocene XRF data (Ca/Fe ratio) at IODP Sites U1408 and U1410 (North Atlantic Southeast Newfoundland Ridge) indicate pronounced variations in carbonate versus clay contents, controlled by paleoclimate and paleoceanographic change. The prominent, high-frequency variations recorded by the Ca/Fe signal match the obliquity cycle band over several million years (~38.5 to ~48 Ma) and are amplitude modulated by s3-s6 (173 kyr) orbital cycles. After testing the astronomical stability of s3-s6, we used it to calibrate chrons C18n.1n through C21n.

Our estimates of the durations of chrons C18n.1n and C18n.1r are significantly different from those in previous geological timescales. The high quality of cyclo-magnetostratigraphic data at IODP 342 sites proposes significant revisions of these chrons. Durations of chrons C18n.2n and C18r are close to previous ATS estimates, hence pointing towards a consistent timescale for these chrons. Chrons C19n and C19r are calibrated only from IODP 342 sites because of a problem in the completeness of these chrons at other (I)ODP sites. Chron C20n is tuned with high precision at both Sites U1408 and U1410, and correlated to ODP Site 1260 (Equatorial Atlantic) and ODP Site 1263 and Hole 702B (South Atlantic). This resulted in a highly resolved C20n timescale. Finally, chrons C20r and C21n are calibrated at U1410 and validated by correlation to the South Atlantic (Site 1263). The strong imprint of s3-s6 cycles modulating the pronounced, high-frequency obliquity cycles throughout all chrons, as well as the stability of this orbital component reveal that IODP 342 sites possess the potential to close the middle Eocene timescale gap.

Acknowledgements

This research used samples and data provided by the International Ocean Discovery Program (IODP). S.B. was generously supported by IODP France. This work is a continuation of French ANR ASTS-CM project by J.L. et al. S.B. thanks Alexandre Lethiers (Paris VI University) for help in generating composite core images. M.V., D.D.V and H.P. were supported by ERC Consolidator Grant 617462 “EarthSequencing”. We are grateful to the IODP 342 XRF scanning team for generating XRF records at Scripps Institution of Oceanography (SIO) and at MARUM. We thank Alex Hangsterfer (at SIO), who kindly helped in XRF scanning. Y.Y. was supported by IODP Exp. 342 After Cruise Research Program, JAMSTEC, and JSPS KAKENHI Grant Number JP16H04043. Financial support for this research was provided to U.R. and T.W. by the Deutsche Forschungsgemeinschaft (DFG).

References

Billups, K., Pälike, H., Channell, J., Zachos, J., Shackleton, N.J., 2004. Astronomical calibration of the Late Oligocene through Early Miocene Geomagnetic Polarity Time Scale. Earth Planet. Sci. Lett. 224, 33–44.

Boulila, S., Galbrun, B., Laskar, J., Pälike, H., 2012. A ~9 Myr cycle in Cenozoic 13C record and long-term orbital eccentricity modulation. Is there a link?. Earth Planet. Sci. Lett. 317–318, 273–281.

Boyle, P.R., Romans, B.W., Tucholke, B.T., Norris, R.D., Swift, S.A. and Sexton, P.F. (in press), Cenozoic North Atlantic circulation from seismic stratigraphy off Newfoundland Ridge contourite drifts, offshore Canada, Marine Geology.

Cande, S.C., Kent, D.V., 1992. A New Geomagnetic Polarity Time Scale for the late Cretaceous and Cenozoic. J. Geophys. Res. 97, 13917–913951.

Cande, S.C., Kent D.V., 1995. Revised calibration of the geomagnetic polarity timescale for the Late Cretaceous and Cenozoic. J. Geophys. Res. 100, 6093–6095.

Clyde, W.C., Ramezani, J., Johnson, K.R., Bowring, S.A., Jones, M.M., 2016. Direct high-precision U–Pb geochronology of the end-Cretaceous extinction and calibration of Paleocene astronomical timescales. Earth Planet. Sci. Lett. 452, 272–280.

Dinarès-Turell, J., Westerhold, T., Pujalte, V., Röhl, U., and Kroon, D., 2014. Astronomical calibration of the Danian stage (Early Paleocene) revisited: Settling chronologies of sedimentary records across the Atlantic and Pacific Oceans. Earth Planet. Sci. Lett. 405, 119–131.

Expedition 342 Scientists, 2012. Paleogene Newfoundland sediment drifts. IODP Prel. Rept., 342. doi:10.2204/iodp.pr.342.2012.

Fienga, A., Laskar, J., Kuchynka, P., Manche, H., Desvignes, G., Gastineau, M., Cognard, I., Theureau, G., 2011. The INPOP10a planetary ephemeris and its applications in fundamental physics Celestial Mechanics and Dynamical Astronomy, Springer. An International Journal of Space Dynamics 111, 363–385.

Fienga, A., Laskar, J., Morley, T., Manche, H., Kuchynka, P., Le Poncin-Lafitte, C., Budnik, F., Gastineau, M., Somenzi, L., 2009. INPOP08, a 4-D planetary ephemeris: from asteroid and timescale computations to ESA Mars Express and Venus Express contributions. Astronom. Astrophys. 507, 1675–1686.

Fienga, A., Manche, H., Laskar, J., Gastineau, M., 2008. INPOP06: a new numerical planetary ephemeris. Astronom. Astrophys. 477, 315–327.

Fischer, A.G., 1991. Orbital cyclicity in Mesozoic strata. In Cycles and Events in Stratigraphy, ed. G Einsele, W Ricken, A Seilacher, pp. 48–62. Berlin: Springer-Verlag.

Folkner, W. M., Williams, J. G., Boggs, D. H., 2009. The Planetary and Lunar Ephemeris DE421, The Interplanetary Network Progress Report, vol. 42-178, JPL, Pasadena, pp. 1–34.

Gradstein, F.M., Ogg, J.G., Schmitz, K., Ogg, G., 2012. The Geologic Time Scale 2012. Elsevier, volume 2, 1144 p.

Herbert, T.D., 1992. Paleomagnetic calibration of Milankovitch cyclicity in Lower Cretaceous sediments. Earth. Planet. Sci. Lett. 112, 15–28.

Hilgen, F.J., Abdul Aziz, H., Krijgsman, W., Raffi, I., Turco, E., 2003. Integrated stratigraphy and astronomical forcing of the Serravallian and lower Tortonian at Monte dei Corvi (Middle-Upper Miocene, northern Italy). Palaeogeogr. Palaeoclimatol. Palaeoecol. 199, 229–264.

Hilgen, F.J., Abels, H.A., Kuiper, K.F., Lourens, L.J., and Wolthers, M., 2015. Towards a stable astronomical time scale for the Paleocene: Aligning Shatsky Rise with the Zumaia – Walvis Ridge ODP Site 1262 composite. Newsletters on Stratigraphy 48, 91–110.

Hilgen, F.J., Krijgsman, W., Langereis, C.G., Lourens, L.J., 1997. Breakthrough made in dating of the geological record. Eos 78, 285–288.

Hilgen, F.J., Kuiper, K. 2009. A critical evaluation of the numerical age of the Eocene-Oligocene boundary, in Koeberl, C., and Montanari, A., eds., The Late Eocene Earth—Hothouse, Icehouse, and Impacts. Geological Society of America, Special Paper 452, p. 1–10, doi: 10.1130/2009.2452(09).

Hilgen, F.J., Kuiper, K., Krijgsman, W., Snel, E., van der Laan, E., 2007. Astronomical tuning as the basis for high resolution chronostratigraphy: The intricate history of the Messinian Salinity Crisis. Stratigraphy 4, 231–238.

Hilgen, F.J., Kuiper, K.F., Lourens, L.J., 2010. Evaluation of the astronomical time scale for the Paleocene and earliest Eocene. Earth Planet. Sci. Lett. 300, 139–151.

Hilgen, F. J., Lourens, L.J., Van Dam, J.A., 2012. The Neogene Period, in: The Geologic Timescale 2012, edited by: Gradstein, F.M., Ogg, J.G., Schmitz, M.D., and Ogg, G.M., Elsevier, 923–978, doi:10.1016/B978-0-444-59425-9.00028-7.

Hinnov, L.A., 2000. New perspectives on orbital stratigraphy. Ann. Rev. Earth Planet. Sci. 28, 419–475.
Holbourn, A., Kuhnt, W., Schulz, M., Flores, J.-A., Andersen, N., 2007. Orbitally-paced climate evolution during the middle Miocene "Monterey" carbon-isotope excursion. Earth. Planet. Sci. Lett. 261, 534–550.
Hüsing, S.K., Kuiper, K.F., Link, W., Hilgen, F.J., Krijgsman, W., 2009. The upper Tortonian-lower Messinian at Monte dei Corvi (Northern Italy): Completing a Mediterranean reference section for the Tortonian Stage. Earth. Planet. Sci. Lett. 282, 140–157.
Hüsing, S.K., Cascella, A., Hilgen, F.J., Krijgsman, W., Kuiper, K.F., Turco, E., Wilson, D., 2010. Astrochronology of the Mediterranean Langhian between 15.29 and 14.17 Ma. Earth. Planet. Sci. Lett. 290, 254–269.
Jovane, L., Sprovieri, M., Coccioni, R., Florindo, F., Marsili, A., Laskar, J., 2010. Astronomical calibration of the middle Eocene Contessa Highway section (Gubbio, Italy). Earth Planet. Sci. Lett. 298, 77–88.
Kuiper, K.F., Deino, A., Hilgen, F.J., Krijgsman, W., Renne, P.R., Wijbrans, J.R., 2008. Synchronizing rock clocks of Earth history. Science 320, 500–504.
Laskar, J., 1989. A numerical experiment on the chaotic behaviour of the Solar System. Nature 338, 237–238.
Laskar, J., 1990. The chaotic motion of the Solar System: a numerical estimate of the size of the chaotic zone. Icarus 88, 266–291.
Laskar, J., Fienga, A., Gastineau, M., Manche, H., 2011a. La2010: a new orbital solution for the long term motion of the Earth. Astron. Astrophys. 532, A89. doi:10.1051/0004-6361/201116836.
Laskar, J., Gastineau, M., Delisle, J.-B., Farrés, A., Fienga, A., 2011b. Strong chaos induced by close encounters with Ceres and Vesta Astron. Astrophys. 532, L4. doi:10.1051/0004-6361/201117504.
Laskar, J., Robutel, P., Joutel, F., Gastineau, M., Correia, A.C.M., Levrard, B., 2004. A long-term numerical solution for the insolution quantities of the Earth. Astron. Astrophys. 428, 261–285.
Lourens, L.J., Hilgen, F.J., Laskar, J., Shackleton, N.J., Wilson, D., 2004. The Neogene Period, in: A Geologic Timescale 2004, edited by: Gradstein, F., Ogg, J., and Smith, A., 409–440, Cambridge, University Press, Cambridge, UK, doi:10.1017/CBO9780511536045.022.
Lourens, L.J., Sluijs, A., Kroon, D., Zachos, J.C., Thomas, E., Röhl, U., Bowles, J., Raffi, I., 2005. Astronomical pacing of late Palaeocene to early Eocene global warming events. Nature 435 1083–1087, doi:10.1038/nature03814.
Lyle, M., Wilson, P.A., Janecek, T.R., et al., 2002. Initial Reports volume citation, in: Proceedings of the Ocean Drilling Program Initial Reports, Leg 199: College Station, TX (Ocean Drilling Program), USA.
Mann, M.E., Lees, J.M., 1996. Robust estimation of background noise and signal detection in climatic time series. Clim. Change 33, 409–445.
Norris, R.D., Wilson, P.A., Blum, P., and the Expedition 342 Scientists, eds., 2014. Proceedings of the Integrated Ocean Drilling Program, Volume 342: College Station, TX.
Ogg, J.G., Smith, A.G., 2004. The geomagnetic polarity time scale, in: A Geological Timescale 2004, edited by: Gradstein, F., Ogg, J., and Smith, A., Cambridge University Press, Cambridge University Press, Cambridge, UK, 63–86.
Olsen, P.E., Kent, D.V., 1999. Long-term Milankovitch cycles from the Late Triassic and Early Jurassic of eastern North America and their implications for the calibration of the Early Mesozoic timescale and the long term behavior of the planets. Royal Soc. (London) Phil. Trans. Ser. A. 357, 1761–1788.
Pälike, H., Lyle, M.W., Nishi, H., Raffi, I., Ridgwell, A., Gamage, K., Klaus, A., Acton, G., Anderson, L., Backman, J., 2012. A Cenozoic record of the equatorial Pacific carbonate compensation depth. Nature 488, 609–614.
Pälike, H., Norris, R.D., Herrle, J.O., Wilson, P.A., Coxall, H.K., Lear, C.H., Shackleton, N.J., Tripati, A.K., Wade, B.S., 2006. The heartbeat of the Oligocene climate system. Science 314, 1894–1898.
Pälike, H., Shackleton, N.J., Röhl, U., 2001. Astronomical forcing in Late Eocene marine sediments. Earth Planet. Sci. Lett. 193, 589–602.
Prothero, D.R., Emry, R.J., 1996. Summary, in Prothero, D.R., and Emry, R.J., eds., The Terrestrial Eocene-Oligocene Transition in North America. Cambridge, UK, Cambridge University Press, p. 664–683.
Robinson, P., Gunnell, G.F., Walsh, S.L., Clyde, W.C., Storer, J.E., Stucky, R.K., Froehlich, D.J., Ferrusquia-Villafranca, I., McKenna, M.C., 2004. Wasatchian through Duchesnean biochronology, in Woodburne, M.O., eds., Late Cretaceous and Cenozoic Mammals of North America. New York, Columbia University Press, p. 106–155.

Sexton, P.F., Wilson, P.A., Norris, R.D., 2006. Testing the Cenozoic multisite composite 18O and 13C curves: new monospecific Eocene records from a single locality, Demerara Rise (Ocean Drilling Program Leg 207). Paleoceanography, 21(2):PA2019, doi:10.1029/ 2005PA001253.

Shackleton, N.J., Crowhurst, S.J., Weedon, G.P., Laskar, J., 1999. Astronomical calibration of Oligocene–Miocene time. Philos. Trans. R. Soc. London A 357, 1907–1929.

Smith, M.E., Chamberlain, K.R., Singer, B.S., and Carroll, A.R., 2010, Eocene clocks agree: Coeval 40Ar/39Ar, U-Pb, and astronomical ages from the Green River Formation. Geology 38, no. 6, 527–530, doi:10.1130/G30630.1.

Standish, E.M., 1998. JPL Planetary and Lunar Ephemerides, DE405/LE405. Jet Propulsion Laboratory, Interoffice Memorandum, IOM 312.F – 98 – 048.

Thomson, D.J., 1982. Spectrum estimation and harmonic analysis. IEEE Proc. 70, 1055–1096.

Tsukui, K., Clyde, W. C., 2012. Fine-tuning the calibration of the early to middle Eocene geomagnetic polarity time scale: Paleomagnetism of radioisotopically dated tuffs from Laramide foreland basins. Geol. Soc. Am. Bull. 124, 870–885.

Vandenberghe, N., Hilgen, F.J., and Speijer, R.P., 2012. The Paleogene Period, in: The Geological Timescale 2012, edited by: Gradstein, F. M., Ogg, J. G., Schmitz, M. D., and Ogg, G. M., Elsevier, 855– 922, doi:10.1016/B978-0-444-59425-9.00028-7.

Walsh, S.L., 1996. Theoretical biochronology, the Bridgerian-Uintan boundary and the “Shoshonian subage” of the Uintan, in Prothero, D.R., and Emry, R.J., eds., The Terrestrial Eocene-Oligocene Transition in North America. Cambridge, UK, Cambridge University Press, p. 52–74.

Westerhold, T., Röhl, U., Frederichs, T., Bohaty, S.M., Zachos, J.C., 2015. Astronomical calibration of the geological timescale: closing the middle Eocene gap. Clim. Past 11, 1181–1195.

Westerhold, T., Röhl, U., 2009. High resolution cyclostratigraphy of the early Eocene – new insights into the origin of the Cenozoic cooling trend. Clim. Past 5, 309–327, doi:10.5194/cp-5-309-2009. Westerhold, T., Röhl, U., 2013. Orbital pacing of Eocene climate during the Middle Eocene climate optimum and the chron C19r event: Missing link found in the tropical western Atlantic. Geochem. Geophy. Geosy. 14, 4811–4825, doi:10.1002/ggge.20293.

Westerhold, T., Röhl, U., Laskar, J., 2012. Time scale controversy: Accurate orbital calibration of the early Paleogene. Geochem. Geophy. Geosy. 13, Q06015, doi:10.1029/2012gc004096.

Westerhold, T., Röhl, U., Laskar, J., Bowles, J., Raffi, I., Lourens, L.J., and Zachos, J.C., 2007. On the duration of magnetochrons C24r and C25n and the timing of early Eocene global warming events: Implications from the Ocean Drilling Program Leg 208 Walvis Ridge depth transect. Paleoceanography 22, PA2201, doi:10.1029/2006PA001322.

Westerhold, T., Röhl, U., Pälike, H., Wilkens, R., Wilson, P. A., Acton, G., 2014. Orbitally tuned timescale and astronomical forcing in the middle Eocene to early Oligocene. Clim. Past 10, 955–973, doi:10.5194/cp-10-955-2014.

Westerhold, T., Röhl, U., Raffi, I., Fornaciari, E., Monechi, S., Reale, V., Bowles, J., Evans, H.F., 2008. Astronomical calibration of the Paleocene time. Palaeogeogr. Palaeoclimatol. Palaeoecol. 257, 377–403.

Zachos, J.C., Pagani, M., Sloan, L., Thomas, E., Billups, K., 2001. Trends, rhythms, aberrations in global climate 65 Ma to present. Science 292, 686–693.

Chapter 3: *Astronomically Paced Changes in Overturning Circulation in the Western North Atlantic during the Middle Eocene*

Maximilian Vahlenkamp[1], Igor Niezgodzki[2,3], David De Vleeschouwer[1], Torsten Bickert[1], Dustin Harper[4], Sandra Kirtland Turner[5], Gerrit Lohmann[2], Philip Sexton[6], James Zachos[4], Heiko Pälike[1]

[1] MARUM - Center for Marine Environmental Sciences, University of Bremen, Leobener Str. 8, 28359 Bremen, Germany

[2] Alfred Wegener Institute - Helmholtz Centre for Polar and Marine Research, Bussestr. 24, 27570 Bremerhaven, Germany

[3] ING PAN - Institute of Geological Sciences Polish Academy of Sciences, Research Center in Kraków, Kraków, Poland

[4] Department of Earth & Planetary Science, University of California, Santa Cruz, CA 95064, USA

[5] Department of Earth Sciences, University of California, Riverside, CA 92521, USA

[6] School of Environment, Earth & Ecosystem Sciences, The Open University, Milton Keynes MK7 6AA, UK

Abstract

North Atlantic Deep Water (NADW) currently redistributes heat and salt between Earth's ocean basins, and plays a vital role in the ocean-atmosphere CO_2 exchange. Despite its crucial role in today's climate system, vigorous debate remains as to when deep-water formation in the North Atlantic started. Here, we present middle Eocene sediments from the Newfoundland Ridge, revealing a unique carbonate-rich archive of paleoceanographic change, from the extreme warmth of the early Eocene into the progressively cooling climate of the middle Eocene. Well-defined lithologic alternations between calcareous ooze and clay-rich intervals occur at the ~41-kyr beat of axial obliquity. Hence, we identify obliquity as the driver of middle Eocene Northern Component Water (NCW, the predecessor of modern NADW) variability. High-resolution benthic $\delta^{18}O$ and $\delta^{13}C$ indicate that obliquity minima correspond to cold, nutrient-depleted, western North Atlantic deep-waters. We thus link stronger NCW formation with obliquity minima. In contrast, during obliquity maxima, Western Boundary Currents were weaker and warmer, while abyssal nutrients were more abundant and oxygen levels lower. These aspects likely reflect a more sluggish NCW formation. This obliquity-driven paleoceanographic regime is in excellent agreement with results from an Earth system model, in which obliquity minima configurations enhance NCW formation.

3.1 Introduction

Modern North Atlantic Deep Water (NADW) production accounts for ~40-50 % of Atlantic Meridional Overturning Circulation (AMOC) (Broecker, 1998). As an important part of global thermohaline circulation, the AMOC helps regulate global climate in three primary ways: i) through the zonal and latitudinal redistribution of heat, salt, and nutrients (Broecker and Peng, 1982), ii) via the carbon cycle, by AMOC's dominant role in moderating oceanic CO_2 uptake (Zickfeld et al., 2008) and iii) by its effect on atmospheric circulation through modulation of global sea surface temperatures (SST) (Mulitza et al., 2008). Accordingly, variations in AMOC intensity can cause large-scale perturbations to global and regional climates.

The modern AMOC is characterized by overturning cells in the Southern Ocean (Antarctic Bottom Water) and the in North Atlantic (NADW). The two major components of modern NADW are Nordic Sea Overflow Water and Labrador Sea Water. Nordic Sea Overflow Water is the densest part of NADW and is formed through convection of highly saline surface water in the Greenland-Norwegian Sea induced by cooling. Nordic Sea Overflow Water is fed back into the North Atlantic by overflow over the Greenland-Scotland Ridge and forms the lower part of the Deep Western Boundary Current down to about ~3500 m. Labrador Sea Water, on the other hand, is less dense than Nordic Sea Overflow Water and forms the upper part of the Western Boundary Current after convection to a depth of about ~2000 m in the Labrador Sea.

Modern ocean circulation evolved in response to changes in paleogeographic configurations over time. During the early Paleocene, the oceanic connection between the Greenland-Norwegian Sea and the North Atlantic was not yet established and the Atlantic was a much narrower elongated basin with extended adjacent shallow shelf areas (Scotese et al., 1988). Overturning principally occurred in the Southern Ocean during the late Paleocene to early Eocene (Pak and Miller, 1992; Thomas et al., 2003), with possible contribution of deep-water sources in the North Pacific (Thomas, 2004) and warm saline deep-water originating in the Tethys (Scher and Martin, 2004). Extremely high deep ocean temperatures (up to 12 °C higher than modern) (Cramer et al., 2011; Zachos et al., 2001) and elevated atmospheric CO_2 (Anagnostou et al., 2016) were associated with decreased latitudinal temperature gradients (Tripati and Elderfield, 2005) and an enhanced hydrological cycle (Barron et al., 1989) that freshened the surface ocean at high latitudes. During the early Eocene, rifting in the Greenland-Norwegian Sea (Mosar et al., 2002) created the necessary paleogeographic preconditions for the onset of a deep-water source in the North Atlantic. In addition, global cooling increased the importance of sea surface salinity relative to sea surface temperature in the formation of deep water (De Boer et al., 2007), thus accentuating the potential for deep-water formation in the North Atlantic (De Boer et al., 2008). The input of mechanical

energy triggered by winds, tides and eddies induces diapycnal mixing (Kuhlbrodt et al., 2007), adding to the buoyancy forcing, which results from differences in water temperature and salinity. This mixing drives the exchange between the surface ocean and deeper layers through overturning and upwelling of deep water masses around the Antarctic Circumpolar Current (Toggweiler and Bjornsson, 2000; Toggweiler and Samuels, 1998). The modern four layer ocean structure and increased export of Northern Component Water to the South Atlantic has been related to the development of the Antarctic Circumpolar Current during the late Eocene to early Oligocene when the Drake and Tasman Passages began to open (Cramer et al., 2009; Katz et al., 2011; Scher and Martin, 2008). Studies based on paleoceanographic circulation tracers such as Nd isotopes and interbasinal benthic isotope gradients propose similar ages for the initiation of deep water formation in the North Atlantic, ranging from the late middle Eocene to the early Oligocene (Borrelli et al., 2014; Langton et al., 2016; Via and Thomas, 2006). It should be noted though, that an unradiogenic Nd isotope signature, characteristic of modern NADW has been observed in the South Atlantic as early as the middle Eocene from 48-40 Ma (Scher and Martin, 2006; Via and Thomas, 2006). Moreover, past and recent work based on the seismic interpretation of North Atlantic contourites in combination with borehole stratigraphies and large scale erosion in the Atlantic which indicates invigoration of deep ocean circulation in the Atlantic at the early/middle Eocene boundary (Berggren and Hollister, 1974; Boyle et al., 2017; Hohbein et al., 2012). This paleoceanographic change has been linked with the onset of NCW formation (Boyle et al., 2017; Hohbein et al., 2012). The timing of these changes coincides with warming of the Atlantic relative to Pacific bottom waters (Cramer et al., 2009), enhanced global productivity (Nielsen et al., 2009) and the onset of Cenozoic climatic cooling (Cramer et al., 2011; Zachos et al., 2001) around 49 Ma.

Most studies of the oceanic response to orbital forcing have focused on a modern icehouse world. Those who did study astronomical forcing under greenhouse conditions during the Cenozoic aimed their attention at the early Eocene greenhouse, before the onset of NCW formation (e.g. Lunt et al., 2011; Sloan and Huber, 2001). Here, we particularly focus on the response to changes in obliquity (i.e. the tilt of Earths' rotational axis) after the onset of NCW (Boyle et al., 2017; Hohbein et al., 2012).

The effect of obliquity is largest at high latitudes, where the climate response to obliquity forcing is often enhanced by various feedback mechanisms (Mantsis et al., 2011). Nevertheless, several mechanisms including atmospheric and ocean circulation are known to transfer high latitude insolation forcing into mid or low latitudinal climate signals (Liu and Herbert, 2004). During the Pleistocene, overturning in the North Atlantic was hampered by freshwater release from ice sheet collapse during intervals with unusually warm summers caused by maxima in obliquity (Sigman et al., 2007). Furthermore, in pre-Pleistocene times

when Northern Hemisphere ice sheets were absent or smaller, the cooler global temperatures usually associated with minima in obliquity (De Vleeschouwer et al., 2017; Hays et al., 1976) facilitated sea ice formation and thus stimulated NCW formation. This is consistent with strong NADW formation during early Pliocene (4.7-4.2 Ma) obliquity minima (Billups et al., 1997). The absence of large continental ice sheets aided NCW production, as suggested by a vigorous conveyor belt in the early Pliocene that weakened in synchrony with the intensification of Northern Hemisphere Glaciation (Raymo et al., 1996). In the absence of continental ice sheets, obliquity can regulate the strength of the thermohaline circulation via its influence on temperature and density gradients, the hydrological cycle, the extent of sea ice, and via with the carbon cycle (Kuhlbrodt et al., 2009; Rahmstorf, 1995).

Constraining the timing of a switch from monosourced deep-water formation in the Southern Ocean towards a bipolar regime with NCW as a significant component of the AMOC is crucial for explaining long-term climate trends and abrupt events throughout the Cenozoic. Sediments at Site U1410, drilled during IODP Expedition 342 at the Newfoundland Ridge (Norris et al., 2014) provide a unique opportunity to study middle Eocene deep ocean circulation in the Western North Atlantic on orbital timescales. Here, we compare three deep-water proxies indicative of (1) deep-water paleotemperature (2) deep-water nutrient availability and (3) the intensity of the western boundary currents to constrain the deep ocean circulation in the western North Atlantic during the middle Eocene cooling trend. We illustrate, how deep ocean circulation responds to astronomical parameters and complement our observations by simulations in the coupled Earth System Model *COSMOS*.

3.2 Material and Methods

Site U1410 (41°19.6993'N, 49°10.1847'W; ~3400 m water depth) (Figure 3.1) was drilled during Integrated Ocean Drilling Program (IODP) Expedition 342 Paleogene Newfoundland Sediment Drifts (Norris et al., 2014). Middle Eocene sedimentation at this site occurred at a paleodepth of ~2950 m at ~50 Ma (Norris et al., 2012; Tucholke and Vogt, 1979). The recovered middle Eocene sediments hold a record of carbonate-rich, cyclic sequences. Moreover, relatively high sedimentation rates (2-4 cm/kyr) (Norris et al., 2014) characterize these sediments, allowing for a high-resolution reconstruction of oceanographic and climatic change.

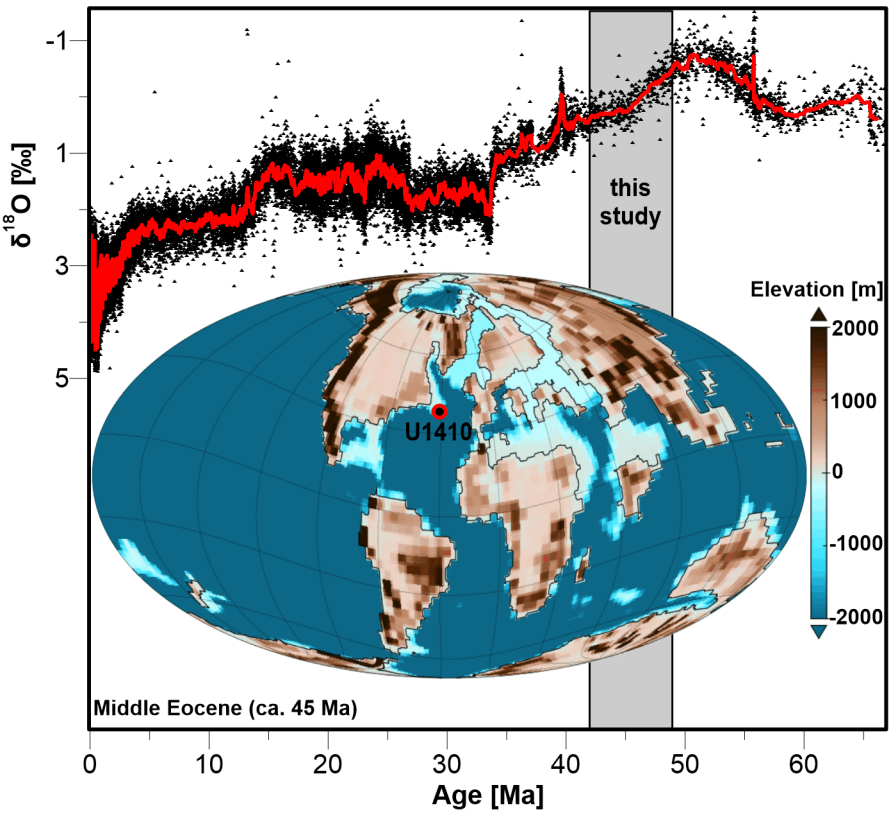

Figure 3.1: Paleoclimate setting of the middle Eocene (45 Ma). The middle Eocene represents one of the warmest climates of the Cenozoic, as indicated by a global compilation of Cenozoic $\delta^{18}O_{benthic}$ records (Cramer et al., 2009). Global topography and bathymetry used for middle Eocene model simulations in this study.

3.2.1 Isotope Sampling Strategy and Chronology

For benthic foraminifer stable isotopes, we sampled the sedimentary record of Site U1410 at 4 cm intervals (ca. 2 kyr/sample). Some samples were taken from sections that are not incorporated in the latest version of the splice, as the initial shipboard splice was revised based on onshore-acquired XRF data (Supplementary Tables 1 and 2). We aligned all cores of Site U1410 on a centimeter scale to the depth scale of this revised splice (Supplementary Figure 3.1). All isotope data are placed on a common depth scale, and are directly

comparable to other geochemical measurements presented here, though not consistently obtained from the same hole.

We updated the shipboard age model for Site U1410 by using the GTS 2012 Astronomic Age Model (Gradstein et al., 2012) ages of chron boundaries: 42.351 Ma for C19r/20n (131.76 mcd in Hole U1410A); 43.505 Ma for C20n/C20r (163.86 mcd in Hole U1410A); 45.942 Ma for C20r/C21n (218.40 mcd in Hole U1410A); 47.837 Ma for C21n/C21r (252.53 mcd in Hole U1410A) (Norris et al., 2014)). In between these chron boundaries, we use linear interpolation to transfer the XRF and stable isotope depth-series into time-series.

3.2.2 Analytical Methods for Stable Isotopes of Benthic Foraminifera

Sediment samples were soaked in sodium metaphosphate (according to a cleaning protocol for Eocene Exp. 342 samples; Hull et al. (2017)) and washed through a 150 μm sieve. Based on availability, 5-15 well preserved, glassy specimens of the benthic foraminifera *Nuttallides truempyi* without any visible infillings were picked from the >150 μm fraction in order to generate stable carbon and oxygen isotope data. Samples were measured on a Finnigan MAT 251 gas isotope ratio mass spectrometer connected to a Kiel III automated carbonate preparation device at MARUM, Bremen. Data are reported in the usual delta-notation versus V-PDB. The instrument was calibrated against the in-house standard (ground Solnhofen limestone), which in turn was calibrated against the NBS-19 standard reference material. Over the measurement period the standard deviations of the in-house standard were 0.03 ‰ for $\delta^{13}C$ and 0.07 ‰ for $\delta^{18}O$.

3.2.3 XRF data

X-ray fluorescence measurements in the studied intervals were carried out on the Avaatech XRF Core Scanner at Scripps Institution of Oceanography Geological Collections, U.C. San Diego. Elemental intensities were collected every 2 cm (ca. 1 kyr/sample) down-core over a 1.2 cm^2 area with a down-core slit size of 10 mm using generator settings of 10 kV and a current of 0.1 mA. The split surface of the archive half was covered with a 4μm thick SPEXCerti Prep Ultralene 1 foil to avoid contamination of the XRF measurement unit and desiccation of the sediment. The sampling time at the split core surface was 20 seconds.

3.2.4 Time-Series Analysis

Time Series Analysis was carried out using the REDFIT algorithm (Schulz and Mudelsee, 2002) for unevenly spaced time series as implemented in the PAST software (Hammer et al., 2001). The analyses were performed in the time-domain with a Welch-window and without oversampling or segmentation. Prior to spectral analyses a *Lowess* smoother (smoothing

factor=0.66 equal to ~1.7 Myr) was applied to all data series to remove long-term trends. Bandpass filters isolate and extract the components of signals associated with a specific range of frequencies. We employed band-pass filters to assess the behavior of a specific range of frequencies in a studied signal using the R astrochron package (Meyers, 2014). The periodicity range for bandpass filtering of obliquity cycles is between 29 and 55 kyr. We chose such a relatively broad range in order to capture the major obliquity components at 41 kyr, 54 kyr and 29 kyr (Laskar et al., 2004), which is crucial for a correct representation of amplitude modulation patterns. We obtained the amplitude envelope of the obliquity-filtered signal by the application of the Hilbert Transform, as implemented in astrochron. A lowpass filter at 130 kyr was applied to the obliquity amplitude modulation to capture the main obliquity amplitude modulation periods. The frequency range for the direct 173-kyr filter is between 130 and 220 kyr. Phase estimates and coherences were calculated with the Blackman-Tukey method using the *Analyseries* software (Paillard et al., 1996).

3.2.5 Earth System Model

Eocene climate simulations were performed using the Earth System Model *COSMOS*, in the coupled atmosphere-ocean configuration with prescribed vegetation. The model configuration includes the atmosphere component ECHAM5 at T31/L19 resolution, i.e. a horizontal resolution of ~3.75° with nineteen vertical layers (Roeckner et al., 2006). The Max Planck Institute Ocean Model (MPI-OM) runs in a GR30/L40 configuration, i.e. has an average horizontal resolution of 3º x 1.8° with 40 uneven vertical layers (Marsland et al., 2003). MPI-OM includes the dynamics of sea ice formulated using viscous-plastic rheology (Hibler III, 1979). Our version of *COSMOS* has been extensively used and validated in the context of glacial (Werner et al., 2016; Zhang et al., 2014), interglacial (Lohmann et al., 2013; Pfeiffer and Lohmann, 2016), and Miocene (Knorr et al., 2011; Knorr and Lohmann, 2014) climates.

We employ the paleogeography created for the Ypresian compiled by GETECH (Lunt et al., 2016) for the middle Eocene simulations. We have modified the original paleogeography by closing the Gibraltar Straits following the reconstruction by Stampfli et al. (2002). A deep connection between the Greenland-Norwegian Sea and the North Atlantic via the deepest part of the Greenland-Scotland Rift was established by at least ~48.5 Ma (Hohbein et al., 2012). The Arctic Ocean was an isolated, poorly ventilated basin, comparable to the modern Black Sea (Stein et al., 2006) and the Fram Strait only connected the Greenland-Norwegian Sea and the Arctic from the early Miocene onwards (Jakobsson et al., 2007). For this reason, we employ a paleogeography with a closed Fram Strait and a Greenland-Norwegian Sea gateway of 500 m water depth in our obliquity minimum/maximum experiments.

Based on this paleogeography, the boundary conditions to run the model include the prescription of vegetation distribution (Sewall et al., 2007), the set-up of the hydrological discharge model (Hagemann and Dümenil, 1997), orography related parameters for the gravity wave drag parameterization (Lott and Miller, 1997), glacier mask, the concentration of greenhouse gases in the atmosphere, and orbital parameters. The solar constant was reduced by 0.6 % compared to present-day and is equal to 1358.8 W/m^2. Eccentricity and precession were set to present day values. The CO_2 level was set to 3x pre-industrial level (840 ppm), while other greenhouse gases were set to present day values. We prescribed no ice sheets in either hemisphere.

We set up two experiments, with different obliquity angles, keeping eccentricity and precession constant. In the first experiment (OBL_{MIN}), obliquity is set to a minimum value of 22.1°, while in the second (OBL_{MAX}) to a maximum value of 24.5°. Both simulations were integrated for 7000 model years to reach steady state. The analysis is based on a climatology (long-term average) calculated from the last 100 years of simulations. We run an additional minimum obliquity experiment with an adjusted Greenland-Scotland Ridge sill depth of 200 m to test the sensitivity of NCW formation to this bathymetric feature. The simulation was restarted from experiment OBL_{MIN} at a model year 6200 and was further run for 800 years to the model year 7000.

3.3 Results

3.3.1 Paleoceanographic Proxies and their Astronomical Interpretation

Cyclic drift deposits replace continuous pelagic sediment at 244 mcd within the deeper third of chron C21n. The investigated sediment section (~158-219 mcd) in chron C20r contains middle Eocene sediment drift deposits composed of light grayish green nannofossil clay interlayered with nannofossil ooze. These well-developed alternations between nannofossil clay and nannofossil ooze reflect the primary lithological cycle in carbonate content. Carbonate content varies between ~30 wt% in the darker nannofossil clay and 80 wt% in the nannofossil ooze (Boyle et al., 2017; Norris et al., 2014). The alternation between both lithologies is well captured by the XRF-derived ratio between calcium and iron (Ca/Fe), with high Ca/Fe ratios in the nannofossil ooze and low ratios in the clay-rich intervals. The onset of the drift sediments is marked by a sharp decrease in the Ca/Fe ratio (Figure 3.2a).

The Ca/Fe ratio in chron C20r is characterized by low amplitude cycles of less than 10 in the older part of the chron (46-44.1 Ma) and high amplitude of up to 80 in its younger part (44.1-43.5 Ma). The duration of the cycles is ~41 kyr and suggests obliquity as the main driver of Ca/Fe variance. This is also indicated by the spectrum of the log(Ca/Fe) time series, which exhibits a double spectral peak exceeding the 99 % confidence level at obliquity-related periods (between 33-50 kyr; Figure 3.3a).

Another strong spectral peak emerges at a period of 18.7 kyr, very close to the frequency where one would expect the imprint of the ~20-kyr precession cycle. However, this spectral peak is more likely to be the first harmonic of the fundamental frequency of the obliquity cycles. Indeed, the log(Ca/Fe) cycles are characterized by a non-sinusoidal periodic waveform (Supplementary Figure 3.2a). Using Fourier expansion, such a signal is represented by the sum of an infinite series of all-integer harmonic frequencies. This means that a power spectrum of such a signal will have a harmonic peak at all multiples of the fundamental frequency, in this case obliquity (Supplementary Figure 3.2b). Hence, we interpret the observed peak at 18.7 kyr as the first harmonic of obliquity, rather than as the imprint of precession. Apparent amplitude modulations of obliquity with a frequency of ~173 kyr result from the resonance or "beat" between the (present-day) 41-kyr and 53-kyr obliquity cycles, for which the frequencies are determined by the precession constant and the frequency of the ascending node precession of respectively the Earth-Moon body ($p+s_3$) and Saturn ($p+s_6$) (Laskar et al., 2004).

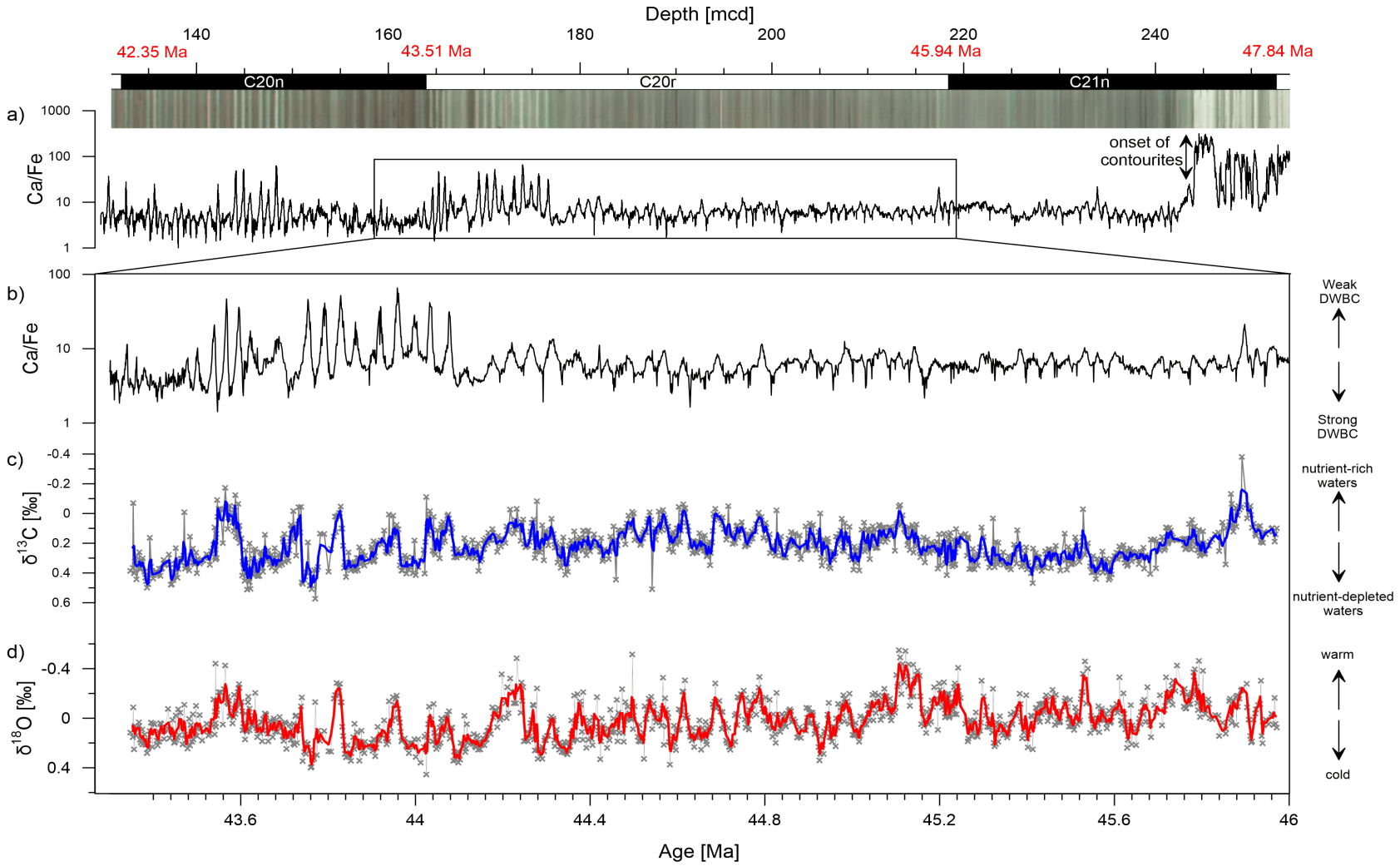

Figure 3.2: Obliquity-paced paleoceanographic proxy records from IODP Site U1410. (a) XRF-derived Ca/Fe indicate the onset of drift sedimentation at 244 mcd. (b-d) Ca/Fe, $\delta^{13}C_{benthic}$ and $\delta^{18}O_{benthic}$ records of chron C20r in the time domain. We consider C20r boundary ages of 43.51 and 45.94 Ma and apply linear interpolation in between these tie-points, so to convert depth into time. Blue and Red lines on the isotopic curves represent the 6-kyr running averages.

Our benthic foraminiferal isotope record consists of 1185 measurements between 43.35-46 Ma. Benthic carbon isotopes in chron C20r range between -0.3 ‰ and 0.4 ‰. Peaks exceeding the 95 % confidence level in the power spectrum of $\delta^{13}C$ appear at frequencies related to short eccentricity (~115 kyr), obliquity (43 kyr) and precession (17 kyr) (Figure 3.3b). Other significant peaks at frequencies of 1.29 Myr and 173 kyr are at the timescale of the long-term response of the carbon cycle to the 1.2 Myr and the 173-kyr obliquity amplitude modulation, while another significant peak appears at a frequency of 800 kyr. The carbon isotope record thus seems characterized by short and long-term orbital variability superimposed on a low amplitude increase of 0.02 ‰/Myr throughout chron C20r.

Benthic oxygen isotope values range between -0.4 ‰ and 0.3 ‰ and follow the previously-observed general cooling trend in benthic oxygen stable isotopes throughout the middle Eocene (Cramer et al., 2009). In our record, this increase amounts 0.08 ‰/Myr throughout chron C20r. Significant peaks in the power spectrum of benthic $\delta^{18}O$ occur close to the periods of obliquity (41 kyr) and long eccentricity (405 kyr) (Figure 3.3c).

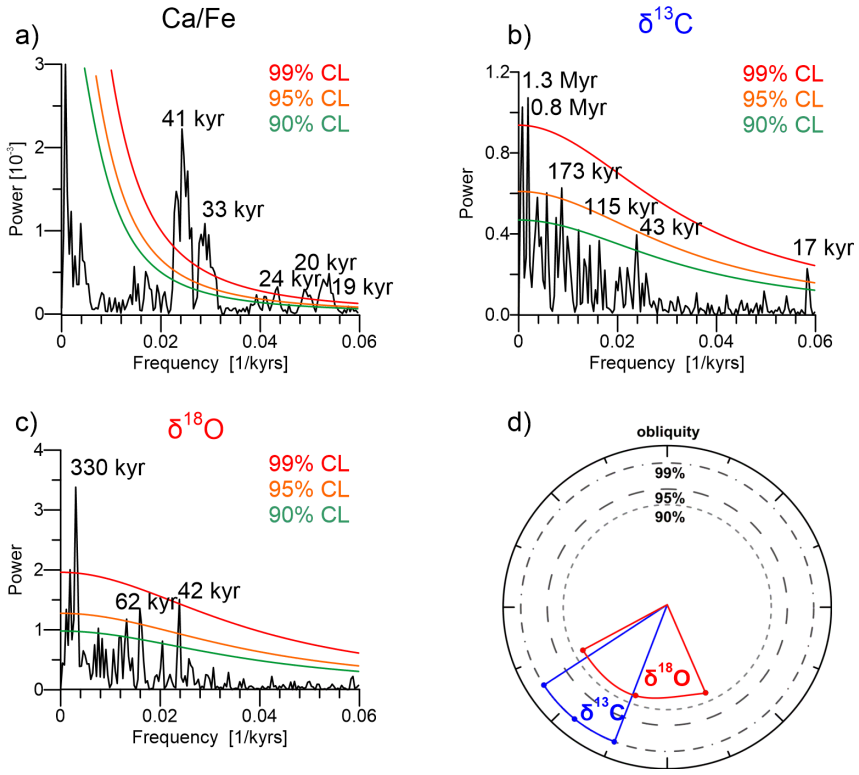

Figure 3.3: Spectral and phase analysis of proxy records. Redfit power spectra of the a) Ca/Fe, b) $\delta^{13}C_{benthic}$, and c) $\delta^{18}O_{benthic}$. Main periods are highlighted. d) Phase wheel illustrating the phase relations between benthic foraminiferal stable isotopes and Ca/Fe at the obliquity band (41 kyr). In the phase wheel representation, vectors in the 12 o'clock position are in phase with maximum Ca/Fe, and phase lags increase in the clockwise direction (for example, 3 o'clock represents a 90° lag relative to Ca/Fe, 6 o'clock represents an antiphase response, and 9 o'clock represents a 90° lead). Vector length (from circle centre to middle of arc) represents coherence, and the associated arc denotes the phase within 2σ phase error. Circles mark 99 % (dashed-dotted), 95 % (dashed) and 90 % (dotted) coherence.

The fit between observed frequencies and expected orbital frequencies in all three proxy records is remarkable given the fact that the age model is based on linear interpolation between the chron boundaries rather than astronomical tuning and thus prevents circular reasoning by introducing power into expected orbital frequencies.

The isotopes of benthic $\delta^{13}C$ and $\delta^{18}O$ are in phase (i.e. positively correlated). Minima in $\delta^{13}C$ correspond to minima in $\delta^{18}O$ and vice versa. On the other hand, benthic isotopes are in antiphase (i.e. negatively correlated) with log (Ca/Fe). Minima in $\delta^{13}C$ and $\delta^{18}O$ lead maxima in log (Ca/Fe) by ~4.5 kyr and ~2.5 kyr, and vice versa. The coherence between $\delta^{13}C$ and Ca/Fe exceeds the 99 % confidence level and thus indicates a very stable phase difference between the two proxy records.

3.3.2 Earth System Model

Figures 3.4a and 3.4d display global SSTs, as simulated by the Earth System model, under minimum and maximum obliquity respectively. On average, SSTs are 1.5 °C cooler during obliquity minima relative to obliquity maxima (Figure 3.4g). The average deep-water temperature difference between both astronomical configurations is 0.2 °C, with the obliquity minimum simulation being cooler than the obliquity maximum simulation. The amount of relative cooling gradually increases towards the poles; the Arctic is characterized by a 5.9 °C difference between both simulations. The latitudinal SST gradient increases by 5.5 °C during obliquity minima compared to obliquity maxima, a feature seen in other models (Mantsis et al., 2011).

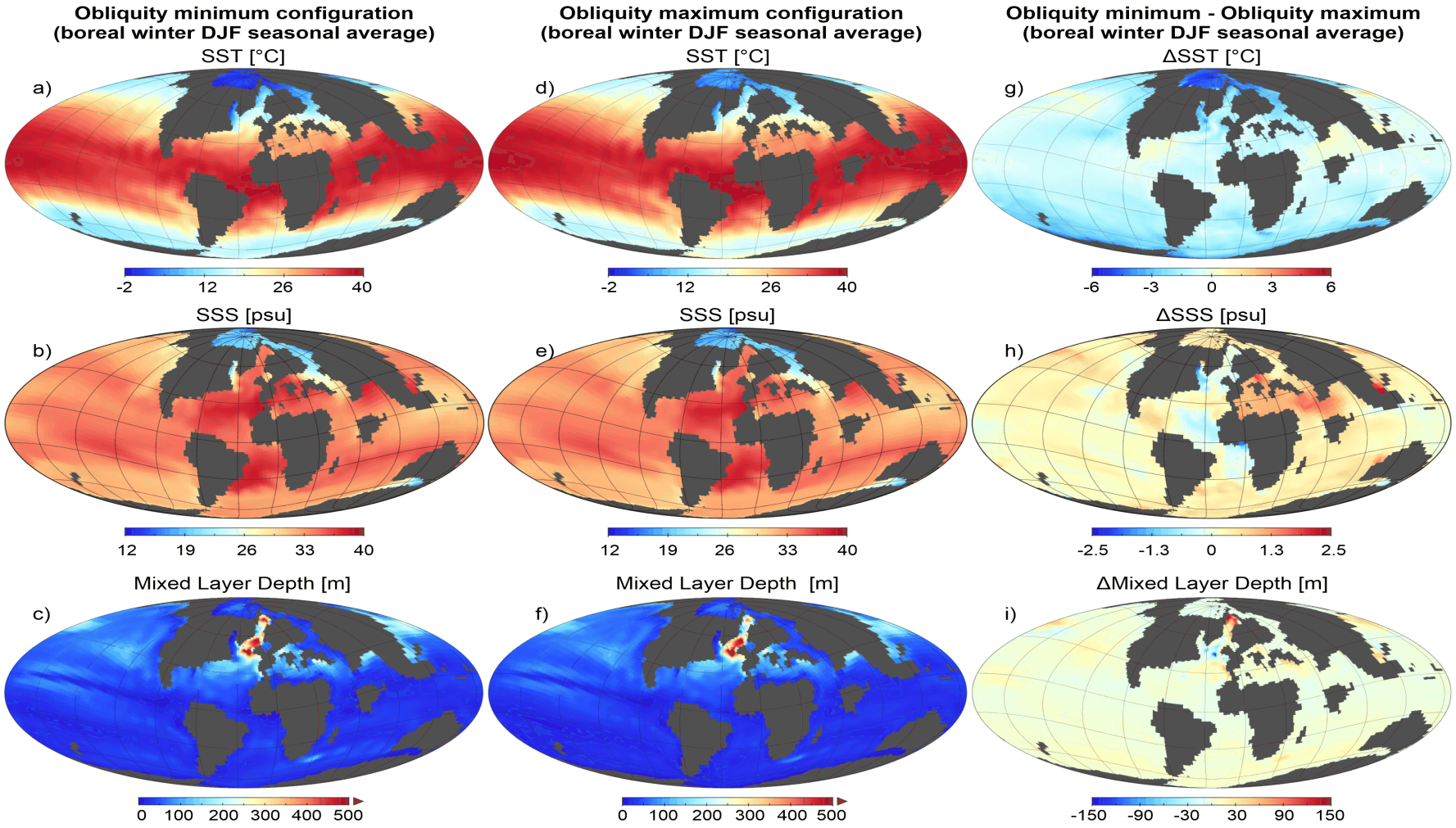

Figure 3.4: Boreal winter paleoceanography as simulated by the *COSMOS* model. Seasonally averaged Sea Surface Temperature (SST), Sea Surface Salinity (SSS) and mixed layer depth for boreal winter under (a-c) obliquity minimum configuration, and under (d-f) obliquity maximum configuration. (g-i) Seasonal differences in SST, SSS and mixed layer depth between the obliquity minimum and obliquity maximum simulations.

Deep-water cooling of up to 1.3 °C occurs during obliquity minima in the Arctic Ocean, the North Atlantic and the Nordic Sea. The model predicts that Site U1410 was exposed to ~1.2 °C cooling during middle Eocene obliquity minima compared to obliquity maxima (Figure 3.5).

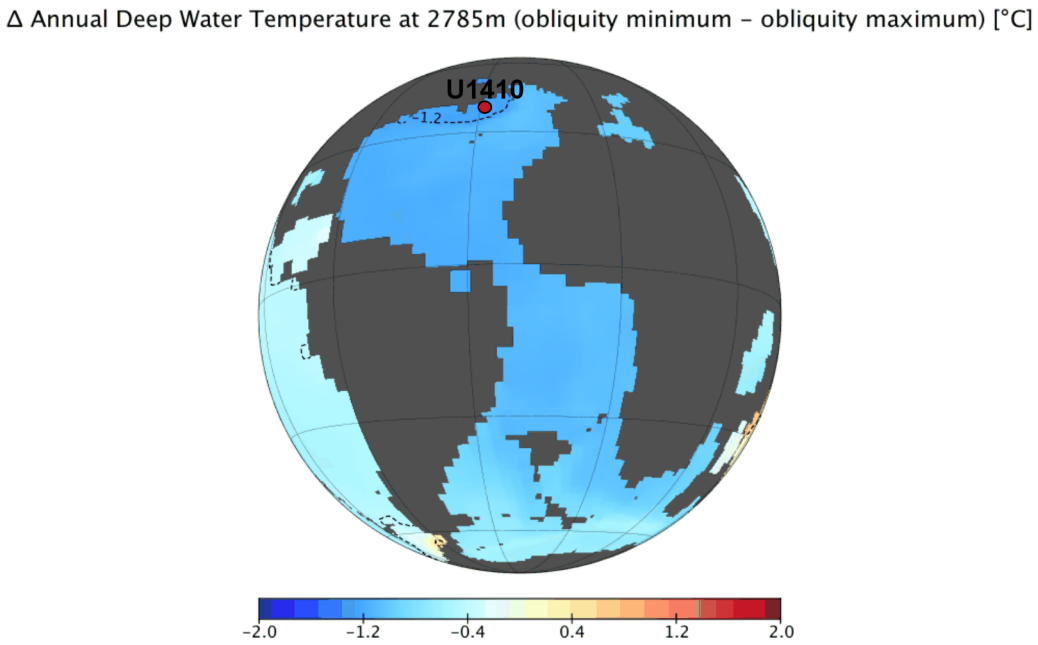

Figure 3.5: Annual difference in temperature at 2785 m water depth between the obliquity minimum and the obliquity maximum simulation. The depth of 2785 m corresponds to the approximate paleodepth of Site U1410 during the middle Eocene.

Average global sea surface salinities (SSS) are 0.4 psu higher during obliquity minima compared to obliquity maxima. Differences are most pronounced in the Tethys, where surface salinities increase by more than 2 psu during obliquity minima (Figure 3.4h). At the same time, SSS decreases by ~0.5 psu in the Labrador Sea, while SSS in the Greenland-Norwegian Sea is barely affected by variations in obliquity.

The simulated deep-water formation is strongly seasonal and occurs primarily in the Weddell Sea and Ross Sea during boreal summer and in the Eastern North Atlantic and the Greenland-Norwegian Sea during boreal winter. Mixed Layer depth is deeper during obliquity minima in boreal winter in the Greenland-Norwegian Sea (Figure 3.4i). Western boundary currents at the paleodepth of Site U1410 (~2950 m) are ~33 % faster during obliquity minima, while stronger currents during obliquity maxima occur in intermediate water depth ~1500 m.

Our simulations exhibit deep-water formation and a Deep Western Boundary Current in the North Atlantic in all three simulations (Figure 3.6), indicated also in the global meridional ocean circulation. Enhanced overturning with depth down to 4200 m is detected for minimum obliquity, whereas a reduced overturning with depths down to 3500 m is detected for

maximum obliquity, and for the model set up with minimum obliquity and 200 m sill depth of the Greenland-Scotland Ridge (Figure 3.6).

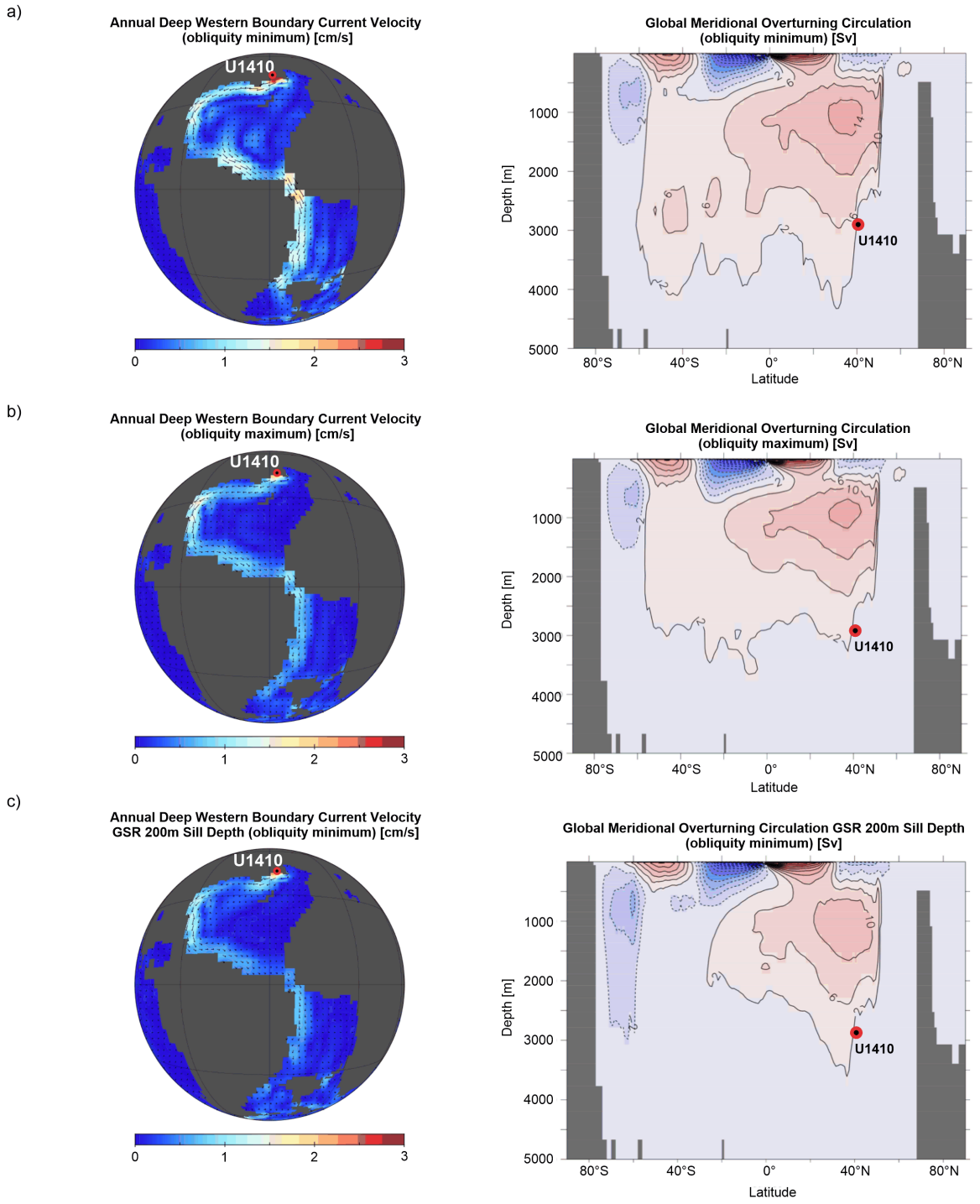

Figure 3.6: Western deep boundary current velocity and global meridional overturning circulation. Annually averaged current velocities during (a) the obliquity minimum and (b) the obliquity maximum simulation. (c) Annually averaged current velocities under a minimum obliquity configuration and for a Greenland-Scotland Ridge 200 m sill depth (500 m in nominal simulations in panels (a-b)). Positive values (red) indicate clockwise overturning cells; negative values (blue) indicate counter-clockwise overturning cells. The contour spacing is 4 Sverdrup.

The simulation with the shallower Greenland-Scotland Ridge sill depth shows that the exact geometry of NCW and SCW is susceptible to changes in the overflow capacity out of the Greenland-Norwegian Sea. The deep-water formation is weaker and shallower in the shallow sill simulation compared to simulations with a 500 m deep Greenland-Scotland Ridge, while the Southern Ocean component is strengthened.

3.4 Discussion

In this section, we will use the results from our paleoclimate simulation experiments to illustrate the mechanism involved in the invigoration of NCW formation in response to orbital forcing. It should be noted, however, that the exact amplitude of astronomically-forced change depends on different boundary conditions (e.g. paleobathymetry, atmospheric CO_2 level, vegetation distribution, continental ice volume).

3.4.1 Paleoceanographic Changes in the Western North Atlantic

Proxy records at Site U1410 in the western North Atlantic off Newfoundland reveal a strong imprint of obliquity. During the middle Eocene, Site U1410 was located at a paleolatitude of ~41°N, where 83 % of the variability in incoming summer insolation (June 21) is ascribed to precession and only 17 % to obliquity. In that respect, it is quite remarkable that the log (Ca/Fe) and stable isotope proxy records exhibit an astronomical imprint that is dominated by obliquity. The most likely explanation for this observation is an oceanographic teleconnection between the paleolocation of Site U1410 and high latitudes, where obliquity has its maximum influence on insolation variability.

A mechanism to enable such an oceanographic teleconnection is the invigoration of Deep Western Boundary Currents in response to the onset of NCW formation, which has previously been linked with the deposition of contourite drift sediments at the early-middle Eocene boundary in different locations of the North Atlantic (Boyle et al., 2017; Hohbein et al., 2012). At Site U1410, this change in bottom water circulation is marked by the sharp decrease in Ca/Fe at ~47 Ma coinciding with a lithology change from biogenic pelagic sediments to muddy drift sediments. Several lines of evidence imply that the lithological variability in carbonate content is related to the input of clay: (1) Middle Eocene carbonate deposition between 3800 and 4900 m at Expedition 342 sites indicate a deep North Atlantic carbonate compensation depth at this time (Norris, 2014). The good preservation of calcareous microfossils at Site U1410 further strengthens these observations. (2) An order-of-magnitude increase in mass accumulation rates, mostly due to an increase in the terrigenous component (Boyle et al., 2017) corresponds to the onset of the drifts at all Expedition 342 sites. (3) Increases in the sedimentation rate at Site U1410 with the onset of

drift sediments have the same proportional magnitude as decreases in $CaCO_3$ content at the same time (Norris et al., 2014). These arguments suggest changes in productivity are not the primary driver of the Ce/Fe signal. For this reason, we attach great confidence in the interpretation of the ratio of Ca/Fe as a proxy for Western Boundary Current velocity, with low Ca/Fe corresponding to strong Western Boundary Currents and vice versa.

Benthic carbon isotope ratios are primarily controlled by deep-water nutrient availability. NCW is a young deep water formed by convection of surface water from high productivity areas. Its carbon isotopic signature reflects the nutrient-depleted surface water from which it is derived. Typically, plankton preferentially extracts ^{12}C from surface waters. As a result, young deep-water masses (i.e. close to their source region) from convection of high productivity surface waters are enriched in ^{13}C and can thus can be distinguished by their respective $\delta^{13}C$ values (Kroopnick, 1985). The phase relation between our proxies (Figure 3.3d) reveals that the invigoration of Deep Western Boundary Currents (Ca/Fe minima) corresponds to the influence of nutrient-depleted bottom waters ($\delta^{13}C$ maxima) and cold bottom water temperatures ($\delta^{18}O$ maxima) at Site U1410 on obliquity timescales. The strong coherence between Ca/Fe and $\delta^{13}C$ (Figure 3.3) further indicates common mechanisms driving both proxies, related to NCW variability in the western North Atlantic at the rhythm of obliquity.

We propose that episodes of strong NCW formation correspond to obliquity minima based on following arguments: (1) The phase relationship between obliquity amplitude modulation patterns and a direct 173-kyr filter exhibit a positive phase relationship for Ca/Fe (Figure 3.7) and negative phase relationships for $\delta^{18}O$. These phase relationships indicate that increased Ca/Fe ratios correspond to high variability in Ca/Fe. Thus, we can link high Ca/Fe to obliquity maxima. In the benthic foraminiferal isotopes, the direct 173-kyr filter and the obliquity amplitude modulation are in antiphase, linking high obliquity-variability in $\delta^{18}O$ (during a 173-kyr obliquity maximum) with low $\delta^{18}O$. In other words, minima in benthic stable oxygen isotopes correspond to maxima in obliquity. However, the phase analysis between the 173-kyr $\delta^{13}C$ filter and the $\delta^{13}C$ obliquity envelope did not yield results that were statistically significant. Nevertheless, we infer the same obliquity phase relationship for $\delta^{13}C$ as for $\delta^{18}O$, as both are in phase with each other (and in antiphase with Ca/Fe). (2) $\delta^{18}O$ maxima in the deep ocean are generally linked to global cooling in response to obliquity minima (De Vleeschouwer et al., 2017b; Hays et al., 1976). (3) Our simulations in *COSMOS* show the same proportional cooling and invigoration of Deep Western Boundary Currents during obliquity minima that we see in our data, providing independent support for the astronomical phasing of our data.

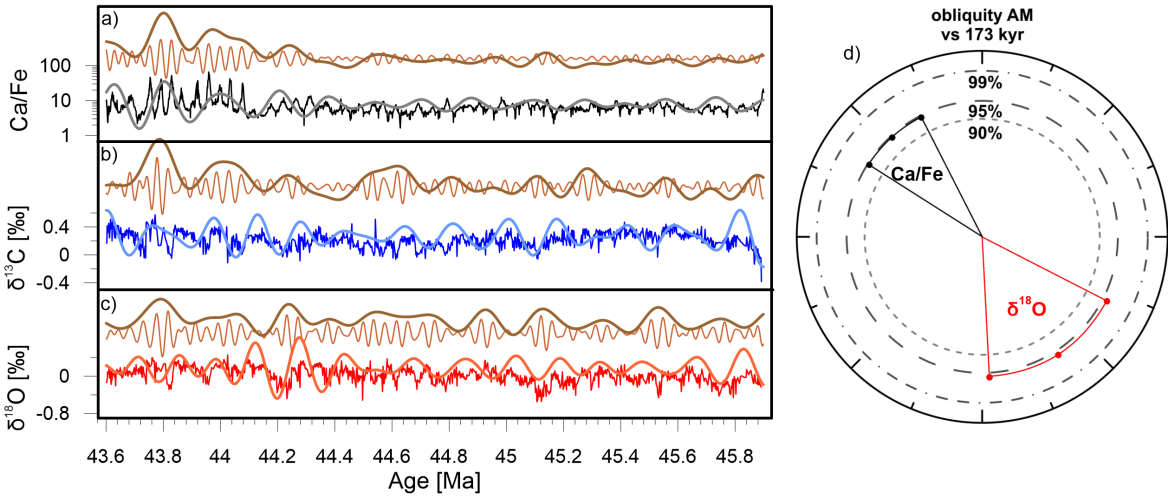

Figure 3.7: The 173-kyr cycle in the amplitude modulation of obliquity. The amplitude envelope (light brown) of the obliquity band-pass filtered signal (brown) generally exhibits an in-phase relation with the direct 173-kyr band-pass filtered signal, as extracted from the (a) Ca/Fe (black/grey), (b) $\delta^{13}C_{benthic}$ (blue), (c) $\delta^{18}O_{benthic}$ (red). Phase wheel (d) illustrating the phase relations between benthic foraminiferal stable oxygen isotopes (red) and Ca/Fe (black) at the obliquity amplitude modulation band (173 kyr). In the phase wheel representation, vectors in the 12 o'clock position are in phase with maximum Ca/Fe, and phase lags increase in the clockwise direction (for example, 3 o'clock represents a 90° lag relative to Ca/Fe, 6 o'clock represents an antiphase response, and 9 o'clock represents a 90° lead). Vector length (from circle centre to middle of arc) represents coherence, and the associated arc denotes the phase within 2σ phase error.

The amplitude of benthic oxygen isotope variability at the 41 kyr rhythm of obliquity ranges between 0.2 and 0.4 ‰. Using the equation from Epstein et al. (1953), this variability corresponds to deep-water temperature changes between 0.8 and 1.6 °C over the course of a middle Eocene obliquity cycle. These values are in excellent agreement with the results from our climate simulations, which exhibit a 1.2 °C difference between the obliquity minimum and obliquity maximum simulation in the deep northwestern Atlantic (Figure 3.5).

In accordance with our data, Deep Western Boundary Currents are invigorated during obliquity minima, transporting more clay to the Newfoundland Ridge than during obliquity maxima (Figure 3.6). At the same time, our ocean circulation simulations indicate a larger amount of nutrient-depleted NCW reaching the core location during obliquity minima (Figure 3.6a,b). This is in accordance with our paleoceanographic proxy data.

3.4.2 Source of Middle Eocene NCW

Our proxy data do not allow us to distinguish between deep waters convected in the Greenland-Norwegian Sea versus Labrador Sea. Yet several lines of evidence suggest the Greenland-Norwegian Sea as the (primary) source of NCW in the middle Eocene: (1) The paleodepth of Site U1410 is ~3000 m, much deeper than the convection depth of modern

Labrador Sea Water; (2) the onset of drift sedimentation at the Judd Falls Drift suggests deep water formation in the Greenland-Norwegian Sea in the middle Eocene (Hohbein et al., 2012); (3) the neodymium isotope signature of middle Eocene North Atlantic (Scher and Martin, 2006) is more radiogenic than during the late Eocene, indicating a later contribution of the less radiogenic Labrador Sea Water; and (4) our modeling results show the eastern North Atlantic and the Greenland-Norwegian Sea as the primary overturning locations during boreal summer, while no deep-water formation occurs in the Labrador Sea. A later onset of Labrador Sea Water in the Late Eocene to early Oligocene is in agreement with previous studies (Borrelli et al., 2014; Kaminski et al., 1989). Based on the available paleoceanographic evidence, we hypothesize the onset of NCW in the Greenland-Norwegian Sea at the middle-early Eocene boundary and a later initiation of deep-water formation in the Labrador Sea.

3.4.3 Development of NCW

Our benthic carbon isotopes are in the range of existing North Atlantic benthic isotope values for the middle Eocene. Inter-basinal $\delta^{13}C$ gradients have been utilized to distinguish between water masses during the Cenozoic (Cramer et al., 2009). However, the nutrient characteristics of deep-waters during the Paleogene were very similar. Thus, inter-basinal $\delta^{13}C$ gradients are low to non-existent before the divergence of the Pacific at ca. 14 Ma and the Southern Ocean at ca. 8 Ma (Poore et al., 2006), from the relatively high values that still characterize the North Atlantic, towards their more negative modern values (Poore et al., 2006).

Our North Atlantic benthic oxygen isotope values are at the low end of values in the global stack (i.e., warmer/less salty) (Zachos et al., 2001). This pattern reflects the warming of the Atlantic and the Southern Ocean relative to the Pacific, which starts at ~47 Ma as indicated by diverging inter-basinal $\delta^{18}O$ gradients (Cramer et al., 2009). The relative warming of the Atlantic can be explained by the onset of convection in the North Atlantic and thus the increased export of energy from the surface to the deep North Atlantic. Thermal differentiation of the Atlantic followed at ~38 Ma (Langton et al., 2016) likely in response to the opening of the Drake Passage and the establishment of the proto-Antarctic Circumpolar Current (Borrelli et al., 2014) that enabled the modern structure of the ocean (Cramer et al., 2009; Toggweiler and Samuels, 1998).

ε_{Nd} from the South Atlantic has been used to argue for an Oligocene onset of NCW (Via and Thomas, 2006). However, waters at Walvis Ridge and Agulhas Ridge show unradiogenic ε_{Nd} signatures of ~-9.5 between 48-40 Ma. These values are very close to Holocene samples from a nearby location and similar depth (Rutberg et al., 2000). Thus the influence of NCW in

the South Atlantic is plausible until the Middle Eocene Climatic Optimum, when South Atlantic ε_{Nd} become more radiogenic (Scher and Martin, 2008).

Another possibility is that the influence of middle Eocene NCW is limited to the northernmost North Atlantic and only reaches the South Atlantic after being enhanced by the establishment of the Antarctic Circumpolar Current (Borrelli et al., 2014; Toggweiler and Samuels, 1998). Ocean circulation simulations (this study and Nisancioglu et al., 2003) also indicate that a significant portion of NCW passes through the Central American Seaway into the Pacific. The influence of NCW on the Pacific could provide an explanation for subsequent trend to more non-radiogenic ε_{Nd} signature from ~at 45 Ma in the North Pacific before the opening of the Drake Passage and the Tasmanian Passage (Thomas, 2004).

Integrating our results with existing results we propose the onset of NCW formation at ~49 Ma. Subsequent subsidence of the Greenland-Scotland Ridge together with declining CO_2 invigorated the Deep Western Boundary Currents and increased the portion of NCW in the South Atlantic as reflected by low ε_{Nd} between 48-40 Ma and Atlantic warming relative to the Pacific. At 40 Ma rapidly increasing South Atlantic ε_{Nd} suggests a relative decrease in NCW, possibly related to climatic changes during the Middle Eocene Climatic Optimum. Thereafter it took until the middle Miocene to again reach such negative ε_{Nd} values as in the middle Eocene (Scher and Martin, 2006).

3.4.4 Tectonic Preconditions for the Onset of NCW Formation

The Myr-scale Eocene cooling trend played an important role in the establishment of deep-water formation in the North Atlantic. However, the tectonic prerequisites, essential in triggering NCW, were created at the end of the early Eocene. Sill deepening of the Greenland-Scotland Ridge (Hohbein et al., 2012) and fast rifting in the Greenland-Norwegian Sea (Mosar et al., 2002) enabled deep-water communication with the North Atlantic. The isolation of the Arctic from the global ocean from the late early Eocene onwards further enhanced the potential of NCW formation. Very low sea surface salinity in the Arctic due to the seaway restriction (Brinkhuis et al., 2006) was balanced by increased sea surface salinity in the North Atlantic (Roberts et al., 2009) and thus promoted thermohaline convection in the North Atlantic.

3.4.5 Response of NCW Production to Astronomical Forcing

NCW formation in the Greenland-Norwegian Sea is driven by the density gradient between the surface ocean and underlying water layers. This density gradient responds sensitively to changes in the salt balance and temperatures at the North Atlantic convection sites. We propose a combination of five different climatic feedback mechanisms, responding to

astronomical forcing, explaining the strong NCW signal during obliquity minima in sediments from the Newfoundland Ridge.

Cooler global temperatures during obliquity minima, amplified in the North Atlantic, result in enhanced oceanic heat loss to the atmosphere in the North Atlantic. The strong cooling increases the density of the saline surface waters flowing north from the subtropics. This process could increase surface water density until that water starts to sink.

Moreover, during obliquity minima, comparatively weak insolation at high latitudes cools the water (density increases) while the stronger than normal insolation at low latitudes induces warmer water (density decreases). The resulting enhanced meridional density gradient favors a stronger overturning (Butler et al., 2016). Interestingly, the occurrence of ice rafted debris indicates the initiation of glaciation around the Arctic and the Greenland-Norwegian Sea around the same time as the initiation of NCW at ~47 Ma and ~44 Ma, respectively (Stickley et al., 2009; Tripati et al., 2008). Because lower obliquity decreases annual-average insolation at high latitudes, sea ice growth should peak during localized cold periods coeval with obliquity minima. Sea ice formation removes freshwater from the ocean, leaving behind enough salt to increase the salinity of the upper ~25 m of the water column by 1 psu per meter of sea ice thickness (Maykut, 1985).

A decline in seasonality owing to low obliquity weakens the hydrological cycle in the Northern Hemisphere and preferentially decreases total annual precipitation across the high latitudes (Lawrence et al., 2003). The resulting reduction of freshwater influx into the Greenland-Norwegian Sea and the North Atlantic would increase the density of surface waters, thereby strengthening thermohaline circulation.

The observed changes in North Atlantic circulation in our proxy data could result from changes in atmospheric CO_2 responding to variations obliquity. In the geological record and climate models, elevated temperatures (De Vleeschouwer et al., 2017; Hays et al., 1976) and atmospheric CO_2 concentrations (Scheffer et al., 2006) correspond to obliquity maxima (Lüthi et al., 2008). Consequently, obliquity maxima have the potential to drive an increase in atmospheric CO_2 concentration, which subsequently weakens NCW formation.

In our middle Eocene simulations, SST in the North Atlantic and Greenland-Norwegian Sea respond sensitively to changes in obliquity, while little variance in SSS in these regions suggests only a minor impact of the hydrological cycle on overturning intensity (Figure 3.4b,e,h). Sea ice formation does not occur outside of the Arctic in our middle Eocene simulation, while sedimentological evidence indicates that temperatures were seasonally cold enough to allow the formation of glaciers around the Nordic Seas at ~44 Ma (Tripati et al., 2008). We therefore conclude that temperatures at the deep-water formation areas and increased vertical and meridional density gradients are the main modulators of middle

Eocene overturning intensity. The coherency of $\delta^{13}C$ with $\delta^{18}O$ supports the proposed role of orbital forcing on regional deep-water formation.

3.4.6 NCW Initiation and the Cenozoic Cooling Trend

The approximate correspondence in timing of the onsets of the Cenozoic cooling trend and NCW production (Hohbein et al., 2012), and the previously described mechanistic links between cooling and high latitude meridional overturning, point towards a connection between both events. Cenozoic cooling initiates in most deep sea records at ~49 Ma within the latter part of chron C22n (Mudelsee et al., 2014). This date coincides (within error) with the onset of overflow of NCW into the North Atlantic. The onset of the Newfoundland Drifts, however, occurs later at ~47 Ma (within chron C21n). We propose a scenario to explain the offset between these ages in which the onset of NCW at ~49 Ma followed the crossing of a threshold in the sill depth of the Greenland-Scotland Ridge and overflow from the Greenland-Norwegian Sea formed the Judd Fall Drifts. Later, further subsidence of the sill and declining CO_2 invigorated NCW formation, strengthening Deep Western Boundary Currents and forming the Newfoundland Drifts.

3.5 Conclusions

High-resolution benthic stable oxygen and carbon isotopes from the contourites in the western North Atlantic (IODP Expedition 342, Site U1410) combined with geochemical data from XRF reflect bottom water nutrient-content, temperature and Deep Western Boundary Current velocity. Records from the Newfoundland Drifts indicate variations in NCW formation and associated Deep Western Boundary Current strength on orbital timescales, dominated by obliquity. Paleoceanographic data and global circulation model results show that enhanced overturning is associated with a strong cooling of surface waters in the Greenland-Norwegian Sea during obliquity minima, while NCW formation is weaker with relatively warm temperatures in the Greenland-Norwegian Sea during obliquity maxima. Our modeling results show that middle Eocene NCW was primarily formed in the Eastern North Atlantic and the Nordic Seas. The earliest expression of NCW in Newfoundland Ridge sediments at Site 1410 apparently lags the onset of the Cenozoic cooling trend and the formation of drift sediments south of the Greenland-Scotland Ridge. The most likely explanation is that the subsidence of the Greenland-Scotland ridge crossed a threshold to allow the initiation of NCW formation at 49 Ma. NCW subsequently invigorated in response to ongoing subsidence and decreasing atmospheric CO_2. Thus, increased NCW formation was likely favored by sill deepening of the Greenland-Scotland Ridge and high latitude cooling and Deep Western Boundary Currents were strong enough to form the Newfoundland Drifts by 47 Ma.

Acknowledgements

M.V, D.D.V. and H.P. are funded by European Research Council Consolidator Grant EarthSequencing (grant agreement 617462). I.N. is funded by the National Center of Science, Poland (DEC-2012/07/N/ST10/03419) and the DAAD. I.N. gratefully acknowledges G. Knorr (AWI) and J. Tyszka (ING PAN) for their scientific support. G.L. is funded by the Helmholtz society through the PACES and REKLIM programs. This research used data provided by the Integrated Ocean Drilling Program (IODP). IODP is sponsored by the US National Science Foundation (NSF) and participating countries under the management of Joint Oceanographic Institutions (JOI), Inc. We thank H. Kuhnert and the team of the stable isotope laboratory at MARUM, Bremen, for the support with stable isotope measurements. We thank all participating scientists, technical staff, and crew of IODP Expedition 342 for the acquisition and shipboard analysis of cores used in this study.

References

Anagnostou, E., John, E.H., Edgar, K.M., Foster, G.L., Ridgwell, A., Inglis, G.N., Pancost, R.D., Lunt, D.J., Pearson, P.N., 2016. Changing atmospheric CO2 concentration was the primary driver of early Cenozoic climate. Nature 533, 380-384.

Barron, E.J., Hay, W.W., Thompson, S., 1989. The hydrologic cycle: A major variable during Earth history. Palaeogeography, Palaeoclimatology, Palaeoecology 75, 157-174.

Berggren, W.A., Hollister, C.D., 1974. Paleogeography, paleobiogeography and the history of circulation in the Atlantic Ocean.

Billups, K., Ravelo, A.C., Zachos, J.C., 1997. Early Pliocene deep-water circulation: stable isotope evidence for enhanced northern component deep water, Proc. Ocean Drill. Program, Sci. Results, pp. 319-330.

Borrelli, C., Cramer, B.S., Katz, M.E., 2014. Bipolar Atlantic deepwater circulation in the middle-late Eocene: Effects of Southern Ocean gateway openings. Paleoceanography 29, 308-327.

Boyle, P.R., Romans, B.W., Tucholke, B.E., Norris, R.D., Swift, S.A., Sexton, P.F., 2017. Cenozoic North Atlantic deep circulation history recorded in contourite drifts, offshore Newfoundland, Canada. Marine Geology 385, 185-203.

Brinkhuis, H., Schouten, S., Collinson, M.E., Sluijs, A., Damsté, J.S.S., Dickens, G.R., Huber, M., Cronin, T.M., Onodera, J., Takahashi, K., 2006. Episodic fresh surface waters in the Eocene Arctic Ocean. Nature 441, 606-609.

Broecker, W.S., 1998. Paleocean circulation during the last deglaciation: a bipolar seesaw? Paleoceanography 13, 119-121.

Broecker, W.S., Peng, T.-H., 1982. Tracers in the Sea.

Butler, E.D., Oliver, K.I.C., Hirschi, J.J.-M., Mecking, J.V., 2016. Reconstructing global overturning from meridional density gradients. Climate Dynamics 46, 2593-2610.

Cramer, B., Miller, K., Barrett, P., Wright, J., 2011. Late Cretaceous–Neogene trends in deep ocean temperature and continental ice volume: Reconciling records of benthic foraminiferal geochemistry (δ18O and Mg/Ca) with sea level history. Journal of Geophysical Research: Oceans 116.

Cramer, B., Toggweiler, J., Wright, J., Katz, M., Miller, K., 2009. Ocean overturning since the Late Cretaceous: Inferences from a new benthic foraminiferal isotope compilation. Paleoceanography 24.

De Boer, A., Sigman, D., Toggweiler, J., Russell, J., 2007. Effect of global ocean temperature change on deep ocean ventilation. Paleoceanography 22.

De Boer, G.J., Pietrzak, J.D., Winterwerp, J.C., 2008. Using the potential energy anomaly equation to investigate tidal straining and advection of stratification in a region of freshwater influence. Ocean Modelling 22, 1-11.

De Vleeschouwer, D., Vahlenkamp, M., Crucifix, M., Pälike, H., 2017. Alternating Southern and Northern Hemisphere climate response to astronomical forcing during the past 35 m.y. Geology.

Epstein, S., Buchsbaum, R., Lowenstam, H.A., Urey, H.C., 1953. Revised carbonate-water isotopic temperature scale. Geological Society of America Bulletin 64, 1315-1326.
Gradstein, F.M., Ogg, J.G., Schmitz, M., Ogg, G., 2012. The geologic time scale 2012. elsevier.
Hagemann, S., Dümenil, L., 1997. A parametrization of the lateral waterflow for the global scale. Climate Dynamics 14, 17-31.
Hammer, Ø., Harper, D., Ryan, P., 2001. PAST-palaeontological statistics, ver. 1.89. Palaeontologia electronica 4.
Hays, J., Imbrie, J., Shackleton, N., 1976. Variations in the earth's orbit: pacemaker of the ice ages. Science (Washington, DC);(United States) 194.
Hibler III, W., 1979. A dynamic thermodynamic sea ice model. Journal of Physical Oceanography 9, 815-846.
Hohbein, M.W., Sexton, P.F., Cartwright, J.A., 2012. Onset of North Atlantic Deep Water production coincident with inception of the Cenozoic global cooling trend. Geology 40, 255-258.
Hull, P., Bohaty, S., Cameron, A., Coxall, H., D'haenens, S., De Vleeschouwer, D., Elder, L., Friedrich, O., Kerr, K., Turner, S., 2017. Data report: coarse fraction record for the Eocene megasplice at IODP Sites U1406, U1408, U1409, and U1411, Proc. IODP| Volume, p. 2.
Jakobsson, M., Backman, J., Rudels, B., Nycander, J., Frank, M., Mayer, L., Jokat, W., Sangiorgi, F., O'Regan, M., Brinkhuis, H., 2007. The early Miocene onset of a ventilated circulation regime in the Arctic Ocean. Nature 447, 986-990.
Kaminski, M., Gradstein, F., Berggren, W., 1989. Paleogene benthic foraminifer biostratigraphy and paleoecology at Site 647, southern Labrador Sea, Proceedings of the Ocean Drilling Program: Scientific Results, pp. 705-730.
Katz, M.E., Cramer, B.S., Toggweiler, J., Esmay, G., Liu, C., Miller, K.G., Rosenthal, Y., Wade, B.S., Wright, J.D., 2011. Impact of Antarctic Circumpolar Current development on late Paleogene ocean structure. Science 332, 1076-1079.
Knorr, G., Butzin, M., Micheels, A., Lohmann, G., 2011. A warm Miocene climate at low atmospheric CO2 levels. Geophysical Research Letters 38.
Knorr, G., Lohmann, G., 2014. Climate warming during Antarctic ice sheet expansion at the Middle Miocene transition. Nature Geoscience 7, 376-381.
Kroopnick, P., 1985. The distribution of 13 C of ΣCO 2 in the world oceans. Deep Sea Research Part A. Oceanographic Research Papers 32, 57-84.
Kuhlbrodt, T., Griesel, A., Montoya, M., Levermann, A., Hofmann, M., Rahmstorf, S., 2007. On the driving processes of the Atlantic meridional overturning circulation. Reviews of Geophysics 45.
Kuhlbrodt, T., Rahmstorf, S., Zickfeld, K., Vikebø, F.B., Sundby, S., Hofmann, M., Link, P.M., Bondeau, A., Cramer, W., Jaeger, C., 2009. An integrated assessment of changes in the thermohaline circulation. Climatic Change 96, 489-537.
Langton, S.J., Rabideaux, N.M., Borrelli, C., Katz, M.E., 2016. Southeastern Atlantic deep-water evolution during the late-middle Eocene to earliest Oligocene (Ocean Drilling Program Site 1263 and Deep Sea Drilling Project Site 366). Geosphere 12, 1032-1047.
Laskar, J., Robutel, P., Joutel, F., Gastineau, M., Correia, A., Levrard, B., 2004. A long-term numerical solution for the insolation quantities of the Earth. Astronomy & Astrophysics 428, 261-285.
Lawrence, K., Sloan, L.C., Sewall, J., 2003. Terrestrial climatic response to precessional orbital forcing in the Eocene. Special Papers-Geological Society of America, 65-78.
Liu, Z., Herbert, T.D., 2004. High-latitude influence on the eastern equatorial Pacific climate in the early Pleistocene epoch. Nature 427, 720-723.
Lohmann, G., Pfeiffer, M., Laepple, T., Leduc, G., Kim, J.-H., 2013. A model-data comparison of the Holocene global sea surface temperature evolution. Climate of the Past, 1807-1839.
Lott, F., Miller, M.J., 1997. A new subgrid-scale orographic drag parametrization: Its formulation and testing. Quarterly Journal of the Royal Meteorological Society 123, 101-127.
Lunt, D.J., Foster, G.L., O'Brien, C.L., Pancost, R.D., Robinson, S.A., 2016. Palaeogeographic controls on climate and proxy interpretation. Climate of the Past 12, 1181.
Lunt, D.J., Ridgwell, A., Sluijs, A., Zachos, J., Hunter, S., Haywood, A., 2011. A model for orbital pacing of methane hydrate destabilization during the Palaeogene. Nature Geosci 4, 775-778.
Lüthi, D., Le Floch, M., Bereiter, B., Blunier, T., Barnola, J.-M., Siegenthaler, U., Raynaud, D., Jouzel, J., Fischer, H., Kawamura, K., 2008. High-resolution carbon dioxide concentration record 650,000–800,000 years before present. Nature 453, 379-382.
Mantsis, D.F., Clement, A.C., Broccoli, A.J., Erb, M.P., 2011. Climate feedbacks in response to changes in obliquity. Journal of Climate 24, 2830-2845.
Marsland, S.J., Haak, H., Jungclaus, J.H., Latif, M., Röske, F., 2003. The Max-Planck-Institute global ocean/sea ice model with orthogonal curvilinear coordinates. Ocean modelling 5, 91-127.
Maykut, G.A., 1985. An Introduction to Ice in the Polar Oceans. DTIC Document.

Meyers, S.R., 2014. astrochron: AN R Package for Astrochronology. http://cran.r-project.org/package=astrochron.
Mosar, J., Eide, E.A., Osmundsen, P.T., Sommaruga, A., Torsvik, T.H., 2002. Greenland–Norway separation: a geodynamic model for the North Atlantic, Norwegian Journal of Geology, p. 282.
Mudelsee, M., Bickert, T., Lear, C.H., Lohmann, G., 2014. Cenozoic climate changes: A review based on time series analysis of marine benthic δ18O records. Reviews of Geophysics 52, 333-374.
Mulitza, S., Prange, M., Stuut, J.B., Zabel, M., von Dobeneck, T., Itambi, A.C., Nizou, J., Schulz, M., Wefer, G., 2008. Sahel megadroughts triggered by glacial slowdowns of Atlantic meridional overturning. Paleoceanography 23.
Nielsen, S.G., Mar-Gerrison, S., Gannoun, A., LaRowe, D., Klemm, V., Halliday, A.N., Burton, K.W., Hein, J.R., 2009. Thallium isotope evidence for a permanent increase in marine organic carbon export in the early Eocene. Earth and Planetary Science Letters 278, 297-307.
Nisancioglu, K.H., Raymo, M.E., Stone, P.H., 2003. Reorganization of Miocene deep water circulation in response to the shoaling of the Central American Seaway. Paleoceanography 18.
Norris, R., Wilson, P., Blum, P., 2014. the Expedition 342 Scientists: Proceedings IODP, 342. College Station, TX (Integrated Ocean Drilling Program), doi 1.
Norris, R.D., Wilson, P.A., Blum, P., Fehr, A., Agnini, C., Bornemann, A., Boulila, S., Brown, P.R., Cournede, C., Friedrich, O., 2012. Paleogene Newfoundland sediment drifts. Integrated Ocean Drilling Program Management International, Inc.
Norris, R.D., Wilson, P.A., Blum, P., Fehr, A., Agnini, C., Bornemann, A., Boulila, S., Bown, P.R., Cournede, C., Friedrich, O., Ghosh, A.K., Hollis, C.J., Hull, P.M., Jo, K., Junium, C.K., Kaneko, M., Liebrand, D., Lippert, P.C., Liu, Z., Matsui, H., Moriya, K., Nishi, H., Opdyke, B.N., Penman, D., Romans, B., Scher, H.D., Sexton, P., Takagi, H., Turner, S.K., Whiteside, J.H., Yamaguchi, T., and Yamamoto, Y., 2014. Site U1410. In Norris, R.D., Wilson, P.A., Blum, P., and the Expedition 342 Scientists, 2014. Proc. IODP, 342: College Station, TX (Integrated Ocean Drilling Program).
Paillard, D., Labeyrie, L., Yiou, P., 1996. Macintosh program performs time-series analysis. Eos, Transactions American Geophysical Union 77, 379-379.
Pak, D.K., Miller, K.G., 1992. Paleocene to Eocene benthic foraminiferal isotopes and assemblages: Implications for deepwater circulation. Paleoceanography 7, 405-422.
Pfeiffer, M., Lohmann, G., 2016. Greenland Ice Sheet influence on Last Interglacial climate: global sensitivity studies performed with an atmosphere–ocean general circulation model. Climate of the Past, 1313-1338.
Poore, H., Samworth, R., White, N., Jones, S., McCave, I., 2006. Neogene overflow of Northern Component Water at the Greenland-Scotland Ridge. Geochemistry, Geophysics, Geosystems 7.
Rahmstorf, S., 1995. Bifurcations of the Atlantic thermohaline circulation in response to changes in the hydrological cycle. Nature 378, 145.
Raymo, M., Grant, B., Horowitz, M., Rau, G., 1996. Mid-Pliocene warmth: stronger greenhouse and stronger conveyor. Marine Micropaleontology 27, 313-326.
Roberts, C.D., LeGrande, A.N., Tripati, A.K., 2009. Climate sensitivity to Arctic seaway restriction during the early Paleogene. Earth and Planetary Science Letters 286, 576-585.
Roeckner, E., Brokopf, R., Esch, M., Giorgetta, M., Hagemann, S., Kornblueh, L., Manzini, E., Schlese, U., Schulzweida, U., 2006. Sensitivity of simulated climate to horizontal and vertical resolution in the ECHAM5 atmosphere model. Journal of Climate 19, 3771-3791.
Rutberg, R.L., Hemming, S.R., Goldstein, S.L., 2000. Reduced North Atlantic Deep Water flux to the glacial Southern Ocean inferred from neodymium isotope ratios. Nature 405, 935-938.
Scheffer, M., Brovkin, V., Cox, P.M., 2006. Positive feedback between global warming and atmospheric CO2 concentration inferred from past climate change. Geophysical Research Letters 33.
Scher, H.D., Martin, E.E., 2004. Circulation in the Southern Ocean during the Paleogene inferred from neodymium isotopes. Earth and Planetary Science Letters 228, 391-405.
Scher, H.D., Martin, E.E., 2006. Timing and climatic consequences of the opening of Drake Passage. Science 312, 428-430.
Scher, H.D., Martin, E.E., 2008. Oligocene deep water export from the North Atlantic and the development of the Antarctic Circumpolar Current examined with neodymium isotopes. Paleoceanography 23.
Schulz, M., Mudelsee, M., 2002. REDFIT: estimating red-noise spectra directly from unevenly spaced paleoclimatic time series. Computers & Geosciences 28.
Scotese, C.R., Gahagan, L.M., Larson, R.L., 1988. Plate tectonic reconstructions of the Cretaceous and Cenozoic ocean basins. Tectonophysics 155, 27-48.

Sewall, J.v., Van De Wal, R., Van Der Zwan, K., Van Oosterhout, C., Dijkstra, H., Scotese, C., 2007. Climate model boundary conditions for four Cretaceous time slices. Climate of the Past 3, 647-657.
Sigman, D.M., De Boer, A.M., Haug, G.H., 2007. Antarctic stratification, atmospheric water vapor, and Heinrich events: A hypothesis for late Pleistocene deglaciations. Ocean Circulation: Mechanisms and Impacts-Past and Future Changes of Meridional Overturning, 335-349.
Sloan, L.C., Huber, M., 2001. Eocene oceanic responses to orbital forcing on precessional time scales. Paleoceanography 16, 101-111.
Stampfli, G., Borel, G.D., Marchant, R., Mosar, J., 2002. Western Alps geological constraints on western Tethyan reconstructions. Journal of the Virtual Explorer 8, 77.
Stein, R., Boucsein, B., Meyer, H., 2006. Anoxia and high primary production in the Paleogene central Arctic Ocean: First detailed records from Lomonosov Ridge. Geophysical Research Letters 33.
Stickley, C.E., St John, K., Koç, N., Jordan, R.W., Passchier, S., Pearce, R.B., Kearns, L.E., 2009. Evidence for middle Eocene Arctic sea ice from diatoms and ice-rafted debris. Nature 460, 376-379.
Thomas, D.J., 2004. Evidence for deep-water production in the North Pacific Ocean during the early Cenozoic warm interval. Nature 430, 65-68.
Thomas, D.J., Bralower, T.J., Jones, C.E., 2003. Neodymium isotopic reconstruction of late Paleocene–early Eocene thermohaline circulation. Earth and Planetary Science Letters 209, 309-322.
Toggweiler, J., Bjornsson, H., 2000. Drake Passage and palaeoclimate. Journal of Quaternary Science 15, 319-328.
Toggweiler, J., Samuels, B., 1998. On the ocean's large-scale circulation near the limit of no vertical mixing. Journal of Physical Oceanography 28, 1832-1852.
Tripati, A., Elderfield, H., 2005. Deep-sea temperature and circulation changes at the Paleocene-Eocene thermal maximum. Science 308, 1894-1898.
Tripati, A.K., Eagle, R.A., Morton, A., Dowdeswell, J.A., Atkinson, K.L., Bahé, Y., Dawber, C.F., Khadun, E., Shaw, R.M., Shorttle, O., 2008. Evidence for glaciation in the Northern Hemisphere back to 44 Ma from ice-rafted debris in the Greenland Sea. Earth and Planetary Science Letters 265, 112-122.
Tucholke, B., Vogt, P., 1979. Western North Atlantic: Sedimentary evolution and aspects of tectonic history. Initial Rep. Deep Sea Drill. Proj 43, 791-825.
Via, R.K., Thomas, D.J., 2006. Evolution of Atlantic thermohaline circulation: Early Oligocene onset of deep-water production in the North Atlantic. Geology 34, 441-444.
Werner, M., Haese, B., Xu, X., Zhang, X., Butzin, M., Lohmann, G., 2016. Glacial–interglacial changes in H218O, HDO and deuterium excess–results from the fully coupled ECHAM5/MPI-OM Earth system model. Geoscientific Model Development 9, 647-670.
Zachos, J., Pagani, M., Sloan, L., Thomas, E., Billups, K., 2001. Trends, rhythms, and aberrations in global climate 65 Ma to present. Science 292, 686-693.
Zhang, X., Lohmann, G., Knorr, G., Purcell, C., 2014. Abrupt glacial climate shifts controlled by ice sheet changes. Nature 512, 290-294.
Zickfeld, K., Eby, M., Weaver, A.J., 2008. Carbon-cycle feedbacks of changes in the Atlantic meridional overturning circulation under future atmospheric CO2. Global Biogeochemical Cycles 22.

Chapter 4: *Sensitivity of the Climate System and Ocean Circulation to Atmospheric CO_2 and Ocean Gateway Configurations during the Middle Eocene*

Maximilian Vahlenkamp[1], Igor Niezgodzki[2,3], David De Vleeschouwer[1], Gerrit Lohmann[2], Heiko Pälike[1]

[1] MARUM - Center for Marine Environmental Sciences, University of Bremen, Leobener Strasse 8, 28359 Bremen, Germany

[2] Alfred Wegener Institute Helmholtz Centre for Polar and Marine Research, Bussestr. 24, 27570 Bremerhaven, Germany

[3] ING PAN - Institute of Geological Sciences Polish Academy of Sciences, Research Center in Kraków, Kraków, Poland

Abstract

Changes in ocean circulation occurred at ~48 Ma coinciding with the onset of Cenozoic cooling from the Paleogene greenhouse climate towards the modern icehouse. The cause for these large-scale changes in ocean circulation is poorly understood as reliably reconstructing the development of Eocene atmospheric CO_2 and the depth and geometry of developing and closing passages between ocean basins remains a challenge. However, the identification of thresholds of tectonic gateway passages and the atmospheric CO_2 concentration can unravel the physical processes driving deep water formation in a greenhouse world.

The Earth System Model *COSMOS* is used to evaluate middle Eocene global climate and ocean circulation sensitivity to changes in atmospheric CO_2 concentration and the connectivity between convection sites in the Greenland-Norwegian Sea with the North Atlantic, the Arctic Ocean and the Tethys via the Atlantic.

We find a substantial deepening of Northern Component Water and an invigoration of the thermohaline circulation in response to the drawdown of atmospheric CO_2 through increased surface water density in the primary overturning location in the southern Greenland-Norwegian Sea. The critical role of the Greenland-Scotland Ridge for the formation of Northern Component Water (NCW) is reflected in our simulations with sill depths of 50, 200 and 500 m. We find a threshold between 50-200 m that allows for sufficient inflow of warm, salty Atlantic surface waters into the Greenland-Norwegian Sea to initiate convection during winter cooling. Further deepening of the sill leads to an increase of the overflow capacity of the sill and results in invigoration and deepening of the thermohaline circulation. A seaway between the Greenland-Norwegian Sea and the Arctic allows inflow of low-density surface waters into the northern Greenland-Norwegian Sea. The influence of these waters on surface water density hinders deep-water formation in the Greenland-Norwegian Sea and strengthens convection in the Southern Ocean. Finally, the influence of Tethyan waters to the subtropical North Atlantic does not substantially influence the strength or geometry of NCW formation in our simulations.

4.1 Introduction

Variations in global surface and deep ocean temperatures on different timescales have been linked with variations in the rate of the Atlantic Meridional Overturning Circulation (AMOC) driven by vertical density gradients at deep water formation sites in the North Atlantic for more than three decades (Broecker et al., 1985). Two physical processes exemplify the importance of the global deep ocean circulation: Firstly, the deep ocean stores and releases vast amounts of heat and chemical tracers (salt, nutrients, greenhouse gases, etc.) and restricts exchange with the atmosphere on centennial to millennial timescales (Bigg, 2003; Matsumoto, 2007; Metz et al., 2005). Some of the past changes in atmospheric CO_2, (e.g. during Pleistocene glacial-interglacial cycles) were driven at least partially by changes in the rates of overturning and upwelling in polar regions (Francois et al., 1997; Haug et al., 1999; Toggweiler, 1999). The other principal role of the AMOC is the redistribution of heat and chemical tracers around the globe in response to the imbalance between incoming solar radiation in the summer and winter hemisphere on one side and low and high latitudes on the other (Broecker, 1992).

In the modern ocean, overturning occurs in the high latitudes of the North Atlantic and the Atlantic sector of the Southern Ocean. The reason is that the density of seawater is strongly dependent on temperature and salinity. As the Atlantic Ocean is saltier than the Pacific Ocean, convection presently occurs here. Convection in the Greenland-Norwegian Sea and the Labrador Sea is fed by northward flow of warm, salty surface waters in the upper thousand meters of the water column. The release of heat into the Northern Hemisphere atmosphere when the Atlantic Surface Water cools down results in relatively warm conditions in the North Atlantic region compared to the Pacific (Broecker, 1992). From the Greenland-Norwegian Sea salty, cold Nordic Sea Overflow Water (NSOW) surpasses the Greenland-Scotland Ridge (GSR) to the North Atlantic, where it forms the densest component of the NCW and flows southward at depths of 3500-4500 m. The upper branch of NCW consists of less dense Labrador Sea Water (LSW) which is formed in the central Labrador Sea during winter season and sinks down to ~2500 m. On its way South, it forms the Atlantic Deep Western Boundary Current (DWBC) along the eastern continental slope of the American continent. The basin-wide transport of 15-18 Sv (=10^6 m^3 s^{-1}) (Ganachaud and Wunsch, 2000; Lumpkin and Speer, 2003) associated with Deep Western Boundary Currents and AMOC imposes climate signals from the northern high latitudes on the tropics and the Southern Hemisphere (Fine et al., 2002; He et al., 2013).

Geographic gateways and barriers are the fundamental basis for changes in the pathways of ocean circulation. To understand the long-term climatic trends in global climate, it is thus crucial to evaluate the role of ocean gateways and barriers together with the atmospheric concentration of CO_2. Over the course of the Cenozoic, changes in ocean gateway configurations and their respective impact on global ocean circulation have been linked to large-scale climatic change:

In the early Cenozoic, deep-water formation occurred primarily in the Southern Ocean (Mountain and Miller, 1992; Pak and Miller, 1992; Thomas et al., 2003; Via and Thomas, 2006). In the early Eocene, the Greenland-Norwegian Sea began to open, but was still separated from the Atlantic by the Greenland-Scotland Ridge.

The subsidence of the Greenland-Scotland Ridge and later the closure of the Central American Seaway due to the emergence of the Panama Isthmus are associated with the initiation and intensification of a deep-water source in the North Atlantic (Burton et al., 1997; Haug and Tiedemann, 1998; Poore et al., 2006; Wright, 1998).

The onset of a Northern Component deep-water source is part of a general development from a latitudinal towards a meridional oceanic circulation that had started during the Cretaceous and continued during the Paleogene with the cessation of the circumglobal Tethys seaway (Luyendyk et al., 1972).

The opening of the Drake Passage and the Tasman Passage around the time of the Eocene-Oligocene boundary resulted in the establishment of the Antarctic Circumpolar Current. This cold current gave rise to the thermal isolation of Antarctica. This change in ocean circulation has been proposed as a promoter of Antarctic Glaciation together with declining CO_2 (Bijl et al., 2013; Bjornsson and Toggweiler, 2001; DeConto and Pollard, 2003; Huber and Nof, 2006; Nong et al., 2000).

One of the challenges of modelling ocean circulation and climate is defined by the large uncertainties in climatic boundary conditions like atmospheric CO_2 and the exact timing of the opening and the respective paleodepth of oceanic gateways. Particularly during the middle Eocene these uncertainties are large, as this interval is characterized by a shallow and variable carbonate compensation depth (Pälike et al., 2012), preventing the deposition of carbonate-rich, high-resolution sedimentary sections. The sedimentary record obtained by scientific ocean drilling is incomplete in both, time resolution and global distribution compared to other time slices of the Cenozoic. After more than three decades of discussion about the timing of the onset of the modern style bimodal regime with deep-water formation in the North Atlantic and the Southern Ocean (Berggren and Hollister, 1977; Davies et al., 2001; Stoker et al., 2005; Via and Thomas, 2006), more and more evidence is accumulating for an early-middle Eocene initiation of NCW formation. Hohbein et al. (2012) and Boyle et al. (2017) dated the onset of NCW formation close to the early-middle Eocene boundary based on seismic interpretation of the Judd Fall Drifts in the Faeroe-Shetland Basin and the Newfoundland contourite drifts drilled during IODP Expedition 342. Geochemical data from a middle Eocene section of Site U1410 (as discussed in Chapter 3) showed that NCW formation was active by 46 Ma, and modulated on obliquity timescales. Distinct climatic and tectonic changes occurred coinciding with the onset of NCW at ~48 Ma. These include the decline of atmospheric CO_2, likely through the deposition of large amounts of carbon in the Arctic, as well as the opening of the Greenland-Norwegian Sea

and the subsidence of the Greenland-Scotland Ridge. However, the exact timing, the sequence of these events and their relative importance for the onset of NCW is still poorly understood.
In this study, we use the fully coupled Earth System Model *COSMOS* to assess the sensitivity of Earth's climate system to changes in atmospheric CO_2 and different configurations of ocean gateways during the early-middle Eocene. In this way, we evaluate the importance of these individual events that happened at the early-middle Eocene boundary and to test the sensitivity of the ocean circulation to the configurations of additional gateways such as the Greenland-Norwegian Sea - Arctic and western Tethys - Atlantic connection. These simulations thus provide in-depth insights into particular role of mechanisms that played a crucial role in the initiation of NCW at the early-middle Eocene boundary or shortly thereafter.

4.2 Model and Experiment Design

We use the Community Earth System Model (*COSMOS*) in the coupled atmosphere-ocean configuration with prescribed vegetation. The model setup includes the atmosphere component ECHAM5 at T31/L19 resolution, i.e. a horizontal resolution of ~3.75° with nineteen vertical layers. A detailed description of the ECHAM5 model is given by Roeckner et al. (2003). The Max Planck Institute Ocean Model (MPI-OM) runs in a GR30/L40 configuration with an average horizontal resolution of 3° x 1.8° and 40 unevenly-spaced vertical layers (Marsland et al., 2003) and includes a dynamic-thermodynamic sea ice model after (Hibler III, 1979) that simulates the distribution and thickness of sea ice considering surrounding climatic conditions, while overturning by convection is implemented via increased vertical diffusion (Jungclaus et al., 2006). The boundary conditions (Stepanek and Lohmann, 2012) to run the model include the prescription of vegetation distribution (Sewall et al., 2007), the set-up of the hydrological discharge model (Hagemann and Dümenil, 1997), orography related parameters for the gravity wave drag parameterization (Lott and Miller, 1997), glacier mask, the concentration of the greenhouse gases in the atmosphere and orbital parameters. The solar constant was reduced by 0.6 % compared to present-day and equals 1358.8 W/m^2. As obliquity minimum is the favorable astronomical configuration for NCW formation (as discussed in Chapter 3), we set obliquity to 22.1°, while using present-day eccentricity and precession values. We prescribed no ice sheets in either hemisphere. The *COSMOS* model has been extensively used and validated by paleoclimatological studies of glacial (Werner et al., 2016; Zhang et al., 2014), interglacial (Lohmann et al., 2013; Pfeiffer and Lohmann, 2016), Miocene climates (Knorr et al., 2011; Knorr and Lohmann, 2014), and ocean circulation (Stärz et al., 2017). We use a paleogeography compiled by the GETECH for the Ypresian (Lunt et al., 2016) for our middle Eocene simulations, which has been modified by closing the proto-Gibraltar Strait.
This paleogeography has been used to evaluate the influence of obliquity on North Atlantic

deep-water formation in Chapter 3. Details of the paleogeography are given in Table 4.1 and Figure 4.1.

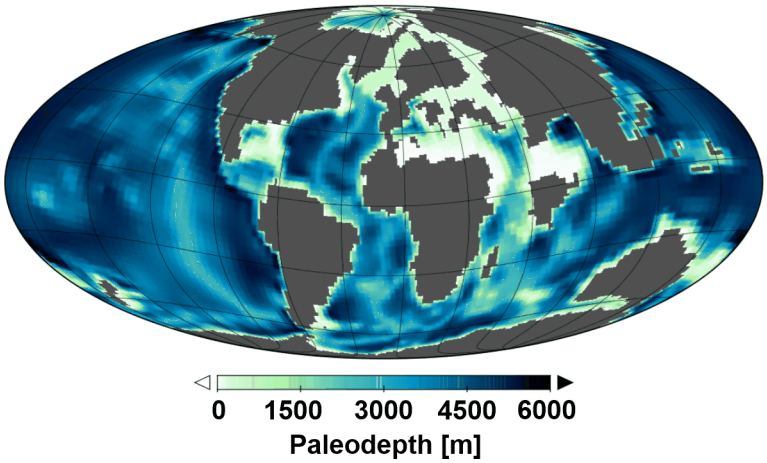

Figure 4.1: Global paleogeography of the middle Eocene as used for the base configuration and the CO_2 sensitivity study. Depth of gateways are given in for this base paleogeography and adjustments are given in Table 1 and illustrated in Figure 4.2-4.4.

4.2.1 Early-Middle Eocene Atmospheric CO_2

Long-term Cenozoic CO_2 concentrations peaked during the Early Eocene Climatic Optimum (52-50 Ma). Estimates for the early Eocene have been made primarily based on paleosols (e.g. Cerling, 1992; Hyland and Sheldon, 2013; Royer et al., 2001), leaf stomata (Beerling et al., 2009; Greenwood et al., 2003; Royer et al., 2003; Smith et al., 2010), marine boron isotopes (Anagnostou et al., 2016; Pearson and Palmer, 1999; Pearson and Palmer, 2000) and nahcolite minerals (Jagniecki et al., 2015; Lowenstein and Demicco, 2006). All these proxies are characterized by uncertainties based on various assumptions and calibrations in order to arrive at realistic atmospheric CO_2 estimates and have their respective advantages and shortcomings (Royer, 2014). For some of these proxies, estimates have been updated (Franks et al., 2014; Greenwood et al., 2003; Hyland and Sheldon, 2013; Smith et al., 2010) and now estimates for the early and middle Eocene atmospheric CO_2 concentrations range from 680-1260 ppm (Anagnostou et al., 2016; Breecker et al., 2010; Franks et al., 2014; Jagniecki et al., 2015).

In the Arctic, high concentrations of the floating fern *Azolla* have been found in 49 Myr old sediments from the early Eocene (Backman et al., 2006; Brinkhuis et al., 2006). The burial of vast amounts of organic carbon during this so-called 1.2 Myr long *Azolla* phase coincides with the onset of Cenozoic cooling (Backman et al., 2008). For this reason, the Arctic *Azolla* phase has been invoked for a crucial role in the Cenozoic cooling during the middle Eocene. Based on flux calculations on sediments from the *Azolla* phase Speelman et al. (2009) estimated 55-470

ppm of CO_2 to be removed from the atmosphere during this 1.2 Myr long interval. This study is designed to get insights into the effects of the drawdown of CO_2 that occurred during the middle Eocene. To do so, we use our base paleogeography with 840 and 1000 ppm atmospheric CO_2, respectively (Table 1, "CO_2-1000"). The drawdown of 160 ppm is a rather conservative estimate of the ~55-470 ppm minimum and maximum amount of atmospheric CO_2 removed from the atmosphere during the 1.2 Myr long *Azolla* phase starting ~49 Ma.

4.2.2 Greenland-Scotland Ridge

The sill depth of the Greenland-Scotland Ridge directly controls both, the inflow of saline North Atlantic surface water into the Greenland-Norwegian Sea and the deep-water overflow capacity across the ridge from the Nordic Seas that is the source for lower North Atlantic Deep Water (NADW) (Dickson and Brown, 1994; Hansen and Østerhus, 2000). It is thus recognized as a critical gateway affecting Cenozoic deep-water circulation patterns and climate change. Today, the deepest part is the Faroe-Shetland Channel forms the deepest part of the GSR with ~1000 m sill depth, whereas most parts are shallower than 500 m. Subsidence history of the Greenland-Scotland Ridge is complicated and simple thermal subsidence models cannot be applied to the region (Talwani and Eldholm, 1977; Thiede and Eldholm, 1983; Vogt, 1972). Large parts of the Greenland-Scotland Ridge were relatively shallow until the end of the Eocene and have been an obstacle for deep water overflow until 35 Ma (Davies et al., 2001). However, the northern Faeroe-Shetland Basin lay in deep water from the Paleocene onward (Robinson, 2004) and was characterized by a stable, southwest deep water flow by ca. 49 Ma and throughout the middle Eocene. The initiation of overflow here is attested by the Judd Fall Drifts (Hohbein et al., 2012) and later the Southeast Faroe Drifts (Davies et al., 2001). Using the Earth System Model *COSMOS*, Stärz et al. (2017) found a critical sill depth of only 30-80 mbsl for the Greenland-Scotland Ridge to force major reorganizations in the bidirectional seaway circulation. This finding signifies that NCW formation and overflow from the Nordic Seas to the Atlantic can occur at relatively shallow paleodepth of the Greenland-Scotland Ridge.

In addition to our "base" paleogeography we use two setups in which we set the sill depth of the Greenland-Scotland Ridge to 200 m and 50 m, respectively (Table 4.1 and Figure 4.2, "GSR200 and "GSR50"). These experiments are designed to simulate the subsidence of the GSR and to approach the threshold in the GSR sill depth for the onset of NCW formation.

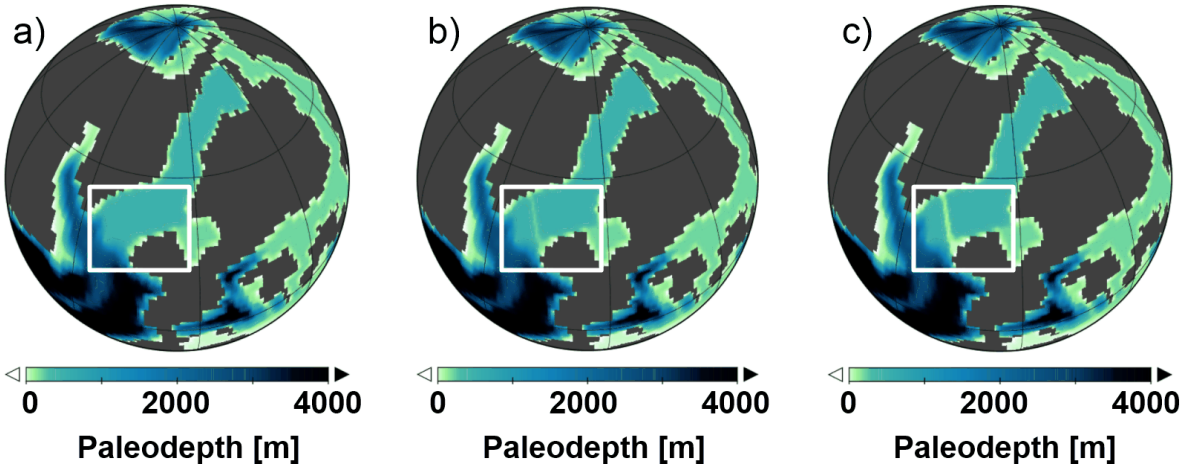

Figure 4.2: Paleogeography of the Greenland-Scotland Ridge sill depth sensitivity simulations of the sensitivity a) Greenland-Scotland Ridge sill depth 500 m, b) Greenland-Scotland Ridge sill depth 200 m and c) Greenland-Scotland Ridge sill depth 50 m.

4.2.3 Arctic Seaway

Since the early Miocene, the Fram Strait connects the Arctic with the North Atlantic via the Greenland-Norwegian Sea (Jakobsson et al., 2007). It is the only deep-water connection between the Arctic and adjacent ocean basins. From its formation in the early Cretaceous until the opening of the Fram Strait however, the Arctic Ocean was a largely landlocked basin with limited, periodic shallow water connections to the global oceans (Jakobsson et al., 2007). During the early-middle Eocene low salinities in the Arctic during the *Azolla* phase supports that oceanic exchange between the Arctic Ocean and adjacent seas was inhibited (Brinkhuis et al., 2006). Freshening of a landlocked Arctic would be compensated by salinity increase in the North Atlantic, which in turn enhances NCW formation (Roberts et al., 2009). The termination of *Azolla* at ~48 Ma in the Arctic and the coinciding positive temperature and salinity anomaly could on the other hand be related to an overspill of warm salty waters from adjacent seas into the Arctic (Brinkhuis et al., 2006). Therefore, it cannot be excluded that a very narrow and shallow connection between the Arctic and the Greenland-Norwegian Sea has periodically existed during the Eocene.

We adjust our base paleogeography by opening a seaway between the Arctic and the Greenland-Scotland Ridge at the maximum depth of the shelf (200 m) (Table 4.1 and Figure 4.3, “Arctic seaway”). In this simulation, we closed the connection between the Turgai Strait and the Arctic. This setup reflects a possible scenario of inflow of saline North Atlantic surface waters as invoked for the termination of *Azolla* at ~48.5 Ma (Brinkhuis et al., 2006).

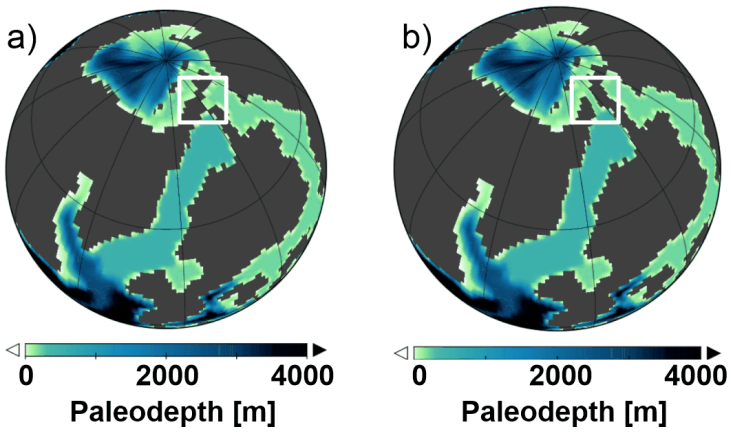

Figure 4.3: Paleogeography of the Arctic seaway sensitivity simulations. a) no connection between the Arctic and the Greenland-Norwegian Sea, b) connection of the Arctic to the Greenland-Norwegian Sea at a of depth 200 m**.**

4.2.4 Tethyan-Atlantic Seaway

During the Late Cretaceous and Paleogene, northward movement and rotation of Africa continued to close the Tethys Sea in the east. In the west, right-lateral motion between Africa and Europe narrowed the western junction of the Tethys with the Atlantic between Spain and Morocco. In the middle Eocene, the Tethyan likely was already separated in the Neo-Tethys in the East and the Alpine Tethys in the west (Schettino and Turco, 2011) with only shallow shelf connections between the two. The Alpine Tethys in the West was a much smaller, narrow, elongated and mostly shallow ocean basin compared to the modern Mediterranean. The depth and flow capacity through the seaway between Africa in the South and Iberia in the North are poorly constrained. Plate reconstructions range from a relatively shallow water connection to a deep-water connection that would allow large scale exchange of deep water (Schettino and Turco, 2011; Stampfli and Hochard, 2009).

In the modern Atlantic, saline Mediterranean Outflow Water contributes to the formation of dense waters and thus enhances the Atlantic Meridional overturning circulation and deep-water formation in the North Atlantic (Bethoux and Gentili, 1999; Rahmstorf, 1998). Many other studies have shown the reinforcing effect of salty Mediterranean Outflow Water on the Atlantic Meridional Overturning Circulation from the Pliocene to the Holocene (Hernández-Molina et al., 2006; Loubere, 1987; Maldonado and Nelson, 1999; Schönfeld and Zahn, 2000; Stumpf et al., 2010). On the other hand, very little is known about the history of Mediterranean Outflow Water prior to the Messinian Salinity Crisis in the Miocene, when the connection between North Atlantic and Mediterranean temporarily ceased. Hamon et al. (2013) demonstrated in a modeling study, that when the Tethys seaway towards the Indian Ocean is closed as during the middle Eocene, the warm and salty water from the proto-Mediterranean Basin is transported into the Atlantic Ocean through the proto-Gibraltar Strait, enhancing the AMOC. On the other

hand, their results also indicate the salinities in the Tethys are lower compared to the subtropical North Atlantic when the Tethyan seaway allows throughflow from the Indian to the Atlantic Ocean. Consequently, their results suggest, that the effect of Tethyan outflow depends on the restriction of the seaway between the Indian Ocean and the Tethys.

We employ a setup that is used to explore the impact of Tethyan saline waters on the early Atlantic Meridional Overturning Circulation. For this purpose, we use the base configuration, but open a seaway between the subtropical North Atlantic and the Tethys ("Tethyan seaway") at 1800 m (Table 4.1 and Figure 4.4).

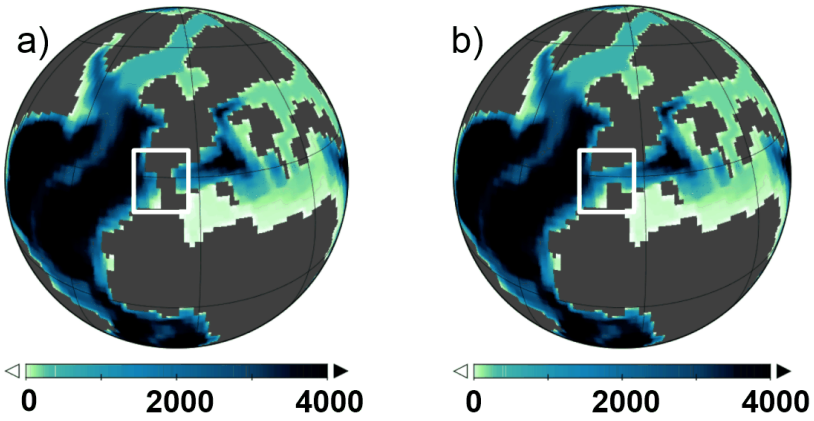

Figure 4.4: Paleogeography of the Tethys seaway sensitivity simulations. a) No connection between the Tethys and the subtropical North Atlantic b) Deep-water connection at 1800 m depths between the Tethys and the subtropical North Atlantic.

For all tectonic gateway simulations, the CO_2 level was set to 3 x pre-industrial level (840 ppm), while other greenhouse gases were set to present day values. The base experiment was simulated to year 7000. All other experiments (tectonic gateways) were restarted from the base configuration year 6200 and were simulated to year 7000. The exception is the simulation CO_2-1000 that was simulated to year 8000 to allow more time to reach equilibrium. The last 100 years of each experiment were used for our analysis.

Table 4.1: Boundary conditions for Paleoceanographies

	base	GSR200	GSR50	Arctic seaway	Tethyan seaway	CO_2-1000
Greenland-Norwegian Sea [m]	500	500	500	500	500	500
Greenland-Scotland Ridge [m]	500	200	50	500	500	500
Arctic seaway [m]	closed	closed	closed	200	closed	closed
Tethyan seaway [m]	closed	closed	closed	closed	1800	closed
CO_2 atm. [ppm]	840	840	840	840	840	1000

4.3 Results and Discussion

In all simulations, deep-water formation is a strongly seasonal process and occurs generally in the respective winter hemisphere. In all our simulations except the “GSR50” and “Arctic seaway”, the Northern Hemisphere overturning is the dominant source of deep waters.

For our “base” configuration we simulate global mean sea surface temperatures of 28 °C ranging between 1.1 °C in the Arctic and 38.5 °C in the around the equator. Deep-ocean temperatures at 3000 m water depth are 14.1 °C on average, 13.5 °C in the Pacific and 15 °C in the Atlantic. These deep-ocean temperatures are on the higher end of the 11-16°C reconstructed between 50-45 Ma (Zachos et al., 2001) and thus reflect the situation in the early middle Eocene, close to the onset of NCW at ~48 Ma.

4.3.1 CO_2 Drawdown

As a result of diminishing atmospheric CO_2 by 160 ppm from 1000 to 840 ppm, global annual mean sea surface temperatures in our simulation decrease by 1.9 °C. Temperatures drop relatively uniform around the globe. Thus, the meridional temperature gradient does not significantly increase (+0.1 °C) due to a 160 ppm drawdown in CO_2. During the winter season, when overturning occurs, the cooling due to the CO_2 drawdown is more pronounced north of 60°N (up to 3 °C) than further south (less than 2 °C) in the Greenland-Norwegian Sea (Figure 4.5 a & b).

Annual sea surface salinity on the other hand increases in most of the global ocean, except for the tropical Atlantic. In particular, the Arctic, the Southern Ocean and the Tethys gain more salinity than the rest of the global ocean. In the Greenland-Norwegian Sea a moderate salinity increase of ~0.4 psu is equal to the global average (Figure 4.5 c & d).

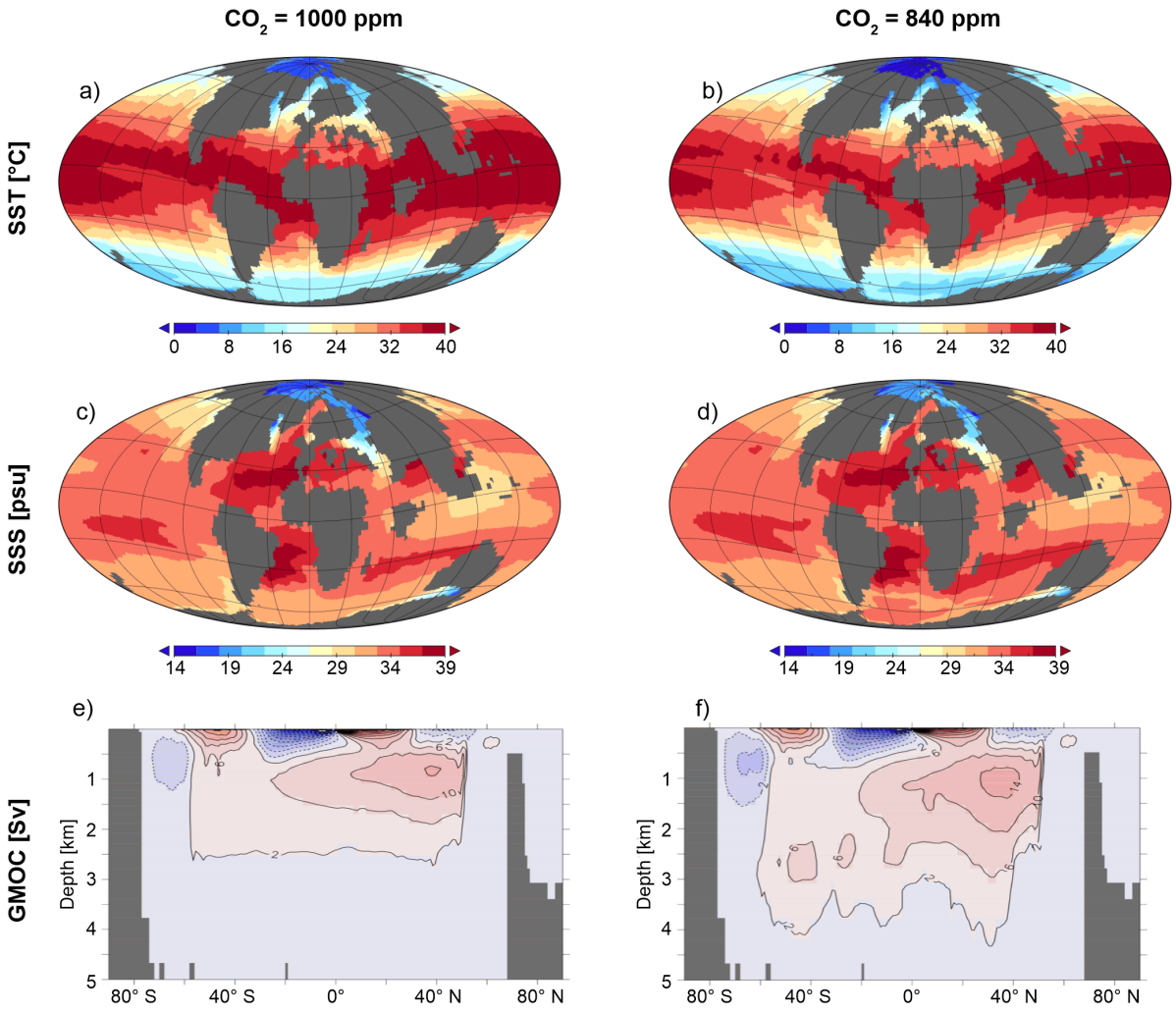

Figure 4.5: Annual Sea Surface Temperature (SST), Sea Surface Salinity (SSS) and Global Meridional Overturning Circulation (GMOC) for the middle Eocene simulations with different atmospheric CO_2 concentrations. a) SST for CO_{2atm}=1000ppm, b) SST for CO_{2atm}=840ppm, c) SSS for CO_{2atm}=1000ppm, d) SSS for CO_{2atm}=840ppm, e) GMOC for CO_{2atm}=1000ppm, f) GMOC for CO_{2atm}=840ppm

As a result of these changes in surface water temperature and salinity, the sea surface density increases in Greenland-Norwegian Sea by ~0.7 kg/m^3 in the simulation with the lower CO_2 level (Figure 4.6a). South of 60°N in the Greenland-Norwegian Sea, the density gradient between the surface water and underlying water masses is nullified, enabling convection, as this is the primary location of vertical mixing in our simulations. The prominent role of this region is supported by the location of the mixed layer depth (Figure 4.6). The mixed layer depth is the depth where the temperature or density of the water differs by a more than a predefined value from the surface ocean temperature or density (Kara et al., 2000) and is therefore greatest in locations where stratification of the water column is broken by overturning (Schmittner, 2005) and surface waters sink to depth. The sinking of dense surface waters intensifies meridional

overturning in the North Atlantic and increases the maximum depth reached by NCW from ~2500 m up to 4500 m (Figure 4.5 e & f).

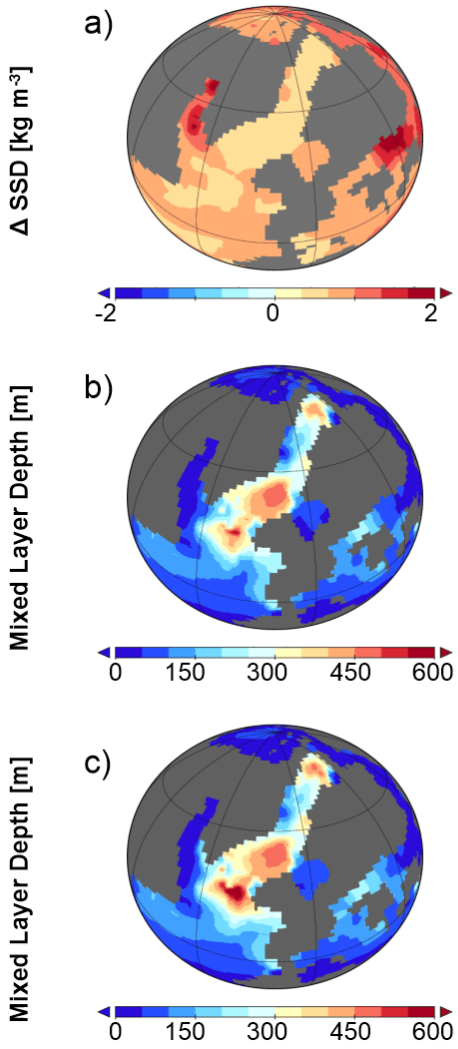

Figure 4.6: Surface ocean properties in the Greenland-Norwegian Sea in response to changes in atmospheric CO_2. a) ΔSea Surface Density (SSD) CO_{2atm} 840-1000 ppm, b) mixed layer depth CO_{2atm}=1000ppm, c) mixed layer depth CO_{2atm}=840ppm.

The onset of overflow of deep-water from the Greenland-Norwegian Sea to the North Atlantic has been dated to 51.5-48.5 Ma (Hohbein et al., 2012).

We ran simulations with two different atmospheric CO_2 concentrations, representing the conditions before and after the *Azolla* phase, which removed a considerable amount of CO_2 from the atmosphere. Our simulation with high CO_2 ("CO_2-1000") is characterized by high Arctic SST, low cloud cover, and low salinity. These conditions are favourable for the growth of *Azolla*, even though salinity in our simulations does not reach values low enough to sustain *Azolla* growth. In the geologic record, the *Azolla* phase occurs just prior to the onset of NCW, which points to the hypothesis that the *Azolla* triggered CO_2 drawdown is the direct cause for this

change in ocean circulation. Our simulations confirm the mechanistic link between a moderate CO_2 drawdown and the intensity of the AMOC. A conservative estimate of a drawdown of 160 ppm from 1000 ppm to 840 ppm already acts substantially reinforcing towards NCW formation and considerably changes in the geometry and maximum depth of North Atlantic overturning. The close timing and the large uncertainties about the exact timing do not allow to rule out a mechanistic link between sinking atmospheric CO_2 and the onset of a NCW. Given that the threshold depth of the Greenland-Scotland Ridge allowed for sufficient water exchange at that, more effective winter cooling of surface waters in the Greenland-Norwegian Sea could have facilitated NCW formation. Other mechanisms including enhanced continental weathering, decreased CO_2 outgassing and the invigoration of ocean circulation due to further subsidence of the Greenland-Scotland Ridge would have further been influential towards enhancing NCW formation and the Cenozoic global cooling.

It is important to note, that *COSMOS* does not include carbon cycle modelling. We can therefore not constrain carbon cycle feedbacks resulting from the invigoration of NCW. Studies of future climate change (Köhler et al., 2005; Schmittner et al., 2007; Zickfeld et al., 2008) found an ~20-40 ppm increase in atmospheric CO_2 on centennial to millennial timescales following a freshwater-induced AMOC shutdown. Other carbon cycle feedbacks, in particular the increase in ocean uptake due to decreasing temperatures by increased CO_2 solubility (Klepper and de Haan, 1995; Maier-Reimer et al., 1996; Sarmiento et al., 1998; Sarmiento and Le Quere, 1996) could provide further positive feedbacks of up to 200 ppm CO_2 decrease on initial decrease in atmospheric CO_2 (Plattner et al., 2001). An initial CO_2 drawdown due to burial of organic carbon and resulting oceanic carbon cycle feedbacks thus have the potential to account for a significant part of the CO_2 drawdown and global cooling between the early Eocene and the Eocene-Oligocene boundary.

4.3.2 Greenland-Scotland Ridge

The sill depth in our experiments influences surface water salinity, temperature and density by regulating the inflow of warm, salty Atlantic surface waters into the Greenland-Norwegian Sea. As a result of the Greenland-Scotland Ridge subsidence, minimal annual temperatures in the Greenland-Norwegian Sea increase by ~1 °C between 50 and 200 m sill depth and by an additional 5 °C between 200-500 m sill depth (Figure 4.7 a,b,c). Due the subsidence of the Greenland-Scotland Ridge also leads to increasing annual salinity in the Greenland-Norwegian Sea. For a subsidence from 50 to 200 m salinity increases by ~8 psu. A further subsidence to 500 m sill depth leads to an additional increase of 3 psu salinity (Figure 4.7 d,e,f). Resulting from these changes in temperature and salinity, sea surface density increases with the sill depth of the Greenland-Scotland Ridge. In particular, between 50 and 200 m sill depth, a rapid gain in

surface density of up to 6 kg/m^3 is observed in the Greenland-Norwegian Sea, suggesting a threshold of surface water flow above 50 m sill depth (Figure 4.7 h). When this threshold is exceeded, surface water density allows for breaching the stratification between surface water and intermediate water in the Greenland-Norwegian Sea. This finding is in line with an estimated threshold of 30-80 m in the Greenland-Scotland Ridge sill depth (Stärz et al., 2017) and further delimit the threshold to be greater than 50 m. Interestingly, NCW formation takes place in the North Atlantic, just south of the Greenland-Scotland Ridge, when the sill depth is limited to 200 m. Further deepening of the sill to 500 m only leads to an additional increase of surface density by <2 kg/m^3 (Figure 4.7 i). However, the Atlantic Meridional Overturning Circulation is largely invigorated and NCW is occurring in the Greenland-Norwegian Sea and Nordic Overflow Water is transported deeper (Figure 4.7 j,k,l).

A bipolar seesaw with Northern Hemisphere warming on account of the Southern Hemisphere is initiated, as the surface branch of the Atlantic Meridional Overturning Circulation starts to transport heat towards the North Atlantic with increasing sill depth of the Greenland-Scotland Ridge. Global sea surface temperatures decrease by 0.4 °C as more heat is transported towards the deep ocean when the sill depth of the Greenland-Scotland Ridge allows for NCW formation. With the onset of NCW heat is transported from the upper ocean layer of the ocean (~0-2000 m) to greater depth (~2000-4000 m). Deep-water temperatures are increased due to the onset and invigoration of AMOC, however the amount of warming is about one magnitude smaller compared to our CO_2 sensitivity experiment (160 ppm CO_2 drawdown). Changes in deep-sea temperature due to the onset of NCW are <0.2 °C and thus too small to reliably detect with paleotemperature proxies. The subsidence of the Greenland-Scotland Ridge has the strongest impact on AMOC by governing the temperature and salinity of the GNS surface water and the overflow capacity of NCW into the Atlantic.

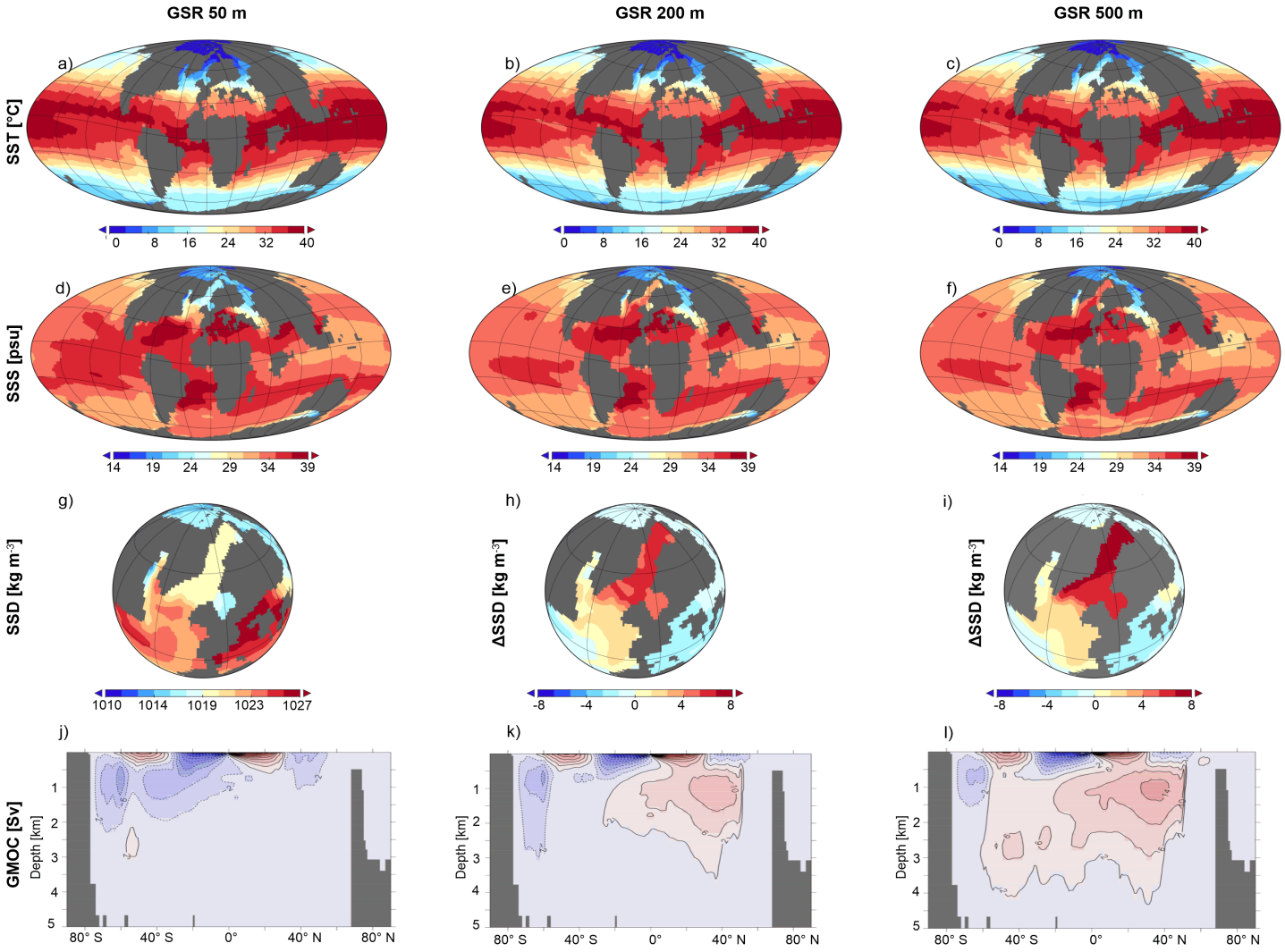

Figure 4.7: Surface ocean properties and Global Meridional Overturning Circulation (GMOC for the Greenland-Scotland Ridge (GSR) sensitivity simulations. a) Sea surface temperature (SST) at GSR sill depth 50 m, b) SST GSR sill depth 200 m, c) SST GSR sill depth 500 m, d) Sea surface salinity (SSS) GSR sill depth 50 m, e) SSS GSR sill depth 200 m, f) SSS GSR sill depth 500 m, g) ΔSSD GSR sill depth 50 m, h) ΔSSD GSR sill depth 200m - 50 m, i) ΔSSD GSR sill depth 500m - 50 m j) GMOC GSR sill depth 50 m k) GMOC GSR sill depth 200 m, l) GMOC GSR sill depth 500 m. Panels a)-f) and j)-l) show annual means, while g)-i) represent northern hemisphere winter (DJF) mean values.

4.3.3 Arctic Seaway

Sea surface temperatures in the Greenland-Norwegian Sea cool by up to 12 °C when a shallow seaway to the Arctic is opened (Figure 4.8a). In the simulated scenario of an open Arctic Seaway, the Arctic is gaining up to 4 psu salinity, while salinity drops by about 10 psu in the northern Greenland-Norwegian Sea and up to 6 psu in the southern Greenland-Norwegian Sea (Figure 4.8b). Even the shallow simulated Arctic Seaway lowers the surface density considerably (Figure 4.8c) and results in a density gradient between the surface water and underlying water layers that prevents convection (Figure 4.9).

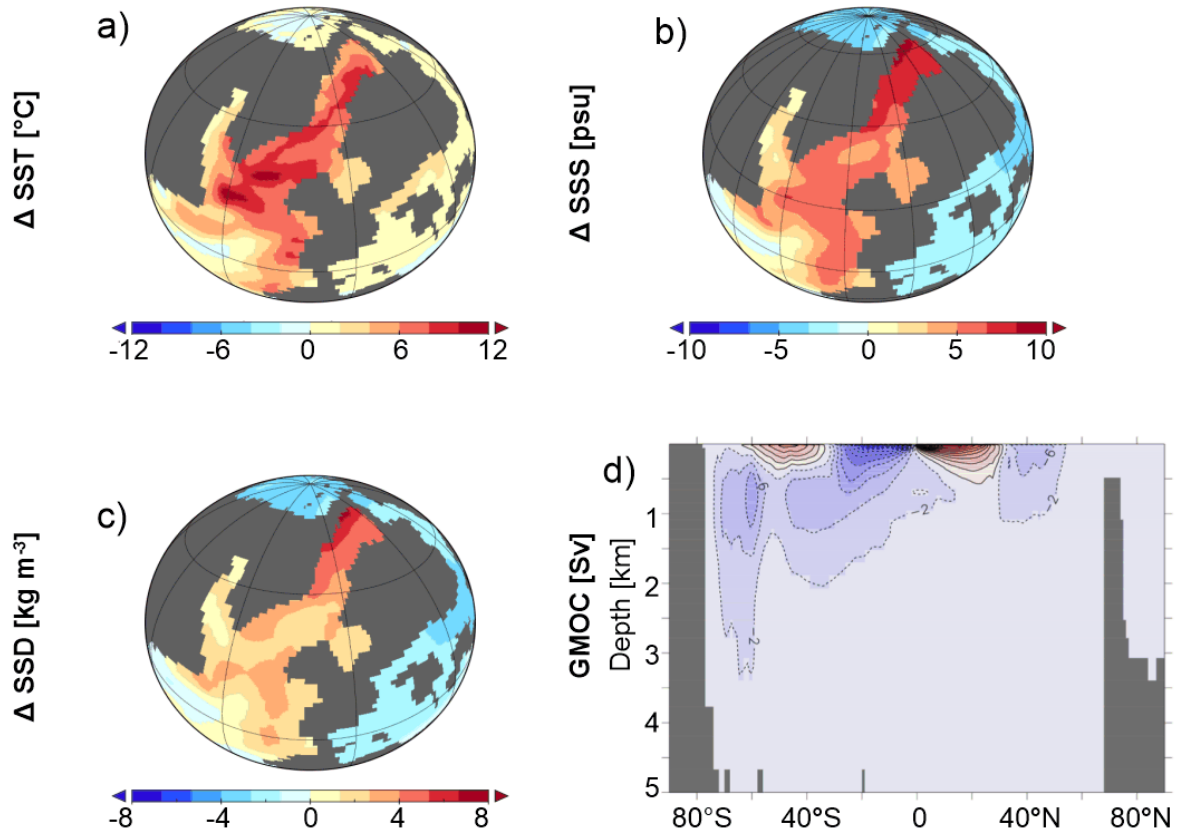

Figure 4.8: Difference in surface ocean properties (base-Arctic seaway open) and global meridional overturning for the Arctic seaway open scenario. a) ΔSea Surface Temperature (SST), b) ΔSea Surface Salinity (SSS), c) ΔSea Surface Density (SSD) d) Global Meridional Overturning Circulation (GMOC) a-c) represent northern hemisphere winter (DJF) mean values, d) shows the annual mean

In the Southern Ocean, convection is strengthened by the open seaway between the Arctic and the North Atlantic (Figure 4.8d). This exemplifies how high latitude climate signals can be introduced into the other hemisphere by ocean circulation. Our results suggest that not even a shallow connection between the Greenland-Norwegian Sea and the Arctic existed during the early-middle Eocene boundary. This is in agreement with conclusions from previous simulations (Roberts et al., 2009).

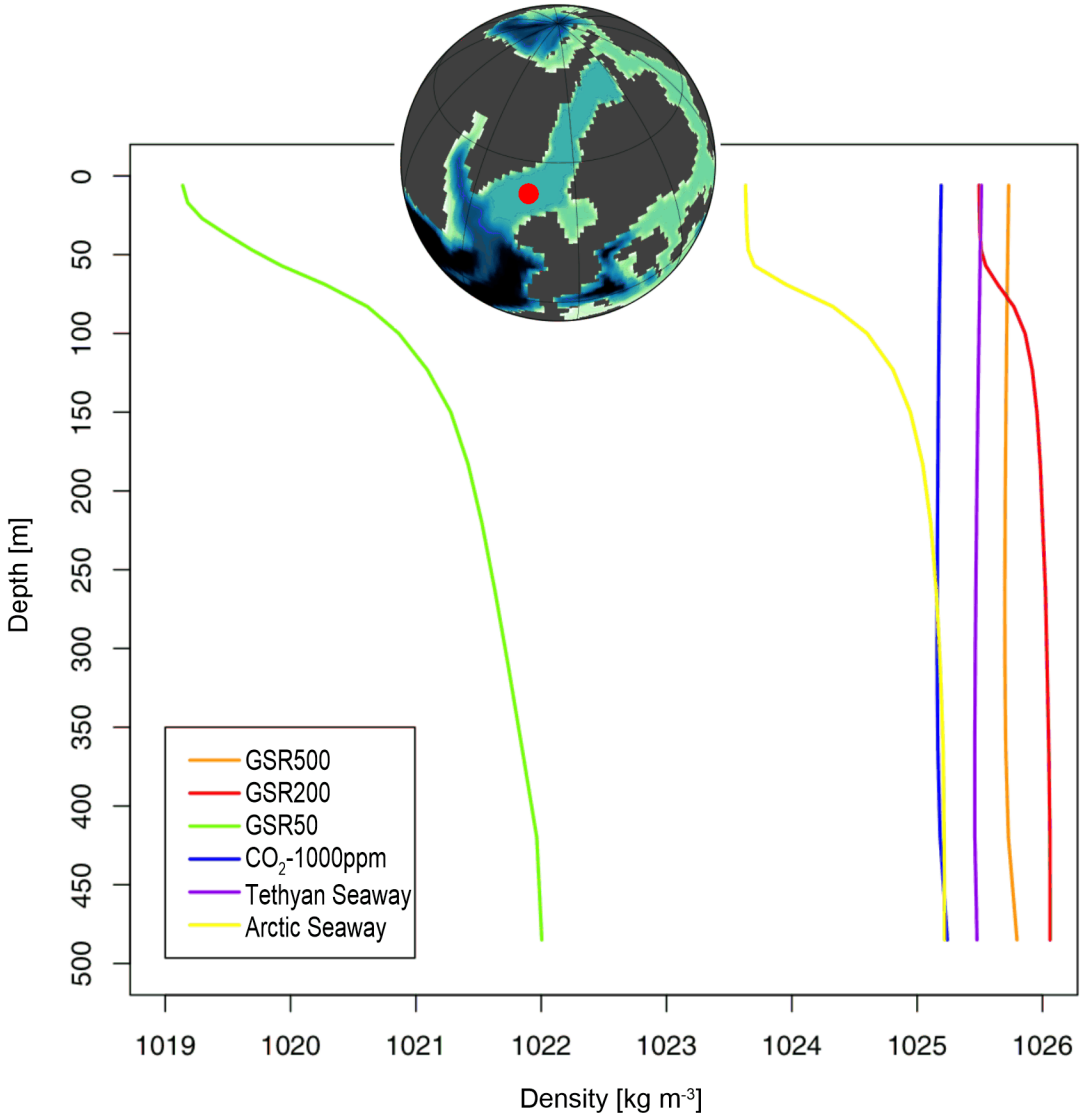

Figure 4.9: Density profiles of the southern Greenland-Norwegian Sea in the different simulations Coloured lines indicate the density vs. depth for the six different simulations. The red dot in the map marks the location of the profiles.

4.3.4 Tethys-Atlantic Seaway

The opening of a seaway between the Tethys and the subtropical Atlantic allows for a circumglobal surface flow from the Indian Ocean via the Tethyan Seaway into the subtropical North Atlantic and via the Central American Seaway into the Pacific. As an enclosed basin in a high evaporation, low precipitation zone, the Tethys accumulates high salinity. Opening of the Tethys seaway on the other hand leads to the throughflow of less saline tropical Indian Ocean waters into the Atlantic Ocean (Figure 4.10b). While parts of the surface water pass through the Central American Seaway into the Pacific, another branch invigorates the Gulf Stream and which in turn transports more warm, saline waters into the Greenland-Norwegian Sea compared to a scenario with a closed Tethys-Atlantic seaway. Here, salinity and temperature are

enhanced due to the opening. Curiously, the southward flow of NCW is enhanced above and weakened below 2000 m water depth. Altogether, under Eocene boundary conditions, the Tethyan seaway does not play an important role for the formation of NCW, even though it alters the conditions in the Greenland-Norwegian Sea. The depth and shape of the North Atlantic overturning cell remains stable in both experiments and weakens slightly in response to the opening of a Tethys-Atlantic seaway. However, as mentioned earlier, the response of the AMOC to Tethys outflow depends on the properties of Tethyan waters. These in turn are altered by the depth of the gateways between the Tethys and the adjacent Indian and Atlantic Oceans (Butzin et al., 2011; Hamon et al., 2013). With the narrowing between Tethys and Indian Ocean, the role of Tethyan waters switch from hampering to enforcing with respect to NCW formation as the Tethyan outflow becomes more saline.

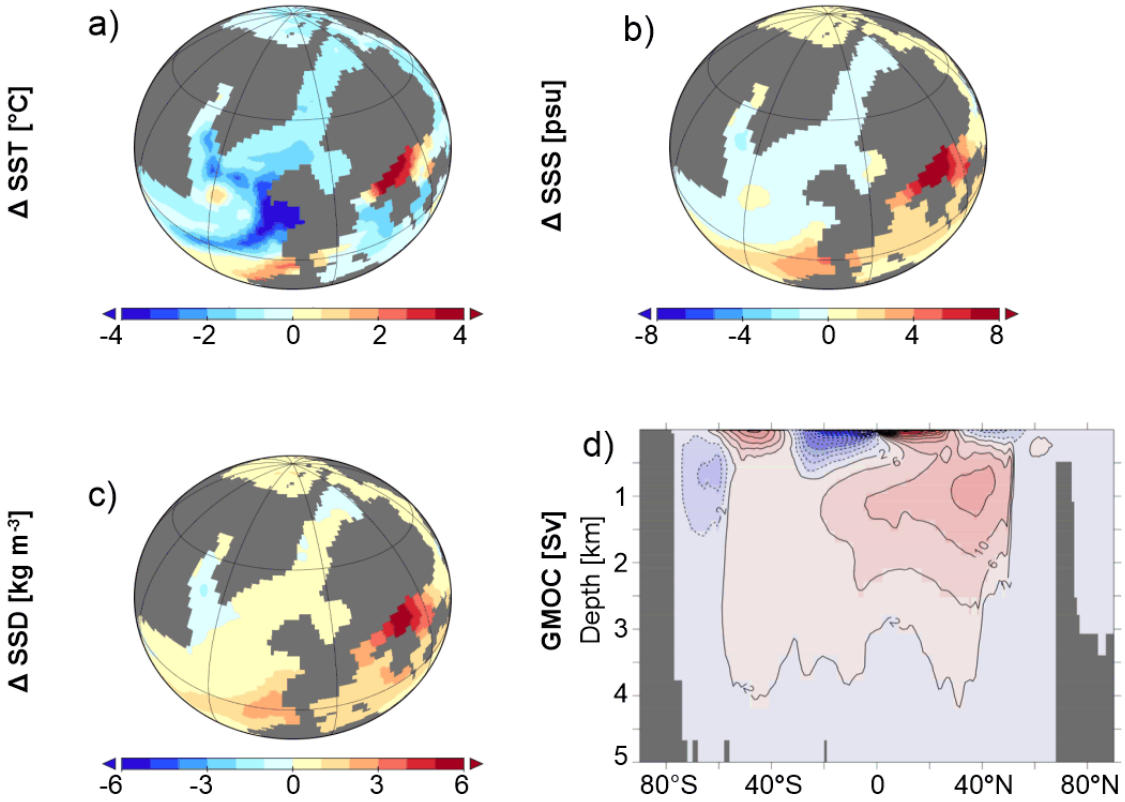

Figure 4.10: Difference in surface ocean properties (base-Tethys seaway open) and global meridional overturning for the Tethys seaway open scenario. a) ΔSea Surface Temperature (SST), b) ΔSea Surface Salinity (SSS), c) ΔSea Surface Density (SSD) d) Global Meridional Overturning Circulation (GMOC).

4.4 CO_2 or Gateways?

Our results indicate that both, changes in atmospheric CO_2 and tectonic changes in gateway configuration have favoured the initiation of a North Atlantic deep-water source and thus the invigoration of Atlantic circulation close to the early-middle Eocene boundary (Figure 4.11). Global sea surface cooling in our simulations due to the onset of overturning in the North Atlantic equals roughly one third of the surface cooling due to the drawdown in atmospheric CO_2 from 1000 to 840 ppm. This finding is in agreement with sensitivity studies attributing global climate change to CO_2 instead of changes in ocean circulation (DeConto and Pollard, 2003; Huber et al., 2004; Huber and Nof, 2006; Lunt et al., 2008).

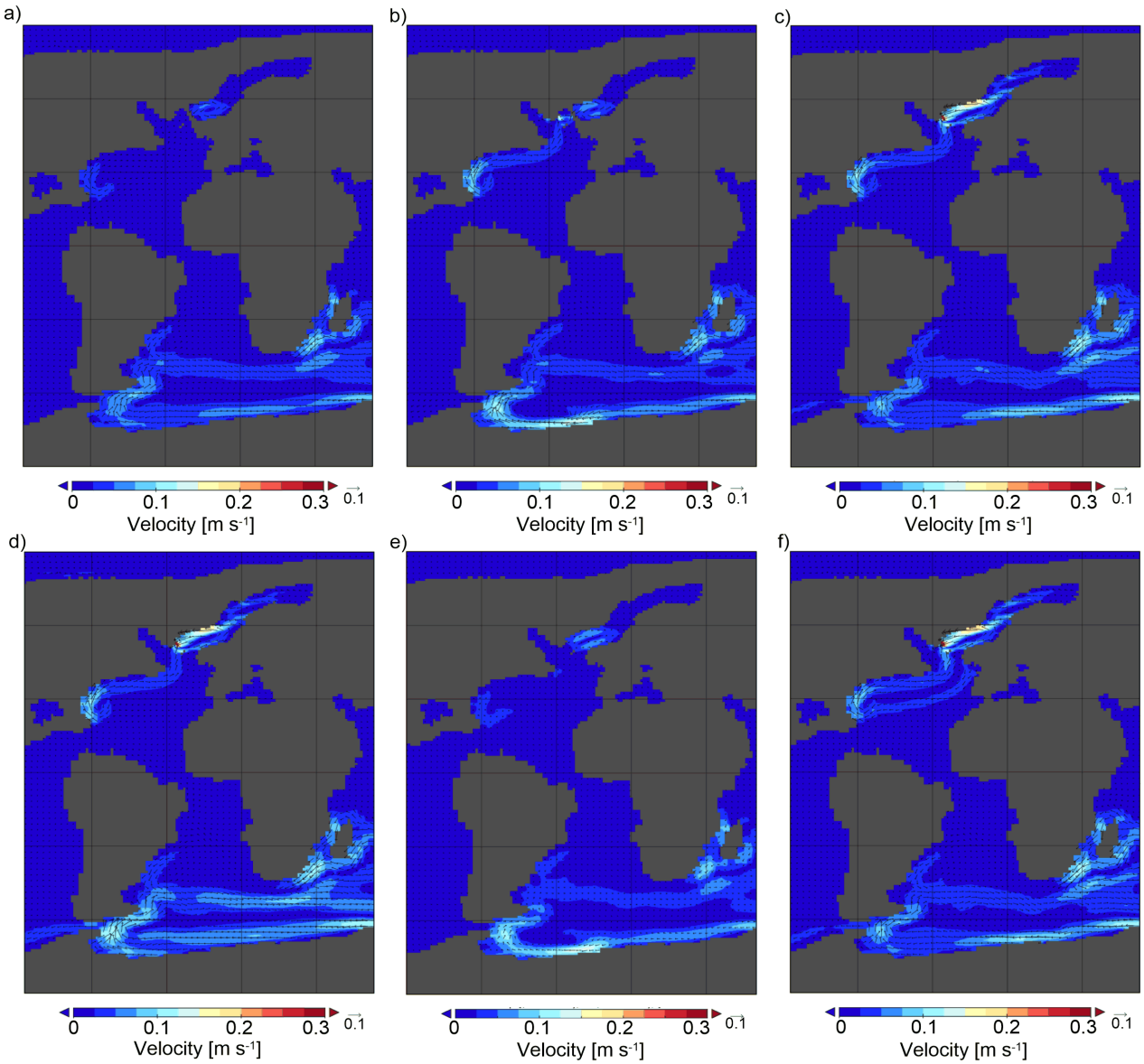

Figure 4.11: Atlantic Ocean circulation velocity at the lowest depth of the Greenland-Norwegian Sea (485 m). a) Greenland-Scotland Ridge (GSR) sill depth 50 m, b) GSR sill depth 200 m, c) base with GSR sill depth 500 m, d) 1000 ppm CO_2atm with GSR sill depth 500 m, e) Arctic seaway open with GSR sill depth 500 m, f) Tethys seaway open with GSR sill depth 500 m.

While atmospheric composition plays a role in the intensity and depth of overturning, the sill depth of the Greenland-Scotland Ridge is the ultimate factor controlling the formation of NCW. In all simulations with a sill depth of 500 m, there is no density stratification in the Southern Greenland-Norwegian Sea, except when the Arctic seaway is open. This highlights the importance of the supply of saline surface waters into the Greenland-Norwegian Sea for the formation of deep-waters.

After NCW initiated through the subsidence of the sill below the discussed threshold, NCW formation intensity was prone to modification by variations in atmospheric CO_2, on-going subsidence of the Greenland-Scotland Ridge and other Atlantic seaways and to orbital forcing.

5. Conclusions

Simulations in the Earth System Model *COSMOS* reveal the effect of changes in atmospheric CO_2 concentration and of various possible characteristic seaway configurations for the middle Eocene on global climate and the early North Atlantic Deep Water formation. Our experiments reveal that the formation of NCW responds sensitively to changes in the atmospheric CO_2 concentration, the sill depth of the Greenland-Scotland Ridge and the potential existence of a shallow water connection between the Greenland-Norwegian Sea and the Arctic. The influence of the inflow of warm saline Tethyan waters on the formation of NCW on the other hand is minor.

Declining CO_2 from 1000 to 840 ppm leads to enhancement and deepening of NCW formation. This scenario reflects the rapid drawdown of CO_2 as it happened at ~49 Ma in response to the Arctic *Azolla* phase. The subsidence of the Greenland-Scotland Ridge is the governing factor for the onset and variability of NCW formation on tectonic timescales as shown by our simulations. A threshold between 50-80 m in the sill depth of the Greenland-Scotland Ridge allows for sufficient inflow of warm, salty surface water from the North Atlantic. The cooling of the salty North Atlantic water increases surface water density and initiates convection in the Greenland-Norwegian Sea. Subsidence of the Greenland-Scotland Ridge below this threshold increases the overflow capacity of NCW in depth and invigorates and deepens the thermohaline circulation substantially. A possible shallow water connection between the Arctic and the Greenland-Norwegian Sea allows for the inflow of low density Arctic waters into the Greenland-Norwegian Sea. The low salinity in the Greenland-Norwegian Sea hampers deep-water formation here and strengthens convection in the Southern Ocean.

Our simulations indicate that overturning most effectively takes place south of 60°N in the Greenland-Norwegian Sea. The thermohaline circulation is strongest and deepest, when sea surface densities are high in this area and positive surface-intermediate water vertical density gradients are achieved here to break the stratification of the water column. The thermohaline

circulation in our simulations transfers heat from the surface ocean (0-1800 m) to the intermediate ocean (1800-2500 m). The effects of the energy transport by the thermohaline circulation on surface and deep-sea temperatures are however minor compared to changes in response to atmospheric CO_2. Further investigations of oceanic carbon cycle feedbacks will be needed to provide further constrains about the role of the ocean during the middle Eocene climatic cooling.

References

Anagnostou, E., John, E. H., Edgar, K. M., Foster, G. L., Ridgwell, A., Inglis, G. N., Pancost, R. D., Lunt, D. J., and Pearson, P. N., 2016, Changing atmospheric CO2 concentration was the primary driver of early Cenozoic climate: Nature, v. 533, no. 7603, p. 380-384.

Backman, J., Jakobsson, M., Frank, M., Sangiorgi, F., Brinkhuis, H., Stickley, C., O'Regan, M., Løvlie, R., Pälike, H., and Spofforth, D., 2008, Age model and core-seismic integration for the Cenozoic Arctic Coring Expedition sediments from the Lomonosov Ridge: Paleoceanography, v. 23, no. 1.

Backman, J., Moran, K., McInroy, D. B., and Mayer, L., 2006, Arctic Coring Expedition (ACEX): Paleoceanographic and Tectonic Evolution of the Central Arctic Ocean.

Beerling, D. J., Fox, A., and Anderson, C. W., 2009, Quantitative uncertainty analyses of ancient atmospheric CO2 estimates from fossil leaves: American Journal of Science, v. 309, no. 9, p. 775-787.

Berggren, W. A., and Hollister, C., 1977, Plate tectonics and paleocirculation—commotion in the ocean: Tectonophysics, v. 38, no. 1, p. 11-48.

Bethoux, J., and Gentili, B., 1999, Functioning of the Mediterranean Sea: past and present changes related to freshwater input and climate changes: Journal of Marine Systems, v. 20, no. 1, p. 33-47.

Bigg, G. R., 2003, The oceans and climate, Cambridge University Press.

Bijl, P. K., Bendle, J. A. P., Bohaty, S. M., Pross, J., Schouten, S., Tauxe, L., Stickley, C. E., McKay, R. M., Röhl, U., Olney, M., Sluijs, A., Escutia, C., Brinkhuis, H., and Scientists, E., 2013, Eocene cooling linked to early flow across the Tasmanian Gateway: Proceedings of the National Academy of Sciences, v. 110, no. 24, p. 9645-9650.

Bjornsson, H., and Toggweiler, J., 2001, The climatic influence of Drake Passage: The Oceans and Rapid Climate Change: Past, Present, and Future, p. 243-259.

Boyle, P. R., Romans, B. W., Tucholke, B. E., Norris, R. D., Swift, S. A., and Sexton, P. F., 2017, Cenozoic North Atlantic deep circulation history recorded in contourite drifts, offshore Newfoundland, Canada: Marine Geology, v. 385, p. 185-203.

Breecker, D., Sharp, Z., and McFadden, L., 2010, Atmospheric CO2 concentrations during ancient greenhouse climates were similar to those predicted for AD 2100: Proceedings of the National Academy of Sciences, v. 107, no. 2, p. 576-580.

Brinkhuis, H., Schouten, S., Collinson, M. E., Sluijs, A., Damsté, J. S. S., Dickens, G. R., Huber, M., Cronin, T. M., Onodera, J., and Takahashi, K., 2006, Episodic fresh surface waters in the Eocene Arctic Ocean: Nature, v. 441, no. 7093, p. 606-609.

Broecker, W. S., The great ocean conveyor, *in* Proceedings AIP Conference Proceedings1992, Volume 247, AIP, p. 129-161.

Broecker, W. S., Peteet, D. M., and Rind, D., 1985, Does the ocean-atmosphere system have more than one stable mode of operation?: Nature, v. 315, no. 6014, p. 21-26.

Burton, K. W., Hong-Fei, L., and O'nions, R. K., 1997, Closure of the Central American Isthmus and its effect on deep-water formation in the North Atlantic: Nature, v. 386, no. 6623, p. 382.

Butzin, M., Lohmann, G., and Bickert, T., 2011, Miocene ocean circulation inferred from marine carbon cycle modeling combined with benthic isotope records: Paleoceanography, v. 26, no. 1.

Cerling, T. E., 1992, Use of carbon isotopes in paleosols as an indicator of the P (CO2) of the paleoatmosphere: Global Biogeochemical Cycles, v. 6, no. 3, p. 307-314.

Davies, R., Cartwright, J., Pike, J., and Line, C., 2001, Early Oligocene initiation of North Atlantic deep water formation: Nature, v. 410, no. 6831, p. 917-920.

DeConto, R. M., and Pollard, D., 2003, Rapid Cenozoic glaciation of Antarctica induced by declining atmospheric CO2: Nature, v. 421, no. 6920, p. 245-249.

Dickson, R. R., and Brown, J., 1994, The production of North Atlantic Deep Water: sources, rates, and pathways: Journal of Geophysical Research: Oceans, v. 99, no. C6, p. 12319-12341.
Fine, R. A., Rhein, M., and Andrié, C., 2002, Using a CFC effective age to estimate propagation and storage of climate anomalies in the deep western North Atlantic Ocean: Geophysical Research Letters, v. 29, no. 24.
Francois, R., Altabet, M., Yu, E., Sigman, D., Bacon, M., Frank, M., Bohrmann, G., Bareille, G., and Labeyrie, L., 1997, Water column stratification in the Southern Ocean contributed to the lowering of glacial atmospheric CO2: Nature, v. 389, p. 929-935.
Franks, P. J., Royer, D. L., Beerling, D. J., Van de Water, P. K., Cantrill, D. J., Barbour, M. M., and Berry, J. A., 2014, New constraints on atmospheric CO2 concentration for the Phanerozoic: Geophysical Research Letters, v. 41, no. 13, p. 4685-4694.
Ganachaud, A., and Wunsch, C., 2000, Improved estimates of global ocean circulation, heat transport and mixing from hydrographic data: Nature, v. 408, no. 6811, p. 453-457.
Greenwood, D. R., Scarr, M. J., and Christophel, D. C., 2003, Leaf stomatal frequency in the Australian tropical rainforest tree Neolitsea dealbata (Lauraceae) as a proxy measure of atmospheric pCO 2: Palaeogeography, Palaeoclimatology, Palaeoecology, v. 196, no. 3, p. 375-393.
Hagemann, S., and Dümenil, L., 1997, A parametrization of the lateral waterflow for the global scale: Climate Dynamics, v. 14, no. 1, p. 17-31.
Hamon, N., Sepulchre, P., Lefebvre, V., and Ramstein, G., 2013, The role of eastern Tethys seaway closure in the Middle Miocene Climatic Transition (ca. 14 Ma): Climate of the Past, v. 9, no. 6, p. 2687-2702.
Hansen, B., and Østerhus, S., 2000, North Atlantic–Nordic Seas exchanges: Progress in Oceanography, v. 45, no. 2, p. 109-208.
Haug, G. H., Sigman, D. M., Tiedemann, R., Pedersen, T. F., and Sarnthein, M., 1999, Onset of permanent stratification in the subarctic Pacific Ocean: Nature, v. 401, no. 6755, p. 779-782.
Haug, G. H., and Tiedemann, R., 1998, Effect of the formation of the Isthmus of Panama on Atlantic Ocean thermohaline circulation: Nature, v. 393, no. 6686, p. 673.
He, F., Shakun, J. D., Clark, P. U., Carlson, A. E., Liu, Z., Otto-Bliesner, B. L., and Kutzbach, J. E., 2013, Northern Hemisphere forcing of Southern Hemisphere climate during the last deglaciation: Nature, v. 494, no. 7435, p. 81-85.
Hernández-Molina, F. J., Llave, E., Stow, D., García, M., Somoza, L., Vázquez, J. T., Lobo, F., Maestro, A., del Río, V. D., and León, R., 2006, The contourite depositional system of the Gulf of Cadiz: a sedimentary model related to the bottom current activity of the Mediterranean outflow water and its interaction with the continental margin: Deep Sea Research Part II: Topical Studies in Oceanography, v. 53, no. 11, p. 1420-1463.
Hibler III, W., 1979, A dynamic thermodynamic sea ice model: Journal of Physical Oceanography, v. 9, no. 4, p. 815-846.
Hohbein, M. W., Sexton, P. F., and Cartwright, J. A., 2012, Onset of North Atlantic Deep Water production coincident with inception of the Cenozoic global cooling trend: Geology, v. 40, no. 3, p. 255-258.
Huber, M., Brinkhuis, H., Stickley, C. E., Döös, K., Sluijs, A., Warnaar, J., Schellenberg, S. A., and Williams, G. L., 2004, Eocene circulation of the Southern Ocean: Was Antarctica kept warm by subtropical waters?: Paleoceanography, v. 19, no. 4.
Huber, M., and Nof, D., 2006, The ocean circulation in the southern hemisphere and its climatic impacts in the Eocene: Palaeogeography, Palaeoclimatology, Palaeoecology, v. 231, no. 1, p. 9-28.
Hyland, E. G., and Sheldon, N. D., 2013, Coupled CO 2-climate response during the early Eocene climatic optimum: Palaeogeography, Palaeoclimatology, Palaeoecology, v. 369, p. 125-135.
Jagniecki, E. A., Lowenstein, T. K., Jenkins, D. M., and Demicco, R. V., 2015, Eocene atmospheric CO2 from the nahcolite proxy: Geology, v. 43, no. 12, p. 1075-1078.
Jakobsson, M., Backman, J., Rudels, B., Nycander, J., Frank, M., Mayer, L., Jokat, W., Sangiorgi, F., O'Regan, M., and Brinkhuis, H., 2007, The early Miocene onset of a ventilated circulation regime in the Arctic Ocean: Nature, v. 447, no. 7147, p. 986-990.
Jungclaus, J., Keenlyside, N., Botzet, M., Haak, H., Luo, J.-J., Latif, M., Marotzke, J., Mikolajewicz, U., and Roeckner, E., 2006, Ocean circulation and tropical variability in the coupled model ECHAM5/MPI-OM: Journal of climate, v. 19, no. 16, p. 3952-3972.
Kara, A. B., Rochford, P. A., and Hurlburt, H. E., 2000, An optimal definition for ocean mixed layer depth: DTIC Document.
Klepper, O., and de Haan, B. J., 1995, A sensitivity study of the effect of global change on ocean carbon uptake: Tellus B, v. 47, no. 4, p. 490-500.

Knorr, G., Butzin, M., Micheels, A., and Lohmann, G., 2011, A warm Miocene climate at low atmospheric CO2 levels: Geophysical Research Letters, v. 38, no. 20.
Knorr, G., and Lohmann, G., 2014, Climate warming during Antarctic ice sheet expansion at the Middle Miocene transition: Nature Geoscience, v. 7, no. 5, p. 376-381.
Köhler, P., Joos, F., Gerber, S., and Knutti, R., 2005, Simulated changes in vegetation distribution, land carbon storage, and atmospheric CO2 in response to a collapse of the North Atlantic thermohaline circulation: Climate Dynamics, v. 25, no. 7-8, p. 689.
Lohmann, G., Pfeiffer, M., Laepple, T., Leduc, G., and Kim, J.-H., 2013, A model-data comparison of the Holocene global sea surface temperature evolution: Climate of the Past, no. 9, p. 1807-1839.
Lott, F., and Miller, M. J., 1997, A new subgrid-scale orographic drag parametrization: Its formulation and testing: Quarterly Journal of the Royal Meteorological Society, v. 123, no. 537, p. 101-127.
Loubere, P., 1987, Changes in mid-depth North Atlantic and Mediterranean circulation during the late Pliocene—Isotopic and sedimentological evidence: Marine Geology, v. 77, no. 1-2, p. 15-38.
Lowenstein, T. K., and Demicco, R. V., 2006, Elevated Eocene atmospheric CO2 and its subsequent decline: Science, v. 313, no. 5795, p. 1928-1928.
Lumpkin, R., and Speer, K., 2003, Large-scale vertical and horizontal circulation in the North Atlantic Ocean: Journal of Physical Oceanography, v. 33, no. 9, p. 1902-1920.
Lunt, D. J., Foster, G. L., O'Brien, C. L., Pancost, R. D., and Robinson, S. A., 2016, Palaeogeographic controls on climate and proxy interpretation: Climate of the Past, v. 12, no. 5, p. 1181.
Lunt, D. J., Valdes, P. J., Haywood, A., and Rutt, I. C., 2008, Closure of the Panama Seaway during the Pliocene: implications for climate and Northern Hemisphere glaciation: Climate Dynamics, v. 30, no. 1, p. 1-18.
Luyendyk, B., Forsyth, D., and Phillips, J. D., 1972, Experimental Approach to the Paleocirculation of the Oceanic Surface Waters: Geological Society of America Bulletin, v. 83, no. 9, p. 2649-2664.
Maier-Reimer, E., Mikolajewicz, U., and Winguth, A., 1996, Future ocean uptake of CO2: interaction between ocean circulation and biology: Climate Dynamics, v. 12, no. 10, p. 711-722.
Maldonado, A., and Nelson, C. H., 1999, Interaction of tectonic and depositional processes that control the evolution of the Iberian Gulf of Cadiz margin: Marine Geology, v. 155, no. 1, p. 217-242.
Marsland, S. J., Haak, H., Jungclaus, J. H., Latif, M., and Röske, F., 2003, The Max-Planck-Institute global ocean/sea ice model with orthogonal curvilinear coordinates: Ocean modelling, v. 5, no. 2, p. 91-127.
Matsumoto, K., 2007, Radiocarbon-based circulation age of the world oceans: Journal of Geophysical Research: Oceans, v. 112, no. C9.
Metz, B., Davidson, O., De Coninck, H., Loos, M., and Meyer, L., 2005, IPCC special report on carbon dioxide capture and storage: Intergovernmental Panel on Climate Change, Geneva (Switzerland). Working Group III.
Mountain, G. S., and Miller, K. G., 1992, Seismic and geologic evidence for early Paleogene deepwater circulation in the western North Atlantic: Paleoceanography, v. 7, no. 4, p. 423-439.
Nong, G. T., Najjar, R. G., Seidov, D., and Peterson, W. H., 2000, Simulation of ocean temperature change due to the opening of Drake Passage: Geophysical Research Letters, v. 27, no. 17, p. 2689-2692.
Pak, D. K., and Miller, K. G., 1992, Paleocene to Eocene benthic foraminiferal isotopes and assemblages: Implications for deepwater circulation: Paleoceanography, v. 7, no. 4, p. 405-422.
Pälike, H., Lyle, M. W., Nishi, H., Raffi, I., Ridgwell, A., Gamage, K., Klaus, A., Acton, G., Anderson, L., and Backman, J., 2012, A Cenozoic record of the equatorial Pacific carbonate compensation depth: Nature, v. 488, no. 7413, p. 609-614.
Pearson, P. N., and Palmer, M. R., 1999, Middle Eocene seawater pH and atmospheric carbon dioxide concentrations: Science, v. 284, no. 5421, p. 1824-1826.
Pearson, P. N., and Palmer, M. R., 2000, Atmospheric carbon dioxide concentrations over the past 60 million years: Nature, v. 406, no. 6797, p. 695-699.
Pfeiffer, M., and Lohmann, G., 2016, Greenland Ice Sheet influence on Last Interglacial climate: global sensitivity studies performed with an atmosphere–ocean general circulation model: Climate of the Past, no. 12, p. 1313-1338.
Plattner, G. K., Joos, F., Stocker, T., and Marchal, O., 2001, Feedback mechanisms and sensitivities of ocean carbon uptake under global warming: Tellus B, v. 53, no. 5, p. 564-592.
Poore, H., Samworth, R., White, N., Jones, S., and McCave, I., 2006, Neogene overflow of Northern Component Water at the Greenland-Scotland Ridge: Geochemistry, Geophysics, Geosystems, v. 7, no. 6.
Rahmstorf, S., 1998, Influence of Mediterranean outflow on climate: Eos, Transactions American Geophysical Union, v. 79, no. 24, p. 281-282.

Roberts, C. D., LeGrande, A. N., and Tripati, A. K., 2009, Climate sensitivity to Arctic seaway restriction during the early Paleogene: Earth and Planetary Science Letters, v. 286, no. 3, p. 576-585.
Robinson, A. M., 2004, Stratigraphic development and controls on the architecture of Eocene depositional systems in the Faroe-Shetland Basin: Cardiff University.
Roeckner, E., Bäuml, G., Bonaventura, L., Brokopf, R., Esch, M., Giorgetta, M., Hagemann, S., Kirchner, I., Kornblueh, L., and Manzini, E., 2003, The atmospheric general circulation model ECHAM 5. PART I: Model description.
Royer, D., 2014, Atmospheric CO2 and O2 during the Phanerozoic: Tools, patterns, and impacts: Treatise on Geochemistry, v. 6, p. 251-267.
Royer, D. L., Osborne, C. P., and Beerling, D. J., 2003, Carbon loss by deciduous trees in a CO2-rich anient polar environment: Nature, v. 424, no. 6944, p. 60.
Royer, D. L., Wing, S. L., Beerling, D. J., Jolley, D. W., Koch, P. L., Hickey, L. J., and Berner, R. A., 2001, Paleobotanical evidence for near present-day levels of atmospheric CO2 during part of the Tertiary: Science, v. 292, no. 5525, p. 2310-2313.
Sarmiento, J. L., Hughes, T. M., Stouffer, R. J., and Manabe, S., 1998, Simulated response of the ocean carbon cycle to anthropogenic climate warming: Nature, v. 393, no. 6682, p. 245-249.
Sarmiento, J. L., and Le Quere, C., 1996, Oceanic carbon dioxide uptake in a model of century-scale global warming: Science, v. 274, no. 5291, p. 1346.
Schettino, A., and Turco, E., 2011, Tectonic history of the western Tethys since the Late Triassic: Geological Society of America Bulletin, v. 123, no. 1-2, p. 89-105.
Schmittner, A., 2005, Decline of the marine ecosystem caused by a reduction in the Atlantic overturning circulation: Nature, v. 434, no. 7033, p. 628-633.
Schmittner, A., Brook, E. J., and Ahn, J., 2007, Impact of the ocean's overturning circulation on atmospheric CO2: Ocean Circulation: Mechanisms and Impacts-Past and Future Changes of Meridional Overturning, p. 315-334.
Schönfeld, J., and Zahn, R., 2000, Late Glacial to Holocene history of the Mediterranean Outflow. Evidence from benthic foraminiferal assemblages and stable isotopes at the Portuguese margin: Palaeogeography, Palaeoclimatology, Palaeoecology, v. 159, no. 1, p. 85-111.
Sewall, J. v., Van De Wal, R., Van Der Zwan, K., Van Oosterhout, C., Dijkstra, H., and Scotese, C., 2007, Climate model boundary conditions for four Cretaceous time slices: Climate of the Past, v. 3, no. 4, p. 647-657.
Smith, R. Y., Greenwood, D. R., and Basinger, J. F., 2010, Estimating paleoatmospheric pCO 2 during the early Eocene climatic optimum from stomatal frequency of Ginkgo, Okanagan Highlands, British Columbia, Canada: Palaeogeography, Palaeoclimatology, Palaeoecology, v. 293, no. 1, p. 120-131.
Speelman, E. N., van Kempen, M. M., Barke, J., Brinkhuis, H., Reichart, G.-J., Smolders, A. J., Roelofs, J. G., Sangiorgi, F., de Leeuw, J. W., and Lotter, A. F., 2009, The Eocene Arctic Azolla bloom: environmental conditions, productivity and carbon drawdown: Geobiology, v. 7, no. 2, p. 155-170.
Stampfli, G. M., and Hochard, C., 2009, Plate tectonics of the Alpine realm: Geological Society, London, Special Publications, v. 327, no. 1, p. 89-111.
Stärz, M., Jokat, W., Knorr, G., and Lohmann, G., 2017, Threshold in North Atlantic-Arctic Ocean circulation controlled by the subsidence of the Greenland-Scotland Ridge, v. 8, p. 15681.
Stepanek, C., and Lohmann, G., 2012, Modelling mid-Pliocene climate with COSMOS: Geoscientific Model Development, v. 5, no. 5, p. 1221.
Stoker, M. S., Praeg, D., Hjelstuen, B. O., Laberg, J. S., Nielsen, T., and Shannon, P. M., 2005, Neogene stratigraphy and the sedimentary and oceanographic development of the NW European Atlantic margin: Marine and Petroleum Geology, v. 22, no. 9, p. 977-1005.
Stumpf, R., Frank, M., Schönfeld, J., and Haley, B. A., 2010, Late Quaternary variability of Mediterranean outflow water from radiogenic Nd and Pb isotopes: Quaternary Science Reviews, v. 29, no. 19, p. 2462-2472.
Talwani, M., and Eldholm, O., 1977, Evolution of the Norwegian-Greenland sea: Geological Society of America Bulletin, v. 88, no. 7, p. 969-999.
Thiede, J., and Eldholm, O., 1983, Speculations about the paleodepth of the Greenland-Scotland Ridge during late Mesozoic and Cenozoic times, Structure and development of the Greenland-Scotland Ridge, Springer, p. 445-456.
Thomas, D. J., Bralower, T. J., and Jones, C. E., 2003, Neodymium isotopic reconstruction of late Paleocene–early Eocene thermohaline circulation: Earth and Planetary Science Letters, v. 209, no. 3, p. 309-322.
Toggweiler, J., 1999, Variation of atmospheric CO2 by ventilation of the ocean's deepest water: Paleoceanography, v. 14, no. 5, p. 571-588.

Via, R. K., and Thomas, D. J., 2006, Evolution of Atlantic thermohaline circulation: Early Oligocene onset of deep-water production in the North Atlantic: Geology, v. 34, no. 6, p. 441-444.

Vogt, P., 1972, The Faeroe-Iceland-Greenland aseismic ridge and the western boundary undercurrent: Nature, v. 239, p. 79-81.

Werner, M., Haese, B., Xu, X., Zhang, X., Butzin, M., and Lohmann, G., 2016, Glacial–interglacial changes in H218O, HDO and deuterium excess–results from the fully coupled ECHAM5/MPI-OM Earth system model: Geoscientific Model Development, v. 9, no. 2, p. 647-670.

Wright, J. D., 1998, The role of the Greenland-Scotland ridge in Neogene climate changes: OXFORD MONOGRAPHS ON GEOLOGY AND GEOPHYSICS, v. 39, p. 192-211.

Zachos, J., Pagani, M., Sloan, L., Thomas, E., and Billups, K., 2001, Trends, rhythms, and aberrations in global climate 65 Ma to present: Science, v. 292, no. 5517, p. 686-693.

Zhang, X., Lohmann, G., Knorr, G., and Purcell, C., 2014, Abrupt glacial climate shifts controlled by ice sheet changes: Nature, v. 512, no. 7514, p. 290-294.

Zickfeld, K., Eby, M., and Weaver, A. J., 2008, Carbon-cycle feedbacks of changes in the Atlantic meridional overturning circulation under future atmospheric CO2: Global Biogeochemical Cycles, v. 22, no. 3.

Chapter 5: *Conclusions, Limitations and Outlook*

5.1 Conclusions

This dissertation addresses the fundamental challenge of providing an astrochronological framework for the middle Eocene, thus working towards a robust astronomical time scale for the entire Cenozoic. Our astrochronology provides a temporal template essential for improving understanding of the climate and ocean circulation during the transition from the early Cenozoic greenhouse into the cooler modern-day climate. In particular, we combine our astronomical interpretations with the highest-resolution benthic isotope record (Site U1410) currently available for the middle Eocene. This combination allows to evaluate the response of deep-water formation to astronomical forcing, as well as to weigh the relative influence of atmospheric greenhouse gas concentration versus tectonic changes on million-year scale climate evolution during the middle Eocene.

A dominant imprint of obliquity characterizes XRF-derived proxy records of the two middle Eocene Expedition 342 key sites, U1408 and U1410. As these sedimentary sections lack a significant eccentricity component, it was not possible to use the standard stable long-term 405-kyr eccentricity record as a tuning target. Therefore, an alternative tuning target was determined. In this dissertation, the stable 173-kyr obliquity amplitude modulation was evaluated and established as a tuning target for the Cenozoic, back to 48 Ma. This new methodological advancement is instrumental for tuning of high latitude records that are often characterized by a dominant imprint of obliquity, rather than eccentricity. Furthermore, the 173-kyr component could be used as a validation of astrochronologies based on the 405-kyr eccentricity cycle. Using this key advancement in methodology this thesis presents an astrochronologic duration estimate of 9.37 Myr for the middle Eocene chrons C18n.1n through C21n. This estimate agrees in its total length with previous estimates (while significantly differing in estimates for individual chron durations) and can thus be integrated with existing ages on both sides of the geological record.

Another major accomplishment of this dissertation was the generation of a stable oxygen and carbon isotope record of <2 kyr/sample resolution for chron C20r. This record increases the resolution of existing records by 5-10 times and allows, for the first time, the detailed evaluation of the astronomical imprint on benthic stable isotopes for the middle Eocene. The stable isotope record presented in this thesis offers a significant addition and advancement to existing global compilations. Once combined with other records from Expedition 342 a high-resolution benthic isotope record from a single locality, covering the entire middle Eocene, will be provided.

In this dissertation, the generated isotope record is combined with XRF-derived Ca/Fe ratio and used to evaluate the paleoceanographic and paleoclimatic response of the western North Atlantic to astronomical insolation forcing. Proxy records are astronomically paced and dominated by a 41-kyr obliquity beat. The strong imprint of obliquity at a mid-latitude site suggests that a climate signal from the high latitudes is introduced by a paleoceanographic teleconnection. The onset of a Northern Component deep-water source at the early-middle Eocene boundary (Boyle et al., 2017; Hohbein et al., 2012) provides a mechanism for such a teleconnection. Simulations in the coupled Earth System Model *COSMOS* complement the proxy records. The phase relationship of proxies from Site U1410 together with simulations in *COSMOS* reveals that obliquity minima correspond to cold, nutrient-depleted, western North Atlantic deep-waters. Thus, intervals of stronger Northern Component Water formation are linked with obliquity minima. Conversely, during obliquity maxima, Deep Western Boundary Currents were weaker and warmer and abyssal nutrients were more abundant. During obliquity minima, the cooling of surface waters in the Greenland-Norwegian Sea helps to diminish stratification and to decrease the vertical density gradient to enhance overturning. The hampering of the geological cycle due to the cooler obliquity minima is, on the other hand, insignificant. Fluctuations of CO_2 on obliquity timescales could provide another mechanism of governing the Atlantic circulation. Sensitivity studies for different atmospheric CO_2 levels and different tectonic constellations reveal the mechanisms that governed Eocene deep water formation during the Eocene. The same sensitivity study reveals how decreasing CO_2 at the end of the Early Eocene Climatic Optimum could have facilitated the formation of Northern Component Water.

Other sensitivity studies with varying oceanic gateway configurations are used to evaluate the role exchange between the basins on the Eocene North Atlantic overturning. The Greenland-Scotland Ridge is the most important seaway with respect to overturning in the Greenland-Norwegian Sea. It controls the flow of warm saline North Atlantic surface water into the Greenland-Norwegian Sea and thus governs sea surface salinity in the Greenland-Norwegian Sea. To increase surface salinities to a level where cooling of surface waters can break stratification in the Greenland-Norwegian Sea, a threshold between 50-200 m sill depth has to be reached. Furthermore, our results indicate that the Arctic isolation was a critical factor in the development of Northern Component Water.

5.2 Limitations

While the drift sediments allow for the recovery of high-resolution sedimentary successions do not come without challenges. The exposure to the strong Deep Western Boundary Currents and variable sedimentation rates, due to complicated bathymetry, implies that the drill sites were exposed to variable bottom water conditions over time. The studied sites thus reflect a mix between local and global climate signals. Indeed, the strong obliquity imprint on middle Eocene sections at sites from IODP Expedition 342 is an uncommon feature compared to other locations in the Atlantic or the Pacific. Moreover, fast-changing pathways of ocean currents imply that lithological expression of stratigraphic intervals may vary considerably between nearby sites. This complicates splicing and correlation between sites.

Even though most key objectives of this dissertation have been addressed, it has not been possible to eliminate all issues and uncertainties associated with analysing drift sediments. In particular issues concerning the stratigraphic completeness of Sites U1408 and U1410 and the inter-site correlation between these two important middle Eocene records from Expedition 342 should be addressed by subsequent studies.

The reason for the absence of chron C19n at Site U1408, as well as the different lithological expressions of the Middle Eocene Climatic Optimum between Sites U1408 and U1410 are still unresolved in the current inter-site correlation. On the other hand, the total duration estimates for C18-C21 between Westerhold et al. (2015) and this work are in good agreement. Using an alternative correlation between sites would imply that all recovered middle Eocene records are characterized by a number unidentified small-scale hiatuses and thus not stratigraphically complete. This hypothesis would provide an alternative explanation to why the ages presented in Chapter 2 are non-complementary with the interpretations by Westerhold et al. (2015) who used records from the equatorial and South Atlantic to close the Eocene tuning gap.

The isotopic dataset covering chron C20r presented in this dissertation is the first piece of a planned record spanning more than 10 Myr at the Newfoundland Ridges. However, work on other chrons is still in progress by other lab groups. At this moment, the early-middle Eocene boundary, characterized by the onset of drift sedimentation through initiation of Northern Component Water is not yet covered by high-resolution benthic foraminiferal isotopes or Nd isotope data. These datasets will be fundamental in understanding the succession of events and interplay between Northern Component Water and Deep Western Boundary Currents. Complementation of both datasets could also help to better understand the nutrient properties of Atlantic deep waters during the Cenozoic and the behaviour of NCW during extreme climatic periods such as the Middle Eocene Climatic Optimum.

5.3 Outlook

Integrated Ocean Drilling Program Expedition 342 successfully recovered high-resolution archives of the transition from the Eocene greenhouse into the Oligocene icehouse. With the generation of more proxy records from Expedition 342 there will be a significant increase and improvement in the resolution of global and Atlantic benthic stable isotope compilations. This will help to answer key questions about middle Eocene oceanic heat, nutrient and carbon cycling.

While Expedition 342 delivered high-quality sections for the Paleogene for the North Atlantic, it is important to provide similar records for other ocean basins. In this context, efforts have been made to locate more drill sites in areas with relatively poor coverage for the Paleogene and will be cored during a number of upcoming IODP Expeditions (Expedition 371: Tasman Frontier Subduction and Climate, Expedition 373: Antarctic Cenozoic Paleoclimate, Expedition 377: Arctic Ocean Paleoceanography, Expedition 378: South Pacific Paleogene Climate). Over the next 10 years these expeditions combined with ongoing work on samples from Expedition 342, should substantially expand knowledge about Paleogene climate. An increase in high-resolution sedimentary successions will also provide an independent test of the astrochronology based on Expedition 342 sites. This will allow us to finally resolve the issue of the Eocene astronomical tuning gap, with particular regards to confirming the completeness of existing deep-sea records including the Expedition 342 sites.

In the absence of interbasinal $\delta^{13}C$ gradients (see Chapter 3), records of Nd isotopes will play a prominent role in constraining the ratios of Northern vs Southern Component Water in the Cenozoic Ocean basins on orbital timescales. Expedition 342 sites are excellently located to provide a North Atlantic end-member for Cenozoic Nd isotope records of high resolution.

While humans continue to emit CO_2 into the atmosphere leading to the transformation of environmental conditions on Earth, it is more important than ever to understand the nature of processes that occur in response to these changes. In particular, how they will affect physical processes, ecosystems and the global population over the coming decades, centuries and millennia.

References

Boyle, P. R., Romans, B. W., Tucholke, B. E., Norris, R. D., Swift, S. A., and Sexton, P. F., 2017, Cenozoic North Atlantic deep circulation history recorded in contourite drifts, offshore Newfoundland, Canada: Marine Geology, v. 385, p. 185-203.

Hohbein, M. W., Sexton, P. F., and Cartwright, J. A., 2012, Onset of North Atlantic Deep Water production coincident with inception of the Cenozoic global cooling trend: Geology, v. 40, no. 3, p. 255-258.

Westerhold, T., Röhl, U., Frederichs, T., Bohaty, S., and Zachos, J., 2015, Astronomical calibration of the geological timescale: closing the middle Eocene gap: Climate of the Past, v. 11, no. 9, p. 1181.

Acknowledgements

Writing this thesis would have been a much greater challenge and less enjoyable without the help, company and friendship of many people I met over the last years. You have been a constant source of energy, motivation, support, fun and comfort.

First of all, I want to thank my supervisor Heiko Pälike who gave me the opportunity to work on these fascinating topics. Thank you for your exceptional support and for giving me the scientific freedom to follow the tracks I was most interested in. Your comfortable and relaxed manner was much needed in some of the more troubled moments.

David De Vleeschouwer has been the best imaginable one-man colleague/mentor/friend over the last years. Thank you so much for all the interesting discussions, great lessons and making science fun and exciting and most of all for always being there.

I would also like to thank the working group Paleoceanography for a lot of fun over the last three years and especially Mathias and Fiona for making me look forward to go to the office in the morning.

I am especially grateful to Torsten Bickert for guiding my early scientific path and attracting my interest in paleoclimatology in the first place.

Furthermore, I would like to thank Ulla Röhl for her participation in my thesis committee and for sharing her advice and experience generously.

I thank Jim Zachos for giving me the opportunity to spend three wonderful and educational months at UCSC and Jim, Dustin and Tali for becoming friends and making my time in Santa Cruz so unforgettable.

I would like to thank Lucas Lourens for agreeing to review this thesis.

I thank the IODP Expedition 342 shipboard science party for their dedication onboard without which this work would not have been possible and all the co-authors of the presented chapters. I would especially like to thank Phil Sexton, Pincelli Hull, Steve Bohaty, Paul Wilson, Simon D'haenens, Igor Niezgodzki, Gerrit Lohmann, Rüdiger Stein and Don Penman for interesting discussions and helpful advice.

Henning Kuhnert and the stable isotope laboratory at MARUM are gratefully acknowledged for support with isotope measurements.

I would further like to thank the teaching staff and the participants of the Urbino Summer School in Paleoclimatology 2015 for one of the most memorable experiences during my time as a PhD candidate.

All my friends have bravely dealt with my moods during the harder times of this work and I feel listing them here does in any way reflect my strong feelings for all of you. I just trust that you know what you mean to me. Thank you for being you.

Most of all I want to thank my parents who have always given me unconditional support and always believed in me and Nicole for being the most genuine, giving and loving partner in life I could have wished for.

Supplementary Information Chapter 2: *Towards a Constrained Middle Eocene Astronomical Timescale*

Slah Boulila[1,2], Maximilian Vahlenkamp[3], David De Vleeschouwer[3], Jacques Laskar[2], Yuhji Yamamoto[4], Heiko Pälike[3], Sandra Kirtland Turner[5], Philip F. Sexton[6], Thomas Westerhold[3], and Ursula Röhl[3]

[1] *Université Paris VI, CNRS - UMR 7193 ISTeP 'Institut des Sciences de la Terre-Paris', case 117, 4, place Jussieu, 75252 Paris cedex 05, France.*

[2] *ASD, IMCCE-CNRS UMR 8028, Observatoire de Paris, UPMC, 77 avenue Denfert-Rochereau, 75014 Paris, France.*

[3] *MARUM – Center for Marine Environmental Sciences, University of Bremen, Leobener Strasse, 28359 Bremen, Germany.*

[4] Center for Advanced Marine Core Research, Kochi University, B200 Monobe, Nankoku, Kochi 783-8502, Japan.

[5] School of Earth Sciences, University of California, Riverside, Riverside, CA 92521, USA.

[6] Department of Environment, Earth and Ecosystem Sciences, The Open University, Walton Hall, Milton Keynes, Buckinghamshire, MK7 6AA, UK.

The supplementary information contains seven figures and five tables. Supplementary Figure 2.1 extends the demonstration of the astronomical stability of the s3-s6 term in the amplitude modulation of obliquity. Supplementary Figure 2.2 shows exceptionally expressed s3-s6 obliquity related amplitude modulation cycles over an extended interval at Site U1410. Supplementary Figure 2.3 shows time-series analysis of high-resolution XRF (Fe) data at ODP Site 1260, of the interval from 90 to ~135 m (rmcd), supporting the cyclostratigraphic interpretation of Westerhold and Röhl (2013). Supplementary Figure 2.4 reevaluates time-series analysis of high-resolution XRF (Fe) data at ODP Site 1260, of the interval from ~58 to 90 m (rmcd), suggesting a cyclostratigraphic reinterpretation of Westerhold and Röhl (2013), and the sedimentary incompleteness of chrons C19n and C19r. Supplementary Figure 2.5 highlights significant differences in duration of chrons C19n and C19r between Sites 1260 and U1410 that we relate to the incompleteness of the sedimentary record at Site 1260. An associated text to Supplementary Figures 2.3, 2.4 and 2.5 describes the cyclostratigraphic interpretation and durations of chrons at Site 1260 (compared to U1410). Supplementary Figures 2.6 and 2.7 with an associated text highlight the source of differences and similarities in durations of chrons C20n, C20r and C21n between ODP Site 1263 and IODP Expedition 342 Site U1410. Supplementary Figures 2.8 and 2.9 show the cyclostratigraphic interpretation of Hole 702B and correlation with Site 1263 in detail.

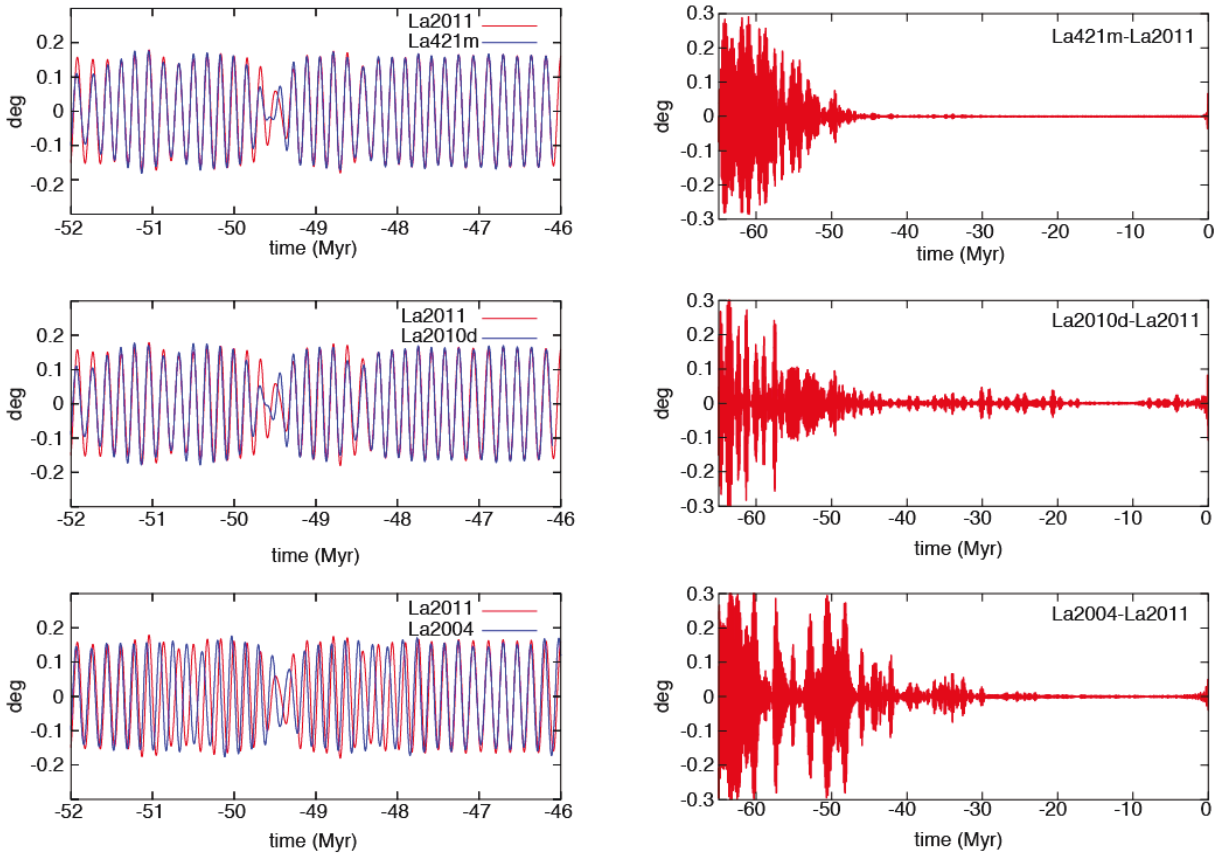

Supplementary Figure 2.1: Testing the stability of s3-s6 related obliquity cycles using four orbital solutions La2004, La2010d, La2011 and La421m (see references and characteristics of each solution

in the main text). Left panel: s3-s6 variations over the critical interval 46-52 Ma, when orbital solutions start to diverge. Right panel: differences in s3-s6 between orbital solutions over the past 65 Ma, considering La2011 as a reference.

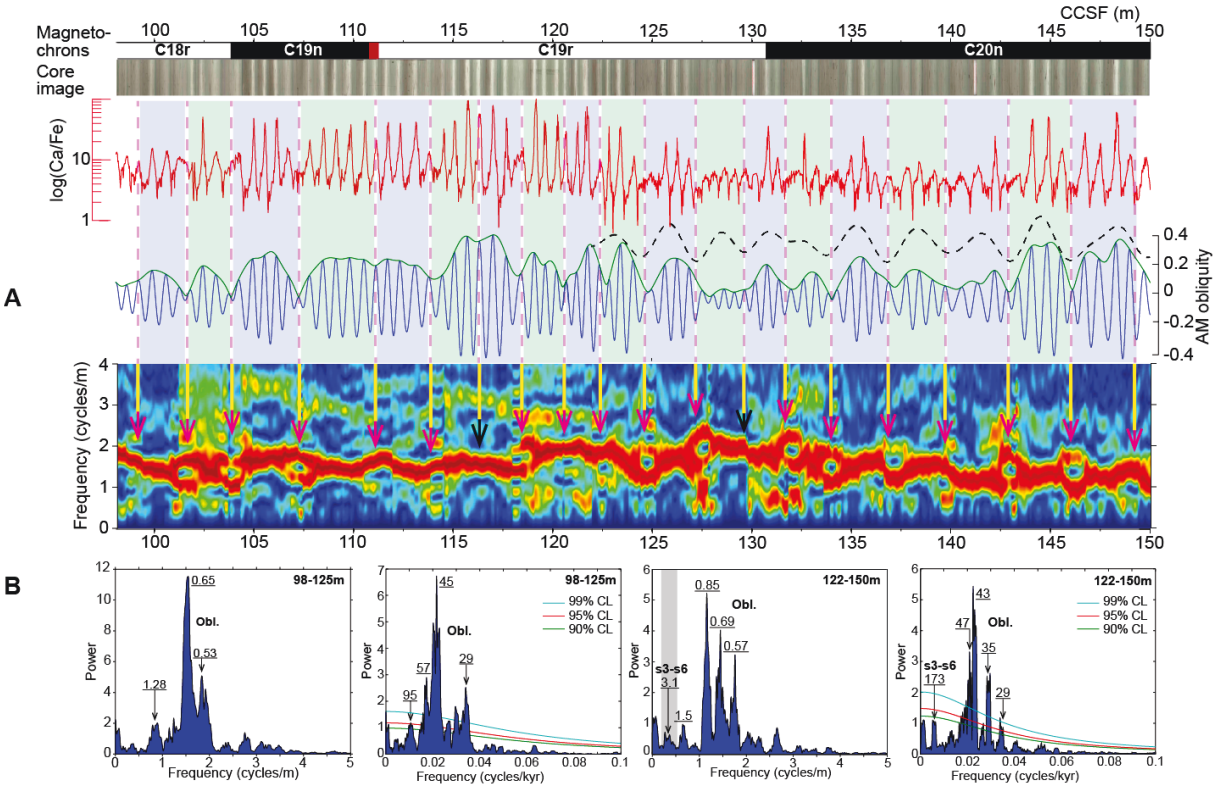

Supplementary Figure 2.2: Time-series analysis at Site U1410 showing strong obliquity amplitude modulation in an interval with continuous sedimentation and exceptionally well-developed lithologic couplets. **(A)** Obliquity amplitude modulation analysis of site U1410 using both Hilbert transform and evolutive FFT. Note the expression of AM envelope cycles (s3-s6) as bifurcations (pink arrows) in the spectrogram (black arrows indicate exceptions where minima in AM output don't correspond to bifurcations in the spectrogram). **(B)** 2 π-MTM power spectra in depth and time domains. Spectral analysis in time domain is applied to 173 kyr (s3-s6) tuned signals.

Supplementary Text on Supplementary Figures 2.3, 2.4 and 2.5:

An astronomical calibration for chrons C19n, C19r and C20n was previously published based on data from ODP Site 1260 (tropical western Atlantic, Westerhold and Röhl, 2013). Site 1260 possesses high-resolution XRF (Fe) data that captures sedimentary cycles related to precession and its modulation by eccentricity. The 405 kyr eccentricity cycle, which strongly modulates pronounced precession cycles (e.g., Supplementary Figure 2.3) was used to calibrate chrons C19n, C19r and C20n.

Duration of combined C19n, C19r and C20n is 3.294 to 3.314 Myr at Site U1410 versus only 2.388 Myr at Site 1260 (Supplementary Figure 2.5 and Table 2.2). A possible cause for this large discrepancy is the incompleteness of the sedimentary record at Site 1260.

To further explore this hypothesis, we analyzed Site 1260's Fe data in detail. We analyzed the data in intervals because of the weak expression (or no expression, see below) of 405 kyr

cyclicity in the upper part of the record (C18r p.p., C19n and C19r).

Results of time-series analysis (summarized in Supplementary Figures 2.3, 2.4 and 2.5) indicate that the recorded 405 kyr cycles, as well as the number of short eccentricity cycles (Supplementary Figure 2.5), were adequately interpreted in the lower part of the record, ~90 to ~135 rmcd, i.e., C20r p.p. and C20n (Supplementary Figure. 2.3 and Westerhold and Röhl, 2013). However, in the upper part ~58 to ~90 rmcd (C18r p.p., C19n and C19r), the 405 kyr eccentricity cycles are poorly expressed in Fe data. The interpretations of Westerhold and Röhl (2013) were based on $\delta^{13}C$ data to extract the 405 kyr cycles within this interval (Supplementary Figure 2.4), but their filtering gives only two and a half 405 kyr related $\delta^{13}C$ cycles for the combined C19n-C19r interval, thus providing a duration of about 1 Myr, which is again much shorter than the ~1.8 Myr duration as inferred from U1410.

In Supplementary Figure 2.3 we show ODP Site 1260's Fe count record of precession cycles, modulated by the short (both e1 and e2 components) and 405 kyr (g2-g5) eccentricity cycles. The strong expression of these three astronomical periodicities together hints at a continuous sedimentation in the lower part of the record, i.e., ~90 to ~135 rmcd. In particular, chron C20n is interpreted to be continuous at Site 1260 (discussion below).

In Supplementary Figure 2.4 we show that there is no spectral power (or trend) at the 405 kyr eccentricity band (Supplementary Figure 2.4A,B) in the upper part of the record (C18r p.p., C19n and C19r), while Westerhold and Röhl's (2013) interpreted three 405 kyr repetitions (Supplementary Figure 2.5). The absence of g2-g5 related variations (or trends) in Fe record indicates the distortion of such cycles by hiatuses. We have tuned the signal using the short eccentricity to seek for g2-g5 related variation in time domain, but no spectral peak emerges at the 1/405 kyr frequency band (Supplementary Figure 2.4C,D). We suggest that hiatuses may have caused the relative short durations of chrons C19n and C19r at this site.

We have further explored this hypothesis by examining chrons individually and by looking either at precession vs obliquity or short eccentricity vs s3-s6 (173 kyr) cycles at Sites 1260 and U1410 (Supplementary Figure 2.4). Below, we give rough estimates based on short (100 kyr) eccentricity cycle counting at Site 1260 (esp. in the upper part where g2-g5 component is not expressed), and precise estimates using the s3-s6 tuning at U1410.

Chron C19n contains approximately two short eccentricity cycles (almost ten precession cycles) implying a duration of ~0.2 Myr (based on short eccentricity) as reported in Westerhold and Röhl (2013). At Site U1410, the same chron contains almost two s3-s6 cycles (ten to eleven obliquity cycles) implying a duration of about ~0.35 Myr (based on s3-s6 tuning). A difference of 0.15 Myr could thus be ascribed to hiatuses or magnetostratigraphically poorly defined C19n at 1260. The examination of the inclination data at this site shows that the upper boundary of C19n is defined by only one inclination value (Fig. S4). Considering this data point as incorrect, another stratigraphic position for this boundary is possible, thus giving a more

extended C19n (Fig. S4). This additional interval includes approximately three precession cycles providing a total duration of C18n of about 273 kyr (13 x 21 kyr), which is still shorter than the ~350 kyr duration inferred from U1410.

Chron C19r includes approximately 9.5 short eccentricity cycles (44 precession cycles, according to Westerhold and Röhl, 2013) and only 7.5 short eccentricity cycles (44 precession cycles, according to our tuning, Supplementary Figure 2.4C,D) implying a duration of ~0.95 Myr and ~0.75 Myr, respectively. This duration is much shorter than the 1.463 Myr duration at U1410 (almost 8.5 s3-s6 cycles). A difference of ~0.5 Myr could also be linked to hiatuses.

Chron C20n consists of nearly 14 short eccentricity cycles (almost 3.5 g2-g5 cycles) implying a duration of ~1.4 Myr, while Westerhold and Röhl (2013) reported a duration of only 1.298 Myr (Table 2.2). They were based on precession cycle counting, which would provide a duration between 1.26 Myr (60 x 21 kyr) and 1.302 Myr (62 x 21 kyr). At U1410, we can count almost 9 s3-s6 cycles yielding a duration of 1.534 Myr. The strong record of the three astronomical parameters, precession, short and 405 kyr eccentricity cycles and the spectacular spectral expression of short eccentricity e1 and e2 components in the lower interval at Site 1260 (~90 to ~135 rmcd, Supplementary Figure 2.3B) provide compelling evidence for the completeness of chron C20n, at least at the scale of g2-g5 and short eccentricity. If we consider a mean period of e1 and e2 (see Supplementary Figure 2.3C), we arrive at a duration of 1.54 Myr for C20n, which is identical to that (1.534 Myr) inferred from U1410.

In summary, chrons C19n and especially C19r at Site 1260 are very likely the subject of hiatuses. In contrast, chron C20n could be considered as complete, and Site 1260 record with its high resolution and high fidelity provides strong additional constraints on the duration of this chron.

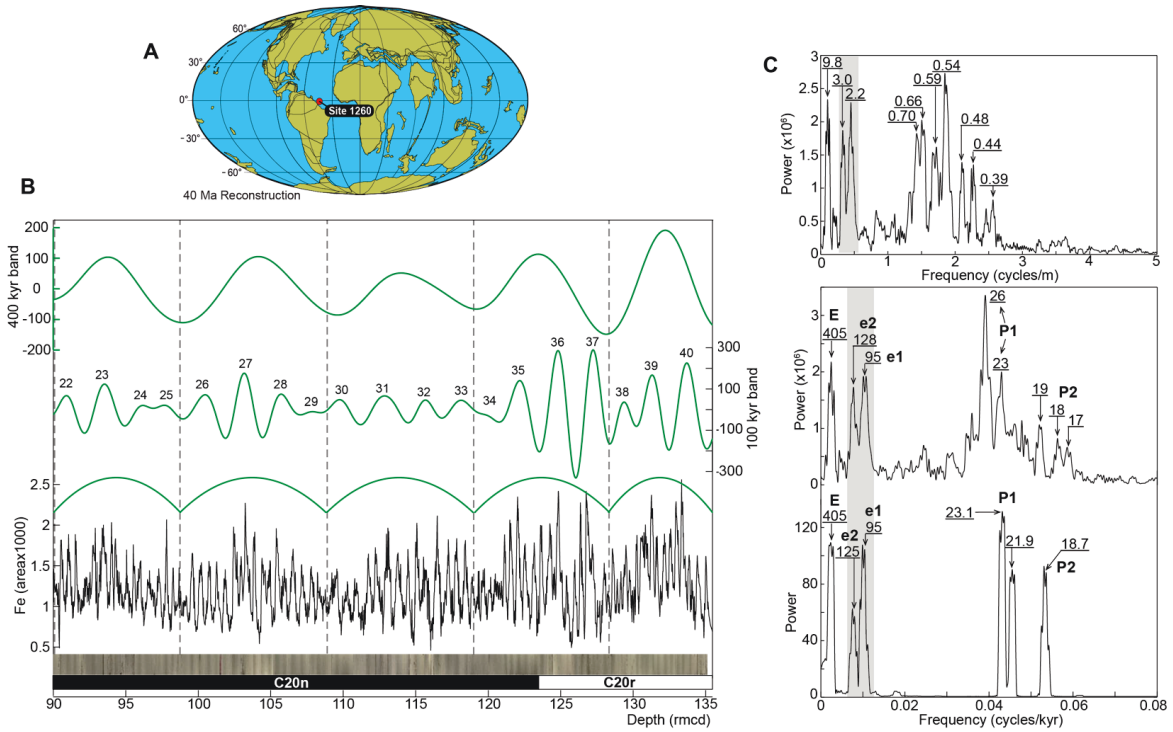

Supplementary Figure 2.3: Time-series analysis of XRF (Fe) data at ODP Site 1260. **(A)** Paleogeographic location of ODP Site 1260. **(B)** XRF (Fe intensity) data and bandpass filtering at short (100 kyr) and 405 kyr eccentricity bands of the interval ~90 m to ~135 m (chrons C20r *p.p.* and C20n p.p.). Numbers of short eccentricity cycles, from 22 to 40, are as in Westerhold and Röhl (2013) (see also Supplementary Figure 2.5). The arcs indicate the interpreted wavelengths related to the 405 kyr eccentricity related. **(C)** 2π-MTM power spectra, with the upper spectrum in depth domain, the middle spectrum in time domain using 405 kyr tuning, the lower spectrum is the middle Eocene equivalent time interval of precession and eccentricity signals in La2004 astronomical model (Laskar et al., 2004). Symbols 'P1 and P2' for precession, 'e1 and e2' for short (100 kyr) eccentricity, and 'E' for 405 kyr eccentricity. Note that the precession band is not properly calibrated, likely because of significant change in sedimentation rate at this band. Short eccentricity cycles, on the other hand, correspond to periods close to those in the astronomical model. In particular, the double peaks e1 and e2 in depth and time domains (vertical grey bar) are characteristics of the dominant short eccentricity periods, further supporting such calibration. This result concurs with Westerhold and Röhl's (2013) interpretation.

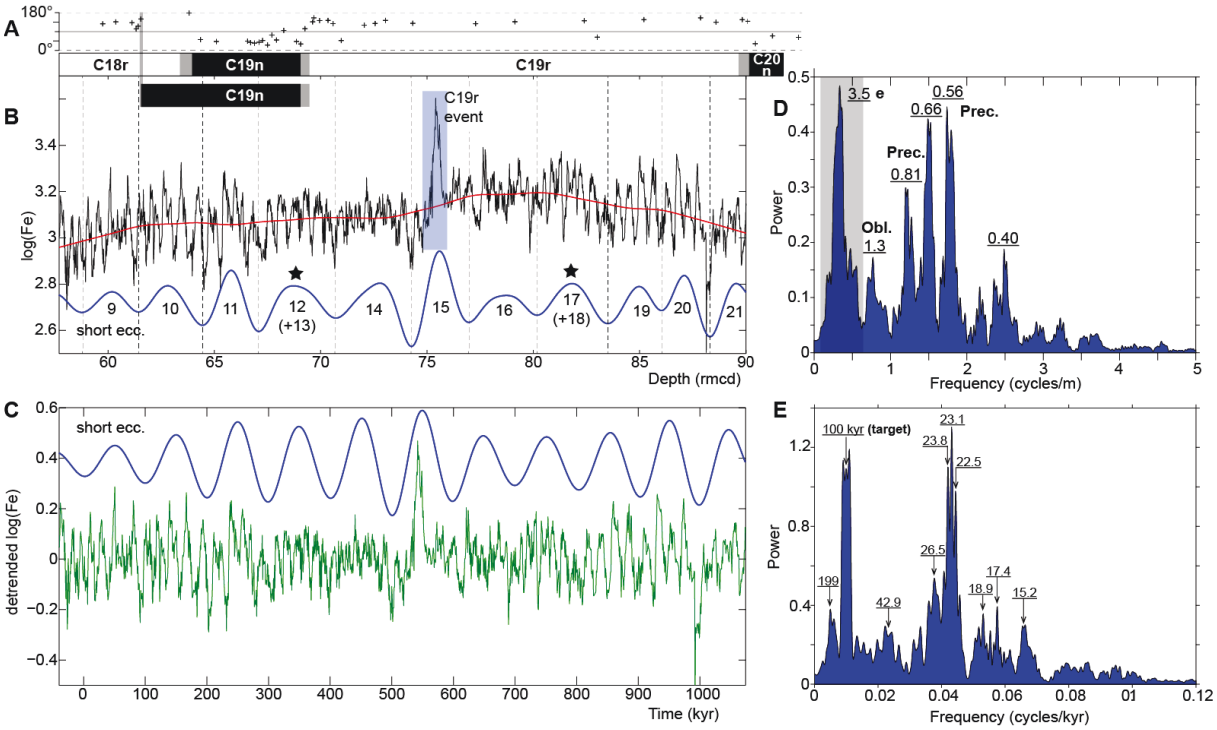

Supplementary Figure 2.4: Time-series analysis of XRF (Fe) data at ODP Site 1260 of the interval from ~58 to ~90 m (rmcd). **(A)** Inclination curve and the interpreted chrons according to Westerhold and Röhl (2013). The upper boundary of C19n is poorly defined. We thus propose another possible stratigraphic position for this boundary giving a more extended C19n (see text for discussion). **(B)** Raw log(Fe) data together with weighted average fit curve, removed prior spectral analysis (for detrended data, see 'C'). Bandpass filtered short eccentricity cycles (the band is centered on 3.5 m wavelength, shown in 'D'). Numbers of short eccentricity cycles, from 9 to 21, are as in Westerhold and Röhl (2013) (see also Supplementary Figure. 2.5). Note that cycles no. 12 and 17 in our filtering (indicated by stars) include each one two cycles according to Westerhold and Röhl (2013). The C19r event is shown in the blue shaded area. **(C)** 100 kyr tuned log(Fe). **(D)** 2π-MTM power spectrum of the detrended log(Fe) data. Abbreviations and symbols: 'prec.' for precession, 'obl.' For obliquity, and 'e' for short (100 kyr) eccentricity. **(E)** 2π-MTM power spectrum of the 100 kyr tuned log(Fe) data. Such tuning aligns the two strongest wavelength peaks (0.56 and 0.66 m) at period peaks centered on 23.1 kyr, a period very close to the precession (see Supplementary Figure 2. 3C). Note that tuning using all interpreted 100 kyr eccentricity related cycles by Westerhold and Röhl (2013) (i.e., with the two additional cycles indicated in 'B') results in a spectrum (not shown) that has poorly defined 100 kyr and precession peaks.

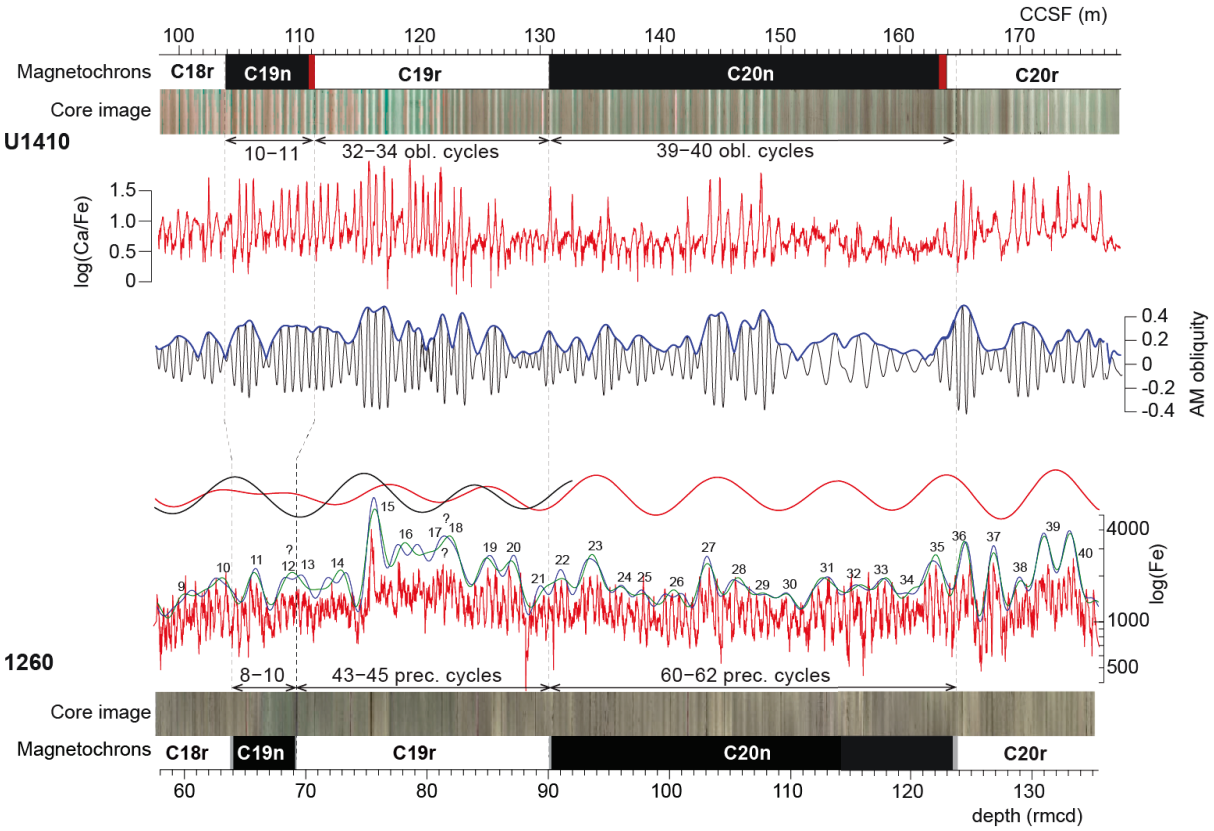

Supplementary Figure 2.5: Cyclo-magnetostratigraphic correlation between IODP Exp. 342 Site U1410 (this study), and ODP Site 1260 (Westerhold and Röhl, 2013). Number of precession cycles (at 1260) versus obliquity cycles (at U1410) in each chron is shown. Amplitude modulation (AM) envelopes of the obliquity au U1410 are shown. The filtered curves at 1260 correspond to 405 kyr cycles from XRF Fe data (red) and benthic $\delta^{13}C$ data (black) are from Westerhold and Röhl (2013). Lowpass filterd short and 405 kyr eccentricity cycles in the XRF Fe data, using appropriate and broad bands are shown. Numbers of short eccentricity cycles, from 9 to 40, are as in Westerhold and Röhl (2013). Question marks on cycles no 12 and 13, and on cycles no 17 and 18 indicate a difference in cycle interpretation between Westerhold and Röhl (2013) and the present study (see Supplementary Figure 2.4 and the text).

Supplementary Text on Supplementary Figure 2.6, 2.7, 2.8 and 2.9:

Comparison of duration of chrons inferred from cyclostratigraphy at IODP342 Site U1410 (North Atlantic, this study) and ODP Site 1263 (South Atlantic, Westerhold et al., 2015, their Table 2) indicates significant differences for individual chron durations (Table 2.2). Nevertheless, when we consider the combined duration of chrons C19r, C20n and C20r at both sites, we find the same duration (4.95 to 4.97 Myr at U1410 versus 4.971 Myr at 1263). We suggest that sedimentation is fairly continuous at Sites U1410 and 1263, while differences in duration within chrons may be related to problems in magnetostratigraphy at Site 1263, because of the excellent magnetostratigraphic data Site from U1410 (Expedition 342 Scientists, 2012, Norris et al., 2014). We have then examined the magnetostratigraphy of Site 1263, but also its cyclostratigraphic interpretation (Supplementary Figures 2.6 and 2.7).

For cyclostratigraphy, we first conducted time-series analysis of $\delta^{13}C$ data in depth domain. $\delta^{13}C$ data were acquired at an equivalent temporal resolution of 5 kyr to 10 kyr (Westerhold et

al., 2015), which is not high enough to capture the precession cycle band. Therefore, we have rather focused on eccentricity cycle band, in particular on the 405 kyr (g2-g5) eccentricity cycles, previously used to calibrate the associated chrons. Results show that there are two possibilities in the number of g2-g5 related cycles (16 versus 17) after several tests of bandpass filtering per intervals and applied to the whole data (Supplementary Figures 2.6A and 2.7). Westerhold et al. (2015) used 17 g2-g5 interpreted cycles in their tuning (discussed below).

In a second step, we tuned the strongest 4.8 m thick cycles at a 405 kyr period to see the alignment of the two couple peaks of 0.9 m and 1.1 m, which would correspond to the short eccentricity (Supplementary Figure 2.6B). Here, we performed two tuning options, one using only 16 g2-g5 related cycles and another using 17 g2-g5 related cycles. Tuning with only 16 cycles better aligns the short eccentricity components, in particular the obtained spectrum shows narrow bandwidth peaks at e1 and e2 (Supplementary Figure 2.6C,D). Finally, we bandpass filtered the short eccentricity (e1 and e2), and performed Hilbert transform to extract the g2-g5 amplitude modulation (AM) envelopes for the two options (Supplementary Figure 2.7A-E). Again, the doubtful interval has better expressed g2-g5 related amplitude modulation envelopes in the option of "16 g2-g5 cycles" (Supplementary Figure 2.6C,D).

We then reexamined magnetostratigraphic interpretation using the inclination curve as provided in Westerhold et al. (2015). We note that the stratigraphic position of C20n/C20r boundary is poorly defined according to these data. Indeed, scattered inclination values in both holes within the transition C20n/C20r, from approximately 172 to 183 rmcd, hamper the precise determination of this boundary (Supplementary Figure 2.9).

We have continued exploration in order to identify the source of difference, by looking at the common, recovered chrons at sites 1260 and U1410. In fact, chrons C19n and C19r are not shown at 1263, while their durations were given (Westerhold et al., 2015, their Table 2). Thus, we considered only the recovered C20n, C20r and C21n from this site, for a possible comparison with their equivalents at Site U1410. We noted that the major difference in duration resides in chrons C20n and C20r (Fig. 2.8 and Table 2.2). The difference of 0.057 Myr (~4 %) in chron C21n, which could be related to the precision in s3-s6 vs g2-g5 orbital tuning.

Indeed, the aforementioned doubtful interval in cycle interpretation (16 versus 17 cycles of g2-g5) falls within chron C20r (Supplementary Figure 2.6). If we adopt the hypothesis of "16 g2-g5 cycles" at Site 1263 (see above), we arrive at a difference of only ~0.119 Myr in duration of the ensemble C20n and C20r, between 1263 and U1410. To further explore this difference, we took into consideration Westerhold et al.'s (2015) cyclostratigraphic interpretation used to estimate durations of C20n, C20r and C21n at Site 1263. We have noted that durations of chrons C20r and C21n were properly reported in their Table 2. However, duration of chron C20n should be ~1.283 Myr according to their tuning (Supplementary Figures 2.6 and 2.7),

instead of 1.41 Myr (their Table 2). Thus, the difference of ~0.119 Myr, very close to the difference between 1.41 Myr and 1.283 Myr, is most likely due to Westerhold et al.'s (2015) transfer of their results into their Table 2.

Another evidence for "16 g2-g5 cycles" comes from Hole 702B (Southwestern South Atlantic on the central part of the Islas Orcadas Rise). Hole 702B $\delta^{13}C$ data possess a strong (long period) cyclostratigraphic signal dominated by s4-s3 (~1.2 Myr) related obliquity and g2-g5 related eccentricity cycles (Supplementary Figure 2.8). Nevertheless, Hole 702B has poorly constrained magnetostratigraphic data, due to very weakly magnetized nannofossil chalks (Clement and Hailwood, 1991). We have examined the combined C20n-C20r interval, where the upper boundary of C20n and lower boundary of C20r could be considered as reliable (Supplementary Figure 2.9). Time-series analysis of 702B $\delta^{13}C$ data (Supplementary Figure 2.8), together with cyclostratigraphic correlation between Hole 702B and Site 1263 strengthen the hypothesis of "16 g2-g5 cycles"(Supplementary Figure 2.9).

In summary, when revising the cyclostratigraphic interpretation of Site 1263 and by considering the interval of uncertainty in the definition of C20n/C20r boundary, which has an equivalent duration of approximately 1.07 Myr (Supplementary Figures. 2.6 and 2.7B), we can retrieve durations of C20n and C20r at Site 1263, identical to those inferred from Site U1410. The latter has constrained cyclo-magnetostratigraphic data. In particular, shifting the base of C20n by only ~299 kyr (~2.5 m down, Supplementary Figure 2.6) and considering the revised cyclostatigraphy of 1263 (Supplementary Figures. 2.6 and 2.7) conjointly with the analyzed cyclostratigraphy of Hole 702B (Supplementary Figure 2.8 and 2.9), lead to similar durations of chrons C20n and C20r in the North and South Atlantic Ocean.

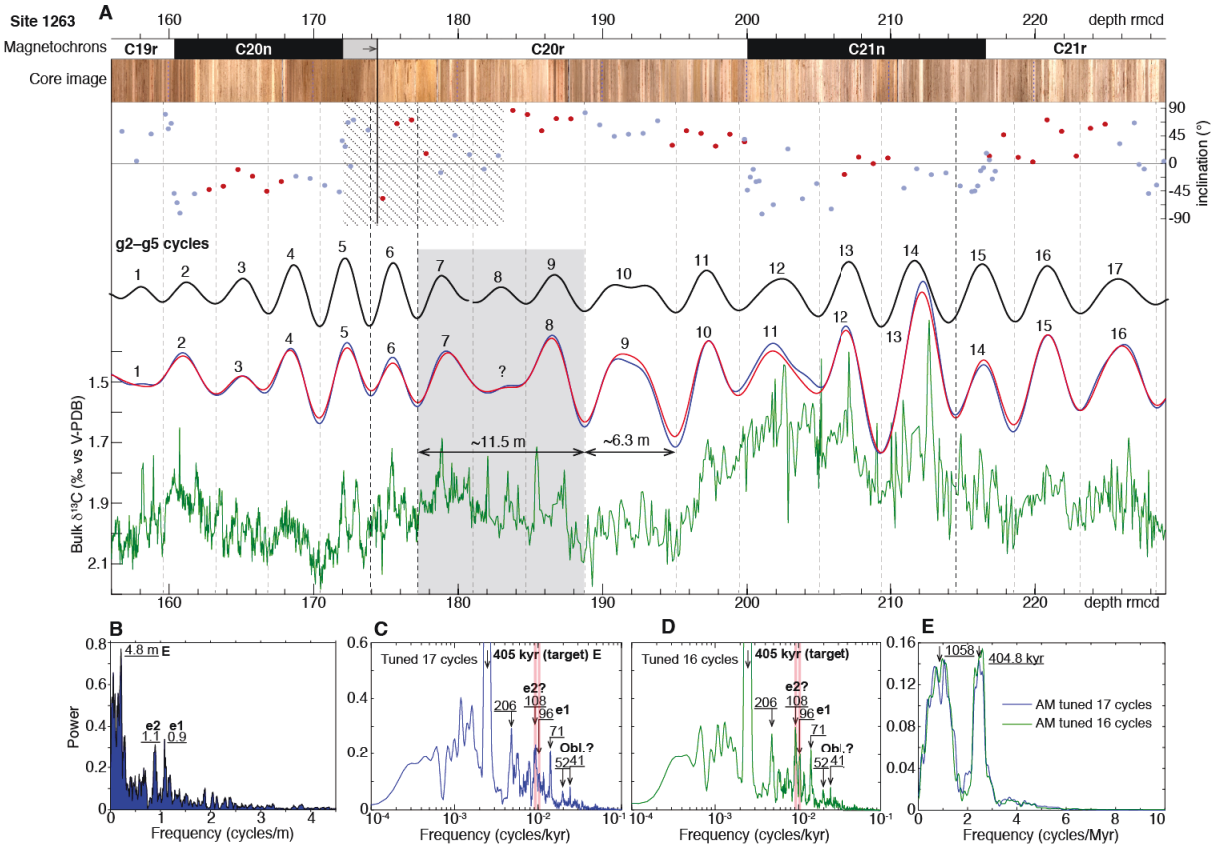

Supplementary Figure 2.6: Cyclo-magnetostratigraphic interpretation at ODP Site 1263 (data are from Westerhold et al., 2015). **(A)** Integrated bulk, stable carbon isotope ($\delta^{13}C$) cyclostratigraphy and magnetostratigraphy. The crosshatched area in the inclination data corresponds to an uncertain interval in the definition of C20n/C20r boundary, that we suggest in the present study. Red dots indicate data from Hole 1263A, and blue dots show data for Hole 1263B. Vertical line in the crosshatched together with grey-shaded rectangle in basal C20n indicate ~2.5 m shift downcore (arrow indicates direction) to reestablish the possible stratigraphic position of the base of C20n. g2-g5 (405 kyr) eccentricity related cycles filtered from $\delta^{13}C$ data (green). The upper black curve along with the identified g2-g5 cycles (numbered 1 to 17) are from Westerhold et al. (2015). The lower curve with possibly only 16 numbered g2-g5 cycles is according to the present study. Additionally, we indicate the thickness of cycle no 10 (~6.3 m) on the basis of Westerhold et al.'s (2015) interpretation, and the thickness of combined three cycles 7, 8 and 9 (~11.5 m) to show that interpretation of three or only two cycles in the grey shaded area does not induce unreasonable change in sedimentation rate. **(B)** 2pi-MTM spectrum of detrended $\delta^{13}C$ in depth domain. **(C)** 2pi-MTM spectrum of 405 kyr tuned $\delta^{13}C$ using the option of 17 cycles. **(D)** 2pi-MTM spectrum of 405 kyr tuned $\delta^{13}C$ using the option of 16 cycles. **(E)** 2pi-MTM spectra of amplitude modulation (AM) envelopes of the $\delta^{13}C$ related short eccentricity cycles using the two options. Spectral peaks 'E' for g2-g5 eccentricity, and 'e1' and 'e2' for short eccentricity

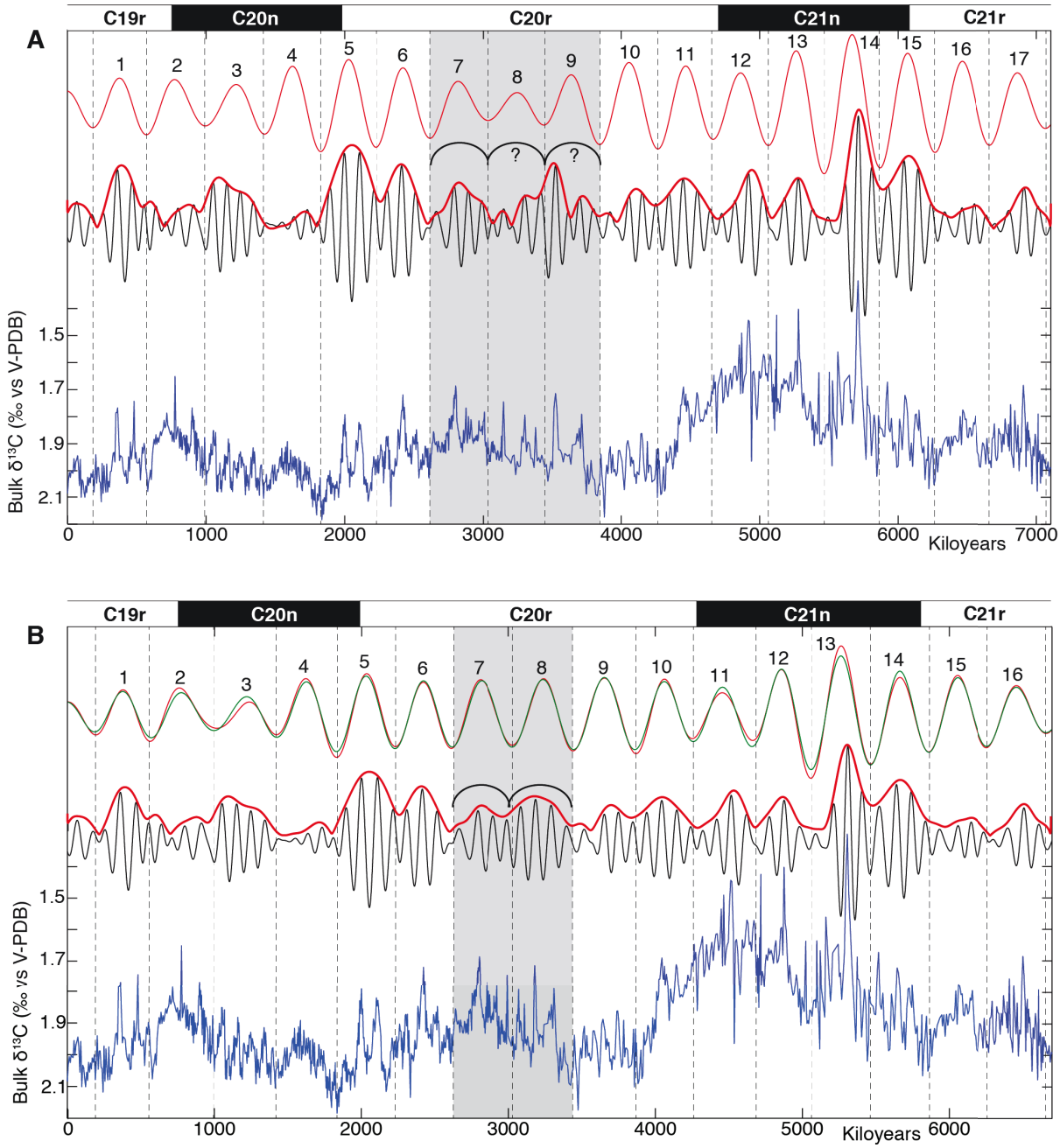

Supplementary Figure 2.7: 405 kyr orbital tuning of $\delta^{13}C$ variations at ODP Site 1263 (data are from Westerhold et al., 2015). **(A)** 405 kyr tuning of the 17 interpreted g2-g5 cycles, according to Westerhold et al. (2015). Amplitude modulation (AM) envelopes of the short eccentricity are also shown. **(B)** 405 kyr tuning of the 16 interpreted g2-g5 cycles, according to the present study. AM envelopes of the short eccentricity are also shown. The grey shaded area indicates the doubtful interval, including three g2-g5 cycles, according to Westerhold et al. (2015), and only two g2-g5 cycles, according to the present study. Black arcs within the doubtful interval indicate well-expressed AM envelopes (without question marks), and poorly expressed AM envelopes (with question marks).

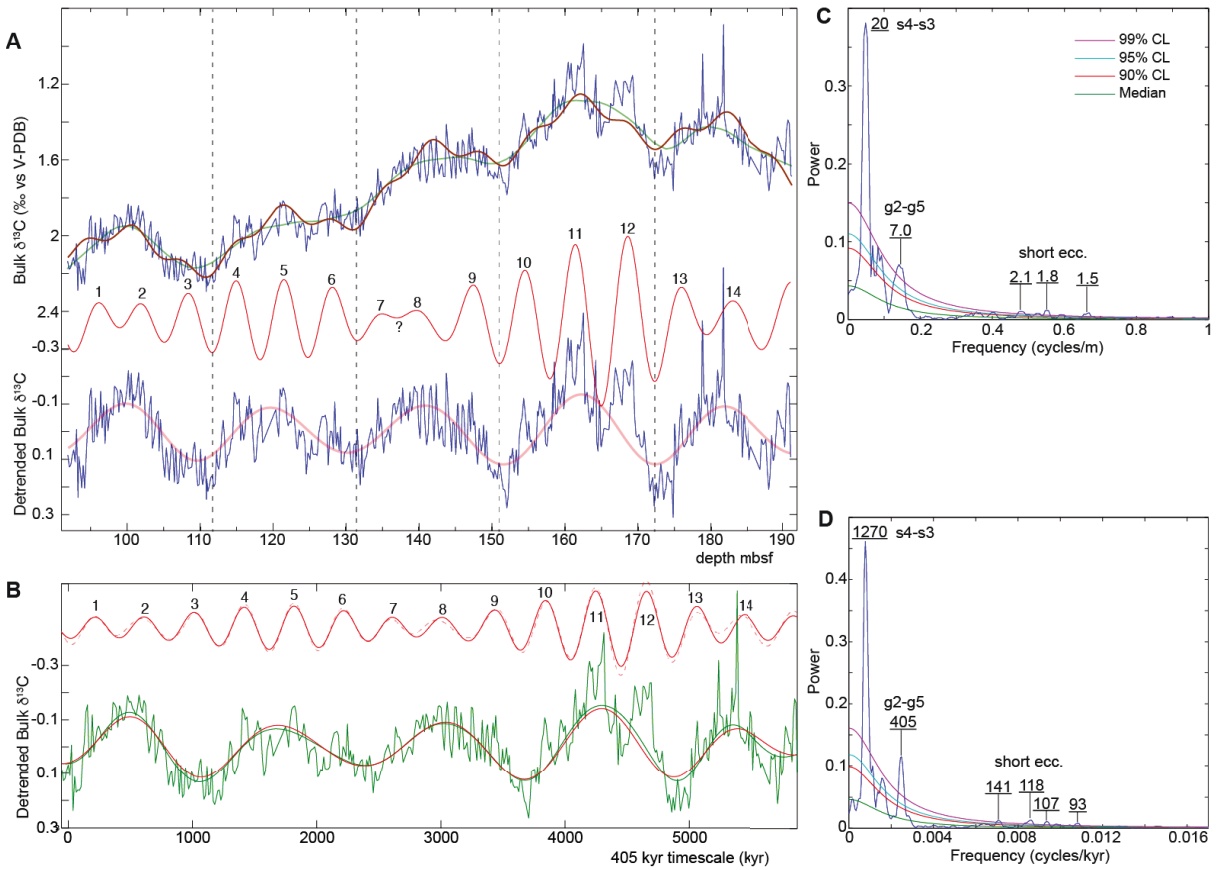

Supplementary Figure 2.8: Time-series analysis of $\delta^{13}C$ variations at Hole 702B (data are from Westerhold et al., 2015). **(A)** Upper curves: the raw $\delta^{13}C$ data for the interval 91.85 to 191.29 mbsf, along with 12% weighted average fit (green curve) and least-square optimal fitting (brown curve). Middle curve: 7 m bandpass filtering to extract the g2-g5 related cycles (numbered from 1 to 14). Question mark indicates the two amalgamated cycles 7 and 8, which are highlighted either in the least-square fit or in the bandpass filter output. Lower curves: Detrended $\delta^{13}C$ data using a 40% weighted average, along with 20 m bandpass filtering to extract the s3-s6 related cycles (see spectra in 'C' and 'D'). **(B)** 405 kyr (g2-g5) tuned (detrended) $\delta^{13}C$ data along with bandpass filtering at g2-g5 eccentricity (upper curve) and s3-s4 (1.2 Myr) obliquity (lower curve) bands. **(C)** 2pi-MTM spectrum of the detrended $\delta^{13}C$ data (in depth domain) after 1x padding of the data. **(D)** 2pi-MTM spectrum of the 405 kyr tuned (detrended) $\delta^{13}C$ data after 1x padding of the data.

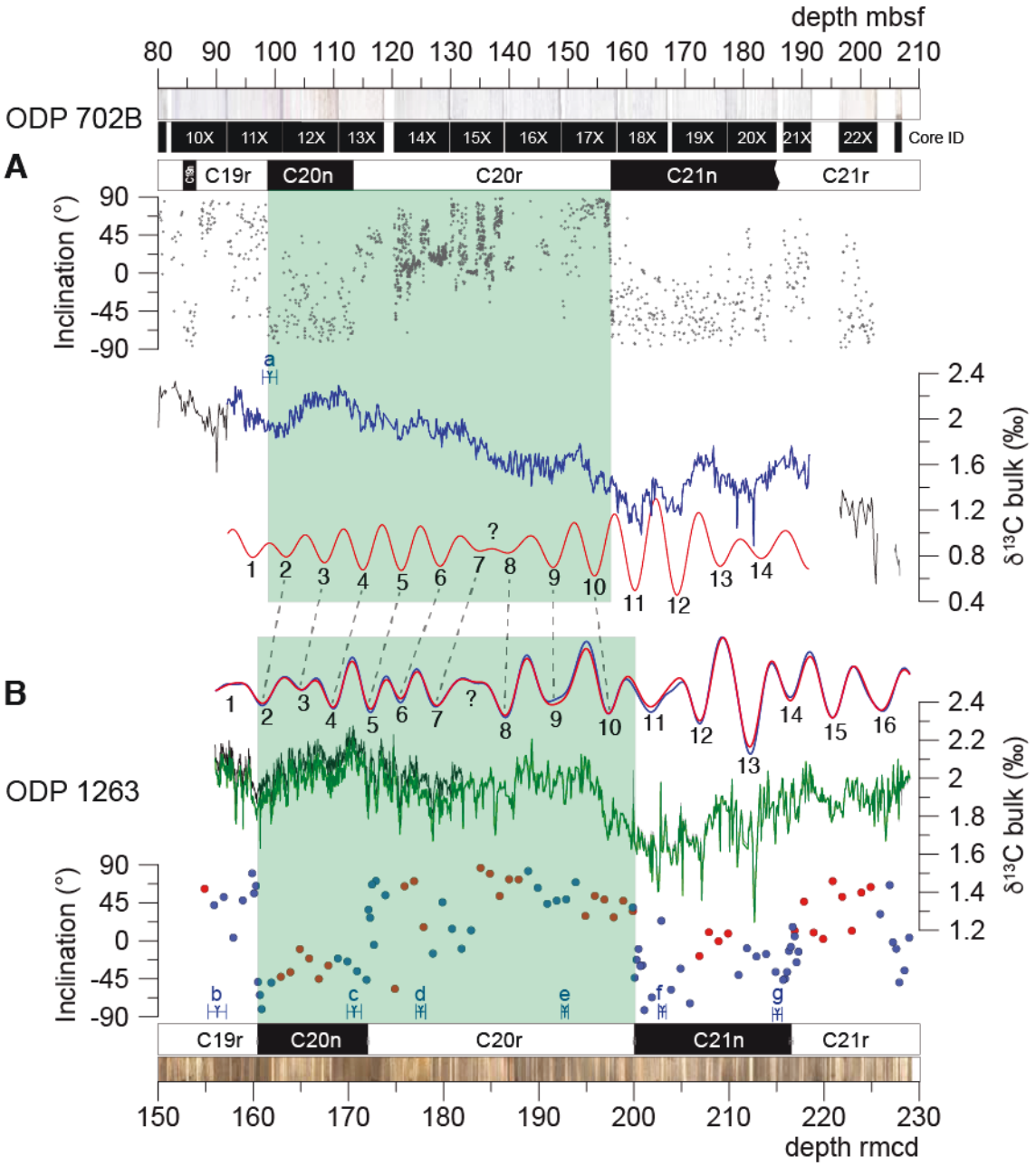

Supplementary Figure 2.9: Integrated stratigraphic correlation between Site 1263 and Hole 702B. **(A)** Hole 702B data: core image and $\delta^{13}C$ data are from Westerhold et al. (2015). Magnetostratigraphic data are from Clement and Hailwood (1991). **(B)** All Site's 1263 data are from Westerhold et al. (2015). Numbers with error bars mark calcareous nannofossil events 'a' to 'g': a, base *R. umbilicus* >14 μm; b, top *Nannotetrina spp.*; c, top *N. fulgens*; d, top *C. gigas*; e, base *C. gigas*; f, base *N. fulgens*; g, top *D. lodoensis*. Bandpass filtering of $\delta^{13}C$ data in depth domain, performed to recover the 405 kyr eccentricity cycles (numbered as in Supplementary Figure 2.8 for Hole 702B, and as in Supplementary Figure 2.6 for Site 1263). Note that Hole 702B data support the hypothesis that the combined C20n and C20r interval contains approximately nine 405 kyr eccentricity cycles (see also Supplementary Figure 2.8).

References

Clement, B.M., Hailwood, E.A., 1991. Magnetostratigraphy of sediments from Sites 701 and 702, in: Proc. ODP, Sci. Results, 114: College Station, TX (Ocean Drilling Program), edited by: Ciesielski, P. F., Kristoffersen, Y., et al., College Station, TX, Publisher: Ocean Drilling Program, Texas Aand M University 359–366, doi:10.2973/odp.proc.sr.114.156.1991.

Expedition 342 Scientists, 2012. Paleogene Newfoundland sediment drifts. *IODP Prel. Rept.,* 342. doi:10.2204/iodp.pr.342.2012.

Laskar, J., Robutel, P., Joutel, F., Gastineau, M., Correia, A.C.M., Levrard, B., 2004. A long-term numerical solution for the insolution quantities of the Earth. Astron. Astrophys. 428, 261–285.

Norris, R.D., Wilson, P.A., Blum, P., and the Expedition 342 Scientists, eds., 2014. Proceedings of the Integrated Ocean Drilling Program, Volume 342: College Station, TX.

Smith, M.E., Chamberlain, K.R., Singer, B.S., and Carroll, A.R., 2010, Eocene clocks agree: Coeval 40Ar/39Ar, U-Pb, and astronomical ages from the Green River Formation. Geology 38, no. 6, 527–530, doi:10.1130/G30630.1.

Tsukui, K., Clyde, W. C., 2012. Fine-tuning the calibration of the early to middle Eocene geomagnetic polarity time scale: Paleomagnetism of radioisotopically dated tuffs from Laramide foreland basins. Geol. Soc. Am. Bull. 124, 870–885.

Walsh, S.L., 1996. Theoretical biochronology, the Bridgerian-Uintan boundary and the “Shoshonian subage” of the Uintan, in Prothero, D.R., and Emry, R.J., eds., The Terrestrial Eocene-Oligocene Transition in North America. Cambridge, UK, Cambridge University Press, p. 52–74.

Westerhold, T., Röhl, U., 2013. Orbital pacing of Eocene climate during the Middle Eocene climate optimum and the chron C19r event: Missing link found in the tropical western Atlantic. Geochem. Geophy. Geosy. 14, 4811–4825, doi:10.1002/ggge.20293.

Westerhold, T., Röhl, U., Pälike, H., Wilkens, R., Wilson, P. A., Acton, G., 2014. Orbitally tuned timescale and astronomical forcing in the middle Eocene to early Oligocene. Clim. Past 10, 955–973, doi:10.5194/cp-10-955-2014.

Westerhold, T., Röhl, U., Frederichs, T., Bohaty, S.M., Zachos, J.C., 2015. Astronomical calibration of the geological timescale: closing the middle Eocene gap. Clim. Past 11, 1181–1195.

Supplementary Information Chapter 3: *Astronomically Paced Changes in Overturning Circulation in the Western North Atlantic during the Middle Eocene*

Maximilian Vahlenkamp[1], Igor Niezgodzki[2,3], David De Vleeschouwer[1], Torsten Bickert[1], Dustin Harper[4], Sandra Kirtland Turner[5], Gerrit Lohmann[2], Philip Sexton[6], James Zachos[4], Heiko Pälike[1]

[1] MARUM - Center for Marine Environmental Sciences, University of Bremen, Leobenerstr, 28359 Bremen, Germany (mvahlenkamp@marum.de),

[2] Alfred Wegener Institute Helmholtz Centre for Polar and Marine Research, Bussestr. 24, 27570 Bremerhaven, Germany

[3] ING PAN - Institute of Geological Sciences Polish Academy of Sciences, Research Center in Kraków, Kraków, Poland

[4] Department of Earth & Planetary Science, University of California, Santa Cruz, CA 95064, USA

[5] Department of Earth Sciences, University of California, Riverside, Riverside, CA 92521, USA

[6] School of Environment, Earth & Ecosystem Sciences, The Open University, Milton Keynes MK7 6AA, UK

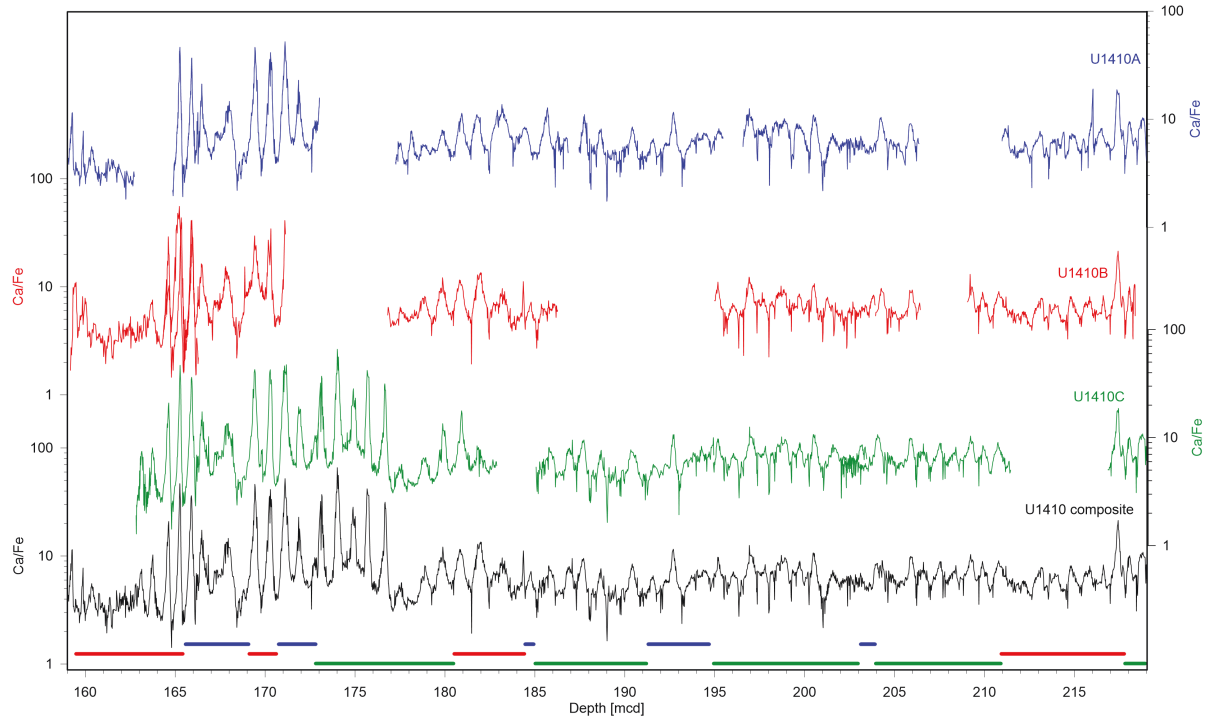

Supplementary Figure 3.1: U1410 splicing strategy. XRF-derived Ca/Fe element ratios for Hole A (blue), B (red), and C (green). The cored depth scale for each Hole has been adjusted to the composite depth scale. The spliced U1410 record (black) is constructed according to the splice table. The coloured bars on the bottom of the figure indicate the Hole from which samples were taken for benthic stable oxygen and carbon isotope measurements.

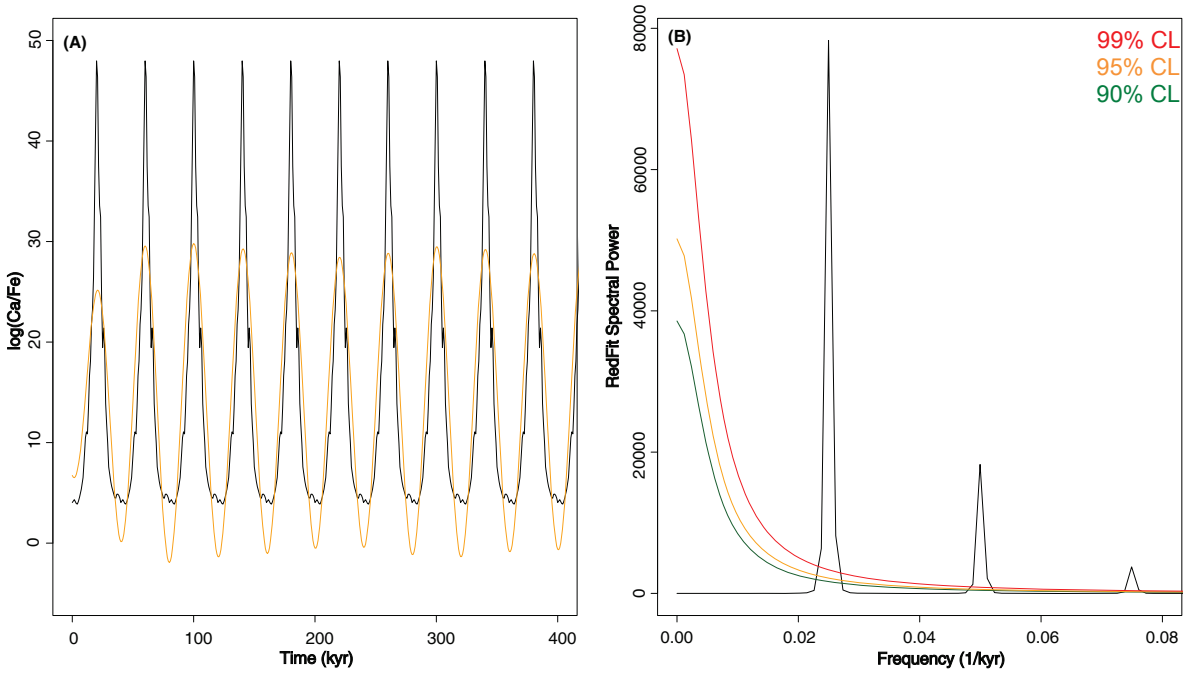

Supplementary Figure 3.2: The effect of harmonics on power spectra. (a) Non-sinusoidal periodic waveform, constructed by repeating the cycle in log(Ca/Fe) between 43.780 – 43.823 Ma (Figure 2b). The orange line represents the obliquity-related fundamental frequency in the time domain. It was obtained by bandpass filtering the non-sinusoidal periodic signal between 0.02 – 0.033 cycles/m. (b) Redfit spectrum, showing the obliquity-related fundamental frequency in the frequency domain at 0.025 cycles/m, as well as the first and second harmonic.

Supplementary Table 3.1: Stable carbon and oxygen isotope values of benthic foraminifera *Nuttalides truempyi* at Site U1410.

Sample Code	Depth (mbsf)	δ13C	δ18O
1410-17A-1-130	152.30	0.06	0.04
1410-17A-1-134	152.34	0.05	-0.06
1410-17A-1-138	152.38	0.12	-0.01
1410-17A-1-142	152.42	-0.01	-0.19
1410-17A-1-146	152.46	0.01	-0.08
1410-17A-2-001	152.51	-0.05	-0.08
1410-17A-2-005	152.55	-0.12	-0.04
1410-17A-2-009	152.59	0.15	-0.07
1410-17A-2-013	152.63	0.09	-0.12
1410-17A-2-017	152.67	0.06	-0.14
1410-17A-2-021	152.71	0.08	-0.11
1410-17A-2-025	152.75	0.16	-0.21
1410-17A-2-029	152.79	-0.06	-0.17
1410-17A-2-033	152.83	0.16	-0.24
1410-17A-2-037	152.87	0.11	-0.28
1410-17A-2-041	152.91	0.08	-0.25
1410-17A-2-045	152.95	0.20	-0.11
1410-17A-2-053	153.03	0.17	-0.13
1410-17A-2-057	153.07	0.17	-0.13
1410-17A-2-061	153.11	0.42	-0.06
1410-17A-2-065	153.15	0.32	0.09
1410-17A-2-069	153.19	0.33	0.04
1410-17A-2-073	153.23	0.37	0.07
1410-17A-2-077	153.27	0.45	0.09
1410-17A-2-081	153.31	0.31	0.17
1410-17A-2-085	153.35	0.24	-0.04
1410-17A-2-089	153.39	0.33	0.07
1410-17A-2-093	153.43	0.40	0.11
1410-17A-2-097	153.47	0.51	0.10
1410-17A-2-101	153.51	0.37	-0.13
1410-17A-2-105	153.55	0.42	-0.18
1410-17A-2-110	153.60	0.46	0.10
1410-17A-2-113	153.63	0.20	-0.08
1410-17A-2-117	153.67	0.51	0.03
1410-17A-2-122	153.71	0.40	0.03
1410-17A-2-125	153.75	0.40	0.06
1410-17A-2-129	153.79	0.41	0.06
1410-17A-2-133	153.83	0.30	0.02
1410-17A-2-137	153.87	0.25	-0.02
1410-17A-2-141	153.91	0.39	0.04
1410-17A-2-145	153.95	0.24	-0.21
1410-17A-2-149	153.99	0.40	0.04
1410-17A-3-003	154.03	0.35	0.08
1410-17A-3-007	154.07	0.41	0.15
1410-17A-3-011	154.11	0.42	0.10
1410-17A-3-015	154.15	0.32	0.06
1410-17A-3-019	154.19	0.42	0.08
1410-17A-3-025	154.23	0.26	0.12
1410-17A-3-031	154.31	0.29	0.03
1410-17A-3-035	154.35	0.36	0.18
1410-17A-3-039	154.39	0.39	0.10
1410-17A-3-043	154.43	0.32	0.01
1410-17A-3-047	154.47	0.27	0.01
1410-17A-3-051	154.51	0.14	-0.04
1410-17A-3-055	154.55	0.25	-0.03
1410-17A-3-058	154.58	0.30	-0.02
1410-17A-3-063	154.63	0.30	0.10
1410-17A-3-067	154.67	0.30	0.12
1410-17A-3-071	154.71	0.25	0.19
1410-17A-3-079	154.79	0.34	0.02
1410-17A-3-083	154.83	0.28	0.07
1410-17A-3-087	154.87	0.28	0.05
1410-17A-3-091	154.91	0.36	0.07
1410-17A-3-095	154.95	0.33	0.15
1410-17A-3-099	154.99	0.35	0.02
1410-17A-3-103	155.03	0.34	0.00
1410-17A-3-107	155.07	0.23	0.08
1410-17A-3-111	155.11	0.39	0.11
1410-17A-3-115	155.15	0.31	0.08
1410-17A-3-119	155.19	0.34	0.11
1410-17A-3-123	155.23	0.33	0.04
1410-17A-3-127	155.27	0.28	0.05
1410-17A-3-131	155.31	0.33	0.03
1410-17A-3-135	155.35	0.35	-0.01
1410-17A-3-139	155.39	0.27	0.08
1410-17A-3-143	155.43	0.33	0.04

Continued on next page

Supplementary Table 3.1 – continued from previous page

Sample Code	Depth (mbsf)	δ13C	δ18O
1410-17A-3-147	155.47	0.34	0.04
1410-17A-4-003	155.53	0.17	0.14
1410-17A-4-007	155.57	0.19	0.18
1410-17A-4-011	155.61	0.14	0.15
1410-17A-4-015	155.65	0.33	0.03
1410-17A-4-019	155.69	0.21	0.04
1410-17A-4-023	155.73	0.28	0.25
1410-17A-4-027	155.77	0.27	0.12
1410-17A-4-035	155.85	0.32	0.12
1410-17A-4-039	155.89	0.25	0.14
1410-17A-4-043	155.93	0.16	0.05
1410-17A-4-047	155.97	0.07	0.17
1410-17A-4-051	156.01	0.11	0.09
1410-17A-4-055	156.05	0.19	0.14
1410-17A-4-059	156.09	-0.02	0.20
1410-17A-4-063	156.13	0.13	0.04
1410-17A-4-067	156.17	0.15	0.21
1410-17A-4-071	156.21	0.11	-0.02
1410-17A-4-075	156.25	0.28	-0.02
1410-17A-4-079	156.29	0.09	0.20
1410-17A-4-083	156.33	0.07	0.09
1410-17A-4-087	156.37	-0.04	0.06
1410-17A-4-095	156.45	0.13	-0.02
1410-17A-4-099	156.49	-0.05	-0.10
1410-17A-5-117	158.17	0.16	-0.16
1410-17A-5-125	158.25	0.02	-0.19
1410-17A-5-129	158.29	0.12	-0.19
1410-17A-5-133	158.33	0.02	-0.28
1410-17A-5-141	158.41	0.01	-0.19
1410-17A-5-145	158.45	0.00	-0.25
1410-17A-6-001	158.51	0.00	-0.28
1410-17A-6-005	158.55	-0.05	-0.13
1410-17A-6-009	158.59	0.10	-0.13
1410-17A-6-013	158.63	0.10	0.07
1410-17A-6-017	158.67	0.22	0.14
1410-17A-6-021	158.71	0.37	0.22
1410-17A-6-025	158.75	0.33	0.29
1410-17A-6-037	158.87	0.43	0.32
1410-17A-6-041	158.91	0.35	0.22
1410-17A-6-045	158.95	0.26	0.31
1410-17A-6-049	158.99	0.33	0.30
1410-17A-6-053	159.03	0.36	0.28
1410-17A-6-057	159.07	0.38	0.34
1410-17A-6-061	159.11	0.34	0.28
1410-17A-6-069	159.19	0.34	0.15
1410-17A-6-073	159.23	0.38	0.25
1410-17A-6-077	159.27	0.33	0.04
1410-17A-6-081	159.31	0.38	0.21
1410-17A-6-085	159.35	0.36	0.19
1410-17A-6-089	159.39	0.30	0.11
1410-17A-6-093	159.43	0.38	0.22
1410-17A-6-097	159.47	0.30	0.18
1410-17A-6-101	159.51	0.23	0.34
1410-17A-6-105	159.55	0.34	0.23
1410-17A-6-109	159.59	0.29	0.10
1410-17A-6-113	159.63	0.30	0.22
1410-17A-6-117	159.67	0.26	0.26
1410-17A-6-121	159.71	0.33	0.20
1410-17A-6-125	159.75	0.35	0.28
1410-17A-6-129	159.79	0.28	0.19
1410-17A-7-11	160.02	0.32	0.23
1410-17A-7-15	160.06	0.32	0.23
1410-17A-7-19	160.10	0.22	0.20
1410-17A-7-23	160.14	0.24	0.24
1410-17A-7-27	160.18	0.32	0.26
1410-17A-7-31	160.22	0.32	0.17
1410-18A-5-053	167.13	0.16	0.19
1410-18A-5-057	167.17	0.26	0.00
1410-18A-5-061	167.21	0.32	0.13
1410-18A-5-065	167.25	0.31	0.06
1410-18A-5-069	167.29	0.24	0.12
1410-18A-5-081	167.41	0.25	0.24
1410-18A-5-085	167.45	0.25	0.08
1410-18A-5-089	167.49	0.31	0.14
1410-18A-5-093	167.53	0.25	0.18
1410-18A-5-097	167.57	0.16	-0.07
1410-19A-4-073	175.43	0.14	-0.02
1410-19A-4-077	175.47	0.20	0.19
1410-19A-4-081	175.51	0.08	-0.04
1410-19A-4-085	175.55	0.13	0.05

Continued on next page

Supplementary Table 3.1 – continued from previous page

Sample Code	Depth (mbsf)	δ13C	δ18O	Sample Code	Depth (mbsf)	δ13C	δ18O
1410-19A-4-089	175.59	0.08	-0.17	1410-19A-5-141	177.61	0.24	0.06
1410-19A-4-093	175.63	0.16	-0.02	1410-19A-6-001	177.71	0.17	0.02
1410-19A-4-097	175.67	0.11	-0.17	1410-19A-6-005	177.75	0.22	0.11
1410-19A-4-105	175.75	0.11	-0.2	1410-19A-6-013	177.83	0.28	-0.03
1410-19A-4-109	175.79	0.06	-0.19	1410-19A-6-021	177.91	0.28	0.05
1410-19A-4-121	175.91	0.11	-0.22	1410-19A-6-025	177.95	0.29	-0.02
1410-19A-4-125	175.95	0.22	0.01	1410-19A-6-029	177.99	0.28	0.04
1410-19A-4-129	175.99	0.14	0.07	1410-19A-6-033	178.03	0.29	0.06
1410-19A-4-133	176.03	0.21	-0.17	1410-19A-6-037	178.07	0.23	-0.04
1410-19A-4-137	176.07	0.20	0.05	1410-19A-6-041	178.11	0.23	-0.02
1410-19A-4-141	176.11	0.21	0.01	1410-19A-6-045	178.15	0.22	-0.02
1410-19A-4-145	176.15	0.15	0.09	1410-19A-6-049	178.19	0.17	-0.06
1410-19A-4-149	176.19	0.19	-0.07	1410-19A-6-053	178.23	0.21	-0.07
1410-19A-5-001	176.21	0.15	-0.14	1410-19A-6-057	178.27	0.18	-0.06
1410-19A-5-005	176.25	0.17	-0.02	1410-19A-6-061	178.31	0.12	-0.06
1410-19A-5-013	176.33	0.17	-0.11	1410-19A-6-065	178.35	0.19	0.03
1410-19A-5-025	176.45	0.11	-0.19	1410-19A-6-069	178.39	0.18	0.01
1410-19A-5-029	176.49	0.12	-0.15	1410-19A-6-073	178.43	0.22	0.01
1410-19A-5-033	176.53	0.07	-0.03	1410-19A-6-081	178.51	0.13	0.02
1410-19A-5-045	176.65	-0.01	-0.25	1410-19A-6-093	178.63	0.26	0.15
1410-19A-5-049	176.69	0.03	-0.34	1410-19A-6-097	178.67	0.26	0.15
1410-19A-5-057	176.77	0.05	-0.15	1410-19A-6-105	178.75	0.15	0.07
1410-19A-5-061	176.81	0.02	-0.13	1410-19A-6-109	178.79	0.31	0.16
1410-19A-5-065	176.85	0.07	-0.08	1410-19A-6-113	177.79	0.16	0.08
1410-19A-5-069	176.89	0.17	0.02	1410-20A-5-071	186.49	0.14	0.04
1410-19A-5-073	176.93	0.10	-0.05	1410-20A-5-077	186.57	0.28	0.03
1410-19A-5-077	176.97	0.11	-0.06	1410-20A-5-081	186.61	0.16	0.18
1410-19A-5-081	177.01	0.06	-0.17	1410-20A-5-085	186.65	0.17	0.16
1410-19A-5-085	177.05	0.09	0.02	1410-20A-5-089	186.69	0.37	0.03
1410-19A-5-093	177.13	0.18	0.08	1410-20A-5-093	186.73	0.30	0.01
1410-19A-5-097	177.17	0.16	0.02	1410-20A-5-097	186.77	0.29	0.11
1410-19A-5-103	177.21	0.14	-0.15	1410-20A-5-101	186.81	0.37	0.15
1410-19A-5-105	177.25	0.27	0.01	1410-20A-5-105	186.85	0.24	0.02
1410-19A-5-113	176.29	0.12	-0.07	1410-20A-5-109	186.89	0.32	0.12
1410-19A-5-113	177.33	0.25	0.08	1410-20A-5-113	186.93	0.37	0.01
1410-19A-5-117	177.37	0.21	0.15	1410-20A-5-121	187.01	0.29	-0.05
1410-19A-5-121	177.41	0.24	-0.03	1410-20A-5-125	187.05	0.28	0.14
1410-19A-5-129	177.49	0.26	0.13	1410-20A-5-129	187.09	0.35	0.15
1410-19A-5-133	177.53	0.28	0.20	1410-20A-5-133	187.13	0.27	0.10
1410-19A-5-137	177.57	-0.02	-0.21	1410-20A-5-137	187.17	0.28	0.08

Continued on next page

Supplementary Table 3.1 – continued from previous page

Sample Code	Depth (mbsf)	δ13C	δ18O	Sample Code	Depth (mbsf)	δ13C	δ18O
1410-20A-5-141	187.21	0.23	0.10	1410-18B-2-075	150.05	0.48	0.09
1410-20A-5-145	187.25	0.22	0.03	1410-18B-2-079	150.09	0.47	0.14
1410-18B-1-040	148.20	0.39	0.12	1410-18B-2-083	150.13	0.38	0.01
1410-18B-1-048	148.28	0.37	0.15	1410-18B-2-087	150.17	0.45	0.12
1410-18B-1-052	148.32	-0.07	-0.09	1410-18B-2-091	150.21	0.42	0.20
1410-18B-1-056	148.36	0.40	0.25	1410-18B-2-095	150.25	0.34	0.19
1410-18B-1-060	148.40	0.32	0.06	1410-18B-2-099	150.29	0.23	-0.03
1410-18B-1-064	148.44	0.29	0.08	1410-18B-2-102	150.32	0.33	0.17
1410-18B-1-068	148.48	0.44	0.14	1410-18B-2-107	150.37	0.43	0.15
1410-18B-1-076	148.56	0.33	0.03	1410-18B-2-111	150.41	0.37	-0.07
1410-18B-1-080	148.60	0.26	0.06	1410-18B-2-115	150.45	0.31	0.14
1410-18B-1-084	148.64	0.37	0.17	1410-18B-2-119	150.49	0.33	-0.04
1410-18B-1-088	148.68	0.37	0.20	1410-18B-2-123	150.53	0.30	0.03
1410-18B-1-092	148.72	0.32	0.09	1410-18B-2-127	150.57	0.33	0.04
1410-18B-1-096	148.76	0.30	0.21	1410-18B-2-131	150.61	0.30	0.21
1410-18B-1-104	148.84	0.39	0.13	1410-18B-2-135	150.65	0.28	0.06
1410-18B-1-108	148.88	0.43	0.21	1410-18B-2-139	150.69	-0.01	-0.11
1410-18B-1-112	148.92	0.45	0.18	1410-18B-2-143	150.73	0.37	0.13
1410-18B-1-116	148.96	0.50	0.28	1410-18B-2-147	150.77	0.35	0.21
1410-18B-1-120	149.00	0.47	0.24	1410-18B-3-001	150.81	0.33	0.17
1410-18B-1-124	149.04	0.44	0.18	1410-18B-3-005	150.85	0.32	0.24
1410-18B-1-128	149.08	0.16	0.10	1410-18B-3-013	150.93	0.38	0.00
1410-18B-1-132	149.12	0.36	0.03	1410-18B-3-017	150.97	0.15	0.22
1410-18B-1-136	149.16	0.41	0.11	1410-18B-3-021	151.01	0.28	0.05
1410-18B-1-140	149.20	0.38	0.23	1410-18B-3-025	151.05	0.30	0.19
1410-18B-1-144	149.24	0.44	0.04	1410-18B-3-029	151.09	0.24	-0.03
1410-18B-1-148	149.28	0.40	0.05	1410-18B-3-033	151.13	0.33	0.17
1410-18B-2-009	149.39	0.39	0.18	1410-18B-3-037	151.17	0.34	0.14
1410-18B-2-013	149.43	0.41	0.22	1410-18B-3-041	151.21	0.33	0.11
1410-18B-2-017	149.47	0.40	0.11	1410-18B-3-045	151.25	0.26	-0.10
1410-18B-2-021	149.51	0.37	0.19	1410-18B-3-049	151.29	0.40	0.14
1410-18B-2-025	149.55	0.42	0.04	1410-18B-3-052.5	151.33	0.30	0.08
1410-18B-2-029	149.59	0.37	0.05	1410-18B-3-061	151.41	0.34	-0.03
1410-18B-2-033	149.63	0.37	0.11	1410-18B-3-065	151.45	0.33	0.08
1410-18B-2-041	149.71	0.31	0.10	1410-18B-3-069	151.49	0.32	0.18
1410-18B-2-043	149.73	0.34	0.17	1410-18B-3-073	151.53	0.31	0.11
1410-18B-2-058	149.88	0.35	0.10	1410-18B-3-085	151.65	0.27	0.04
1410-18B-2-063	149.93	0.33	-0.08	1410-18B-3-089	151.69	0.28	0.09
1410-18B-2-067	149.97	0.27	0.08	1410-18B-3-093	151.73	0.30	0.14
1410-18B-2-071	150.01	0.34	0.16	1410-18B-3-097	151.77	0.34	0.12

Continued on next page

Supplementary Table 3.1 – continued from previous page

Sample Code	Depth (mbsf)	δ13C	δ18O
1410-18B-3-101	151.81	0.25	0.05
1410-18B-3-109	151.89	0.21	-0.15
1410-18B-3-113	151.93	0.09	0.13
1410-18B-3-117	151.97	0.29	-0.06
1410-18B-3-121	152.01	0.24	-0.44
1410-18B-3-125	152.05	0.31	0.04
1410-18B-3-129	152.09	0.18	0.07
1410-18B-3-133	152.13	0.14	-0.12
1410-18B-3-137	152.17	0.30	-0.02
1410-18B-3-141	152.21	-0.09	-0.07
1410-18B-3-145	152.25	0.02	-0.15
1410-18B-3-149	152.29	-0.03	-0.21
1410-18B-4-005	152.35	-0.03	-0.21
1410-18B-4-013	152.43	0.20	0.05
1410-18B-4-017	152.47	-0.03	-0.24
1410-18B-4-021	152.51	-0.17	-0.43
1410-18B-4-025	152.55	-0.04	-0.16
1410-18B-4-029	152.59	-0.01	-0.13
1410-18B-4-033	152.63	0.10	-0.18
1410-18B-4-037	152.67	0.03	-0.12
1410-18B-4-041	152.71	0.03	-0.14
1410-18B-4-045	152.75	-0.05	-0.01
1410-19B-5-101	160.81	0.45	0.27
1410-19B-5-105	160.85	0.42	0.19
1410-19B-5-109	160.89	0.40	0.29
1410-19B-5-113	160.93	0.39	0.20
1410-19B-5-117	160.97	0.19	0.21
1410-19B-5-129	161.09	0.48	0.26
1410-19B-5-133	161.13	0.48	0.40
1410-19B-5-137	161.17	0.51	0.39
1410-19B-5-141	161.21	0.44	0.34
1410-19B-5-149	161.29	0.43	0.31
1410-19B-5-89	160.69	0.46	-0.17
1410-19B-5-93	160.73	0.47	0.34
1410-19B-6-001	161.31	0.38	0.33
1410-19B-6-009	161.39	0.57	-0.13
1410-19B-6-017	161.47	0.37	0.29
1410-19B-6-025	161.55	0.36	0.10
1410-19B-6-037	161.67	0.13	0.18
1410-19B-6-061	161.91	0.14	0.10
1410-19B-6-085	162.15	0.39	0.26
1410-19B-7-009	162.3	0.24	0.27
1410-20B-3-059	167.01	0.20	0.19
1410-20B-3-067	167.09	0.23	0.18
1410-20B-3-071	167.13	0.22	0.16
1410-20B-3-075	167.17	0.22	0.11
1410-20B-3-079	167.21	0.21	0.18
1410-20B-3-087	167.29	0.19	0.15
1410-20B-3-091	167.33	0.12	0.04
1410-20B-3-095	167.37	0.14	0.09
1410-20B-3-099	167.41	0.06	0.01
1410-20B-3-103	167.45	0.06	-0.11
1410-20B-3-107	167.49	0.04	-0.10
1410-20B-3-111	167.53	0.17	0.17
1410-20B-3-115	167.57	0.30	0.26
1410-20B-3-119	167.61	0.25	0.14
1410-20B-3-123	167.65	-0.08	-0.24
1410-20B-3-127	167.69	0.26	0.25
1410-20B-3-131	167.73	0.19	0.33
1410-20B-3-135	167.77	0.21	0.24
1410-20B-3-139	167.81	0.26	0.25
1410-20B-3-143	167.85	0.24	0.31
1410-20B-4-001	167.93	0.08	0.33
1410-20B-4-005	167.97	0.19	0.23
1410-20B-4-009	168.01	0.31	0.27
1410-20B-4-013	168.05	0.13	0.18
1410-20B-4-017	168.09	0.12	0.16
1410-20B-4-021	168.13	0.16	0.18
1410-20B-4-025	168.17	0.16	0.14
1410-20B-4-033	168.25	0.21	0.14
1410-20B-4-041	168.33	0.13	0.00
1410-20B-4-045	168.37	0.11	0.04
1410-20B-4-049	168.41	0.03	-0.01
1410-20B-4-053	168.45	0.16	0.02
1410-20B-4-057	168.49	0.14	0.00
1410-20B-4-061	168.53	0.14	0.02
1410-20B-4-065	168.57	0.18	0.18
1410-20B-4-069	168.61	0.23	0.22
1410-20B-4-073	168.65	0.20	0.12
1410-20B-4-077	168.69	0.23	0.09

Continued on next page

Supplementary Table 3.1 – continued from previous page

Sample Code	Depth (mbsf)	δ13C	δ18O	Sample Code	Depth (mbsf)	δ13C	δ18O
1410-20B-4-085	168.77	0.33	0.20	1410-20B-5-105	170.47	0.20	0.17
1410-20B-4-089	168.81	0.28	0.25	1410-20B-5-109	170.51	0.21	0.22
1410-20B-4-093	168.85	0.23	0.20	1410-20B-5-113	170.55	0.17	0.00
1410-20B-4-097	168.89	0.36	0.23	1410-20B-5-117	170.59	0.14	0.07
1410-20B-4-101	168.93	0.31	0.27	1410-20B-5-133	170.75	0.22	-0.17
1410-20B-4-105	168.97	0.21	0.22	1410-20B-5-137	170.79	0.21	0.13
1410-20B-4-109	169.01	0.16	0.23	1410-20B-5-145	170.87	0.22	0.08
1410-20B-4-113	169.05	0.33	0.27	1410-20B-5-149	170.91	0.25	0.33
1410-20B-4-117	169.09	0.31	0.19	1410-23B-2-057	189.67	0.27	-0.06
1410-20B-4-121	169.13	0.41	0.26	1410-23B-2-061	189.71	0.22	-0.33
1410-20B-4-125	169.17	0.31	0.28	1410-23B-2-069	189.79	0.28	0.02
1410-20B-4-129	169.21	0.33	0.29	1410-23B-2-073	189.83	0.29	0.05
1410-20B-4-133	169.25	0.39	0.19	1410-23B-2-081	189.91	0.21	-0.20
1410-20B-4-137	169.29	0.22	0.27	1410-23B-2-085	189.95	0.31	-0.04
1410-20B-4-141	169.33	0.22	0.23	1410-23B-2-089	189.99	0.33	0.03
1410-20B-4-145	169.37	0.28	0.22	1410-23B-2-093	190.03	0.28	0.09
1410-20B-4-149	169.41	0.18	0.12	1410-23B-2-097	190.07	0.25	0.03
1410-20B-5-001	169.43	0.25	0.02	1410-23B-2-101	190.11	0.35	0.24
1410-20B-5-005	169.47	0.21	0.12	1410-23B-2-105	190.15	0.34	0.17
1410-20B-5-009	169.51	0.28	0.18	1410-23B-2-113	190.23	0.25	0.08
1410-20B-5-013	169.55	0.27	0.17	1410-23B-2-117	190.27	0.23	0.06
1410-20B-5-017	169.59	0.12	-0.18	1410-23B-2-121	190.31	0.30	-0.11
1410-20B-5-021	169.63	0.23	0.07	1410-23B-2-125	190.35	0.32	0.21
1410-20B-5-025	169.67	0.23	0.02	1410-23B-2-129	190.39	0.25	0.06
1410-20B-5-029	169.71	0.31	0.17	1410-23B-2-137	190.47	0.26	0.10
1410-20B-5-033	169.75	0.17	-0.20	1410-23B-2-149	190.59	0.30	0.22
1410-20B-5-037	169.79	0.24	-0.03	1410-23B-3-003	190.63	0.26	0.08
1410-20B-5-045	169.87	0.16	-0.14	1410-23B-3-011	190.71	0.34	0.03
1410-20B-5-049	169.91	0.20	-0.11	1410-23B-3-015	190.75	0.28	0.00
1410-20B-5-053	169.95	0.22	0.11	1410-23B-3-019	190.79	0.28	0.05
1410-20B-5-057	169.99	0.25	0.17	1410-23B-3-023	190.83	0.26	-0.05
1410-20B-5-061	170.03	0.11	-0.21	1410-23B-3-027	190.87	0.29	-0.05
1410-20B-5-065	170.07	0.17	0.00	1410-23B-3-031	190.91	0.31	-0.13
1410-20B-5-077	170.19	0.28	0.24	1410-23B-3-035	190.95	0.23	-0.03
1410-20B-5-081	170.23	0.12	0.05	1410-23B-3-039	190.99	0.37	-0.15
1410-20B-5-085	170.27	0.24	0.08	1410-23B-3-043	191.03	0.28	-0.10
1410-20B-5-089	170.31	0.11	0.17	1410-23B-3-047	191.07	0.28	0.03
1410-20B-5-093	170.35	0.23	0.02	1410-23B-3-059	191.19	0.29	-0.25
1410-20B-5-097	170.39	0.26	0.08	1410-23B-3-063	191.23	0.29	0.03
1410-20B-5-101	170.43	0.22	0.11	1410-23B-3-071	191.31	0.41	0.05

Continued on next page

Supplementary Table 3.1 – continued from previous page

Sample Code	Depth (mbsf)	δ13C	δ18O	Sample Code	Depth (mbsf)	δ13C	δ18O
1410-20B-5-105	170.47	0.20	0.17	1410-23B-3-075	191.35	0.18	0.15
1410-20B-5-109	170.51	0.21	0.22	1410-23B-3-091	191.51	0.17	-0.11
1410-20B-5-113	170.55	0.17	0.00	1410-23B-3-099	191.59	0.37	-0.05
1410-20B-5-117	170.59	0.14	0.07	1410-23B-3-103	191.63	0.18	-0.05
1410-20B-5-133	170.75	0.22	-0.17	1410-23B-3-119	191.79	0.25	-0.19
1410-20B-5-137	170.79	0.21	0.13	1410-23B-3-131	191.91	0.16	0.05
1410-20B-5-145	170.87	0.22	0.08	1410-23B-3-143	192.03	0.25	-0.07
1410-20B-5-149	170.91	0.25	0.33	1410-23B-3-147	192.07	0.23	-0.10
1410-23B-2-057	189.67	0.27	-0.06	1410-23B-4-001	192.11	0.09	-0.33
1410-23B-2-061	189.71	0.22	-0.33	1410-23B-4-005	192.15	0.10	-0.20
1410-23B-2-069	189.79	0.28	0.02	1410-23B-4-009	192.19	0.20	-0.14
1410-23B-2-073	189.83	0.29	0.05	1410-23B-4-013	192.23	0.19	-0.14
1410-23B-2-081	189.91	0.21	-0.20	1410-23B-4-017	192.27	0.10	-0.22
1410-23B-2-085	189.95	0.31	-0.04	1410-23B-4-025	192.35	0.11	-0.15
1410-23B-2-089	189.99	0.33	0.03	1410-23B-4-029	192.39	0.15	-0.26
1410-23B-2-093	190.03	0.28	0.09	1410-23B-4-033	192.43	0.18	-0.11
1410-23B-2-097	190.07	0.25	0.03	1410-23B-4-037	192.47	0.16	-0.30
1410-23B-2-101	190.11	0.35	0.24	1410-23B-4-049	192.59	0.17	-0.22
1410-23B-2-105	190.15	0.34	0.17	1410-23B-4-057	192.67	0.18	-0.43
1410-23B-2-113	190.23	0.25	0.08	1410-23B-4-085	192.95	0.17	-0.21
1410-23B-2-117	190.27	0.23	0.06	1410-23B-4-093	193.03	0.21	-0.09
1410-23B-2-121	190.31	0.30	-0.11	1410-23B-4-098	193.07	0.17	-0.24
1410-23B-2-125	190.35	0.32	0.21	1410-23B-4-101	193.11	0.24	-0.08
1410-23B-2-129	190.39	0.25	0.06	1410-23B-4-105	193.15	0.23	-0.08
1410-23B-2-137	190.47	0.26	0.10	1410-23B-4-109	193.19	0.17	-0.19
1410-23B-2-149	190.59	0.30	0.22	1410-23B-4-117	193.27	0.22	-0.11
1410-23B-3-003	190.63	0.26	0.08	1410-23B-4-121	193.31	0.07	-0.17
1410-23B-3-011	190.71	0.34	0.03	1410-23B-4-125	193.35	0.20	-0.12
1410-23B-3-015	190.75	0.28	0.00	1410-23B-4-129	193.39	0.24	-0.18
1410-23B-3-019	190.79	0.28	0.05	1410-23B-4-133	193.43	0.04	-0.21
1410-23B-3-023	190.83	0.26	-0.05	1410-23B-4-137	193.47	0.19	-0.19
1410-23B-3-027	190.87	0.29	-0.05	1410-23B-4-141	193.51	0.09	-0.37
1410-23B-3-031	190.91	0.31	-0.13	1410-23B-4-145	193.55	0.16	-0.34
1410-23B-3-035	190.95	0.23	-0.03	1410-23B-4-149	193.59	0.08	-0.40
1410-23B-3-039	190.99	0.37	-0.15	1410-23B-5-003	193.63	0.21	-0.22
1410-23B-3-043	191.03	0.28	-0.10	1410-23B-5-007	193.67	0.14	-0.25
1410-23B-3-047	191.07	0.28	0.03	1410-23B-5-011	193.71	0.25	-0.12
1410-23B-3-059	191.19	0.29	-0.25	1410-23B-5-015	193.75	0.25	-0.07
1410-23B-3-063	191.23	0.29	0.03	1410-23B-5-019	193.79	0.11	-0.46
1410-23B-3-071	191.31	0.41	0.05	1410-23B-5-023	193.83	0.26	-0.14

Continued on next page

Supplementary Table 3.1 – continued from previous page

Sample Code	Depth (mbsf)	δ13C	δ18O
1410-23B-5-027	193.87	0.28	-0.01
1410-23B-5-031	193.91	0.20	-0.11
1410-23B-5-035	193.95	0.27	-0.06
1410-23B-5-039	193.99	0.12	-0.38
1410-23B-5-043	194.03	0.20	-0.13
1410-23B-5-047	194.07	0.27	-0.08
1410-23B-5-051	194.11	0.27	-0.06
1410-23B-5-059	194.19	0.25	-0.03
1410-23B-5-067	194.27	0.21	-0.15
1410-23B-5-071	194.31	0.22	-0.12
1410-23B-5-075	194.35	0.19	0.00
1410-23B-5-087	194.47	0.17	0.01
1410-23B-5-103	194.63	0.14	-0.03
1410-23B-5-119	194.79	0.13	-0.02
1410-23B-5-123	194.83	0.25	0.14
1410-23B-5-143	195.03	0.06	0.03
1410-23B-6-001	195.19	0.09	0.09
1410-23B-6-005	195.15	0.34	0.13
1410-23B-6-025	195.35	0.06	-0.14
1410-23B-6-029	195.39	0.09	-0.16
1410-23B-6-033	195.43	-0.13	0.00
1410-23B-6-037	195.47	-0.07	0.04
1410-23B-6-041	195.51	0.08	-0.10
1410-23B-6-045	195.55	0.12	-0.14
1410-23B-6-057	195.67	-0.04	-0.17
1410-23B-6-061	195.71	0.09	0.05
1410-23B-6-065	195.75	-0.03	-0.18
1410-23B-6-069	195.79	0.01	-0.09
1410-23B-6-073	195.83	-0.05	-0.18
1410-23B-6-077	195.87	-0.03	-0.16
1410-23B-6-085	195.95	-0.04	-0.22
1410-23B-6-089	195.99	-0.38	-0.23
1410-23B-6-113	196.23	-0.06	-0.28
1410-23B-6-117	196.27	0.03	-0.09
1410-23B-6-128	196.35	-0.04	0.01
1410-23B-6-133	196.43	-0.05	0.14
1410-23B-6-137	196.47	0.01	0.19
1410-18C-1-055	156.95	0.11	0.02
1410-18C-1-063	157.03	0.26	0.16
1410-18C-1-067	157.07	0.26	0.21
1410-18C-1-071	157.11	0.27	0.17
1410-18C-1-075	157.15	0.27	0.19
1410-18C-1-079	157.19	0.01	-0.14
1410-18C-1-083	157.23	0.20	0.07
1410-18C-1-087	157.27	0.26	0.11
1410-18C-1-095	157.35	0.21	0.02
1410-18C-1-099	157.39	0.01	-0.17
1410-18C-1-107	157.47	0.12	-0.11
1410-18C-1-11	156.51	0.29	0.31
1410-18C-1-111	157.51	0.16	-0.01
1410-18C-1-115	157.55	0.15	-0.16
1410-18C-1-119	157.59	0.08	-0.18
1410-18C-1-127	157.67	0.11	-0.08
1410-18C-1-131	157.71	0.22	0.00
1410-18C-1-135	157.75	0.35	0.04
1410-18C-1-139	157.79	0.30	0.11
1410-18C-1-143	157.83	0.38	0.19
1410-18C-1-147	157.87	0.38	0.17
1410-18C-1-15	156.55	0.20	0.24
1410-18C-1-19	156.59	0.21	0.18
1410-18C-1-27	156.67	0.21	0.07
1410-18C-1-3	156.43	0.18	0.24
1410-18C-1-31	156.71	0.19	0.18
1410-18C-1-39	156.79	0.18	0.13
1410-18C-1-43	156.83	0.21	0.14
1410-18C-1-7	156.47	0.32	0.23
1410-18C-2-009	157.99	0.28	0.16
1410-18C-2-017	158.07	0.40	0.22
1410-18C-2-021	158.11	0.29	0.24
1410-18C-2-029	158.19	0.38	0.28
1410-18C-2-037	158.27	0.36	0.20
1410-18C-2-045	158.35	0.29	0.20
1410-18C-2-049	158.39	0.40	0.24
1410-18C-2-059	158.47	0.18	0.17
1410-18C-2-065	158.55	0.41	0.31
1410-18C-2-077	158.67	0.36	0.17
1410-18C-2-089	158.79	0.32	0.36
1410-18C-2-107	158.97	0.24	0.23
1410-18C-2-111	159.01	0.40	0.15
1410-18C-2-115	159.05	0.19	0.25

Continued on next page

Supplementary Table 3.1 – continued from previous page

Sample Code	Depth (mbsf)	δ13C	δ18O
1410-18C-2-119	159.09	-0.11	0.45
1410-18C-2-123	159.13	0.09	0.13
1410-18C-2-127	159.17	0.14	0.18
1410-18C-2-131	159.21	0.15	0.05
1410-18C-2-135	159.25	0.02	-0.10
1410-18C-2-139	159.29	-0.02	0.00
1410-18C-2-147	159.37	0.09	0.01
1410-18C-3-003	159.43	0.25	0.18
1410-18C-3-007	159.47	0.02	-0.12
1410-18C-3-011	159.51	0.26	0.12
1410-18C-3-015	159.55	0.28	0.21
1410-18C-3-019	159.59	0.20	0.17
1410-18C-3-023	159.63	0.20	0.25
1410-18C-3-027	159.67	0.11	0.13
1410-18C-3-031	159.71	0.22	0.23
1410-18C-3-035	159.75	0.23	0.21
1410-18C-3-039	159.79	0.30	0.07
1410-18C-3-043	159.83	0.22	0.20
1410-18C-3-047	159.87	0.07	0.00
1410-18C-3-051	159.91	0.10	0.04
1410-18C-3-055	159.95	0.20	0.14
1410-18C-3-059	159.99	0.06	0.09
1410-18C-3-067	160.07	0.19	0.10
1410-18C-3-071	160.11	0.10	0.01
1410-18C-3-075	160.15	0.10	-0.01
1410-18C-3-079	160.19	0.02	-0.03
1410-18C-3-083	160.23	0.01	0.09
1410-18C-3-087	160.27	0.03	-0.06
1410-18C-3-091	160.31	0.07	0.17
1410-18C-3-095	160.35	0.06	0.12
1410-18C-3-099	160.39	0.13	0.08
1410-18C-3-103	160.43	0.10	0.08
1410-18C-3-111	160.51	0.24	0.34
1410-18C-3-115	160.55	0.29	0.27
1410-18C-3-119	160.59	0.26	0.33
1410-18C-3-123	160.63	0.29	0.34
1410-18C-3-127	160.67	0.30	0.28
1410-18C-3-131	160.71	0.24	0.27
1410-18C-3-135	160.75	0.27	0.36
1410-18C-3-139	160.79	0.28	0.29
1410-18C-3-143	160.83	0.28	0.33
1410-18C-3-147	160.87	0.28	0.20
1410-18C-4-007	160.97	0.28	0.23
1410-18C-4-011	161.01	0.25	0.21
1410-18C-4-015	161.05	0.17	-0.02
1410-18C-4-019	161.09	0.26	0.27
1410-18C-4-023	161.13	0.20	0.24
1410-18C-4-027	161.17	0.25	0.05
1410-18C-4-031	161.21	0.21	0.20
1410-18C-4-035	161.25	0.30	0.15
1410-18C-4-039	161.29	0.29	0.15
1410-18C-4-047	161.37	0.26	0.19
1410-18C-4-051	161.41	0.28	0.19
1410-18C-4-055	161.45	0.18	0.20
1410-18C-4-059	161.49	0.28	0.21
1410-18C-4-063	161.53	0.25	0.13
1410-18C-4-067	161.57	0.30	0.22
1410-18C-4-071	161.61	0.22	0.23
1410-18C-4-075	161.65	0.27	0.18
1410-18C-4-079	161.69	0.28	0.14
1410-18C-4-083	161.73	0.20	0.25
1410-18C-4-087	161.77	0.38	0.22
1410-18C-4-091	161.81	0.27	0.20
1410-18C-4-095	161.85	0.32	0.25
1410-18C-4-099	161.89	0.29	0.19
1410-18C-4-103	161.93	0.31	0.21
1410-18C-4-107	161.97	0.24	0.16
1410-18C-4-111	162.01	0.18	0.17
1410-18C-4-115	162.05	0.24	0.22
1410-18C-4-119	162.09	0.21	0.18
1410-18C-4-123	162.13	0.16	0.14
1410-18C-4-127	162.17	0.19	0.17
1410-18C-4-131	162.21	0.20	0.10
1410-18C-4-135	162.25	0.13	0.10
1410-18C-4-139	162.29	0.18	0.10
1410-18C-4-143	162.33	0.16	0.08
1410-18C-4-147	162.37	0.18	0.13
1410-18C-5-003	162.43	0.10	-0.09
1410-18C-5-007	162.47	0.13	-0.01
1410-18C-5-015	162.55	0.18	-0.06

Continued on next page

Supplementary Table 3.1 – continued from previous page

Sample Code	Depth (mbsf)	δ13C	δ18O
1410-18C-5-019	162.59	0.17	-0.07
1410-18C-5-023	162.63	0.26	0.07
1410-18C-5-027	162.67	0.15	-0.08
1410-18C-5-035	162.75	0.17	0.01
1410-18C-5-039	162.79	0.22	-0.01
1410-18C-5-043	162.83	0.17	-0.35
1410-18C-5-059	162.99	0.20	-0.12
1410-18C-5-063	163.03	0.09	0.00
1410-18C-5-067	163.07	0.11	-0.25
1410-18C-5-071	163.11	0.12	-0.04
1410-18C-5-079	163.19	-0.03	-0.32
1410-18C-5-091	163.31	0.09	-0.21
1410-18C-5-095	163.35	0.13	-0.12
1410-18C-5-099	163.39	0.04	-0.21
1410-18C-5-103	163.43	0.11	-0.12
1410-18C-5-107	163.47	-0.03	-0.48
1410-18C-5-123	163.63	0.18	-0.04
1410-18C-5-127	163.67	0.06	-0.29
1410-18C-5-131	163.71	0.12	-0.14
1410-18C-5-135	163.75	0.04	-0.25
1410-19C-1-003	166.03	0.20	0.12
1410-19C-1-007	166.07	0.24	0.09
1410-19C-1-011	166.11	0.08	0.00
1410-19C-1-015	166.15	0.23	0.11
1410-19C-1-023	166.23	0.44	0.06
1410-19C-1-027	166.27	0.18	-0.15
1410-19C-1-031	166.31	0.21	0.19
1410-19C-1-035	166.35	0.11	-0.04
1410-19C-1-039	166.39	0.15	0.12
1410-19C-1-043	166.43	0.14	0.00
1410-19C-1-055	166.55	0.11	-0.24
1410-19C-1-059	166.59	0.12	0.12
1410-19C-1-063	166.63	0.16	0.19
1410-19C-1-067	166.67	0.12	0.05
1410-19C-1-071	166.71	0.21	-0.13
1410-19C-1-075	166.75	0.09	0.01
1410-19C-1-079	166.79	0.06	0.01
1410-19C-1-083	166.83	0.09	-0.10
1410-19C-1-087	166.87	0.01	0.00
1410-19C-1-091	166.91	0.08	-0.04
1410-19C-1-099	166.99	0.09	0.01
1410-19C-1-103	167.03	0.07	0.00
1410-19C-1-107	167.07	-0.01	-0.52
1410-19C-1-111	167.11	0.12	0.09
1410-19C-1-115	167.15	0.00	-0.02
1410-19C-1-119	167.19	0.18	-0.10
1410-19C-1-135	167.35	0.16	0.15
1410-19C-1-139	167.39	0.18	0.18
1410-19C-1-143	167.43	0.17	0.05
1410-19C-1-147	167.47	0.21	0.19
1410-19C-2-001	167.51	0.20	0.15
1410-19C-2-005	167.55	0.16	0.17
1410-19C-2-009	167.59	0.14	0.15
1410-19C-2-013	167.63	0.17	0.12
1410-19C-2-017	167.67	0.12	0.33
1410-19C-2-021	167.71	0.11	-0.10
1410-19C-2-025	167.75	0.13	0.01
1410-19C-2-029	167.79	0.12	0.00
1410-19C-2-033	167.83	0.06	-0.07
1410-19C-2-037	167.87	0.04	-0.06
1410-19C-2-041	167.91	0.04	-0.16
1410-19C-2-045	167.95	-0.01	-0.12
1410-19C-2-053	168.03	0.04	-0.17
1410-19C-2-057	168.07	0.51	0.09
1410-19C-2-065	168.15	0.13	-0.12
1410-19C-2-069	168.19	0.12	-0.07
1410-19C-2-073	168.23	0.10	-0.01
1410-19C-2-077	168.27	0.17	0.00
1410-19C-2-081	168.31	0.13	0.03
1410-19C-2-093	168.43	-0.02	0.00
1410-19C-2-097	168.47	0.12	0.04
1410-19C-2-101	168.51	0.08	-0.03
1410-19C-2-105	168.55	0.11	0.06
1410-19C-2-109	168.59	0.03	-0.08
1410-19C-2-113	168.63	-0.02	-0.33
1410-19C-2-117	168.67	0.01	0.21
1410-19C-2-125	168.75	0.03	-0.16
1410-19C-2-129	168.79	0.07	-0.07
1410-19C-2-133	168.83	0.11	0.07
1410-19C-2-137	168.87	0.09	-0.04

Continued on next page

Supplementary Table 3.1 – continued from previous page

Sample Code	Depth (mbsf)	δ13C	δ18O	Sample Code	Depth (mbsf)	δ13C	δ18O
1410-19C-2-141	168.91	0.09	0.20	1410-19C-4-017	170.67	0.15	0.08
1410-19C-2-145	168.95	0.24	0.19	1410-19C-4-021	170.71	0.23	0.17
1410-19C-2-149	168.99	0.14	0.37	1410-19C-4-025	170.75	0.25	0.16
1410-19C-3-003	169.03	0.19	0.20	1410-19C-4-029	170.79	0.15	0.13
1410-19C-3-007	169.07	0.13	0.23	1410-19C-4-033	170.83	0.25	0.03
1410-19C-3-011	169.11	0.20	0.22	1410-19C-4-037	170.87	0.25	0.18
1410-19C-3-015	169.15	0.26	0.14	1410-19C-4-041	170.91	0.29	0.21
1410-19C-3-019	169.19	0.13	0.06	1410-19C-4-045	170.95	0.28	0.08
1410-19C-3-023	169.23	0.17	0.21	1410-19C-4-049	170.99	0.20	0.11
1410-19C-3-031	169.31	0.21	0.26	1410-19C-4-053	171.03	0.19	0.06
1410-19C-3-035	169.35	0.10	0.08	1410-19C-4-057	171.07	0.35	0.11
1410-19C-3-039	169.39	0.17	0.09	1410-19C-4-061	171.11	0.26	0.07
1410-19C-3-043	169.43	0.10	0.09	1410-19C-4-069	171.19	0.19	0.02
1410-19C-3-047	169.47	-0.05	-0.07	1410-19C-4-073	171.23	0.11	-0.11
1410-19C-3-051	169.51	0.19	0.09	1410-19C-4-077	171.27	0.00	-0.09
1410-19C-3-055	169.55	0.11	-0.07	1410-19C-4-081	171.31	0.04	-0.13
1410-19C-3-059	169.59	0.06	-0.05	1410-19C-4-085	171.35	-0.03	-0.28
1410-19C-3-063	169.63	-0.01	-0.22	1410-19C-4-089	171.39	0.03	-0.08
1410-19C-3-067	169.67	-0.06	-0.21	1410-19C-4-093	171.43	0.01	-0.10
1410-19C-3-071	169.71	0.01	-0.10	1410-19C-4-101	171.51	0.02	-0.14
1410-19C-3-075	169.75	0.00	-0.31	1410-19C-4-105	171.55	0.03	-0.05
1410-19C-3-079	169.79	-0.04	0.00	1410-19C-4-109	171.59	0.07	0.09
1410-19C-3-083	169.83	0.06	-0.03	1410-19C-4-113	171.63	0.03	-0.05
1410-19C-3-091	169.91	0.09	-0.01	1410-19C-4-117	171.67	0.10	0.05
1410-19C-3-095	169.95	0.12	0.09	1410-19C-4-121	171.71	0.10	0.04
1410-19C-3-103	170.03	0.21	0.15	1410-19C-4-125	171.75	0.18	0.18
1410-19C-3-107	170.07	0.23	0.14	1410-19C-4-129	171.79	0.15	0.20
1410-19C-3-111	170.11	0.21	0.18	1410-19C-4-133	171.83	-0.05	0.08
1410-19C-3-115	170.15	0.27	0.08	1410-19C-4-137	171.87	0.12	0.23
1410-19C-3-119	170.19	0.18	0.15	1410-19C-4-141	171.91	0.14	0.25
1410-19C-3-123	170.23	0.19	0.23	1410-19C-4-145	171.95	0.13	0.20
1410-19C-3-127	170.27	0.19	0.15	1410-19C-4-149	171.99	0.20	0.22
1410-19C-3-131	170.31	0.26	0.13	1410-20C-1-001	175.61	0.08	0.10
1410-19C-3-135	170.35	0.19	0.15	1410-20C-1-005	175.65	0.22	0.06
1410-19C-3-143	170.43	0.26	0.16	1410-20C-1-017	175.77	0.24	0.03
1410-19C-3-147	170.47	0.22	0.08	1410-20C-1-021	175.81	0.13	-0.08
1410-19C-4-001	170.51	0.13	0.02	1410-20C-1-033	175.93	0.07	-0.04
1410-19C-4-005	170.55	0.23	0.13	1410-20C-1-037	175.97	0.15	0.04
1410-19C-4-009	170.59	0.19	0.25	1410-20C-1-041	176.01	0.08	-0.05
1410-19C-4-013	170.63	0.24	0.12	1410-20C-1-045	176.05	0.17	-0.02

Continued on next page

Supplementary Table 3.1 – continued from previous page

Sample Code	Depth (mbsf)	δ13C	δ18O	Sample Code	Depth (mbsf)	δ13C	δ18O
1410-20C-1-049	176.09	0.16	-0.05	1410-20C-2-065	177.75	0.06	-0.15
1410-20C-1-053	176.13	0.07	-0.03	1410-20C-2-069	177.79	0.14	-0.14
1410-20C-1-057	176.17	0.22	0.04	1410-20C-2-073	177.83	0.16	-0.14
1410-20C-1-061	176.21	0.18	0.13	1410-20C-2-077	177.87	0.20	-0.09
1410-20C-1-065	176.25	0.20	0.08	1410-20C-2-081	177.91	0.17	-0.10
1410-20C-1-069	176.29	0.24	0.09	1410-20C-2-085	177.95	0.21	0.04
1410-20C-1-073	176.33	0.24	0.06	1410-20C-2-089	177.99	0.09	-0.20
1410-20C-1-081	176.41	0.12	0.23	1410-20C-2-093	178.03	0.29	-0.02
1410-20C-1-085	176.45	0.18	0.34	1410-20C-2-097	178.07	0.29	0.00
1410-20C-1-089	176.49	0.00	0.29	1410-20C-2-101	178.11	0.31	0.02
1410-20C-1-093	176.53	0.30	0.15	1410-20C-2-105	178.15	0.27	0.13
1410-20C-1-097	176.57	0.35	0.23	1410-20C-2-109	178.19	0.38	0.05
1410-20C-1-101	176.61	0.18	0.22	1410-20C-2-113	178.23	0.22	0.14
1410-20C-1-105	176.65	0.22	0.29	1410-20C-2-117	178.27	0.25	0.14
1410-20C-1-109	176.69	0.17	0.11	1410-20C-2-121	178.31	0.33	0.04
1410-20C-1-113	175.69	0.25	-0.08	1410-20C-2-125	178.35	0.29	0.11
1410-20C-1-121	176.81	0.31	0.09	1410-20C-2-129	178.39	0.31	0.11
1410-20C-1-125	176.85	0.17	-0.03	1410-20C-2-133	178.43	0.28	0.15
1410-20C-1-129	176.89	0.19	0.01	1410-20C-2-137	178.47	0.38	0.19
1410-20C-1-133	176.93	0.36	-0.13	1410-20C-2-141	178.51	0.25	0.14
1410-20C-1-137	176.97	0.29	0.15	1410-20C-2-145	178.55	0.23	-0.02
1410-20C-1-141	177.01	0.37	0.15	1410-20C-2-149	178.59	0.22	0.10
1410-20C-1-145	175.73	0.23	-0.01	1410-20C-3-001	178.61	0.11	0.09
1410-20C-1-149	177.09	0.26	0.19	1410-20C-3-009	178.69	0.20	0.00
1410-20C-2-001	177.11	0.27	0.07	1410-20C-3-013	178.73	0.06	0.05
1410-20C-2-005	177.15	0.26	0.07	1410-20C-3-017	178.77	0.25	0.00
1410-20C-2-009	177.19	0.31	0.07	1410-20C-3-025	178.85	0.24	0.05
1410-20C-2-013	177.23	0.27	0.13	1410-20C-3-029	178.89	0.10	-0.10
1410-20C-2-017	177.27	0.26	0.22	1410-20C-3-033	178.93	0.11	-0.03
1410-20C-2-021	177.31	0.16	0.00	1410-20C-3-037	178.97	0.21	-0.04
1410-20C-2-025	177.35	0.21	0.07	1410-20C-3-041	179.01	0.30	0.02
1410-20C-2-029	177.39	0.16	-0.12	1410-20C-3-045	179.05	0.21	-0.07
1410-20C-2-033	177.43	0.17	0.02	1410-20C-3-049	179.09	0.12	-0.11
1410-20C-2-037	177.47	0.14	0.02	1410-20C-3-053	179.13	0.22	-0.11
1410-20C-2-041	177.51	0.18	0.02	1410-20C-3-057	179.17	0.09	-0.19
1410-20C-2-045	177.55	0.11	-0.09	1410-20C-3-061	179.21	0.17	0.01
1410-20C-2-049	177.59	0.04	-0.12	1410-20C-3-065	179.25	0.18	-0.09
1410-20C-2-053	177.63	0.25	-0.02	1410-20C-3-069	179.29	0.11	-0.20
1410-20C-2-057	177.67	0.22	-0.19	1410-20C-3-073	179.33	0.23	-0.04
1410-20C-2-061	177.71	0.25	0.03	1410-20C-3-081	179.41	0.23	-0.14

Continued on next page

Supplementary Table 3.1 – continued from previous page

Sample Code	Depth (mbsf)	δ13C	δ18O
1410-20C-3-085	179.45	0.18	-0.19
1410-20C-3-089	179.49	0.08	-0.12
1410-20C-3-093	179.53	0.08	-0.08
1410-20C-3-097	179.57	0.19	0.01
1410-20C-3-101	179.61	0.16	-0.13
1410-20C-3-105	179.65	0.11	-0.08
1410-20C-3-109	179.69	0.09	-0.02
1410-20C-3-113	179.73	0.15	-0.17
1410-20C-3-117	179.77	0.09	-0.24
1410-20C-3-121	179.81	0.19	-0.18
1410-20C-3-125	179.85	0.15	-0.14
1410-20C-3-129	179.89	0.15	-0.18
1410-20C-3-133	179.93	0.17	-0.11
1410-20C-3-137	179.97	0.10	-0.04
1410-20C-3-141	180.01	0.13	-0.06
1410-20C-3-145	180.05	0.09	-0.16
1410-20C-3-149	180.09	0.10	-0.01
1410-20C-4-001	180.11	0.12	0.02
1410-20C-4-005	180.15	0.15	-0.11
1410-20C-4-009	180.19	0.11	-0.03
1410-20C-4-013	180.23	0.14	-0.10
1410-20C-4-021	180.31	0.25	-0.05
1410-20C-4-025	180.35	0.08	-0.09
1410-20C-4-029	180.39	0.07	-0.35
1410-20C-4-033	180.43	0.07	-0.26
1410-20C-4-037	180.47	0.06	-0.28
1410-20C-4-041	180.51	-0.05	-0.55
1410-20C-4-049	180.59	-0.06	-0.49
1410-20C-4-053	180.63	0.07	-0.20
1410-20C-4-061	180.71	0.01	-0.44
1410-20C-4-069	180.79	0.11	-0.29
1410-20C-4-073	180.83	0.11	-0.40
1410-20C-4-081	180.91	0.12	-0.54
1410-20C-4-085	180.95	0.21	-0.34
1410-20C-4-089	180.99	0.18	-0.26
1410-20C-4-093	181.03	0.09	-0.44
1410-20C-4-097	181.07	0.25	-0.10
1410-20C-4-101	181.11	0.15	-0.17
1410-20C-4-109	181.19	0.08	-0.25
1410-20C-4-113	181.23	0.11	-0.43
1410-20C-4-117	181.27	0.26	-0.18
1410-20C-4-121	181.31	0.11	-0.31
1410-20C-4-125	181.35	0.21	-0.32
1410-20C-4-129	181.39	0.07	-0.35
1410-20C-4-133	181.43	0.22	-0.38
1410-20C-4-137	181.47	0.18	-0.33
1410-20C-4-141	181.51	0.25	-0.34
1410-20C-4-145	181.55	0.29	-0.18
1410-20C-4-149	181.59	0.27	0.05
1410-20C-5-001	181.61	0.27	-0.08
1410-20C-5-005	181.65	0.25	-0.04
1410-20C-5-009	181.69	0.16	0.06
1410-20C-5-013	181.73	0.33	0.01
1410-20C-5-017	181.77	0.25	0.12
1410-20C-5-021	181.81	0.17	-0.05
1410-20C-5-025	181.85	0.23	0.05
1410-20C-5-029	181.89	0.27	-0.07
1410-20C-5-033	181.93	0.20	0.03
1410-20C-5-037	181.97	0.21	-0.14
1410-20C-5-041	182.01	0.25	-0.09
1410-20C-5-045	182.05	0.21	-0.25
1410-20C-5-053	182.13	0.19	-0.16
1410-20C-5-057	182.17	0.37	0.09
1410-20C-5-061	182.21	0.14	-0.28
1410-20C-5-065	182.25	0.35	-0.23
1410-20C-5-069	182.29	0.23	-0.13
1410-20C-5-077	182.37	0.24	-0.20
1410-20C-5-081	182.41	0.21	-0.09
1410-20C-5-085	182.45	0.19	-0.19
1410-20C-5-089	182.49	0.13	-0.29
1410-20C-5-093	182.53	0.20	-0.19
1410-20C-5-097	182.57	0.21	-0.09
1410-20C-5-101	182.61	0.23	-0.07
1410-20C-5-105	182.65	0.34	-0.01
1410-20C-5-113	182.73	0.31	-0.01
1410-20C-5-121	182.81	0.31	-0.11
1410-20C-5-129	182.89	0.41	-0.15
1410-20C-5-133	182.93	0.31	-0.16
1410-20C-5-137	182.97	0.23	-0.20
1410-20C-5-141	183.01	0.17	-0.19

Continued on next page

Supplementary Table 3.1 – continued from previous page

Sample Code	Depth (mbsf)	δ13C	δ18O
1410-20C-5-145	183.05	0.25	-0.02
1410-20C-5-149	183.09	0.26	-0.2
1410-20C-6-001	183.11	0.14	-0.08
1410-20C-6-005	183.15	0.28	0.00
1410-20C-6-009	183.19	0.29	-0.02
1410-20C-6-017	183.27	0.13	-0.08
1410-20C-6-021	183.31	0.24	-0.09
1410-20C-6-025	183.35	0.23	-0.12
1410-20C-6-029	183.39	0.32	-0.09
1410-20C-6-037	183.47	0.26	-0.06
1410-20C-6-041	183.51	0.27	-0.14
1410-20C-6-045	183.55	0.34	-0.09
1410-20C-6-053	183.63	0.35	-0.10
1410-20C-6-057	183.67	0.23	-0.09
1410-20C-6-061	183.71	0.33	-0.11
1410-20C-6-065	183.75	0.17	-0.07
1410-20C-6-073	183.83	0.25	-0.25
1410-20C-6-077	183.87	0.35	-0.03
1410-20C-6-081	183.91	0.24	-0.28
1410-20C-6-089	183.99	0.34	-0.16
1410-20C-6-093	184.03	0.26	-0.23
1410-20C-6-097	184.07	0.10	-0.14
1410-20C-6-101	184.11	0.20	-0.14
1410-20C-6-105	184.15	0.21	-0.03
1410-20C-6-109	184.19	0.18	-0.19
1410-20C-6-117	184.27	0.21	-0.22
1410-20C-6-121	184.31	0.17	-0.41
1410-20C-6-125	184.35	0.22	-0.19
1410-20C-6-129	184.39	0.20	-0.22
1410-20C-6-133	184.43	0.19	-0.17
1410-20C-6-141	184.51	0.14	-0.16
1410-21C-2-051	187.21	0.09	-0.30
1410-21C-2-059	187.29	0.16	-0.18
1410-21C-2-067	187.37	0.28	-0.02
1410-21C-2-071	187.41	0.27	-0.10
1410-21C-2-075	187.45	0.30	0.07
1410-21C-2-079	187.49	0.30	0.02
1410-21C-2-083	187.53	0.36	0.07
1410-21C-2-091	187.61	0.32	0.01
1410-21C-2-095	187.65	0.34	0.11
1410-21C-2-099	187.69	0.03	-0.24
1410-21C-2-103	187.73	0.30	0.20
1410-21C-2-107	187.77	0.36	0.22
1410-21C-2-111	187.81	0.19	0.21
1410-21C-2-115	187.85	0.30	0.03
1410-21C-2-119	187.89	0.34	0.08
1410-21C-2-123	187.93	0.20	0.19
1410-21C-2-127	187.97	0.31	0.05
1410-21C-2-131	188.01	0.33	-0.02
1410-21C-2-139	188.09	0.32	0.12
1410-21C-2-147	188.17	0.26	0.06
1410-21C-3-001	188.21	0.34	0.14
1410-21C-3-009	189.09	0.36	0.03
1410-21C-3-017	188.37	0.35	0.15
1410-21C-3-021	188.41	0.36	0.13
1410-21C-3-025	188.45	0.29	0.12
1410-21C-3-029	188.49	0.36	0.08
1410-21C-3-037	188.57	0.37	-0.03
1410-21C-3-041	188.61	0.29	0.04
1410-21C-3-045	188.65	0.30	0.05
1410-21C-3-053	188.73	0.21	-0.05
1410-21C-3-065	188.85	0.34	-0.02
1410-21C-3-069	188.89	0.11	-0.07
1410-21C-3-081	189.01	0.24	-0.20
1410-21C-3-085	189.05	0.23	-0.12
1410-21C-3-093	189.13	0.31	0.16
1410-21C-3-097	189.17	0.29	0.01
1410-21C-3-101	189.21	0.35	0.11
1410-21C-3-105	189.25	0.33	0.05
1410-21C-3-109	189.29	0.27	0.08
1410-21C-3-113	188.29	0.32	0.05
1410-21C-3-113	189.33	0.23	-0.19
1410-21C-3-117	189.37	0.38	0.16
1410-21C-3-121	189.41	0.33	0.23
1410-21C-3-125	189.45	0.35	0.13
1410-21C-3-137	188.33	0.33	0.13
1410-21C-3-137	189.57	0.40	-0.02
1410-21C-3-141	189.61	0.37	-0.02
1410-21C-3-145	189.65	0.47	0.25
1410-21C-3-149	189.69	0.23	0.06

Continued on next page

Supplementary Table 3.1 – continued from previous page

Sample Code	Depth (mbsf)	δ13C	δ18O
1410-21C-4-009	189.79	0.37	0.01
1410-21C-4-013	189.83	0.26	-0.09
1410-21C-4-017	189.87	0.29	-0.08
1410-21C-4-021	189.91	0.32	0.00
1410-21C-4-025	189.95	0.29	-0.01
1410-21C-4-029	189.99	0.30	-0.11
1410-21C-4-033	190.03	0.35	0.03
1410-21C-4-036	190.06	0.34	-0.12
1410-21C-4-040	190.10	0.39	-0.03
1410-21C-4-044	190.14	0.36	-0.07
1410-21C-4-048	190.18	0.32	-0.12
1410-21C-4-052	190.22	0.36	-0.05
1410-21C-4-056	190.26	0.36	-0.07
1410-21C-4-060	190.30	0.25	-0.15
1410-21C-4-064	190.34	0.29	-0.19
1410-21C-4-068	190.38	0.30	-0.14
1410-21C-4-072	190.42	0.30	0.02
1410-21C-4-076	190.46	0.24	-0.07
1410-21C-4-080	190.50	0.24	-0.08
1410-21C-4-084	190.54	0.30	-0.03
1410-21C-4-088	190.58	0.37	-0.01
1410-21C-4-092	190.62	0.30	-0.17
1410-21C-4-096	190.66	0.25	-0.23
1410-21C-4-100	190.70	0.27	-0.12
1410-21C-4-104	190.74	0.30	-0.15
1410-21C-4-108	190.78	0.30	0.05
1410-21C-4-112	190.82	0.22	-0.19
1410-21C-4-120	190.90	0.28	0.03
1410-21C-4-124	190.94	0.33	-0.04
1410-21C-4-128	190.98	0.33	-0.01
1410-21C-4-132	191.02	0.32	0.04
1410-21C-4-136	191.06	0.38	0.02
1410-21C-4-142	191.10	0.30	-0.06
1410-21C-5-005	191.69	0.34	0.02
1410-21C-5-021	191.41	0.38	-0.09
1410-21C-5-029	191.49	0.22	0.01
1410-21C-5-033	191.53	0.31	0.07
1410-21C-5-037	191.57	0.27	-0.15
1410-21C-5-041	191.61	0.34	0.04
1410-21C-5-045	191.65	0.24	0.06
1410-21C-5-053	191.73	0.27	0.06
1410-21C-5-057	191.77	0.33	0.09
1410-21C-5-065	191.85	0.16	-0.09
1410-21C-5-069	191.89	0.20	-0.05
1410-21C-5-073	191.93	0.25	0.05
1410-21C-5-081	192.01	0.29	0.00
1410-21C-5-085	192.05	0.32	0.03
1410-21C-5-089	192.09	0.29	0.02
1410-21C-5-093	192.13	0.27	-0.16
1410-21C-5-097	192.17	0.21	-0.21
1410-21C-5-101	192.21	0.16	-0.21
1410-21C-5-105	192.25	-0.03	-0.36
1410-21C-5-113	192.33	0.28	-0.46
1410-21C-5-117	191.29	0.13	-0.14
1410-21C-5-121	192.41	0.22	-0.12
1410-21C-5-129	192.49	0.20	-0.40
1410-21C-5-137	191.33	0.31	-0.16
1410-21C-5-141	192.61	0.35	0.12
1410-21C-5-145	192.65	0.33	-0.02
1410-21C-5-149	192.69	0.40	0.00
1410-21C-6-001	192.71	0.36	0.00
1410-21C-6-005	192.75	0.28	0.01
1410-21C-6-009	192.79	0.39	0.07
1410-21C-6-013	192.83	0.38	0.09
1410-21C-6-017	192.87	0.37	0.09
1410-21C-6-021	192.91	0.44	0.03
1410-21C-6-025	192.95	0.30	0.00
1410-21C-6-029	192.99	0.40	0.05
1410-21C-6-033	193.03	0.37	-0.10
1410-21C-6-037	193.07	0.33	0.11
1410-21C-6-041	193.11	0.33	0.01
1410-21C-6-045	193.15	0.34	-0.05
1410-21C-6-049	193.19	0.31	-0.08
1410-21C-6-053	193.23	0.26	-0.06
1410-21C-6-057	193.27	0.40	-0.04
1410-21C-6-061	193.31	0.37	0.01
1410-21C-6-065	193.35	0.37	-0.01
1410-21C-6-069	193.39	0.33	-0.03
1410-21C-6-073	193.43	0.30	0.05
1410-21C-6-077	193.47	0.40	0.08

Continued on next page

Supplementary Table 3.1 – continued from previous page

Sample Code	Depth (mbsf)	δ13C	δ18O	Sample Code	Depth (mbsf)	δ13C	δ18O
1410-21C-6-085	193.55	0.44	-0.06	1410-22C-2-005	196.35	0.08	-0.12
1410-21C-6-089	193.59	0.33	0.03	1410-22C-2-009	196.39	0.19	-0.30
1410-21C-6-093	193.63	0.43	0.04	1410-22C-2-013	196.43	0.18	0.14
1410-21C-6-097	193.67	0.36	0.03	1410-22C-2-017	196.47	0.13	0.20
1410-21C-6-101	193.71	0.41	-0.01	1410-22C-2-021	196.51	0.19	0.03
1410-21C-6-105	193.75	0.31	-0.08	1410-22C-2-025	196.55	0.12	0.06
1410-21C-6-117	193.87	0.29	-0.08	1410-22C-2-033	196.63	0.14	0.01
1410-21C-6-121	193.91	0.30	-0.06	1410-22C-2-045	196.75	0.12	0.05
1410-21C-6-125	193.95	0.26	-0.12	1410-22C-2-057	196.87	0.10	-0.04
1410-21C-6-129	193.99	0.31	-0.05	1410-22C-2-061	196.91	0.09	-0.03
1410-22C-1-113	195.93	0.10	0.18	1410-22C-2-065	196.95	0.12	0.05
1410-22C-1-121	196.01	0.07	0.01	1410-22C-2-069	196.99	0.19	-0.17
1410-22C-1-129	196.09	0.14	-0.04	1410-22C-2-073	197.03	0.14	0.04
1410-22C-1-133	196.13	0.15	-0.07	1410-22C-2-077	197.07	0.10	0.08
1410-22C-1-149	196.29	0.09	-0.11				